Stability, Mixing and Asymptotic Modeling in Flows with Well-Separated Characteristic Length Scales

Dissertation
Francesco Romanò

Thèse d'Habilitation à Diriger des Recherches

Stability, Mixing and Asymptotic Modeling in Flows with Well-Separated Characteristic Length Scales

H.D.R. Candidate

Francesco ROMANÒ

July 4, 2024

Doctoral School XPA18

Science for Engineers

Specialty

Fluid Mechanics

H.D.R. Committee:

Oliver E. JENSEN University of Manchester	*Reviewer*
Vincent TERRAPON University of Liege	*Reviewer*
Laurette S. TUCKERMAN CNRS, Sorbonne Université, PMMH	*Reviewer*
Catherine COLIN Toulouse INP, ENSEEIHT	*Examiner*
Sofiane KHELLADI Arts et Métiers, LIFSE	*Examiner*
Jean-Philippe LAVAL CNRS, University of Lille, LMFL	*Examiner (Garant)*

Laboratoire de Mécanique des Fluides de Lille Kampé de Fériet

Arts Sciences et Technologies et Métiers

Acknowledgements

I would like to begin by thanking the colleagues who agreed to be part of my HDR committee. First and foremost, I express my gratitude to Oliver E. Jensen, Vincent Terrapon, and Laurette S. Tuckerman for dedicating their time to reviewing this manuscript and offering insightful feedback that enhances my scientific self-criticism. I am thankful to Catherine Colin and Sofiane Khelladi for serving as examiners during the HDR defense, as their valuable remarks set a standard for my future research endeavors. I also owe my gratitude to Jean-Philippe Laval, the *garant* of my HDR and director of the LMFL. His support and continuous availability were instrumental in preparing this manuscript.

I am also thankful to the colleagues with whom I had the opportunity to collaborate over the last few years, whether as part of the same research team or teaching team. Since joining Arts et Métiers, I have been warmly welcomed at the LMFL, and I believe that preserving and promoting such a positive atmosphere will contribute to the lab's success. Specifically, I want to express my gratitude to Alberto Baretter, Gérard Bois, Antoine Dazin, Paolo Errante, Meng Fan, Pierric Joseph, Marcello Meldi, and Sophie Simonet. I have spent most of my time at Arts et Métiers with them, and I am pleased to acknowledge them as friends. I would also like to acknowledge the people from other French labs with whom I have shared thoughts and friendship since when I joined Arts et Métiers: Amir Bahrani, Teodor Burghelea, Stefano Berti, Enrico Calzavarini, O. Coutier-Delgosha, and Tom Lacassagne. Furthermore, I take the chance of thanking the PhD students and PostDocs enganged in the research projects I co-supervise at Arts et Métiers: Hossameldin Abdelaziz, Mohamed Elhawary, Marwane Elkarii, Meng Fan, Renjie Hao, Zhonxuan Hou, Adou Francis Seka, Bo Wang, and Zhidian Yang. Their dedication, curiosity, and contributions are integral to the dynamics of our research group, and engaging in scientific discussions with them is truly rewarding.

If I have reached this stage in my career, it is due to the invaluable guidance of two mentors who fostered my growth as a researcher during my time as a PhD student and a PostDoc. Prior to relocating to France, I completed a PostDoc under the supervision of James B. Grotberg at the University of Michigan. Jim introduced me to the realm of biofluids, and his exceptional capabilities to navigate between medicine and fluid mechanics enabled me to develop a grasp of the fundamental questions in respiratory flows. For the great time I spent in Ann Arbor and the confidence I gained in pursuing my career, I owe him my gratitude. Before that time, I spent five and a half years in Vienna, first as a PhD student and later as a PostDoc in the research

group led by Hendrik C. Kuhlmann at TU Wien. This marked my first immersive experience in a research environment. The affinity that links me and Hendrik as scientists consists of believing that research is about investigating a question rather than focusing on solving a problem. The curiosity and scientific integrity at the core of our frequent exchanges, assisted by the scientific rigor that he instilled in me, drove endless discussions that I preserve as a vivid and precious memory of my time in Vienna. I thank him for showing me that professional hierarchy does not play any role in genuine scientific inquiry, and openly challenging everyone's view is part of the investigative process. Beyond him serving as an inspiration, I am grateful to Hendrik for the friendship we have cultivated and the meaningful time spent together. I am also thankful to Jim and Hendrik for facilitating connections with various researchers. This helped me to establish my professional network that, sometimes, ended up enlarging my personal circle. Let me therefore mention Pierre-Emmanuel des Boscs, Metin Muradoğlu, Satyajit Pramanik, and Michael Riedl, whom I got in contact with as collaborators and became good friends of mine. Additionally, I also want to thank Haotian Wu and Mario Stojanović, both part of Hendrik's group and excellent researchers, with whom I had the pleasure of collaborating.

Finally, I am deeply thankful to all my friends and especially to my family for their constant support throughout these years. My academic pursuits led me to different countries, and having their unconditional support granted me the emotional stability needed to undertake this path. In particular, I want to express my gratitude to Tuğçe, my wife, for her love and unconditional encouragement, as well as for her invaluable assistance. Her understanding, empathy and patience ensured that I could complete this manuscript to the best of my abilities.

Abstract

The significance of fluid dynamics systems with well-separated length scales is discussed, serving as the motivation for this thesis. To comprehend the interaction among primary physical mechanisms, specific modeling methods are required, as each scale is essential for reproducing and predicting the large-scale phenomena under investigation. Given the diverse fluid dynamics domains addressed in this manuscript, we first start in §1 by revisiting essential concepts frequently employed throughout, including asymptotic theory, hydrodynamic stability theory, chaos theory, and modeling of a dispersed particulate phase.

A first class of problems where well-separated length scales are of crucial importance leads to particle clustering in laminar flows discussed in §2. We demonstrate and explain various cases of particles clustering in steady flows, both in two and three dimensions. These examples of particle accumulations reveal shared features among all the systems studied, leading to the identification of a class of particle attractors called Finite-Size Coherent Structures. The underlying physical mechanism relies on considering the global fluid transport at largest scale, the particle dynamics at intermediate scale, and the particle–boundary interaction at smallest scale.

Thereafter, §3 is dedicated to the application of well-separated-scale flows to turbomachines. A centrifugal pump and an axial compressor are considered, focusing on the instabilities observed upon a variation of the flow rate. It will be discussed how small radial gaps can strongly affect the onset of rotating instabilities at the large flow scale, i.e. impeller or carter radius, potentially leading to rotating stalls. Their significance stems from the reduced safety margin and the impact on the operating conditions of the machine.

A last example of problems with well-separated length scales is discussed in §4 delving into the respiratory fluid mechanics of distal airways. Asymptotic theory and hydrodynamic instability will provide the theoretical tools to understand the occlusion reported in the bronchioles as they undergo an interfacial instability originated in thin non-Newtonian films coating the airway. The impact of mucus rheology and surfactants on the liquid plug formation will be discussed entering in details about the importance of the thin layer of mucus coating the airways (smallest scale) on the potential hindering of gas exchange for large portions of the lungs (largest scale).

Finally, five avenues for future research in multiscale flows with well-separated length scales are discussed in §5. The research vision integrates theory, numerical simulations, machine-learning, reduced-order models, and scale-matching approaches. Given the specific challenges of each proposed project, dedicated multiscale approaches are envisioned and briefly discussed.

Résumé

Dans ce mémoire est discutée l'importance de la dynamique d'écoulements fluides caractérisés par des échelles de longueur bien séparées. Pour comprendre l'interaction entre les mécanismes physiques primaires, chaque échelle est essentielle pour reproduire et prédire les phénomènes aux grandes échelles étudiés. Compte tenu des divers domaines de la dynamique des fluides abordés dans ce manuscrit, nous commençons en §1 par revisiter les concepts essentiels, tels que la théorie asymptotique, la stabilité hydrodynamique, le chaos et la modélisation des particules dispersées.

Une première classe de problèmes, où des échelles de longueur bien séparées jouent un rôle crucial, concerne l'accumulation de particules dans des écoulements laminaires (§2). Nous démontrons et expliquons divers cas d'accumulation de particules en deux et trois dimensions. Ces exemples révèlent des caractéristiques communes à tous les systèmes étudiés, conduisant à l'identification d'une classe d'attracteurs de particules appelés Finite-Size Coherent Structures. Le mécanisme physique sous-jacent implique la prise en compte du transport global des fluides à une échelle macroscopique, de la dynamique des particules à une échelle intermédiaire, et de l'interaction particule-limite à l'échelle la plus petite.

Ensuite, §3 est dédié à l'application aux turbomachines. On examine une pompe centrifuge et un compresseur axial, en mettant l'accent sur les instabilités observées lors de variations du débit. On discute de l'impact que de petits jeux radiaux peuvent avoir sur l'apparition des instabilités tournantes à grande échelle (le rayon de la roue ou du carter), pouvant éventuellement entraîner des décrochages tournants. Leurs influences sur la marge de sécurité et leurs effets sur les conditions de fonctionnement de la machine sont considérés.

Un dernier exemple de problèmes à échelles de longueur bien séparées est abordé dans §4, qui examine la mécanique des voies respiratoires. La théorie asymptotique et les instabilités hydrodynamiques seront utilisées pour comprendre l'occlusion dans les bronchioles due à une instabilité interfaciale. On discutera de l'impact de la rhéologie du mucus et des tensioactifs sur la formation des bouchons liquides, en considérant l'importance de la fine couche de mucus recouvrant les voies respiratoires (échelle la plus petite) sur les obstructions qu'ils impliquent potentiellement sur les échanges gazeux dans de vastes zones des poumons (échelle la plus grande).

Enfin, cinq orientations de recherche future sont abordées dans §5 en intégrant la théorie, les simulations numériques, les modèles d'ordre réduit basés sur le machine learning et les méthodes de couplage des échelles. Étant donné les défis spécifiques de chaque projet proposé, des approches multi-échelles dédiées sont envisagées et succinctement discutées.

Contents

Chapter 1

Motivation and Elements of Theory

Summary

Several flows have key features that originate from the presence of significantly different characteristic length scales. They provide the motivation for this thesis and require dedicated modeling approaches to understand the interplay between leading-order physical mechanisms. The fundamental concepts and methods employed throughout this thesis are therefore recalled in this chapter, with a special focus on asymptotic modeling, stability analysis and chaos theory. The structure of the thesis is finally outlined in the last section of this chapter.

Contents

1.1 Introduction and motivation

In the field of fluid dynamics, the study of flows characterized by a few *well-separated* characteristic scales has gained significant attention due to its relevance in understanding complex phenomena. Characteristic scales separation is often manifested in the form of multiscale interactions, where distinct spatial and temporal scales coexist and significantly influence the macroscopic behavior of the flow. As example of the industrial relevance of such multiscale flows one could consider the combustion process in engines, where the coupling of chemical reactions at molecular scale influences the overall fluid dynamics on a larger scale [1]. In the domain of microfluidics, flows often exhibit distinct characteristic scales, particularly relevant in the context of efficient particle sorting in microchannels [2]. Other examples of multiscale flows with well-separated characteristic scales are found in biological flows, such as blood circulation, where splenic filtration of red cells through narrow interendothelial slits (see fig. 1.1(a)) involves a hierarchy of scales [3]. The significance of distinct well-separated scales in understanding blood rheology and microcirculation [4] is discussed in [5], while [6] considers the coating process in manufacturing, where the role of capillary and viscous forces at the small scales influence the large-scale coating uniformity in industrial processes (see fig. 1.1(b)).

These examples underscore the ubiquitous nature of fluid dynamic systems characterized by a discrete amount of well-separated scales, emphasizing their crucial role in shaping the behavior of complex flows. In this manuscript, we will investigate several examples of flows in which two or three well-separated characteristic scales are simultaneously interacting in such a singular way that neglecting the smallest scale would not allow to identify, understand, and reproduce the dominant phenomena at large scale.

To guide the understanding of the phenomena of interest in this manuscript, we revisit and interconnect several theoretical concepts. Asymptotic series will serve to unravel the behavior as scales diverge (§1.2). In §1.3 stability analysis will be introduced for studying the system dynamics to imposed perturbations. Thereafter, in §1.4, chaos theory will be employed as a framework to deepen into the underlying deterministic yet unpredictable nature of certain flows. Through this structured approach, the ensuing sections aim to recall some elements of theory that will help analyzing and understanding the complexities inherent in flows with well-separated characteristic scales. Finally, the manuscript structure will be summarized in §1.5.

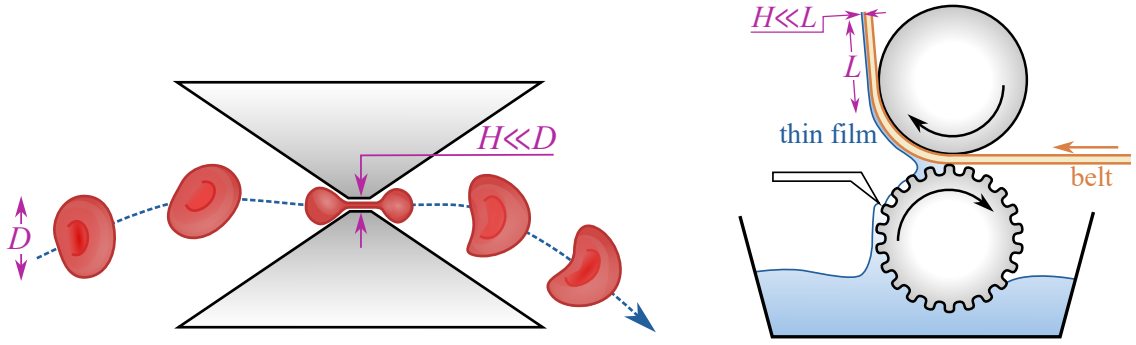

(a) Red blood cell through a narrow slit

(b) Gravure coating process

Figure 1.1: Examples of multiscale flows with well-separated characteristic scales, i.e. $H \ll D,\ L$: (a) a red blood cell across a constriction and (b) the gravure coating system.

1.2 Perturbation theory

The fundamental equations governing the motion of fluids encompass nonlinearities in the continuity, momentum, energy and constitutive law equations, with the exception of irrotational, incompressible, inviscid single-phase fluids with no free boundaries. Owing to the almost ubiquitous nonlinear character of fluid dynamics equations, their exact solutions are know only for a few idealized configurations. On the other hand, the high degree of symmetries encoded in the system of partial differential equations (PDEs) that governs the motion of fluids can lead to so-called *self-similar flows* that consist of invariant solutions in time or space, provided an ad-hoc scaling of the mathematical problem coordinates and variables. Examples of inviscid compressible self-similar flows include the steady supersonic flow past a convex corner [7, 8] or an unyawed circular cone [9, 10], a cylinder uniformly expanding into a still ideal gas [11, 12], as well as an infinite plane wall moved impulsively into a still ideal gas (Riemann problem, [13]). Correspondingly, as examples of incompressible Newtonian flows one can consider the steady flow between parallel plates (Couette and Poiseuille flows), in a circular pipe (Hagen–Poiseuille flow) and for annular configurations [14], as well as the impulsive [15, 16] or sinusoidal motion (Stokes' second problem [17]) of an infinite plate in direction tangential to itself. All such examples of known solutions apply to simplified configurations that respect the symmetries needed for assuming a self-similar ansatz. Whenever intricate space- and time-dependent boundary conditions are applied, or whenever complex geometries are considered, approximating the targeted problem can provide significant insights on the physical mechanisms that drive the flow [18].

There are several conceptually-different ways to provide an approximation for a complex problem. *Data-driven reduced-order modeling* proposes to approximate the dynamics of a system by using Dynamic Mode Decomposition (DMD [19, 20]), Proper Orthogonal Decomposition (POD [21, 22]), Koopman modes [23, 24], or Sparse Identification of Non-linear Dynamics (SYNDy [25]). Such methods have been proven successful in reproducing and sometimes predicting complex dynamics, however, they require some information from the real system and they cannot derive a-priori approximations. More classic approaches do not require solution or measured data of the system to approximate, but they rather assume additional working hypotheses on the expected solution and derive the corresponding approximated dynamics of the flow. Examples of such approximations are the Chester–Chisnell–Whitham theory of shock dynamics [26, 27, 28], the Kármán–Tsien theory of airfoils in subsonic flows [29, 30], and the Spreiter's local linearization in transonic flow [31]. Such theories apply to idealized configurations and can successfully provide an insightful approximation of the flow if and only if the working hypotheses are robustly respected by the original problem within a good degree of accuracy. To date, there is however no well-defined mathematical limit under which such theories provide an exact solution of the fluid dynamics governing equations. They are therefore *heuristic approximations*.

Perturbation theory provides a mathematical framework to systematically tackle the governing equations by employing successive corrections that provide a rational approximation of the original problem. In fact, perturbation theory relies on *asymptotic expansions* of the fluid dynamics equations in terms of a small *perturbation parameter* ϵ. The resulting approximations become

asymptotically accurate in the limit of the perturbation tending to $\epsilon \to 0$. The advantage of such theories over the data-driven and heuristic approximations mentioned above is that perturbation methods help rationalizing the original complex problem splitting it into multiple simpler systems ranked in terms of their generalized order in ϵ. For instance, let us consider the motion of a small spherical particle moving in an unbounded flow. If the Reynolds number of the particle is very small $\mathrm{Re_p} = ||\boldsymbol{u} - \boldsymbol{u}_\mathrm{p}||a_\mathrm{p}/\nu \ll 1$, where $\boldsymbol{u}$ is the unperturbed flow velocity around the particle, $\boldsymbol{u}_\mathrm{p}$ the particle velocity, a_p its radius and ν the kinematic viscosity of the fluid, one can assume that the particle Reynolds number is asymptotically small and derive an infinite set of governing equations that describe the particle motion as superposition of successive corrections. In our example, the solution to the leading-order problem represents the particle dynamics in the inertialess limit (see [32, 33] and §1.4.5 for more details), the linear-order correction includes the most significant inertial contributions [34, 35], and higher-order corrections are provided by including more terms of the asymptotic series in $\mathrm{Re_p}$. Similar asymptotic expansions have been used to tackle a number of fundamental fluid dynamics problems, such as the weakly compressible effects on the velocity potential around a cylinder or an hypersphere (Janzen–Rayleigh expansion for asymptotically-small Mach numbers [11, 12]), the flow field and aerodynamic coefficients for elongated bodies (lifting-line theory for asymptotically-large aspect ratios [36, 37]), as well as the creeping flow regime (Stokes flow for asymptotically-small Reynolds numbers [38, 39]), and boundary-layer flows (for asymptotically-large Reynolds numbers [40]). Such a non-comprehensive list of asymptotic theories helps understanding the range of applications of perturbation methods, even if their mathematical validity strictly holds only when the asymptotic limit is taken. Even if this formally represents a limit of employing asymptotic expansions, most of the solutions, either in closed or in numerical form, provide a remarkably good approximation of the target problem even significantly far from their strict domain of applicability (see e.g. [18]). Known exceptions are however reported in the literature, e.g., for the stability of shear flow to small perturbations (see [41, 42] and §1.3 for more details) or for the dynamics of a gas bubble in a small pipe/channel where the Bretherton solution for asymptotically-small capillary numbers Ca [43] deviates rapidly from the corresponding flow at small, yet finite Ca [44]. In summary, perturbation theory overcomes the need of information proper of data-driven modeling, as well as the lack of mathematical rigour of the working hypothesis for non-asymptotic, but rather heuristic approaches. On the other hand, perturbation methods may suffer rapid deviations of the target flow from its asymptotic limits. Hence, combining such three approaches can strongly expand the domain for complex flow approximations one can deal with.

A last introductory note about perturbation theory deals with the two kind of scenarios reported in the literature. Whenever a perturbation solution is uniformly valid over the whole domain and provides accurate approximation of the target problem within a few terms of the expansion, the problem is said to be a *regular perturbation problem*. An example is presented in §1.2.1 for thin film coating a flat surface. If the perturbation solution rather leads to a violation of the boundary or asymptotic conditions, a *singular perturbation problem* is faced. Among the methods developed for dealing with singular problems there are the *method of strained coordinates* and the *method of matched asymptotic expansions*. The latter will be briefly introduced in §1.2.2.

1.2.1 Long-scale asymptotic theory

When subjected to mechanical, thermal, or structural perturbations, thin fluid films manifest dynamic phenomena encompassing propagation and steepening of waves, wetting fronts due to ruptures or spreading of the film (examples of singular problems), as well as the emergence of chaotic responses. Leveraging the inherent disparities in length scales, perturbation theory is widely employed to simplify the complete set of governing equations and boundary conditions into a highly nonlinear evolution equation or a set of equations. They conserve most of the essential physics and yet yield a mathematical approximation notably more tractable than the original one. For an extensive survey of asymptotic approximations applied to thin films, we refer to [45, 46, 47, 48, 49].

Perturbation theory is here demonstrated by considering a two-dimensional liquid film bounded, on the one side, by a flat horizontal solid wall and, on the other side, by an interface with a passive gas (see fig. 1.2(a)). The isothermal, incompressible thin film flow is governed by the continuity and momentum equation:

$$\partial_x u + \partial_y v = 0, \tag{1.1a}$$

$$\rho\left(\partial_t u + u\partial_x u + v\partial_y u\right) = -\partial_x p + \mu\nabla^2 u, \tag{1.1b}$$

$$\rho\left(\partial_t v + u\partial_x v + v\partial_y v\right) = -\partial_y p + \mu\nabla^2 v - \rho g, \tag{1.1c}$$

where the t and $\boldsymbol{x} = (x, y)$ are the time and the spatial coordinates, $\boldsymbol{u} = (u, v)$ is the velocity field of the film, p its pressure field measured relatively to the gas pressure, ρ is the liquid density, μ its dynamic viscosity, and $\boldsymbol{g} = (0, -g)$ the acceleration of gravity. The film is assumed to be infinitely extended and the boundary conditions are enforced at the wall, i.e. at $y = 0$, and at the interface, i.e. at $y = h(x, t)$, where h denotes the local instantaneous thickness of the film. Assuming no slip and no penetration at the wall, defining the kinematic relation between film deformation and vertical flow velocity, accounting for the normal stress jump at the interface and in the absence of an imposed shear stress, the boundary conditions (BCs) read:

$$y = 0: \quad u = v = 0, \tag{1.2a}$$

$$y = h(x,t): \quad v = \partial_t h + u\partial_x h, \quad \boldsymbol{n}\cdot\boldsymbol{\tau}\cdot\boldsymbol{n} - p = \kappa\sigma, \quad \boldsymbol{t}\cdot\boldsymbol{\tau}\cdot\boldsymbol{n} = 0, \tag{1.2b}$$

σ being the surface tension, κ the mean curvature, $\boldsymbol{n}$ the outward-pointing unit normal vector at the interface, $\boldsymbol{t}$ the tangent vector and $\boldsymbol{\tau} = \mu\left(\nabla\boldsymbol{u} + \nabla^T\boldsymbol{u}\right)$ the viscous stress tensor. Expressing

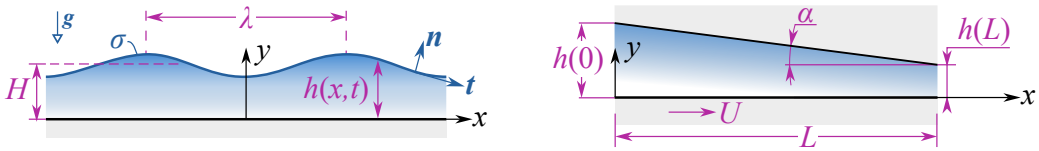

(a) Bounded thin-film problem (b) Reynolds' lubrication problem

Figure 1.2: Schematic of (a) a bounded thin film and (b) the Reynolds' lubrication problem.

κ, $\boldsymbol{n}$ and $\boldsymbol{t}$ in terms of h yields

$$\kappa = \frac{\partial_x^2 h}{\left[1+(\partial_x h)^2\right]^{3/2}}, \quad \boldsymbol{n} = \frac{(-\partial_x h,\ 1)}{\left[1+(\partial_x h)^2\right]^{1/2}}, \quad \boldsymbol{t} = \frac{(1,\ \partial_x h)}{\left[1+(\partial_x h)^2\right]^{1/2}}. \tag{1.3}$$

As thin films are considered, the characteristic lengths in $x-$ and $y-$direction are expected to be different. We aim to derive an asymptotic approximation valid for *long-wave* deformations of the thin film interface, hence we scale the horizontal coordinate with a characteristic wavelength λ. On the other hand, the characteristic length for the vertical direction must relate to the film thickness. Here we use the average film thickness H (see fig. 1.2(a)). Consistently, the scaling of $\boldsymbol{u}$ must rely on two different characteristic velocities for u and v, i.e. U and V, respectively. Finally, scaling the time with the characteristic length and velocity of the interface long-wave propagation, i.e. $T = \lambda/U$, and the pressure field by P yields

$$U\lambda^{-1}\partial_{x^*}u^* + UH^{-1}\partial_{y^*}v^* = 0, \tag{1.4a}$$

$$\rho U^2\lambda^{-1}\left[\partial_{t^*}u^* + u^*\partial_{x^*}u^* + VU^{-1}\lambda H^{-1}v^*\partial_{y^*}u^*\right] = -P\lambda^{-1}\partial_{x^*}p^* + \mu U\lambda^{-2}\left(\partial_{x^*}^2u^* + \lambda^2H^{-2}\partial_{y^*}^2u^*\right), \tag{1.4b}$$

$$\rho VU\lambda^{-1}\left[\partial_{t^*}v^* + u^*\partial_{x^*}v^* + VU^{-1}\lambda H^{-1}v^*\partial_{y^*}v^*\right] = -PH^{-1}\partial_{y^*}p^* - \rho g + \mu V\lambda^{-2}\left(\partial_{x^*}^2v^* + \lambda^2H^{-2}\partial_{y^*}^2v^*\right) \tag{1.4c}$$

for the governing equations in the bulk. The asterisk in (1.4) refer to the nondimensional variables, i.e. $t^* = tU/\lambda$, $\boldsymbol{x}^* = (x^*, y^*) = (x/\lambda, y/H)$, $\boldsymbol{u}^* = (u^*, v^*) = (u/U, v/V)$ and $p^* = p/P$. Defining the small parameter $\epsilon = H/\lambda \ll 1$ and the Reynolds number $\mathrm{Re} = \rho UH/\mu$, it yields

$$\partial_{x^*}u^* + V(\epsilon U)^{-1}\partial_{y^*}v^* = 0, \tag{1.5a}$$

$$\epsilon^{-1}\mathrm{Re}\left[\partial_{t^*}u^* + u^*\partial_{x^*}u^* + V(\epsilon U)^{-1}v^*\partial_{y^*}u^*\right] = -P\lambda\mu^{-1}U^{-1}\partial_{x^*}p^* + \partial_{x^*}^2u^* + \epsilon^{-2}\partial_{y^*}^2u^*, \tag{1.5b}$$

$$\epsilon^{-1}\mathrm{Re}\left[\partial_{t^*}v^* + u^*\partial_{x^*}v^* + V(\epsilon U)^{-1}v^*\partial_{y^*}v^*\right] = -P\epsilon^{-1}\lambda\mu^{-1}V^{-1}\partial_{y^*}p^* - \rho g\mu^{-1}\lambda^2V^{-1} + \partial_{x^*}^2v^* + \epsilon^{-2}\partial_{y^*}^2v^*. \tag{1.5c}$$

In view of the asymptotic expansion, one has to define the physics to retain at the leading order of the approximation. From the continuity equation, the solenoidal flow at leading order requires that $V(\epsilon U)^{-1} = \mathcal{O}(1)$, hence $V = \epsilon U$. Moreover, as we will consider moderately small Reynolds numbers, the pressure gradient in the $x-$momentum should balance the leading order viscous term, i.e. $\epsilon^{-2}\partial_{y^*}^2u^*$. Hence, $P\lambda\mu^{-1}U^{-1} = \mathcal{O}(\epsilon^{-2})$ that yields $P = \mu U/\epsilon H$. Re-writing (1.5) in light of the characteristic scaling adapted to the dynamics of a low-inertial incompressible viscous thin film and removing the asterisk for ease of readability, yields:

$$\partial_x u + \partial_y v = 0, \tag{1.6a}$$

$$\epsilon\mathrm{Re}\left[\partial_t u + u\partial_x u + v\partial_y u\right] = -\partial_x p + \epsilon^2\partial_x^2 u + \partial_y^2 u, \tag{1.6b}$$

$$\epsilon^3\mathrm{Re}\left[\partial_t v + u\partial_x v + v\partial_y v\right] = -\partial_y p - \epsilon\mathrm{Fr}^{-1} + \epsilon^4\partial_x^2 v + \epsilon^2\partial_y^2 v, \tag{1.6c}$$

where $\mathrm{Fr} = \mu U/\rho gH^2$ denotes the Froude number. Consistently, the non-dimensional form of the

BCs reads:

$$y = 0: \quad u = 0, \tag{1.7a}$$

$$v = 0, \tag{1.7b}$$

$$y = \eta(x,t): \quad v = \partial_t \eta + u\partial_x \eta, \tag{1.7c}$$

$$p = 2\epsilon^2 \left\{ \partial_x u \left[\epsilon^2 \left(\partial_x \eta \right)^2 - 1 \right] - \partial_x \eta \left(\partial_z u + \epsilon^2 \partial_x v \right) \right\} \left[1 + \epsilon^2 \left(\partial_x \eta \right)^2 \right]^{-1} - \epsilon^3 \mathrm{Ca}^{-1} \partial_x^2 \eta \left[1 + \epsilon^2 \left(\partial_x \eta \right)^2 \right]^{-3/2}, \tag{1.7d}$$

$$\left(\partial_y u + \epsilon^2 \partial_x v \right) \left[1 - \epsilon^2 \left(\partial_x \eta \right)^2 \right] - 4\epsilon^2 \left(\partial_x \eta \right) \left(\partial_x u \right) = 0, \tag{1.7e}$$

where $\eta(x,t) = h(x,t)/H$ is the film thickness adimensionalized with H, and $\mathrm{Ca} = U\mu/\sigma$ the capillary number. The non-dimensional problem is partially reformulated to express the continuity equation and the kinematic boundary condition in a mathematically more convenient way. Let us integrate (1.6a) from $y = 0$ to $y = \eta(x,t)$. Thereafter, by applying the integration by parts and using the no-penetration (1.7b) and kinematic (1.7c) BCs, the following equation is derived:

$$\partial_t \eta + \partial_x \int_0^\eta u dy = 0. \tag{1.8}$$

Despite the asymptotic-convenient scaling and the multiple manipulations of the equations, no approximations has yet been made. The asymptotic approximation is undertaken by seeking for solutions in form of a perturbation power series in the small parameter ϵ:

$$u = u_0 + \epsilon u_1 + \epsilon^2 u_2 + \mathcal{O}(\epsilon^2), \tag{1.9a}$$

$$v = v_0 + \epsilon v_1 + \epsilon^2 v_2 + \mathcal{O}(\epsilon^2), \tag{1.9b}$$

$$p = p_0 + \epsilon p_1 + \epsilon^2 p_2 + \mathcal{O}(\epsilon^2), \tag{1.9c}$$

$$\eta = \eta_0 + \epsilon \eta_1 + \epsilon^2 \eta_2 + \mathcal{O}(\epsilon^2), \tag{1.9d}$$

where the index 0 denotes the *leading order*, 1 the *linear order*, 2 the *quadratic order*, etc. All the corresponding solutions, for instance u_k, are assumed to be of $\mathcal{O}(1)$ because they are multiplied by their corresponding power of the small parameter ϵ^k in the power-law asymptotic series, where $k \in \mathbb{N}_0$. Within the perturbation theory framework, we take the limit for $\epsilon \to 0$ and derive consistent approximations $\forall \mathcal{O}(\epsilon^k)$. Before doing so, one still needs to specify how the other parameters relate to ϵ, so to specify the physics to study within the perturbation theory.

Let us consider weakly inertial flows such that $\mathrm{Re} = \mathcal{O}(1)$. Moreover, we assume that gravitational forces can be neglected up to first order, i.e. $\mathrm{Fr} = \mathcal{O}(1)$, while capillary stresses are taken as leading order effects in the dynamics of the thin film we want to investigate, i.e. $\mathrm{Ca} = \mathcal{O}(\epsilon^{-3})$. The corresponding leading-order approximation reads:

$$\text{leading order } \mathcal{O}(1): \quad \partial_t \eta_0 + \partial_x \int_0^{\eta_0} u_0 dy = 0, \quad \partial_x p_0 = \partial_y^2 u_0, \quad \partial_y p_0 = 0, \tag{1.10a}$$

$$u_0(y=0) = 0, \quad p_0(y=\eta_0) = -\epsilon^3 \mathrm{Ca}^{-1} \partial_x^2 \eta_0, \quad \partial_y u_0(y=\eta_0) = 0, \tag{1.10b}$$

and it includes simplified viscous effects in the bulk, capillary effects at the interface, and no iner-

tial effects. The resulting problem is strongly non-linear, as one can appreciate by reformulating it in terms of the sole leading-order PDE for the film thickness h_0:

$$\text{leading order } \mathcal{O}(1): \quad 3\partial_t\eta_0 + \epsilon^3 \mathrm{Ca}^{-1}\partial_x^2\left(\eta_0^3\partial_x^2\eta_0\right) = 0. \tag{1.11}$$

Appropriate leading-order BCs on the left and right boundaries are needed to solve it. We further stress that the solution in the primary variables at leading order, i.e. u_0, v_0, and p_0 can be computed a-posteriori once the dynamic equation for the interface h_0 has been solved. In fact, in the considered asymptotic limit, the pressure $p_0 = -\epsilon^3\mathrm{Ca}^{-1}\partial_x^2\eta_0$ is a projected capillary pressure due to the interface curvature, $u_0 = -\epsilon^3\mathrm{Ca}^{-1}\partial_x^3\eta_0\left(y^2 - 2\eta_0 y\right)$, and $v_0 = \epsilon^3\mathrm{Ca}^{-1}\partial_x^4\eta_0\left(y^3 - 3\eta_0 y^2\right)/3$.

If we carry on with the asymptotic expansion up to linear-order, it yields:

$$\begin{aligned}
\text{linear order } \mathcal{O}(\epsilon): \quad & \partial_x u_1 + \partial_y v_1 = 0, && \text{(1.12a)}\\
& \mathrm{Re}\left[\partial_t u_0 + u_0\partial_x u_0 + v_0\partial_y u_0\right] = -\partial_x p_1 + \partial_y^2 u_1, && \text{(1.12b)}\\
& \partial_y p_1 + \mathrm{Fr}^{-1} = 0, && \text{(1.12c)}\\
& u_1(y=0) = 0, && \text{(1.12d)}\\
& v_1(y=0) = 0, && \text{(1.12e)}\\
& p_1(y=\eta_0) = -\epsilon^3\mathrm{Ca}^{-1}\partial_x^2\eta_1, && \text{(1.12f)}\\
& \partial_y u_1(y=\eta_0) = 0, && \text{(1.12g)}\\
& v_1(y=\eta_0) = \partial_t\eta_1 + u_0\partial_x\eta_1 + u_1\partial_x\eta_0. && \text{(1.12h)}
\end{aligned}$$

The inertial term is included in the linear-order $x-$momentum equation, and the gravitational force in the $y-$momentum. Hence, $p_1 = -\epsilon^3\mathrm{Ca}^{-1}\partial_x^2\eta_1 + \mathrm{Fr}^{-1}(\eta_0 - y)$ results from the combination of linear-order capillary effects and the hydrostatic pressure.

The consistent asymptotic approximations derived for the long-wave perturbation theory in thin films demonstrate the remarkable simplification provided by such methods when used to tackle a complex problem. Employing such systematic approximations greatly helps in the physical interpretation of leading-order effects, as well as in their correction at higher order. Moreover, perturbation theory has been proven extremely successful in identifying asymptotic scaling laws that extensively helped rationalizing the solution of the original (non-asymptotic) problem, and they have been used to propose leading-order design rules for complex engineering applications. For instance, the earliest example of the long-scale asymptotics applied to fluid dynamics is due to the lubrication theory of Reynolds [50]. He considered a slipper bearing problem in two-dimensional Cartesian coordinates (see fig. 1.2(b)), assuming that the bottom wall moves at velocity U, the lubrication film thickness varies slowly with time, and inertial terms do not affect the leading-order solution. The small parameter in Reynolds' lubrication theory is $\epsilon = [h(0) - h(L)]/L = \tan(\alpha_\mathrm{t}) \ll 1$ and $\eta(x) = \eta(0) - \left[\alpha_\mathrm{t} + \mathcal{O}(\alpha_\mathrm{t}^2)\right]x$, where α_t is the tilt angle. The most significant result of Reynolds' lubrication theory is the inverse proportionality of the lubrication pressure with the tilt angle $p \sim \alpha_\mathrm{t}^{-1}$, hence the upward force exerted by the viscous stresses F_v on the top inclined wall scales like $F_\mathrm{v} \sim \alpha_\mathrm{t}^{-2}$ for $\epsilon \to 0$, hence for $\alpha_\mathrm{t} \to 0$.

1.2.2 Method of matched asymptotic expansions

When singular perturbation problems are tackled, a given asymptotic series does not uniformly converge over the whole set of mathematical constraints for the asymptotically approximated problem (refer to [18, 51] for more details). A first singularity scenario is represented by an asymptotic expansion that diverges upon a breakup of the asymptotic limit $\epsilon \to 0$. This is the case, for instance, of the rupture of a thin film or the pinch-off of a slender liquid column, for which the small parameter $\epsilon = H/\lambda \ll 1$ is not appropriate to describe localized breakups of the interface. As a result, the asymptotic series for $\epsilon = H/\lambda \to 0$ diverges where $\eta \to 0$ (see fig. 1.3(a)) and a second asymptotic problem is required [52]. Localized stretching of coordinates near the interface breakup region is usually employed to tackle the singular region. The matching between the long-wave asymptotic and the breakup asymptotic provides the global perturbation theory approximation of the original non-asymptotic problem.

Another singular perturbation scenario is represented by an asymptotic expansion that does not respect the BCs. For instance, let us consider a two-dimensional viscous flow past flat plate at angle of attack null. The leading-order asymptotics for $\epsilon^{-1} = \mathrm{Re} = \rho U x/\mu \to \infty$ leads to the inviscid Euler equations that do not respect the no-slip condition at the wall. The singular perturbation problem requires therefore to employ another leading-order asymptotic expansion in the region of non-uniformity of the solution [53]. A local stretching of the coordinates in wall-normal direction with the boundary-layer thickness $\delta_\mathrm{B} \sim \sqrt{\epsilon}$ leads to the Blasius boundary-layer that includes viscous stresses capable of enforcing the no-slip boundary condition at the wall [54]. We stress that such a near-wall asymptotic approach still provides a great simplification with respect to the non-asymptotic problem. In fact, the Blasius boundary-layer equations are steady and parabolic along the coordinate tangential to the flat plate. Such symmetries lead to self-similar solutions that allow to combine the asymptotic continuity and Navier–Stokes equations in a sole third-order non-linear ordinary differential equation. The matching between the inviscid Euler solution and the Blasius boundary-layer provides the global asymptotic solution for the two-dimensional viscous flow past flat plate at angle of attack null for $\mathrm{Re} \gg 1$. However, in a neighborhood of the flat plate leading edge, i.e. for $x \ll L$, $\mathrm{Re} = \rho U x/\mu$ is small and another asymptotic singularity is encountered because $\epsilon = \mathcal{O}(1)$. Such a singularity is tackled either by applying optimal coordinates [55, 18] or by dedicated jump conditions [56, 57], where three rather than two asymptotic approximations are employed (see fig. 1.3(b)). Similar triple-deck matching methods are employed when separation of boundary layers occurs [58, 59].

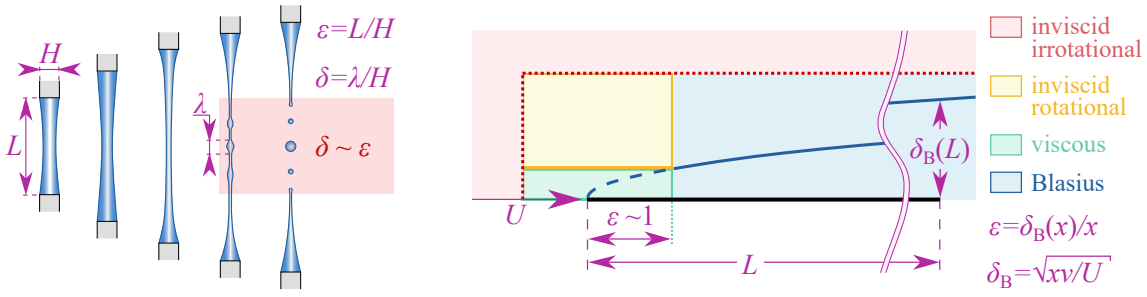

(a) Thin-film breakup

(b) Flow past flat plate

Figure 1.3: Schematic of singular perturbation examples.

Following [18] and motivated by the previous applications, a simplified example is hereinafter discussed to demonstrate the method of matched asymptotic expansions. This will give us the chance of introducing the corresponding technical nomenclature. Let us consider the following second-order ordinary differential equation defined on $x \in [0,\ 1]$ as prototype problem

$$\epsilon\, \mathrm{d}_x^2 \Upsilon + \mathrm{d}_x \Upsilon = c, \quad \Upsilon(x=0) = 0, \quad \Upsilon(x=1) = 1, \tag{1.13}$$

where $\Upsilon(x)$ denotes the dimensionless solution of (1.13) and x the sole coordinate Υ depends upon. Taking the asymptotic limit for $\epsilon \to 0$ leads to a first-order ordinary differential equation ($\mathrm{d}_x \Upsilon = c$) that cannot satisfy both the boundary conditions. We ran therefore into a nonuniform perturbation problem.

Considering that x has been scaled on the total domain length, i.e. $\max(x) = 1$, the singularity of the problem must occur for values of x such that $x = \mathcal{O}(\epsilon)$. We can therefore assume that the $\lim_{\epsilon \to 0}$(1.13) is valid for $x = \mathcal{O}(1)$, hence

$$\mathrm{d}_x \Upsilon = c, \quad \Upsilon(x=1) = 1, \tag{1.14}$$

where (1.14) is said *outer expansion* and x *outer independent variable*. When taking the limit $\epsilon \to 0$ for values of x such that $x = \mathcal{O}(\epsilon)$, we can stretch the outer independent variable such that the singularity is locally removed. Reformulating (1.13) in terms of $\check{x} = x/\epsilon$ leads to

$$\mathrm{d}_{\check{x}}^2 \Upsilon + \mathrm{d}_{\check{x}} \Upsilon = \epsilon c, \quad \Upsilon(\check{x}=0) = 0, \quad \Upsilon(\check{x}=1/\epsilon) = 1. \tag{1.15}$$

However, this limit holds true only for $x = \mathcal{O}(\epsilon)$, hence the boundary condition at $\check{x} = 1/\epsilon$ must be dropped. Taking $\lim_{\epsilon \to 0}$(1.15) leads to the *inner expansion*, whose *inner independent variable* is $\check{x}$, and employing the matching principle that the limit of the outer expansion for the outer variable tending to zero should tend to the limit of the inner expansion for the inner variable tending to infinite yields:

$$\mathrm{d}_{\check{x}}^2 \Upsilon + \mathrm{d}_{\check{x}} \Upsilon = 0, \quad \Upsilon(0) = 0, \quad [\Upsilon(x \to 0)]_{\text{outer}} = [\Upsilon(\check{x} \to \infty)]_{\text{inner}}\,. \tag{1.16}$$

We can therefore solve the matching problem by finding the outer and the inner solutions:

$$\text{Outer expansion } \forall\ x = \mathcal{O}(1): \quad \Upsilon = (1-c) + cx, \tag{1.17a}$$

$$\text{Inner expansion } \forall\ \check{x} = \mathcal{O}(1): \quad \Upsilon = (1-c)\left(1 - e^{-\check{x}}\right). \tag{1.17b}$$

Summing up the inner and outer expansion and removing the matching condition not to take it into account twice at $x \to 0$ and $\check{x} \to \infty$, one can retrieve the asymptotic limit of the exact solution for $\epsilon \to 0$:

$$\begin{aligned} \lim_{\epsilon \to 0} \Upsilon = \lim_{\epsilon \to 0} \overbrace{\left[(1-c)\,\frac{1 - e^{-x/\epsilon}}{1 - e^{-1/\epsilon}} + cx\right]}^{\text{exact solution of (1.13)}} &= \overbrace{(1-c) + cx}^{\text{outer expansion}} + \overbrace{(1-c)\left(1 - e^{-\check{x}}\right)}^{\text{inner expansion}} - \overbrace{(1-c)}^{\text{matching BC}} \\ &= (1-c)\left(1 - e^{-x/\epsilon}\right) + cx \end{aligned} \tag{1.18}$$

1.3 Hydrodynamic stability

Hydrodynamic stability is a branch of fluid dynamics that aims to assess if a flow state is stable when subjected to finite or infinitesimal perturbations. Let us assume that an initially stable, steady or unsteady, flow can be defined under controlled conditions. We refer to such a flow as the *basic state* and denote it by $\boldsymbol{q}_0$. The study of its stability investigates an initial disturbance $\tilde{\boldsymbol{q}}$ injected in the basic state at time $t = 0$ grows or decays over time, ultimately determining whether the flow remains stable, i.e. it returns to $\boldsymbol{q}_0$, or it transitions into another configuration $\boldsymbol{q}$ resulting from the non-linear interaction between $\boldsymbol{q}_0$ and $\tilde{\boldsymbol{q}}$.

Hydrodynamic instabilities manifest ubiquitously in nature and engineering applications changing the structure of the flow and inducing a complex dynamics. Three illustrative examples are hereinafter presented to demonstrate the crucial role played by flow instabilities:

(a) Capillary instabilities [52] lead to the interfacial break-up of a liquid column (see fig. 1.4(a) [60, 61, 62]) or a liquid film coating a pipe [63, 64] and hold relevance in most multiphase microfluidic applications [65], ink-jet printing [66] and biological flows [67].

(b) Shear-flow instabilities [68, 69] are responsible for cloud waves (see fig. 1.4(b) [70, 71, 72, 73]) as well as laminar-to-turbulence transition [74, 75] in boundary layers [76, 77], channels [78] and pipe flows [79] leading to a significant increase of drag forces and macroscopic mixing.

(c) Buoyancy-driven instabilities [80, 81, 82, 83, 84] are responsible of the convective flows at geophysical scales (see fig. 1.4(c) [85, 86, 87]) and find extensive use in thermal management systems, such as floor heating [88] or ceiling cooling in buildings [89].

The underlying mechanisms leading to such instabilities are intrinsically different. However, they all derive from the nonlinear character of the Navier–Stokes equations, which allows for multiple solutions given the set of control parameters.

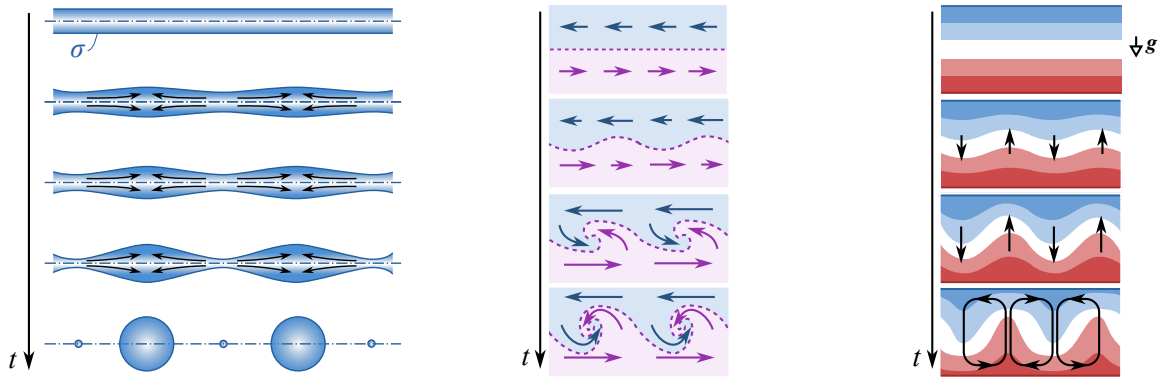

(a) Rayleigh–Plateau instability (b) Kelvin–Helmholtz instability (c) Rayleigh–Bénard instability

Figure 1.4: Examples of hydrodynamic instabilities. (a) Rayleigh–Plateau instability driven by capillary stresses due to the surface tension σ at the axisymmetric interface between two fluids. (b) Kelvin–Helmholtz instability driven by the shear stress concentrated at the shear layer (interface between blue and magenta domains). (c) Rayleigh–Bénard instability driven by buoyancy when hot (light) fluid is initially at the bottom and cold (heavy) fluid at the top.

1.3.1 General definitions

Given an initially perturbed basic state, its global stability can be classified based on the energy associated to the perturbation. The evolution in time of the perturbation kinetic energy is given by $E_{\text{kin}}(t) = (1/2V)\int_V \rho\tilde{\boldsymbol{u}}^2\,\mathrm{d}V$, where $\tilde{\boldsymbol{u}} \in \tilde{\boldsymbol{q}}$ is the perturbation velocity, ρ the fluid density, and V the volume of the domain. Corresponding definitions of other forms of energies, e.g. internal energy, shall also be considered to fully characterize the stability of a system.

Without loss of generality, we will focus on the kinetic energy. A first classification of the global stability of $\boldsymbol{q}_0$ is done based on the initial amplitude of E_{kin}. Two types of global stability are therefore identified:

(i) Conditional stability: The basic state is conditionally stable if $\exists\xi_0 > 0$ such that $\boldsymbol{q}_0$ is stable if $E_{\text{kin}}(t=0) < \xi_0$.

(ii) Unconditional stability: The basic state is unconditionally stable if the ξ_0 defined for the conditional stability tends to infinite, i.e. $\xi_0 \to \infty$.

A second classification of the basic state stability is done based on the scenarios that can be identified for the perturbation energy evolution in time:

(a) Lyapunov stability: The basic state is Lyapunov-stable if $\forall\xi_\epsilon > 0$, $\exists\xi_0(\xi_\epsilon) > 0$ such that if $E_{\text{kin}}(t=0) < \xi_0$, then $E_{\text{kin}}(t) < \xi_\epsilon\ \forall t > 0$ (see fig. 1.5(a)).

(b) Asymptotic stability: The basic state is asymptotically stable if it is Lyapunov-stable and if $\exists\xi_0$ such that if $E_{\text{kin}}(t=0) < \xi_0$, then $\lim_{t\to\infty} E_{\text{kin}}(t) = 0$ (see fig. 1.5(b)).

(c) Monotonic stability: The basic state is monotonically stable if it is asymptotically stable and if $\mathrm{d}_t E_{\text{kin}}(t) < 0\ \forall t$, hence $\lim_{t\to\infty} E_{\text{kin}}(t) = 0$ (see fig. 1.5(c)).

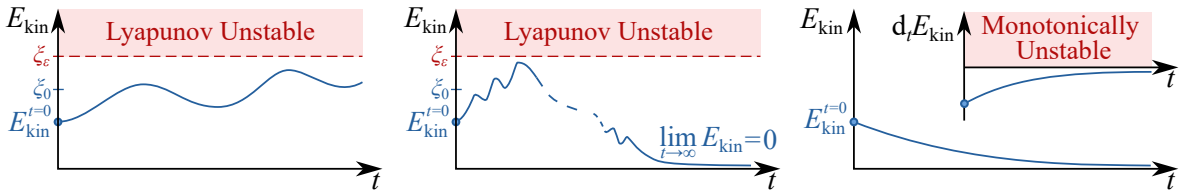

(a) Lyapunov stability (b) Asymptotic stability (c) Monotonic stability

Figure 1.5: Stability scenarios for the perturbation energy evolution: (a) Lyapunov stability, (b) asymptotic stability, and (c) monotonic stability.

The relevance of such definitions for the physical systems considered in this manuscript will become clearer once discussed for specific examples. We anticipate, however, that Lyapunov stability is crucial for Hamiltonian systems that are energy conservative, as well as for phase-space trajectories in dissipative systems. Hence, a change of the perturbation energy due to a perturbation growth/decay feeds back on the flow system leading to a state close but not exactly equal to the unperturbed equilibrium $\boldsymbol{q}_0$. On the other hand, asymptotic stability applies to dissipative systems such as the viscous flows we consider. Finally, monotonic stability is significant to exclude the occurrence of nonmodal phenomena for small, yet finite perturbations.

1.3.2 Linear modal stability analysis of steady basic states

When we restrict the domain of all possible perturbations to the sole infinitesimal $\tilde{\boldsymbol{q}}$, the perturbation dynamics problem results from the $\mathcal{O}(\epsilon)$ of the continuity, Navier–Stokes and energy equations. Expanding the solution $\boldsymbol{q}$ in form of an asymptotic series that relies on the power-law expansion in $\epsilon \to 0$ around the equilibrium state $\boldsymbol{q}_0$:

$$\boldsymbol{q} = \boldsymbol{q}_0 + \epsilon\tilde{\boldsymbol{q}} + \mathcal{O}(\epsilon^2), \tag{1.19}$$

where $\boldsymbol{q}_0$ and $\tilde{\boldsymbol{q}}$ are of $\mathcal{O}(1)$, the perturbation dynamics affects the solution $\boldsymbol{q}$ at $\mathcal{O}(\epsilon)$, hence $\tilde{\boldsymbol{q}}$ must be governed by a linear system of PDEs in $\tilde{\boldsymbol{q}}$ (see also (1.12) in §1.2.1). We stress that the term $\tilde{\boldsymbol{q}}$ would correspond to $\boldsymbol{q}_1$ when employing the notation of (1.9), and we here prefer employing the tilde sign for $\mathcal{O}(\epsilon)$ terms such to recall that the perturbation theory has been applied to linear stability theory where higher order terms are neglected.

Using the Oberbeck–Boussinesq approximation [90, 91], the continuity, Navier–Stokes, and energy equations for an incompressible non-isothermal flow with density ρ, dynamic viscosity μ, thermal conductivity κ and specific heat at constant pressure c_p read:

$$\nabla \cdot \boldsymbol{u} = 0, \tag{1.20a}$$

$$\rho\left(\partial_t \boldsymbol{u} + \boldsymbol{u} \cdot \nabla \boldsymbol{u}\right) = -\nabla p + \mu\nabla^2 \boldsymbol{u} - \boldsymbol{g}\beta\theta, \tag{1.20b}$$

$$\rho c_p\left(\partial_t \theta + \boldsymbol{u} \cdot \nabla\theta\right) = \kappa\nabla^2\theta, \tag{1.20c}$$

where β is the thermal expansion coefficient, and $\boldsymbol{u}$, p and θ are the velocity, reduced pressure and temperature fields, respectively. Note that the reduced pressure already includes the hydrostatic pressure and the thermal correction given by the scalar potential of $\boldsymbol{g}\beta\theta_{\text{ref}}$, where θ_{ref} is the reference temperature at which the thermophysical properties are considered. The total solution of the governing transport equations gathers all scalar and vector fields, i.e. $\boldsymbol{q} = (\boldsymbol{u}, p, \theta)^T$. The BCs that provide mathematical closure of the problem (1.20) are not specified in this section as our aim is to recall the fundamental principles of linear stability analysis (LSA).

If the basic state is a steady solution of (1.20), i.e. $\partial_t \boldsymbol{q}_0 = \partial_t(\boldsymbol{u}_0, p_0, \theta_0) = \boldsymbol{0}$, one can define the linear $[L]$, convective $[C(\boldsymbol{v})]$, and time-derivative $\partial_t[B]$ operators of (1.20)

$$[L] = \begin{bmatrix} \nabla\cdot & 0 & 0 \\ \mu\nabla^2 & -\nabla & -\boldsymbol{g}\beta \\ 0 & 0 & \kappa\nabla^2 \end{bmatrix}, \quad [C(\boldsymbol{v})] = \begin{bmatrix} 0 & 0 & 0 \\ \rho\boldsymbol{v}\cdot\nabla & 0 & 0 \\ 0 & 0 & \rho c_p \boldsymbol{v}\cdot\nabla \end{bmatrix}, \quad [B] = \begin{bmatrix} 0 & 0 & 0 \\ \rho & 0 & 0 \\ 0 & 0 & \rho c_p \end{bmatrix}. \tag{1.21}$$

Hence, the leading and first order governing equations read:

$$\text{leading order } \mathcal{O}(1): \qquad [C(\boldsymbol{u}_0)]\boldsymbol{q}_0 = [L]\boldsymbol{q}_0, \tag{1.22a}$$

$$\text{linear order } \mathcal{O}(\epsilon): \qquad \partial_t[B]\tilde{\boldsymbol{q}} + [C(\boldsymbol{u}_0)]\tilde{\boldsymbol{q}} + [C(\tilde{\boldsymbol{u}})]\boldsymbol{q}_0 = [L]\tilde{\boldsymbol{q}}. \tag{1.22b}$$

The leading order problem for the basic state leads to a system of non-linear partial differential equations in space that does not require $\tilde{\boldsymbol{q}} = (\tilde{\boldsymbol{u}},\ \tilde{p},\ \tilde{\theta})^T$. In the simplest flow configurations, such

as the three examples depicted in fig. 1.4, $\boldsymbol{q}_0$ can be computed analytically. In most of the cases, however, the analytical solution is not known and (1.22a) is solved numerically by employing, e.g., Newton–Raphson [92] or Selective Frequency Damping [93] methods. The $\mathcal{O}(\epsilon)$ problem (1.22b), conversely, is linear in $\tilde{\boldsymbol{q}}$ because the convective operator is employing the pre-computed basic state in the transport terms for the dynamics of $\tilde{\boldsymbol{q}}$. As the problem (1.22b) is linear, it can be reformulated in matrix form as:

$$\left(\partial_t[B] - [A]\right)\tilde{\boldsymbol{q}} = \boldsymbol{0}, \quad \text{where } [A] = -\rho \begin{bmatrix} 0 & 0 & 0 \\ [\boldsymbol{u}_0 \cdot \nabla + (\nabla \boldsymbol{u}_0)\,\cdot] & 0 & 0 \\ c_p\,(\nabla \theta_0)\,\cdot & 0 & c_p \boldsymbol{u}_0 \cdot \nabla \end{bmatrix} + [L]. \tag{1.23}$$

As the matrix $[A]$ does not depend on $\tilde{\boldsymbol{q}}$ and is homogeneous in time, the solution of (1.23) can be decomposed in a linear superposition of normal modes. Hence, the dynamics of the infinitesimal perturbation $\tilde{\boldsymbol{q}}$ must satisfy the ansatz

$$\tilde{\boldsymbol{q}}(\boldsymbol{x}, t) = \sum_i \hat{\boldsymbol{q}}_i(\boldsymbol{x}) e^{\gamma_i t} + \text{c.c.}, \tag{1.24}$$

where $\boldsymbol{x}$ denotes the spatial coordinate, $\gamma_i \in \mathbb{C}$ is the $i-$th normal mode exponent, and the $\hat{\boldsymbol{q}}_i(\boldsymbol{x})$ the corresponding mode. The real part of γ_i represents the growth rate of the $i-$th mode, while its imaginary part is the angular frequency. We stress that $\hat{\boldsymbol{q}}_i(\boldsymbol{x})$ is a vector field that can be complex valued, hence the complex conjugate ('c.c.') has been added in order to retrieve real valued solutions for $\tilde{\boldsymbol{q}}$.

Plugging (1.24) into (1.23) leads to a generalized eigenvalue problem per each normal mode

$$\gamma_i [B] \hat{\boldsymbol{q}}_i = [A] \hat{\boldsymbol{q}}_i, \tag{1.25}$$

where γ_i is the $i-$th eigenvalue and $\hat{\boldsymbol{q}}_i$ the corresponding eigenmode. The *linear modal stability* of a steady basic state is classified based on the maximum real part of the growth rate:

If $\max_i \Re(\gamma_i) < 0$: the basic state $\boldsymbol{q}_0$ is *asymptotically stable* to infinitesimal perturbations $\tilde{\boldsymbol{q}}$.

If $\max_i \Re(\gamma_i) = 0$: the basic state $\boldsymbol{q}_0$ is *marginally stable* to infinitesimal perturbations $\tilde{\boldsymbol{q}}$.

If $\max_i \Re(\gamma_i) > 0$: the basic state $\boldsymbol{q}_0$ is unstable to an arbitrary linear combination of all the infinitesimal perturbation modes with positive growth rate.

In case of marginal (also called neutral) stability, the LSA predicts that the perturbation modes with null growth rate neither grow nor decay. Therefore, in the neighborhood of critical conditions, weakly non-linear $\mathcal{O}(\epsilon^2)$-effects can play a crucial role in determining the character the instability bifurcation. Further information on the instability are provided by the imaginary part of the eigenvalues corresponding to the unstable modes:

If $\Im(\gamma_i) = 0$: the perturbation produced by $\hat{\boldsymbol{q}}_i + c.c.$ is *not* oscillatory.

If $\Im(\gamma_i) \neq 0$: the perturbation produced by $\hat{\boldsymbol{q}}_i + c.c.$ has oscillation frequency $\omega_i = \Im(\gamma_i)$.

1.3.3 Reynolds–Orr equation

Taking the scalar product between $\tilde{\boldsymbol{u}}$ and the linearized momentum equation, an equation for the evolution of the perturbation kinetic energy is obtained. By integration by parts, application of the Green's theorem and of the incompressibility constraint, assuming that the perturbation vanishes at all inlets and no-slip boundaries, we arrive at the so-called Reynolds–Orr equation:

$$\mathrm{d}_t E_{\mathrm{kin}} = \frac{1}{2}\int_V \rho \partial_t \tilde{\boldsymbol{u}}^2 \,\mathrm{d}V = -D_{\mathrm{kin}} + I + B + K_{\mathrm{kin}} + M, \tag{1.26}$$

where $D_{\mathrm{kin}} = \int_V \mu \nabla\tilde{\boldsymbol{u}} : \nabla\tilde{\boldsymbol{u}} \,\mathrm{d}V$ is the viscous dissipation term, $I = -\int_V \rho\tilde{\boldsymbol{u}}\cdot(\tilde{\boldsymbol{u}}\cdot\nabla\boldsymbol{u}_0)\,\mathrm{d}V$ denotes the global kinetic energy production/dissipation due to the convective term, $B = -\int_V \tilde{\boldsymbol{u}}\cdot\boldsymbol{g}\beta\theta\,\mathrm{d}V$ is the energy production/dissipation due to buoyancy, while the two surface integrals $K_{\mathrm{kin}} = \frac{1}{2}\int_{S_{\mathrm{out}}} \rho\tilde{\boldsymbol{u}}^2\boldsymbol{u}_0\cdot\boldsymbol{n}_{\mathrm{out}}\,\mathrm{d}S$ and $M = -\int_{S_{\mathrm{Ma}}} \mu\tilde{\boldsymbol{u}}\cdot(\boldsymbol{n}_{\mathrm{Ma}}\cdot\nabla\tilde{\boldsymbol{u}})\,\mathrm{d}S$ refer to the kinetic energy exchange at the boundaries of V due to the kinetic energy outflowing K_{kin} across an outlet of surface S_{out} and normal vector $\boldsymbol{n}_{\mathrm{out}}$, and the Marangoni stresses on thermocapillary or solutocapillary driven boundaries of surface S_{Ma} and normal vector $\boldsymbol{n}_{\mathrm{Ma}}$, respectively. Note that (1.26) is valid for basic states whose boundaries are not deformed by the perturbation at $\mathcal{O}(\epsilon)$. An additional term is required whenever surface wave instabilities are considered in order to consider the energy transfer due to interface deformations [94, 95].

The counterpart of the kinetic energy budget (1.26) for the thermal energy $\int_V \rho c_p \partial_t\left(\tilde{\theta}^2/2\right)\mathrm{d}V$ is derived by multiplying the linearized energy equation by the perturbation temperature $\tilde{\theta}$:

$$\mathrm{d}_t E_{\mathrm{th}} = \frac{1}{2}\int_V \rho c_p \partial_t \tilde{\theta}^2 \,\mathrm{d}V = -D_{\mathrm{th}} + J + K_{\mathrm{th}} + H, \tag{1.27}$$

where $D_{\mathrm{th}} = \int_V \lambda\nabla\tilde{\theta}\cdot\nabla\tilde{\theta}\,\mathrm{d}V$ is the thermal dissipation, $J = -\int_V \rho c_p\tilde{\theta}\,(\tilde{\boldsymbol{u}}\cdot\nabla\theta_0)\,\mathrm{d}V$ the global thermal energy production/dissipation due to the convective term, and $K_{\mathrm{th}} = \frac{1}{2}\int_{S_{\mathrm{out}}} \rho c_p\tilde{\theta}^2\boldsymbol{u}_0\cdot\boldsymbol{n}_{\mathrm{out}}\,\mathrm{d}S$ and $H = -\int_{S_{\mathrm{int}}} \lambda\tilde{\theta}\left(\boldsymbol{n}_{\mathrm{int}}\cdot\nabla\tilde{\theta}\right)\mathrm{d}S$ are the thermal energy exchange at the boundaries of V due to the thermal energy passing across S_{out} and heat diffusion at the interface S_{int} between two domains, respectively. A generalized form of (1.26) and (1.27) for fully-temperature-dependent thermophysical properties has been recently derived by [96].

Analyzing the energy transfer between the basic state $\boldsymbol{q}_0$ and the marginally stable modes, i.e. all the $\hat{\boldsymbol{q}}_i$ + c.c. such that $\max_i \Re(\gamma_i) = 0$, (1.26) and (1.27) serve the understanding of the instability mechanism, aiding in the comprehension of the underlying physical processes that lead to linear modal instability. As neutral (i.e. marginally stable) conditions are considered, the contributions to $\mathrm{d}_t E_{\mathrm{kin}}$ and $\mathrm{d}_t E_{\mathrm{th}}$ of the neutral modes are null and $\mathrm{d}_t E_{\mathrm{kin}} = \mathrm{d}_t E_{\mathrm{th}} = 0$ if $\tilde{\boldsymbol{q}}$ is built as linear combination of the sole neutral modes. The studies that employ the Reynolds–Orr equation to gain insights on the physics of the modal instability mechanism tend to investigate the perturbation energy production/dissipation for the neutral modes + c.c. (either one if $\Im(\gamma_i) = 0$ or two complex conjugate modes if $\Im(\gamma_i) \neq 0$). The energy dynamics due to the transient interaction of marginally and asymptotically stable modes is rather investigated by nonmodal stability analysis [97].

1.3.4 Beyond infinitesimal perturbations and steady basic states

As stressed in §1.3.2, the eigenvalue spectra produced by the LSA are conclusive solely for infinitesimal perturbations. Despite their linear asymptotic stability, however, some systems can become unstable to small, yet finite, perturbations. In such cases the basic state $\boldsymbol{q}_0$ is said *conditionally stable*.

It is reported in the literature that several linearly stable shear flows such as the Hagen–Poiseuille and the Couette flow undergo a significant amplification of linear perturbations before experiencing their asymptotic exponential decay. This is also true for shear flows that can admit a linear instability, such as the plane Poiseuille flow, for which the transient growth of $\tilde{\boldsymbol{q}}$ can occur at Reynolds numbers much lower than the critical conditions predicted by LSA ($\mathrm{Re}_c = 5772$ for the plane Poiseuille flow [98]). To better understand how a linearly stable equilibrium can become unstable, we first focus on small, yet finite, perturbations, i.e. $\epsilon \ll 1$ and $\epsilon \not\to 0$. Without loss of generality, let us consider the Couette flow as an example of a classic linearly stable steady basic state (see eigenspectrum in fig. 1.6). The Couette flow is here taken a paradigmatic example for shear flows to illustrate the significance of the *non-normality* of the linear operators originating from (1.23) whenever a shear flow is assumed as basic state.

Mathematically, the non-normality property implies that an operator does not commute with its adjoint, hence the eigenvalues are not orthogonal. This results in the potential for a transient growth of the perturbation before its asymptotical exponential decay. It is extensively reported in the literature that linearly stable non-normal dynamical systems may undergo transient growth of several orders of magnitudes bigger than the initial perturbation amplitude. In such cases, it is important to compute the eigenspectra of the perturbed linear system by adding $\epsilon[E]$ to $[A]$, where $\epsilon[E]$ is a matrix of $\mathcal{O}(\epsilon)$ that can be constructed with different properties, e.g. in [41] $[E]$ is an identity matrix, whereas in [99] a normalized matrix of random values produced with a normal distribution of standard deviation 1 and mean 0. Perturbing the linear operator $[A]$ by $\epsilon[E]$ has the aim to investigate the robustness of the modal LSA prediction to small, yet finite, perturbations. We further stress that the perturbation of the linear operator $\epsilon[E]$ enters at $\mathcal{O}(\epsilon)$ in (1.23), hence at $\mathcal{O}(\epsilon^2)$ in (1.22), therefore it does not provide any energy to the perturbation $\tilde{\boldsymbol{q}}$ in asymptotic sense, i.e. for $\epsilon \to 0$. The eigenspectra computed for the perturbed linear

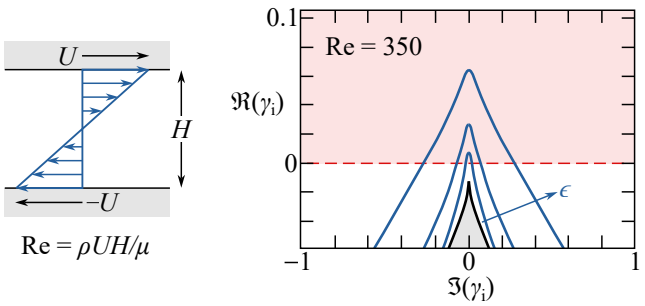

Figure 1.6: Couette flow (left) and spectra (right) for Re = 350. The black line denotes the eigenspectrum, while the blue lines are the $\epsilon-$pseudospectra for $\epsilon = 10^{-2}$, $10^{-2.5}$, and 10^{-3}, and $[E] = [I]$, where $[I]$ is the identity matrix. Figure re-adapted from [41].

operator are termed $\epsilon-$pseudospectra and they are used to determine the minimal perturbation amplitude $\epsilon_{\min}$ capable of turning the linearly stable basic state for the unperturbed operator $[A]$ into a linearly marginally stable equilibrium for the perturbed operator $[A] + \epsilon_{\min}[E]$ (see $\epsilon-$pseudospectrum in fig. 1.6).

We stress, however, that also the stability analysis based on $\epsilon-$pseudospectra relies on the linear superposition of normal modes. However, when the perturbation amplitude becomes significant, $\epsilon\tilde{\boldsymbol{q}}_i$ can grow up to $\mathcal{O}(1)$, hence it can dynamically affect the leading-order basic state. To take such dynamics into account, a nonlinear stability analysis is required (see [100]). In summary, different approaches are used to investigate the stability of a basic state:

Linear modal stability analysis:	It investigates the stability of a basic state subjected to infinitesimal perturbations ($\epsilon \to 0$) based on the eigenspectrum of the unperturbed linear operator $[A]$. The aim of modal LSA is to assess the asymptotic stability of a basic state $\boldsymbol{q}_0$ based on the growth rate $\Re(\gamma_i)$ of every single normal mode $\hat{\boldsymbol{q}}_i$.
Linear nonmodal stability analysis:	It investigates the stability of a basic state subjected to small, yet finite, perturbations ($\epsilon \ll 1$ and $\epsilon \not\to 0$) based on the $\epsilon-$pseudospectra of the perturbed linear operator $[A] + \epsilon_{\min}[E]$. The aim of nonmodal LSA is to assess the minimal perturbation amplitude $\epsilon_{\min}$ below which the perturbed system remains asymptotically stable.
Nonlinear nonmodal stability analysis:	It generalizes the linear nonmodal stability analysis by including nonlinear effects. The concept of minimal perturbation amplitude $\epsilon_{\min}$ is here replaced by the *minimal seed*, i.e. the perturbation of minimal amplitude capable of optimizing its energy growth at a certain time after its initial injection in the basic state.

The considerations discussed so far for LSA assumed that the basic state is steady, i.e. $\partial_t \boldsymbol{q}_0 = \boldsymbol{0}$. Their generalization to time-periodic equilibria of period τ, i.e. $\boldsymbol{q}_0(\boldsymbol{x}, t) = \boldsymbol{q}_0(\boldsymbol{x}, t+\tau)$, implies the introduction of a more complex theoretical framework known as Floquet theory. Following [14], the generalized eigenvalue problem (1.23) for time-periodic basic states reads:

$$(\gamma_F + \partial_t)[B]\tilde{\boldsymbol{q}} = [A]\tilde{\boldsymbol{q}}, \tag{1.28}$$

where γ_F is the Floquet exponent of the perturbation ansatz $\tilde{\boldsymbol{q}}(\boldsymbol{x}, t) = \hat{\boldsymbol{q}}(\boldsymbol{x}, t)e^{\gamma_F t} = \hat{\boldsymbol{q}}(\boldsymbol{x}, t + \tau)e^{\gamma_F t}$, where now $\hat{\boldsymbol{q}}(\boldsymbol{x}, t)$ denotes a time-periodic function. The same definitions of asymptotic and marginal stability detailed for steady LSA apply for time-periodic basic states replacing $\Re(\gamma_i)$ with $\Re(\gamma_F)$. On the other hand, when considering the mode frequency $\Im(\gamma_F)$, three scenarios are possible in Floquet stability: (i) if $\Im(\gamma_F) = 2n\pi/\tau$ where $n \in \mathbb{N}$ then $\tilde{\boldsymbol{q}}(\boldsymbol{x}, t)$ is $\tau-$periodic, (ii) if $\Im(\gamma_F) = \pm\pi/\tau$ then $\tilde{\boldsymbol{q}}(\boldsymbol{x}, t)$ is $2\tau-$periodic, and (iii) if $\Im(\gamma_F) = \alpha_F\pi/\tau$ where $|\alpha_F| \neq 1$ then $\tilde{\boldsymbol{q}}(\boldsymbol{x}, t)$ is quasi periodic with periods τ and $2\tau/\alpha_F$.

1.3.5 Flow control

Control theory provides a general framework for manipulating the evolution of a system based on static or dynamic inputs aimed to achieve the control target [101]. When flow control applications are considered, *passive flow control* refers to control strategies that employ static modifications of the geometry and do not require any injection of energy in the system. Conversely, *active flow control* deals with static or dynamic modifications of the flow energy via static or dynamic jets, as well as dynamic modifications of the boundaries. Whenever the active control is dynamically adjusted on measured states of the controlled system we talk about *closed-loop* control. Vice versa, *open-loop* controls are considered. For an extensive review on open- and closed-loop active flow control by jet actuators, we refer to [102]. For engineering applications, active and passive flow control is used to maintain, recover, or improve the performance of a system by reducing drag, enhancing mixing, and avoiding/promoting unwanted/desired flow configurations.

Stability analysis and receptivity theory are tightly related to optimal flow control. In fact, on the one hand, stability analysis provides a framework to study the flow response to an initial perturbation and, on the other hand, receptivity theory investigates the excitation of potentially unstable perturbations by external disturbances [103]. This provides the cause–effect chain to predict the occurrence of the instability that we may aim to prevent. By combining the direct (linearized or fully non-linear) Navier–Stokes operator and its adjoint, the structural sensitivity of a system can be characterized, together with the most receptive areas of the flow [104]. Such information can then be employed to localize the control strategy in order to hinder the most receptive path leading to the excitation of the potentially unstable disturbance that one wants to avoid.

Breaking the receptivity chain is however just one of the ways to employ flow control. The information on the most receptive areas of the flow could also be employed to trigger rather than to suppress an instability. This is the case, for instance, of passive flow control by vortex generators, an array of optimally designed obstacles placed on a flat plate [105] or an airfoil [106] to favour the transition to turbulence [107] or enhance heat transfer [108] in boundary layers. Owing to its significance for aerodynamic applications, the receptivity of such flows has been extensively investigated in the literature. Most of the recent studies on controlling boundary layers focuses therefore on the optimal perturbation to trigger laminar-to-turbulent transition [57] and shape optimization of the vortex generators for passive flow control.

A final introductory note on optimal flow control is about the theoretical frameworks employed to study it. Beside the so-called *model predictive control* (adjoint-based control optimization approach), other theoretical methods are also employed, such as the *optimal control* (Riccati-based feedback control approach), the *4Dvar* (adjoint-based state estimation approach), and the *Luenberger observer* (Riccati-based state estimation approach) that turns into a *Kalman filter* for stochastic theory. For a review of all such methods, we refer to [109]. Moreover, we stress that the recent development in machine learning greatly enhanced the capabilities of previous control strategies by means of reduced-order modeling [110] and digital twins [111] with multiple levels of granularity [112].

1.4 Chaotic flows

The trajectory of a fluid element is computed integrating the velocity field over time and supplying the initial fluid element position. The dynamics of such a problem is therefore deterministic, given that the flow velocity is exactly known. However, under certain circumstances, the integration of the pathline is so sensitively affected by small uncertainties either on the flow or on the initial fluid element position that the predictability of the system dynamics gets significantly degraded over time [113]. This is known as *deterministic chaos* [114], which notion can be generalized to all dynamical systems governed by the evolution equation $\dot{\boldsymbol{\zeta}} = \boldsymbol{\Xi}(\boldsymbol{\zeta}, s)$, where $\boldsymbol{\zeta}$ denotes the state of the system in phase space, $\boldsymbol{\Xi}(\boldsymbol{\zeta}, s)$ its flow, and s the independent variable such that $\dot{\boldsymbol{\zeta}} = \mathrm{d}_s\boldsymbol{\zeta}$.

Connecting chaos theory with fluid mechanics can be readily achieved when considering the fluid element trajectories by exploiting their Lagrangian description, i.e. for $\boldsymbol{\zeta} = \boldsymbol{x}_\mathrm{f}$ and $\boldsymbol{\Xi}(\boldsymbol{\zeta}, s) = \boldsymbol{u}(\boldsymbol{x}_\mathrm{f}, t)$, where $\boldsymbol{x}_\mathrm{f}(t)$ is the fluid element location at time t. If the flow is two-dimensional and incompressible, a streamfunction $\psi(x, y, t)$ exists such that $\boldsymbol{u} = (\partial_y\psi, -\partial_x\psi)$ in Cartesian coordinates. If the flow is also steady, the fluid trajectories coincide with the flow streamlines, i.e. the isolines of ψ. This implies that the advection problem is *integrable*. Equivalently, in dynamical-systems theory, one would describe such a problem as a Hamilton's canonical equation of one degree of freedom (dof), which implies integrability when the system is *autonomous*, i.e. when the flow $\boldsymbol{\Xi}(\boldsymbol{\zeta}, s)$ does not depend on the independent variable s [115]. As in our two dimensional steady flow $\boldsymbol{u}(\boldsymbol{x}_\mathrm{f}, t)$ does not depend on t, all its streamlines are regular, i.e. non chaotic (addressed as *tori* in dynamical system theory).

Such considerations suggest that the theoretical results on non-integrability (or chaos) of Hamiltonian systems [116, 117, 118, 119, 120] are applicable to the pathlines of a fluid dynamic system. In particular, it is sufficient that the Hamiltonian system becomes non-autonomous in order to admit the existence of chaotic behaviours. This implies that if the generic two-dimensional flow considered above becomes time-dependent, its regular streamlines may lead to chaotic pathlines, regardless of the flow regime. A similar consideration holds true for steady three-dimensional flows that correspond to piecewise Hamiltonian of 1.5 dof [121], hence they admit chaotic dynamics.

Another significant overlap between Hamiltonian and volume-preserving ($\nabla \cdot \boldsymbol{u} = 0$) dynamical systems consists of recognizing that chaos can be traced back to a stretching-and-folding mechanism in phase space, also known as *Smale horseshoe* [122, 123, 124]. To generate a horseshoe map, a flow needs the ability to stretch and fold a section of fluid, then return it—stretched and folded—to its original position, meeting a set of criteria referred to as Moser's conditions [119]. Various theorems and techniques [125, 115, 126] are utilized to understand the behavior under small perturbations, however initial expectations regarding the applicability of established Hamiltonian theories, like Kolmogorov–Arnold–Moser (KAM) theory, have been moderated [127]. Nonetheless, specific methods such as the Melnikov method [125, 126] have proven useful in studying analytical systems with slight deviations from integrability, as first demonstrated by [128, 129, 130, 131]. Such chaotic phenomena, also observed in dissipative systems, are not limited to phase space dynamics, as they represent the backbone of stirring and mixing [132, 133, 134, 135].

1.4.1 Classification of critical points and orbits

Visual representation is often used in chaos theory for summarizing the expected paradigmatic dynamics. This relies on the identification of critical points and orbits, whose interplay induces mathematically rigorous consequences for the system trajectories in phase space. Given a flow $\boldsymbol{\Xi}(\boldsymbol{\zeta}, s)$ and its motion $\boldsymbol{\zeta} = \Phi_s(\boldsymbol{Z})$ that transforms the initial system state $\boldsymbol{Z} = \boldsymbol{\zeta}(s = 0)$ into the current system state $\boldsymbol{\zeta}(s)$ for all s, two kinds of critical points can be identified:

(i) Fixed point: The point $\boldsymbol{\Pi}$ is a fixed point of the flow if $\boldsymbol{\Pi} = \boldsymbol{\Phi}_s(\boldsymbol{\Pi})\ \forall s$.

(ii) Periodic point: The point $\boldsymbol{\Pi}$ is a periodic point of the flow if $\boldsymbol{\Pi} = \boldsymbol{\Phi}_{nS}(\boldsymbol{\Pi})$, where $n \in \mathbb{N}$ and S is the period.

This implies that fixed points keep their location in phase space regardless of the evolution of the surrounding system states, while periodic points get back to their position after every period S. Hence, the fixed point can be intended as a periodic point for $S \to 0$, and a periodic point can be turned into a fixed point for discrete maps or stroboscopic section with period S [114]. We further stress that the identification of critical points depends on the reference frame in which the system is described. Hence, an optimal description of the dynamical system is such that critical points naturally emerge in the phase space picture of the system dynamics.

To further characterize the system dynamics in the neighborhood of a critical point, a local linearization of the motion is used by computing the eigenvalues (or *Lyapunov exponents*) γ_L of the Jacobian $[J]$ for the local flow, such that $J_{ij} = \partial\left[\boldsymbol{\Xi}(\boldsymbol{\Pi}, S)\right]_i / \partial\zeta_j$. For the easy-to-picture case of a two-dimensional flow, the point $\boldsymbol{\Pi}$ is classified based on the trace and determinant of $[J]$ (see fig. 1.7(a)). For generalization of such concepts to three-dimensions, refer to [125, 126, 114].

The eigenvectors of the Jacobian represent a local linearization of the system manifolds. They consist of all points $\boldsymbol{\zeta}$ in the phase space such that the trajectory approaches $\boldsymbol{\Pi}$ as $s \to \infty$ (stable manifold) or as $s \to -\infty$ (unstable manifold). Both such manifolds are invariants of the flow, and a system state initially belonging to them will permanently orbit on such manifolds. These orbits, as well as the critical points, have direct consequences on deterministic chaos implied by: (i) transverse homoclinic or heteroclinic intersections (see fig. 1.7(b)), (ii) positive Lyapunov exponents, or (iii) generation of horseshoe maps (see fig. 1.7(b)).

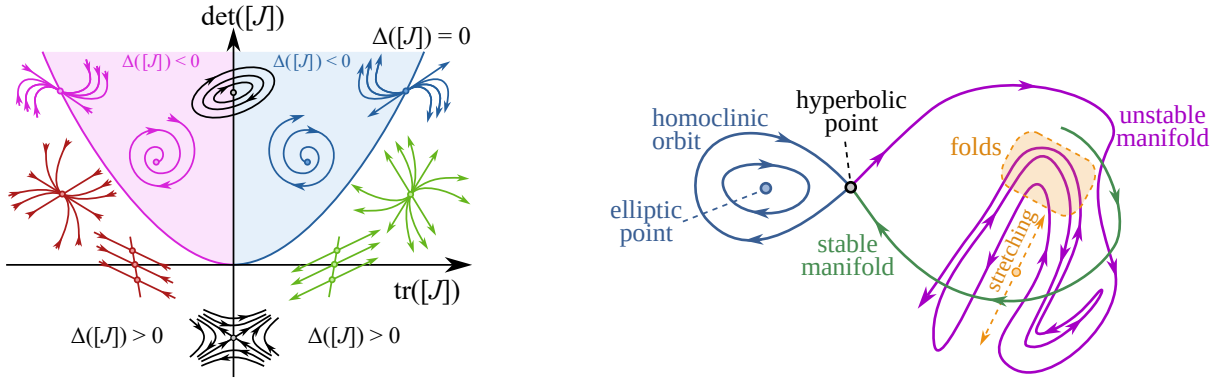

(a) (b)

Figure 1.7: (a) Classification of critical points based on $\Delta([J]) = \{\mathrm{tr}([J])\}^2 - 4\ \det([J])$, (b) stable/unstable manifolds, critical orbits, and chaos scenario by stretching and folding.

1.4.2 Chaotic advection and mixing

In various applications, optimizing the mixing rate of a fluid is a common goal. In its simplest form, this optimization aims to minimize the time required for molecular diffusion to homogenize an initially non-uniform distribution of a scalar tracer. When advection is absent, molecular diffusion alone takes a considerable amount of time to establish homogeneity, especially in compact containers. To expedite this process, chaotic advection is employed. Inertial turbulence, achieved by maintaining a high Reynolds number in a 3D flow, is a classical method for enhancing mixing. This leads to the formation of a Kolmogorov energy cascade, where energy cascades from large to small scales, resulting in the development of small-scale structures in any scalar field advected with the flow. These small-scale structures are then rapidly homogenized by molecular diffusion.

In contrast, laminar flows do not necessarily imply the presence of ubiquitous small scales and chaotic advection [135], based on the stretching and folding property of chaotic flows, offers an alternative to inertial turbulence for generating small-scale structures in the spatial distribution of advected fields. Chaotic dynamics quickly transforms a smooth initial distribution into a complex pattern of filaments or sheets, exhibiting a fractal structure [132]. This dynamic process, independent of high Reynolds numbers, operates even in time-dependent 2D Stokes flows, also known as Basset flows. Unlike turbulent mixing, chaotic advection does not necessitate the significant energy input required to maintain the Kolmogorov cascade and can be applied in scenarios, such as microfluidics, where a high Reynolds number is not feasible.

As recalled in the previous section, the Lagrangian representation of the advection problem for a passive tracer by a prescribed flow defines the dynamical system

$$\dot{\boldsymbol{x}}_{\mathrm{p}} = \boldsymbol{u}, \tag{1.29}$$

where $\boldsymbol{x}_{\mathrm{p}}$ is the tracer position. As discussed in §1.4, for a two-dimensional incompressible flow, this system is an Hamiltonian, with just one degree of freedom. In the case of unsteady flow, the system becomes non-autonomous, and chaotic particle motion is expected [134]. This same consideration can be extended to three-dimensional steady flows, that are piecewise Hamiltonian systems with 1.5 degrees of freedom [121].

In the context of advection, stirring involves purely kinematic transport (1.29), while mixing combines stirring with diffusive effects. The mathematical formulation of advection incorporating molecular diffusion is described by the advection—diffusion equation:

$$\partial_t C + \boldsymbol{u} \cdot \nabla C = \mathrm{Pe}^{-1} \nabla^2 C, \tag{1.30}$$

where C represents the scalar concentration, and the Péclet number $\mathrm{Pe} = UL/D_C$ balances diffusive and advective time-scales, where D_{C} denotes the mass diffusion coefficient of C. A similar equation will be used in §4 for modeling the dynamics of surfactant in the bronchioles, also accounting for adsorption and desorption processes.

The Batchelor scale ($\lambda_{\mathrm{B}} = \sqrt{D_C/\gamma_{\mathrm{L}}}$), where γ_{L} is the Lyapunov exponent of the flow, serves as the natural scale for mixing. At scales smaller than λ_{B}, diffusion smoothens concentration gradients, promoting molecular-scale mixing. For $D_C = 0$, the advection–diffusion equation (1.30) describes the same dynamics of (1.29) from the Eulerian point of view for $C(t = 0) = 1$ on the single particle at $\boldsymbol{x}_{\mathrm{p}}(t = 0)$ and $C(t = 0) = 0$ everywhere else.

1.4.3 Coexistence of chaotic sea, KAM islands and cantori

In open flows, the presence of chaos becomes evident as fractal structures emerge during the advection of initially uniform distributions of passive tracers [136]. Considering tracers originating from the inflow region, most fluid particles have only a finite residence time before exiting the fluid domain through the outlet. Consequently, the advection dynamics in an open flow is to be dealt with as a transient phenomenon, which fundamentally distinguishes the qualitative aspects of mixing in open flows from the closed flows of interest in this manuscript.

Especially for moderate and low-Reynolds-number flows, a key characteristic of the *kinematic template* is the emergence of stable orbits in space, encircled by KAM (Kolmogorov–Arnol'd–Moser) islands or tori [137]. While KAM surfaces can appear in open flows, they are a well-documented feature of closed flows. These islands create a fractal hierarchical structure, where large islands encompass smaller ones, forming nested patterns. The existence of KAM islands implies that considering initial conditions residing within such islands produce a dynamics confined within the KAM tori. Consequently, the set of initial conditions on a KAM surface leads to trajectories moving on such a surface, hence leading to a local violation of the hyperbolicity (see elliptic Poincaré section[1] of KAM tori in fig. 1.8). On the contrary, fluid particles with initial conditions outside each KAM torus cannot penetrate any of the KAM tori. As a consequence, the islands induce significant distinctions in the transient dynamics, contributing to crucial differences between hyperbolic and non-hyperbolic scenarios for the motion of fluid tracers.

Transport near the islands is dominated by cantori, remnants of broken KAM tori. Unlike KAM islands, cantori permit fluid particles to cross their virtual border, acting as partial transport barriers [138, 137, 135]. Although crossing may occur, it often takes extended durations, rendering cantori as quasi-persistent transport barriers. Their presence significantly impacts the advection dynamics, observable in the Poincaré section by noticing the cloud of points surrounding the sub-islands. As a result, they promote *stickiness*, a phenomenon in non-hyperbolic flows leading to exceptionally long escape times compared to hyperbolic dynamics. The overall depiction of *non-hyperbolic transport* is demonstrated in fig. 1.8, where a Poincaré section illustrates the self-similar organization of the kinematic template in a cubic lid-driven cavity for Re = 100.

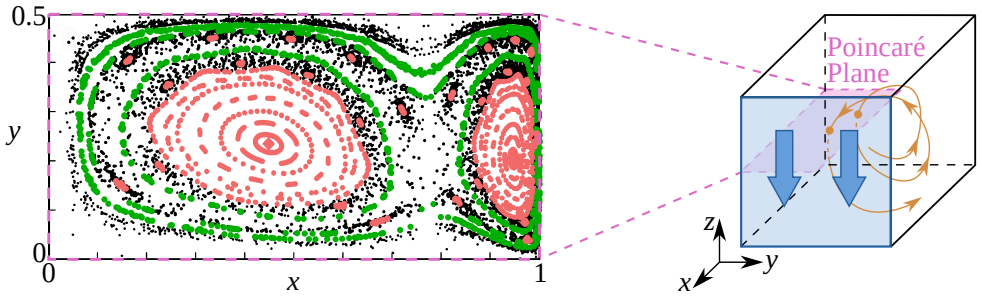

Figure 1.8: Numerical simulation (left) and schematics (right) of a Poincaré section of the streamlines (orange in the schematics) for a cubic one-sided lid-driven cavity flow for Re = 100 (left [139]). Left: Black dots denote the Poincaré returns for chaotic streamlines, green dots refer to the cantori, and pink dots are due to regular streamlines on the KAM surfaces.

[1] We recall that a Poincaré section is a dimensional reduction technique that marks the returns of a system trajectory over a given hypersurface in phase space.

1.4.4 Dilute particle–laden flows

When considering spherical particles of radius a_p and density ρ_p in a fluid of density ρ and kinematic viscosity ν, the particle concentration and size play a crucial role in defining the suspension's characteristics. Under the assumptions of Stokes drag, the particle response time τ_p, intended as the characteristic time to follow a step change of the surrounding fluid velocity, is defined as $\tau_\mathrm{p} = 2\rho_\mathrm{p} a_\mathrm{p}^2/9\rho\nu$. An alternative definition is usually employed when sedimentation phenomena are of primary importance, i.e. when $\rho_\mathrm{p} \gg \rho$. This is not the case for our study, as all the particles we consider are assumed to respect the condition $\varrho = \mathcal{O}(1)$, where $\varrho = \rho_\mathrm{p}/\rho$.

Upon definition of the characteristic time scale of the flow τ_f, a corresponding non-dimensional Stokes numbers $\mathrm{St} = \tau_\mathrm{p}/\tau_\mathrm{f}$ is obtained. The flow time scale is supposed to be chosen based on the phenomenon of interest, such that the corresponding Stokes number is representative of the particle resistance under the assumption of negligible higher-order inertial corrections that scale with the particle Reynolds number Re_p, hence with the particle–fluid slip velocity and the particle radius. To study the behaviour of small particles in turbulence, the characteristic flow time is often assumed to be equal to the Kolmogorov time [140], as the focus of such studies is to investigate the interaction of small particles (typically smaller than the Kolmogorov length). In this manuscript, we will rather study particles mostly in steady laminar cavities of characteristic length L and for which the viscous time scale L^2/ν is most relevant to the phenomenon of interest in §2. Therefore, hereinafter, the Stokes number will be defined as $\mathrm{St} = 2\varrho(a_\mathrm{p}/L)^2/9$ whenever not explicitly mentioned.

The concentration of particles may become important in large-scale suspensions [141] and is often characterized by the volume fraction $\Phi_\mathrm{V} = V_\mathrm{p}/V_\mathrm{tot}$, i.e. the volume occupied by the particles V_p over the total volume encompassing fluid and particulate phases. Additionally, the mass fraction $\Phi_\mathrm{M} = \Phi_\mathrm{V}/[\Phi_\mathrm{V} + \varrho(1 - \Phi_\mathrm{V})]$ is also considered to estimate the expected order of magnitude of the momentum transfer between particles and surrounding fluids. Whenever $\Phi_\mathrm{V} \ll 1$ one talks about dilute particle suspensions, and further considering $\varrho = \mathcal{O}(1)$ and $a_\mathrm{p}/L \ll 1$ allows to model the particles dynamics as an ensemble of non-interacting particles whose feedback on the carrier phase can be neglected. This is known as *one-way coupling*.

Reducing the complexity of a particle-laden flow to an ensemble of single-particle dynamics provides a great simplification for the understanding of leading-order effects as it significantly shrinks the dimensions of the parametric space. Studying clustering/depletion of particles by a one-way coupled approach means searching for attracting/repelling manifolds of a single particle. Particles accumulation would then be assimilated to a single-particle trapping phenomenon driven by the dissipation effects of the single-particle flow $\dot{\boldsymbol{x}}_\mathrm{p} = \boldsymbol{u}_\mathrm{p}$, where $\boldsymbol{x}_\mathrm{p}$ denotes the particle location and $\boldsymbol{u}_\mathrm{p}$ its velocity. The definitions recalled in §1.4.2 could then be applied to the particle flow in order to determine the local character of the attractor based either on an Eulerian estimate of the Lyapunov exponents or on the application of Lyapunov stability to the mutual distance between two trajectories for particles initialized infinitesimally close in phase space. We further stress a major difference between the dynamics of an incompressible fluid tracer $\dot{\boldsymbol{x}}_\mathrm{p} = \boldsymbol{u}$ and the one of a finite-size particle $\dot{\boldsymbol{x}}_\mathrm{p} = \boldsymbol{u}_\mathrm{p}$: the former is a non-dissipative dynamical system, i.e. $\nabla \cdot \boldsymbol{u} \equiv 0$, while the latter can admit local dissipation, i.e. $\nabla \cdot \boldsymbol{u}_\mathrm{p} \lessgtr 0$.

1.4.5 Modeling small inertial particles

The initial effort to derive the equation of motion for an inertial particle in a non-uniform flow is documented in [142]. Further corrections of the inconsistencies on the pressure gradient and viscous stress have been derived in [143] and [144]. The equation proposed in [144] relies on an alternative interpretation for the time derivative of the undisturbed fluid flow velocity, a suggestion later corrected by [145]. A significant contribution by Maxey and Riley [32], as well as by Gatignol [33], was the formulation of the equation for particle motion in a reference frame moving with the particle centroid, establishing a connection between this reference frame and an inertial one. Within the particle's frame of reference, they expanded the continuity and momentum equations based on the relative velocity (slip velocity) between the particle and the fluid. By asymptotic matching the unperturbed velocity field (far from the particle) with the disturbed flow near the particle, they derived an equation of motion for the particle centroid, known as Maxey–Riley–Gatignol (MRG) equation, applicable under specific conditions:

- small particle Reynolds numbers, i.e. $\mathrm{Re}_\mathrm{p} = a_\mathrm{p}|U - U_\mathrm{p}|/\nu \ll 1$, where U is a characteristic velocity of the undisturbed fluid flow and U_p the one of the particle centroid;
- small shear Reynolds numbers, i.e. $\mathrm{Re}_\mathrm{s} = a_\mathrm{p}^2 U/L\nu \ll 1$, where L is a characteristic length of the undisturbed fluid flow;
- small particle $a_\mathrm{p} \ll L$.

The MRG equation is extensively utilized for investigating the motion of an inertial particle within an unsteady and nonhomogeneous flow. The particle acceleration $\mathrm{d}_t \boldsymbol{u}_\mathrm{p}$ is determined in the Lagrangian reference frame by accounting for buoyancy, pressure forces, added mass, Stokes drag, and Basset–Boussinesq history force detailed from left to right in (1.31), respectively:

$$\begin{aligned} m_\mathrm{p}\frac{\mathrm{d}\boldsymbol{u}_\mathrm{p}}{\mathrm{d}t} = (m_\mathrm{p} - m_\mathrm{f})\,\boldsymbol{g} + m_\mathrm{f}\frac{\mathrm{D}\boldsymbol{u}}{\mathrm{D}t} - \frac{m_\mathrm{f}}{2}\frac{\mathrm{D}}{\mathrm{D}t}\left(\boldsymbol{u}_\mathrm{p} - \boldsymbol{u} - a_\mathrm{p}^2\nabla^2\boldsymbol{u}/10\right) - 6\mu a_\mathrm{p}\pi\left(\boldsymbol{u}_\mathrm{p} - \boldsymbol{u} - a_\mathrm{p}^2\nabla^2\boldsymbol{u}/6\right) \\ - 6a_\mathrm{p}^2\sqrt{\pi\mu\rho}\,\frac{\mathrm{d}}{\mathrm{d}t}\int_{t_0}^{t}\frac{\boldsymbol{u}_\mathrm{p} - \boldsymbol{u} - a_\mathrm{p}^2\nabla^2\boldsymbol{u}/6}{\sqrt{t-s}}\mathrm{d}s, \end{aligned} \tag{1.31}$$

where m_p is the mass of the particle, $m_\mathrm{f} = m_\mathrm{p}/\varrho$ the mass of the fluid occupying the same volume of the particle, d_t denotes the time derivative along the particle trajectory, and D_t the material derivative along the fluid trajectory.

The MRG equation (1.31) has undergone extensive mathematical scrutiny, including recent insights into the fractional term of the history force by [146]. Demonstrations of the existence and uniqueness of a mild local solution, particularly when the particle velocity initially matches the fluid velocity, are outlined by [147]. An extension to establish the existence and uniqueness of mild global solutions, encompassing scenarios where there is an initial velocity mismatch between the particle and the fluid, has been validated by [148]. Recent advancements focused on a mathematical reformulation of (1.31), aimed to ease the computation of the history force [149].

While the MRG equation serves as a widely employed model for predicting particle motion, it encounters limitations when the particle approaches a boundary, such as a wall, a free surface, or another particle. This limitation arises from the derivation of the equation, which involves

matching the inner expansion near the particle with an outer expansion assuming the particle perturbation vanishes at an infinite distance from the particle centroid. Near boundaries, corrections to the MRG equation are essential because the asymptotic approach based on the smallest scale being the particle radius breaks down. Specifically, the formulation of the Basset–Boussinesq history force as presented in [32] has its theoretical roots in the work of [150, 151], who derived it for a particle impulsively accelerated in an unbounded flow. As the history force originates from the vorticity diffusion modeled by unsteady Stokes equation, the presence of a boundary changes the vorticity field, hence requires to reconsider the kernel function (see [152] for experimental evidence). Similarly, adjustments are necessary for the added mass term [153, 154] when a confinement is present, and the Stokes drag should incorporate the influence of a boundary [155, 156, 157, 158]. For small, yet finite, particle Reynolds numbers, further corrections to the MRG equations are analytically derived for bounded flows [159].

We anticipate that incorporating boundary-normal Stokes-drag corrections based on the exact creeping-flow solution of Brenner [155] provides the most significant modification to the MRG equation for the boundary-driven flows considered in this manuscript [160, 161]. In fact, our particles rapidly approach the driving boundary [162] and the correction factor $\lambda_\perp$ of [155] tends to infinite as $\sim a_\mathrm{p}/\delta_\mathrm{p}$, where δ_p denotes the distance of the particle surface from the boundary. Figure 1.9(a) depicts $\lambda_\perp$ against the normalized particle–to-wall distance $\delta = \delta_\mathrm{p}/a_\mathrm{p}$.

A further simplification to the particle dynamics model can be derived under the particular asymptotic conditions of density matching particles $\varrho \to 1$ with vanishing Stokes number $\mathrm{St} \to 0$. In such conditions, the MRG equation (1.31) tends to the particle tracer equation $\dot{\boldsymbol{x}}_\mathrm{p} = \boldsymbol{u}$ in the bulk [163]. However, whenever a small, yet finite-size particle approaches an impenetrable boundary, the corresponding corrections to the MRG equation become a leading-order effect that determines the particle dynamics. This allows to propose an heuristic particle-motion model that relies on the perfect tracer equation far from the boundaries and annihilates the normal-wall velocity of the particle within a region of size $\Delta_\mathrm{p} = \delta_\mathrm{p} + a_\mathrm{p}$ from the boundaries (see fig. 1.9(b)). Such a minimal model, termed particle-surface-interaction (PSI) model, has first been proposed in [164] and implies that the particle dynamics is governed by a dissipative Filippov system [165, 162]. This is an essential feature, as it will be discussed in §2.

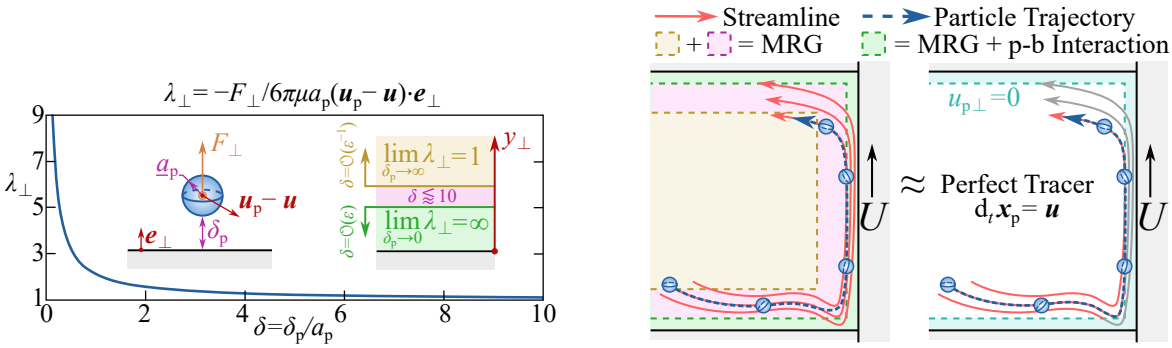

(a) Stokes drag correction normal to a wall [155]

(b) MRG + p.–b. $\approx \dot{\boldsymbol{x}}_\mathrm{p} = \boldsymbol{u}$ + PSI model

Figure 1.9: (a) Correction factor $\lambda_\perp$ [155] for the normal-wall component of the Stokes drag for a particle moving near a solid wall. (b) Schematic of the approximation employed for density-matched particles with vanishing St rapidly approaching a wall ($\dot{\boldsymbol{x}}_\mathrm{p} = \boldsymbol{u}$ + PSI model [164]).

1.5 Structure of the thesis

In this first chapter we established the scientific significance of fluid dynamics systems characterized by two or more distinct length scales. Each of these scales will prove indispensable for understanding, reproducing, and predicting the noteworthy large-scale phenomena under consideration. Systems falling within this category represent an ideal candidate for applying perturbation theory, particularly when dealing with small parameters arising from aspect ratios between distinctly separated characteristic scales. To delve into this, we revisited fundamental concepts of asymptotic theory, recognizing their sensitivity to the smallest scale in play. Anticipating the significant influence of these scales on overall flow stability, we also recalled the basics of hydrodynamic stability theory, laying the groundwork for subsequent chapters. Furthermore, we dedicated attention to multiphase flow systems with well-separated scales, with a specific focus on thin films and dilute particle-laden flows, for which the relevance of chaotic advection and dissipation sources deserved a dedicated section. The remaining part of this manuscript is structured in four chapters dealing with scientific research and future perspectives.

In §2 we will investigate a striking inherently multiscale phenomenon that leads to particle attraction in closed boundary-driven flows. In the considered systems, the particle radius is much smaller than the cavity characteristic length. In turn, the viscous layer between the particle surface and an undeformable boundary – typically the driving boundary of the cavity – is much smaller than the particle radius. This allows to identify two hierarchically-ordered small parameters that, as discussed in §2, will turn out to play a leading-order role at the largest flow scales. Several examples of such a particle focusing process will be discussed for regular and chaotic mixing in cavities in two- and three-dimensional systems, respectively. Beside showcasing several demonstrations of the occurrence of such a phenomenon, we will enter in details about the physical mechanisms responsible for the particle clustering, recalling the equivalence between clustering and trapping of particles within the one-way coupling framework.

In §3 we will focus on the application of well-separated-scale flows to turbomachines. At first, the stability of a centrifugal pump will be investigated, focusing the discussion on the vaneless radial diffuser mounted at the outlet of a pump impeller. In this case, the influence of a small radial gap between rotating and steady components of the pump will be considered in details. Moving forward in the same chapter, we will deal with instabilities in an axial compressor. As for the case of the transition to turbulence along an airfoil or a flat plate, also for the spike instability in axial compressors the most receptive flow region has already been identified in the literature. It corresponds to the thin gap between the rotor blades and the carter, known as tip leakage gap. We will show how active flow control, localized near the tip leakage gap can successfully control the spike instability for the CME2 axial compressor operated at Arts et Métiers, Lille.

Thereafter, §4 discusses typical problems at the core of respiratory fluid mechanics in distal airways. Asymptotic theory and hydrodynamic instability are essential to comprehend the classic results of interfacial instabilities originating in thin non-Newtonian films coating the airway. In this case, the smallest scale is the mesoscopic scale, where constitutive laws for stresses at continuum level are derived in the literature by modeling the response of single polymers to a

given deformation and computing their feedback on the solvent matrix. Several rheological models will be tested, showing how the polymeric scale can greatly impact on the formation of a liquid plug. Moreover, in the same chapter, we will discuss the impact of surfactants on liquid plug formation that, in turns, occludes the considered airway. In particular, the reported research activities about bronchioles occlusion highlights the significance of prevented gas exchange at distal airways, as well as the induced mechanical stresses on the airway epithelium. These two aspects are thoroughly discussed owing to their relevance at the largest scale of the pulmonary network.

Finally, in §5, five in-progress research projects will be discussed, focusing on their multiscale nature and the strategy that will be adopted to tackle them. Necessarily, owing to the challenges involved in each of these projects, dedicated multiscale approaches will be proposed and briefly discussed.

Chapter 2

Finite-Size Coherent Structures in Boundary-Driven Cavity Flows

Summary

Several examples of particles clustering in laminar flows are discussed, focusing on the particle trapping mechanism that relies on the interaction between a finite-size particle of radius a_p and an impenetrable boundary. The corresponding physical mechanism is contingent on considering the global fluid transport (at scale $L \gg a_\mathrm{p}$), the particle dynamics (at scale a_p), and the particle–boundary interaction (at scale $\delta_\mathrm{p} \ll a_\mathrm{p}$). Several examples of particle accumulations in two-dimensional and three-dimensional steady flows are demonstrated and explained, pointing out the features shared by all the investigated systems and leading to the class of particle attractors termed Finite-Size Coherent Structures.

Contents

2.1 Introduction

Particle-laden flows are fluid systems in which solid particles are suspended and transported within a fluid medium. These multiphase flows commonly occur in natural phenomena, such as sandstorms [166], the transport of volcanic ash in plumes [167], and debris flows [168]. Particle-laden flows also play a significant role in human-engineered processes, including combustion [169], the dispersion of pollutants [170], industrial pipelines [171] as well as in biomedical applications like drug delivery [172].

Particles carried by a fluid flow have a tendency to gather in specific areas. This clustering has been extensively studied in turbulent flows, where it typically occurs due to (i) the particles' inertia leading to coherent structures controlled by the Lagrangian transport of material lines for the carrier flow (Lagrangian Coherent Structures [173]), (ii) turbophoresis [174] that relies on the net drag force and the gradient of particle kinetic stresses induced by turbulence acting on the particles, and (iii) the sweep-stick mechanism [175] that implies the tendency of heavy particles with a Stokes number lying in the inertial range of time scales to aggregate in the neighborhood of zero-acceleration points for homogeneous isotropic turbulent flow.

In low- and moderate-Reynolds-numbers flows, a qualitatively similar clustering is also observed even for negligible particle inertia. In particular, the phenomenon of micro- and nano-particles self-organization is reported within millimeter to micrometer-scale systems characterized by laminar flow conditions. Hence, the particles clustering in such flows cannot rely on any of the three dissipative mechanisms listed above. Illustrative examples of the phenomenon of interest encompass particle clustering at fluid interfaces determined by the substrate wetting properties [176], as well as the emergence of bacterial clustering [177, 178] and boundary-induced particle accumulation in various microsystems [179, 180].

These latter class of particle cluster phenomena can be elucidated through the consideration of *finite-particle-size effects* and the interaction of each particle with impenetrable boundaries [164, 181, 182]. In fact, the viscous forces exerted by the fluid on the particle, when the latter is moving in the proximity of a boundary can lead to the transfer of particles to a limit cycle or a quasi-periodic manifold that does not mix with the surroundings. The resulting particle accumulation structures solely rely on the dissipation of kinetic energy produced in the near-boundary region inaccessible to finite-size particles (see fig. 1.9(b)). Such an *energy dissipation* is due to the net repulsive forces primarily generated by the viscous stresses resulting from the interaction of a finite-size particle and a boundary in its proximity (see fig. 1.9(a)). Hence, the resulting particle coherent structures are termed *Finite-Size Coherent Structures* (FSCS).

In this chapter, we will consider FSCS in various boundary–driven cavity flows. We will start with two-dimensional cavities where the flow is regular and particle accumulation is observed in the form of limit cycles or point attractors. Thereafter we will move to flows where three-dimensional effects can lead to chaotic advection that strongly complexifies the understanding of FSCS. Finally, we will conclude by summarizing the class of flows that can lead to FSCS and briefly identify examples of this same clustering phenomenon reported in the literature.

2.2 Two-dimensional FSCS in non-chaotic flows

Whenever a dispersed particulate phase is embedded in an incompressible carrier phase, several two-dimensional flows admit manifolds of attractions for the particles. The resulting coherent particle structure cannot rely on the dissipation of the carrier phase because an incompressible flow is, by definition, a non-dissipative dynamical system ($\nabla \cdot \boldsymbol{u} = 0$). The dissipation source must therefore be looked for in the particulate system. As already briefly discussed in §1.4.5, the Stokesian asymptotic of the flow around the particle provides several mechanisms of kinetic energy dissipation that could lead to particle clustering, even for low-Reynolds-number regimes. Namely, the Maxey–Riley–Gatignol equation identifies Stokes drag, buoyancy, Faxen's forces due to streamline curvature $\sim a_\mathrm{p}\nabla^2\boldsymbol{u}$, the Basset–Boussinesq's memory term and, whenever included, finite Reynolds number corrections such as the Saffmann's lift force. Each of such terms can lead to specific two-dimensional particle clustering phenomena such as light particles clustering at a steady vortex core [183, 184], high-strain induced attractors for density-matched particles [185], and shear-induced particle migration due to the Segre–Sielberg effect [186].

All such particle attractors can be explained by the MRG equation, i.e. neglecting the perturbation of each particle on the carrier flow, as well as collective particle phenomena. Another remarkable feature of such particle coherent structures is that they make use of an asymptotic expansion that assumes an unbounded flow around the particle (see discussion about the MGR equation in §1.4.5). Thereafter, they never require to introduce an additional scale smaller than the characteristic scale of the carrier fluid coherent structures L and the characteristic scale of the particle, i.e. its radius a_p. This does no longer hold when a rigid particle moves near an impenetrable boundary and the Stokes drag gets significantly intensified within a scale $\delta_\mathrm{p} \ll a_\mathrm{p}$, where δ_p measures the distance between the particle surface and the undeformable boundary (see §1.4.5 for a brief discussion [155, 158]). Corresponding corrections are reported for the Basset–Boussinesq term [152] and low-particle-inertia regimes [159].

In the following subsections we will present a few examples of particle coherent structures that inherently rely on the interaction between the particle and the boundary, hence on the viscous forces that become dominant within a distance δ_p from the boundary. Particle attractors either in form of limit cycles or point attractors will be demonstrated for three classes of two-dimensional boundary-driven flows: (i) a confined oscillatory Kirchhoff vortex, (ii) shear-driven cavities, and (iii) a singular dihedral corner. In all such systems, the particle attractor results from the equilibrium between a force pushing the particle towards the boundary and the enhanced Stokes drag due to the particle–boundary interaction that results in a net repulsive effect away from the boundary. The relevant mechanisms leading to such particle coherent structures will be briefly summarized for each of the three examples, demonstrating the non-trivial role that the particle–boundary interaction plays in determining the particle attracting manifolds. Three approaches for simulating the particle dynamics will be employed: (a) one-way coupling with MRG equation supplemented by the PSI model, (b) fully-resolved simulations with a two-dimensional circular particle, and (c) fully-resolved simulations with a spherical particle in Stokesian motion.

2.2.1 Confined oscillatory Kirchhoff vortex

The conventional inertial centrifugation observed in heavy particles within a steady Kirchhoff vortex has been demonstrated to turn into a centripetal motion when subjected to a pulsating Kirchhoff vortex. This phenomenon has first been reported by [187], who termed it *Oscillatory Counter-Centrifugation* (OCC). They further estimated that OCC occurs when a specific threshold of vortex pulsation frequency f is reached in relation to the fluid kinematic viscosity ν, particle radius a_p, and particle-to-fluid density ratio $\varrho = \rho_\mathrm{p}/\rho$. Experimental confirmation of OCC has recently been provided for the agglomeration of fiber particles in periodic flows [188].

The pulsating Kirchhoff vortex has been further investigated by [189]. His work delves into the influence of Coriolis forces, which are responsible for reversing the centrifugal motion, leading to the emergence of a more complex phenomenon that he termed *Oscillatory Switching Centrifugation* (OSC). In fact, depending on Stokes number $\mathrm{St} = 2\varrho a_\mathrm{p}^2/9R^2$ (where R is the characteristic scale of the Kirchhoff vortex) and particle-to-fluid density ratio ϱ, the asymptotic particle repellor at the vortex core can be converted into an asymptotic particle attractor and vice versa, all by altering the vortex Strouhal number $\mathrm{Str} = 2\pi f/\Omega$, where f is the pulsation frequency and Ω the vortex rotation rate. Additionally, [189] explored the intricate dynamics of particles in chaotic motion and their connection to non-trivial limit cycles observed at specific boundaries in parameter space. These boundaries mark the transition where particle centrifugation transforms into centripetal motion and vice versa.

In confined oscillating systems, OSC provides therefore the mechanism that can centrifuge light and heavy particles, i.e. $\varrho \lessgtr 1$, from the bulk towards the cavity wall. An example is shown in fig. 2.1 for $\varrho = 0.9$, $\mathrm{St} = 1$, $\mathrm{Str} = 0.094$. The initial centrifugation of the light particle leads to an increase of its radial coordinate $r_\mathrm{p}(t)$, normalized with the confinement radius R. When the particle reaches the wall proximity, i.e. for $r_\mathrm{p} = \mathcal{O}(a_\mathrm{p})$, the viscous forces between the particle surface and the no-slip wall oppose to the radial acceleration of the particle, potentially leading to non-trivial limit cycles that represent single-particle attractors (see green trajectory in the right panel of fig. 2.1). They are therefore an example of FSCS for a confined pulsating Kirchhoff vortex. For a detailed analysis of the scenarios that can occur in such a system, we refer to [190] who identified steady and rotating FSCS by one-way coupling (see MRG and PSI in fig. 1.9(b)).

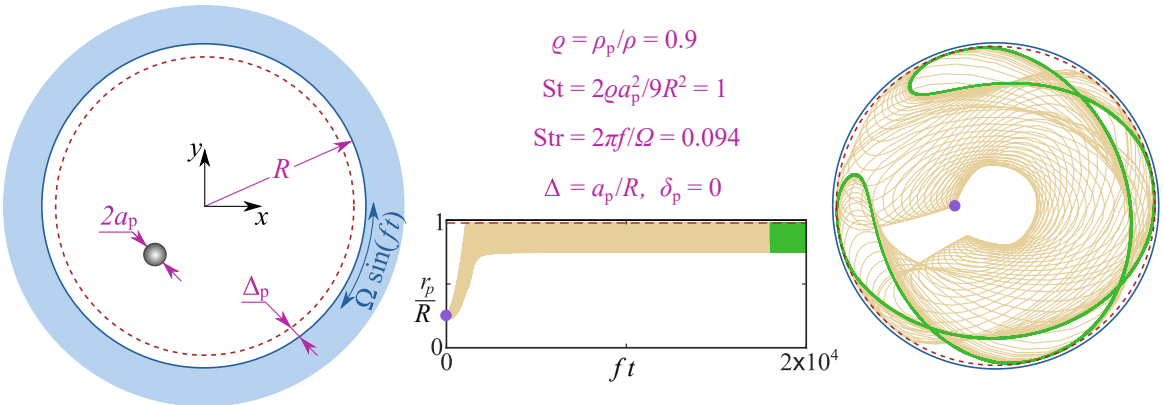

Figure 2.1: Schematic (left), radial coordinate (middle), and particle attractor (right) for FSCS in a confined pulsating Kirchhoff vortex. Non-dimensional parameters are reported in the figure.

2.2.2 Shear-driven cavities

A second class of two-dimensional problems in which finite-size coherent structures are demonstrated deals with steady shear-driven cavities. They are characterized by one or multiple driving boundaries responsible for producing the shear that drives the cavity flow. Consequently, the highest flow velocities produced near the driving boundary lead to a pronounced clustering of streamlines. The presence of surrounding no-slip walls further enhances this streamline crowding at the driving boundary, leading to the frequent transport of particles in its close proximity.

Three examples of cavity flow driven by different kinds of shear are considered: (i) a lid-driven cavity, where the shear is produced by the no-slip condition at the contact with a lid translating at constant velocity U (see fig. 2.2(a)), (ii) a shear-stress-driven cavity, where boundary shear τ_s is constant over the whole driving boundary and directly enforced as a boundary condition (see fig. 2.2(b)), and (iii) a thermocapillary liquid bridge, where the shear driving the flow along the interface is due to a surface tension gradient proportional to the interfacial temperature gradient $\partial_s\sigma = \sigma_\theta \partial_s\theta$ (see fig. 2.2(c)). As the driving mechanism of these three systems produces qualitatively different shears at the moving boundary, the definition of the corresponding Reynolds numbers Re is reported in fig. 2.2 for each flow case.

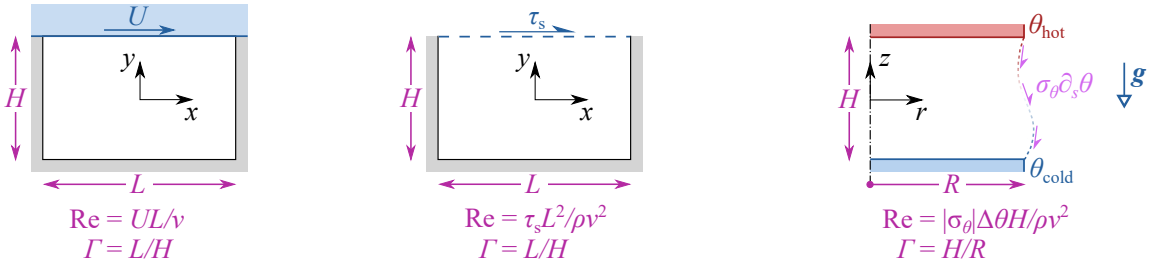

(a) Lid-driven cavity (b) Shear-driven cavity (c) Thermocapillary liquid bridge

Figure 2.2: Schematic of (a) a lid-driven cavity, (b) a shear-stress-driven cavity, and (c) a thermocapillary liquid bridge subject to a gravitational field of acceleration $\boldsymbol{g}$.

Figures 2.3(a,b) demonstrate the occurrence of particle attractors in the form of limit cycles for lid- and shear-stess-driven cavities. Three particle radii, $a_p/H = 0.01$, 0.03 and 0.05, are simulated for $\varrho = 2$ in the lid- and shear-stress-driven cavities using a fully-resolved approach with circular particles. The limit cycles are identified by root-finding of the fixed point on the Poincaré section at $y/H = 0.3$. Regardless of the initial position of the particle, the attracting limit cycles are stable global attractors for the particulate system whenever $\varrho > 1$, even if the location of the attractor slightly depends on the particle-to-fluid density ratio. The variation of the minimum distance Δ_p of the particle centroid from the driving boundary for such two cavity flows is reported in the bottom panels of figs. 2.3(a,b), demonstrating that the minimum lubrication gap δ_p between the particle surface and the impenetrable driving boundary depends significantly on the particle radius a_p, hence on the finite size of the particle.

Figure 2.3(c) reports the numerical prediction (solid line) of a particle limit cycle in a thermocapillary liquid bridge. The thermocapillary flow is first simulated without the particle and then the particle trajectory is obtained by a one-way coupling approach based on a simplified MRG

equation for computing the particle trajectory in the bulk and the PSI model (with Δ taken from fig. 2.3(b)) for taking into account the asymptotic net repulsion of the particle from the driving boundary. The comparison with experiments was carried out in terms of the radial location of the particle (see bottom panel of fig. 2.3(c)) and led to satisfactory agreement assuming that a layer of surfactant of height $6\%H$ deposits on the cold rod and rigidifies the interface.

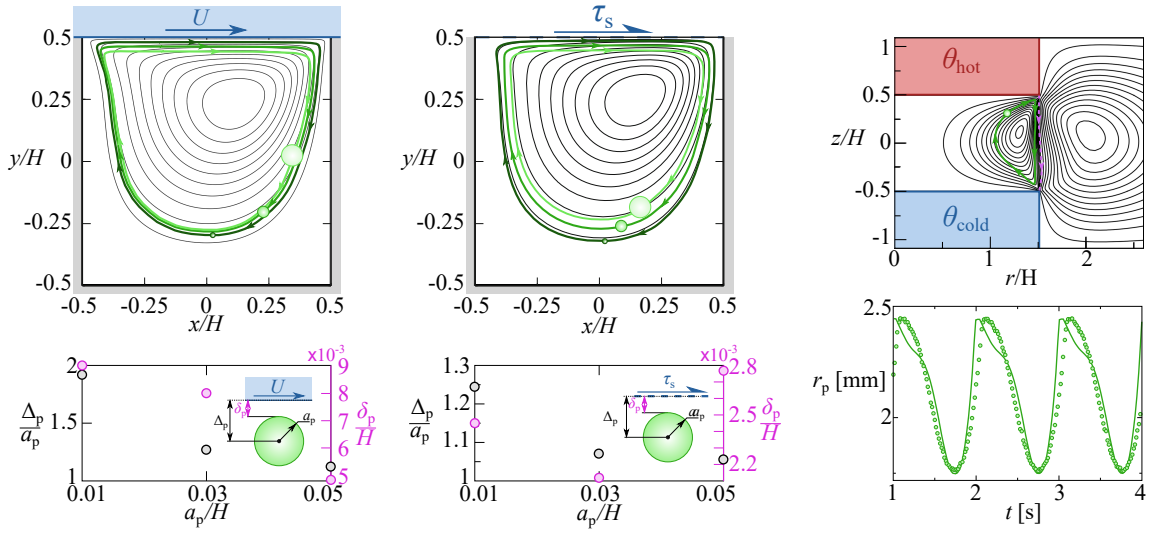

(a) Lid-driven cavity (b) Shear-driven cavity (c) Thermocapillary liquid bridge

Figure 2.3: Two-dimensional limit cycles in (a) a lid-driven cavity, (b) a shear-driven cavity, and (c) a thermocapillary liquid bridge. The bottom panels in (a) and (b) denote the minimum distance of the particle centroid from the driving boundary $\Delta_p = a_p + \delta_p$, normalized with the particle radius a_p, as well as the minimum dimensionless distance δ_p/H of the particle surface from the same boundary. The bottom panel of (c) denotes the comparison between the numerical prediction and the experimental measurement of the radial coordinate of a 30μm-radius particle in a liquid bridge with $H = 1.7$ mm upon assuming a surfactant layer height of $6\%H$ deposited at the cold corner. The aspect ratio equals $\Gamma = 1$ for (a) and (b), while it is 0.66 for (c). The corresponding Reynolds numbers are Re = 100, 1000, and 331. For further details, we refer to [191, 181, 192, 193], respectively.

For particles initially located in the bulk of the cavity, the physical mechanism leading to the emergence of a particle limit cycle relies on inertial centrifugation, which is possible only if the particle-to-fluid density ratio is larger than 1, i.e. $\varrho > 1$ (as the flow is steady). The particle is then pushed from the vortex core towards the boundary, where the viscous forces significantly oppose the centrifugation for $\delta = \mathcal{O}(1)$, leading to an equilibrium trajectory that represents the particle limit cycle. When the particle is initialized in a region of the cavity for which the fluid flow streamlines intersect the prohibited region for the particle centroid (region at distance $< \Delta_p$ from the driving boundary), also neutrally buoyant particles can experience a limit cycle by the sole streamline hopping effect due to particle–boundary interaction (see fig. 1.9(b)). In this sense, the corresponding equilibrium trajectory for $\varrho = 1$ is no longer a global attractor. Owing to the essential role of the particle–boundary interaction, possible only thanks to the finite particle radius, the demonstrated particle limit cycles represent examples of FSCS in shear-driven cavities.

2.2.3 Singular dihedral corner

A last example of finite-size coherent structures in a two-dimensional flow is here considered investigating the Stokesian motion of a spherical particle near a singular dihedral corner formed by a steady vertical wall and an horizontal wall that slides tangentially to itself. As the resulting Stokes problem is linear, [194] employed the superposition principle to solve it numerically by decomposing it in six sub-problems. Each of them allowed to determine very accurate closed-form fitting functions for the force and torque components once the particle is kept fixed. To grant consistency with the dynamics of a particle near a wall and far from the corner, such fits have been constructed to relax to the corresponding asymptotic forces and torques theoretically computed by [195, 155, 157, 156].

Thereafter, assuming that the particle is free to move in the surrounding fluid, its trajectory is determined by enforcing that the resultant force and torque applied to its centroid are null. This is a direct consequence of the quasi-steady approximation implied by the creeping flow as Stokesian dynamics relies on the asymptotic limit of negligible inertial effects, i.e. negligible particle accelerations. The resulting particle dynamics leads to a dissipative system that can admit sinks, hence particle attractors. Upon the consideration of a gravitational field oriented at an angle ϕ_x with respect to the x-axis, [196] characterized such attractors and their correction due to flow inertia in a two-sided lid-driven cavity (see fig. 2.4).

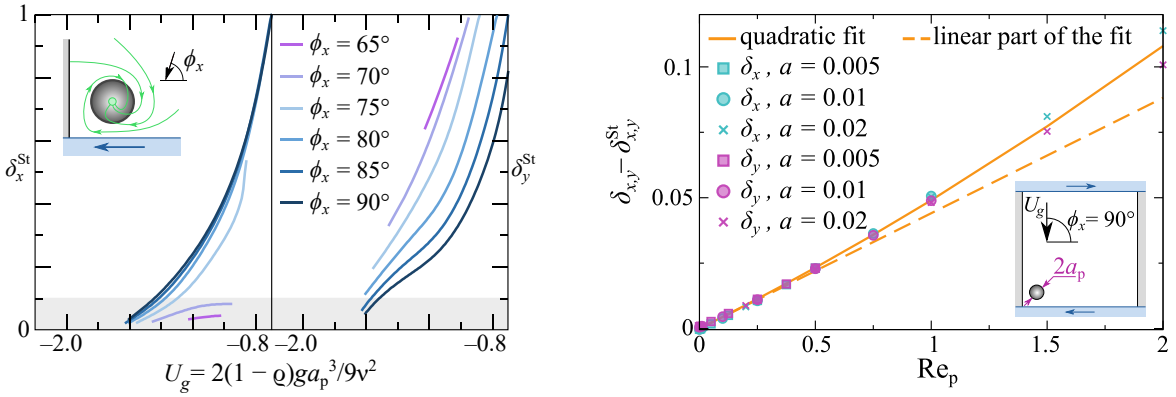

(a) Stokesian attractor

(b) Finite-particle-Reynolds-number correction

Figure 2.4: (a) Normalized gap of the particle attractor $(\delta_x^{St}, \delta_y^{St})$, and (b) correction $(\delta_x - \delta_x^{St}, \delta_y - \delta_y^{St})$ for inertial effects estimated via a two-sided square lid-driven cavity for three particle radii $a = a_p/H = 0.005$, 0.01, and 0.02. The green lines in the inset of (a) are a schematic of the particle flow trajectories leading to the particle attractor located at the stagnation point for $\boldsymbol{u}_p$.

The dissipation mechanism is due to the corrected viscous drag $\boldsymbol{F}_p = 6\pi\mu a_p \boldsymbol{u}[\boldsymbol{K}_F](\boldsymbol{\delta})$ and torque $\boldsymbol{T}_p = 8\pi\mu a_p^2 \boldsymbol{u}[\boldsymbol{K}_T](\boldsymbol{\delta})$ exerted by the fluid on the rigid particle, where the matrices $[\boldsymbol{K}_F](\boldsymbol{\delta})$ and $[\boldsymbol{K}_T](\boldsymbol{\delta})$ correct the Stokes drag and the particle torque taking into account the proximity of the particle to each wall $\boldsymbol{\delta} = \boldsymbol{\delta}_p/a_p = (\delta_x, \delta_y)$, with $\lim_{\boldsymbol{\delta}\to\boldsymbol{\infty}}[\boldsymbol{K}_F] = \lim_{\boldsymbol{\delta}\to\boldsymbol{\infty}}[\boldsymbol{K}_T] = [\boldsymbol{I}]$. Hence, the observed particle attractors are due to the particle finite size ($a_p \neq 0$) and its interaction with the boundaries, provided that the gravitational force drives the particle against the corner or one of the walls. The resulting finite-size coherent structure leads to point attractors in two-dimensions that vary in location with U_g, ϕ_x and Re_p (see fig. 2.4).

2.3 Three-dimensional FSCS in laminar chaotic flows

The major difference between the two-dimensional flows considered so far and the three-dimensional systems dealt with in this section is that the latter can admit chaotic mixing for the carrier phase. Despite the fact that in both the cases the considered regimes are laminar, the two-dimensional flows considered have been carefully selected to limit the generalized non-homogeneous coordinates to two, which prevents chaos to occur. In fact, the generalized coordinates for the oscillatory Kirchoff vortex are r and t, while the other two-dimensional flows only depend on x and y or r and t. Chaos could emerge, for instance, if our two-dimensional lid-driven cavity would have an oscillating lid capable of bringing the generealized non-homogeneous dimensions of the carrier flow system beyond 2, i.e. (x, y, t), see [197, 198].

Laminar chaotic systems can also be studied by steady three-dimensional flows, which are equivalent to Hamiltonian systems with 1.5 dof (see §1.4 [121]). The argument about the non-dissipative nature of incompressible systems ($\nabla \cdot \boldsymbol{u} = 0$) still holds, hence the clustering of particles cannot be directly derived as a consequence of the fluid flow. However the physical constraint that two distinct streamlines cannot cross is far less restrictive in three-dimensional flows. Hence, chaotic advection can repeatedly bring a fluid element near a boundary even if it has been initialized in the bulk, provided that the chaotic sea connects the bulk and the near-boundary regions. This identifies a qualitative difference between regular and chaotic systems: A particle initialized far from a boundary needs a bulk force (e.g. one of the MRG equation terms) to approach a boundary and form a FSCS in regular flow. Conversely, in chaotic systems, the ergodicity of the fluid flow will naturally drive tracer particles near a boundary.

This implies that particle attractors in chaotic systems can also be found for the idealized case of finite-size density-matched particles that behave like perfect tracers in the bulk and experience a net repulsion near an impenetrable boundary (see fig. 1.9(b)). The particle–boundary interaction would then provide the dissipative mechanism capable of reducing the kinetic energy of the particulate system owing to a significant reduction of the boundary-normal particle velocity once the particle moves close to a boundary. As a consequence, the particle hops across fluid flow streamlines near the boundary, leading to two possible scenarios: (a) after the interaction the particle is released inside the chaotic sea, hence it keeps behaving ergodically without giving rise to any cluster, and (b) after the interaction the particle is released inside a regular region of the carrier flow that does not mix with the surrounding chaotic sea. In the latter case, the particle is trapped inside the regular region (corresponding to a KAM torus, see §.1.4.3). This whole process requires at least one KAM torus located close to a boundary, and the right intensity for the particle repulsion in order for the particle to pierce the outer KAM surface an odd amount of times, hence being released inside of the KAM torus upon interaction with the boundary.

Three examples of such systems are: (i) a liquid bridge, (ii) a two-sided lid-driven cavity, and (iii) a cuboidal lid-driven cavity. Linear stability analysis will be employed to determine the critical conditions under which a two-dimensional steady flow undergoes a bifurcation that turns it into a three-dimensional steady flow. The aim is to allow chaotic advection without significantly increasing the flow strength in order to preserve the existence of KAM tori inside the flow.

2.3.1 Thermocapillary liquid bridge

2.3.1.1 Linear stability analysis

In a thermocapillary liquid bridge enclosed in an adiabatic chamber and surrounded by air, we examine the axisymmetric basic state. Thermocapillary stresses induce a clustering of streamlines at the interface, generating a clockwise vortex within the liquid phase (fig. 2.3(c)). Despite the absence of buoyancy-driven instability due to the overall stable thermal stratification [199], buoyancy forces affect the slenderness of the vortex in the liquid phase, as the hot fluid transported near the free surface tends to ascend in the bulk, leading to a significant separation bubble on the cold wall [200]. The boundary layer in the liquid phase results from the sharp temperature gradient near the hot and cold corners, giving rise to peaks in surface velocity close to these corners. Notably, the peak at the cold corner is particularly pronounced because the fluid, accelerated toward the wall, decelerates along the liquid–gas interface to zero velocity at the wall. Due to the gas chamber geometry [201], a much larger vortex forms in the gas phase (counter-clockwise in fig. 2.3(c)). The gas-to-liquid ratio of Rayleigh numbers indicates negligible buoyancy effects in the gas, hence the flow in the gas phase is primarily driven by interfacial shear.

Non-dimensionalizing by using a thermocapillary scaling, i.e. H, H^2/ν, $|\sigma_\theta|\Delta\theta/\rho\nu$, $|\sigma_\theta|\Delta\theta/H$, and $\Delta\theta$ for lengths, time, velocity, pressure and temperature, respectively, it yields

$$\Gamma = \frac{H}{R}, \quad \mathcal{V} = \frac{V_\mathrm{l}}{\pi R^2 H}, \quad \mathrm{Re} = \frac{|\sigma_\theta|\theta H}{\rho\nu^2}, \quad \mathrm{Pr} = \frac{\rho\mu c_p}{\kappa}, \quad \mathrm{Bd} = \frac{\rho g\beta H^2}{|\sigma_\theta|}, \tag{2.1}$$

where V_l is the volume of the liquid bridge, and Pr and Bd the Prandtl and dynamic Bond numbers, respectively. The basic state represents a two-dimensional axisymmetric steady flow that precludes chaotic mixing. When $\Gamma = 0.66$, $\mathcal{V} = 1$, $\mathrm{Bd} = 0.41$, $\mathrm{Pr} = 28$, and $\mathrm{Re}_c = 731$, the basic flow transitions to instability characterized by a pair of azimuthally propagating modes with $\omega_c = \Im(\gamma_c) = \pm 14.85$ and $m = 3$. One of these critical modes is depicted in fig. 2.5(a). Analysis of the global temperature distribution in the horizontal plane at $z = 0.20$ (top-left panel of fig. 2.5(a)) reveals that temperature perturbations primarily occur within the liquid phase, with weak perturbations in the gas phase. The perturbation velocity vector field displays characteristic structures consistent with internal temperature perturbations and axial vortices observed in cases with smaller Pr [202]. Azimuthal temperature gradients on the free surface predominantly drive the perturbation vortices (bottom panel of fig. 2.5(a)), which transport cold (hot) fluid from the interior (free surface) just ahead of the cold (hot) internal perturbation temperature peaks, thereby determining the azimuthal propagation direction of the wave. Conversely, radial conduction of perturbation temperature from internal extrema to the free surface sustains the perturbation flow, driving primarily axial perturbation vortices (seen in the top-left panel of fig. 2.5(a)) through mainly azimuthal thermocapillary stresses. This confirms the nature of the perturbation flow as a hydrothermal wave [203, 202]. The three-dimensional structure of the temperature perturbation field is visualized by isosurfaces in the top-right panel of fig. 2.5(a).

To further confirm such interpretation, the total thermal energy budget is computed

$$\mathrm{d}_t E_\mathrm{th} = \mathcal{D}_{\mathrm{th},i}^{-1}\,\mathrm{d}_t \int_{V_i} (\tilde{\theta}^2/2)\,\mathrm{d}V = -1 + \sum\nolimits_{j=1}^{2} J_{j,i} + H_{\mathrm{fs},i}, \qquad i \in [\mathrm{l},\,\mathrm{g}] \tag{2.2}$$

where all terms have been scaled by the thermal dissipation rate $\mathcal{D}_{\mathrm{th}} = (\alpha_\kappa/\mathrm{Pr}) \int_{V_i} (\nabla\tilde{\theta})^2 \, \mathrm{d}V$, α_κ being the ratio between the local thermal diffusivity and the one of the liquid phase κ. Thus, the scaled dissipation rate $D_{\mathrm{th}} = 1$ is constant. The terms $\sum J_j = \sum \int j_j \, \mathrm{d}V = -(\mathrm{Re}/\mathcal{D}_{\mathrm{th},i}) \int_{V_i} \tilde{\theta} \left(\tilde{u}\partial_r\theta_0 + \tilde{w}\partial_z\theta_0\right) \, \mathrm{d}V$ represent the scaled total production rates of thermal energy, which is transferred between the basic state and the perturbation flow, with corresponding local production densities j_j. Moreover, $H_{\mathrm{fs}} = \pm(2\pi\alpha_\kappa)(\mathcal{D}_{\mathrm{th},i}\mathrm{Pr}) \int_{-1/2}^{1/2} h \left(\partial_r\hat{\vartheta}^2 - h_z\partial_z\hat{\vartheta}^2\right) \, \mathrm{d}z$ denotes the heat transferred through the liquid–gas interface.

The significance of the temperature transport described for the most dangerous perturbation is reaffirmed by the total thermal energy budget illustrated in fig. 2.5(b). In the liquid phase (left panel), thermal perturbation energy primarily originates from J_1 (resulting from radial convection of basic state temperature) and dissipates within the bulk. Notably, the instability cannot be attributed to axial temperature gradients, as their collective contribution to the thermal energy budget is negative: $J_2 < 0$. Only a negligible portion of thermal perturbation energy H_{fs} transfers to the gas phase (consistent with fig. 2.5(a)), which instead emerges as the primary source term $H_{\mathrm{fs,g}} = -H_{\mathrm{fs}}(\mathcal{D}\mathrm{th}/\mathcal{D}\mathrm{th,g})$ in the gas phase (right panel of fig. 2.5(b)) and dissipates rapidly. In this two-phase system with cylindrical gas confinement, the gas phase plays a passive role in the instability mechanism. Furthermore, given the very high Prandtl number, inertial effects do not contribute to the instability [202]. Similarly, buoyancy does not significantly influence the instability in the reference case [199]. Additionally, from the isolines depicted in the top-left panel of fig. 2.5(a), one can observe that thermal perturbation energy is generated just ahead of the instantaneous perturbation temperature peaks, aligning with the clockwise propagation of the hydrothermal wave.

Figure 2.5(c) presents the relationship between the critical Reynolds number Re_c and the length of the liquid bridge, indicated by the aspect ratio Γ. Maintaining a constant relative volume of the liquid bridge at $\mathcal{V} = 1$, we adjust Bd as $\mathrm{Bd} = \mathrm{Bd}_{\mathrm{ref}} \times (\Gamma/\Gamma_{\mathrm{ref}})^2 = 0.41 \times (\Gamma/0.66)^2$. Thin lines denote neutral Reynolds numbers and associated neutral frequencies for $\mathrm{Re} > \mathrm{Re}_c$. The critical azimuthal wave number m is color-coded. Within the range of Γ considered, only critical modes with $m = 1$, $m = 3$, and $m = 4$ emerge. The instability mechanism remains qualitatively consistent across all modes, with similar considerations as discussed for the reference case. For further insights into the impact of volume ratio, buoyancy, gas phase blowing, dynamic surface deformation of the interface, and thermally-dependent properties, refer to [201, 96, 204, 205, 206].

2.3.1.2 Streamline topology of the three-dimensional flow

As the most dangerous mode is three dimensional, the supercritical flow allows for chaos to set in. Therefore, to investigate finite-size coherent structures in laminar, chaotic, thermocapillary liquid bridges we focus on $\mathrm{Re} > \mathrm{Re}_c$. The supercritical flow for $\mathrm{Pr} = 28$, $\mathrm{Re} = 1600$, $\Gamma = 0.68$, $\mathcal{V} = 1$, and $\mathrm{Bd} = 0.43$ is here selected to demonstrate the intricate flow topology in a thermocapillary liquid bridge. As the selected conditions are strongly supercritical, one cannot assume that the flow is given by a direct superposition of the basic state and the corresponding most dangerous. It turns out, however, that simulating the nonlinear Navier–Stokes equations, the mode $m = 3$ predicted by the LSA still largely dominates the Fourier spectrum [200]. A corresponding hydrothermal

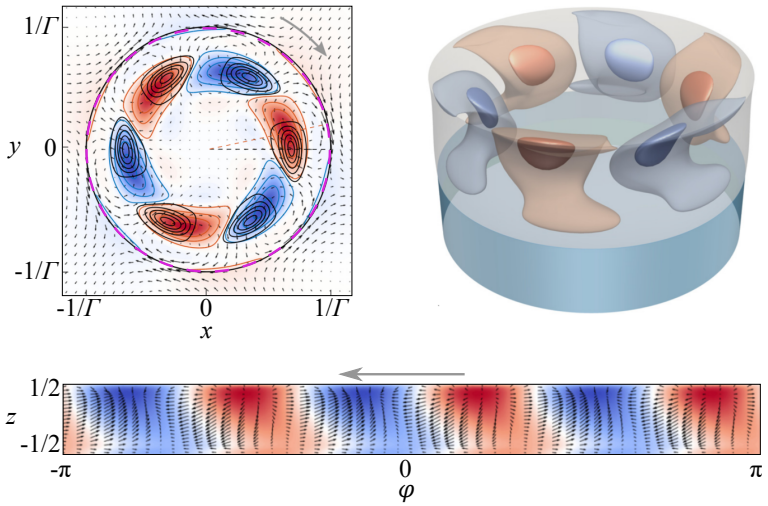

(a) Most dangerous perturbation for $\mathrm{Re}_c = 731$

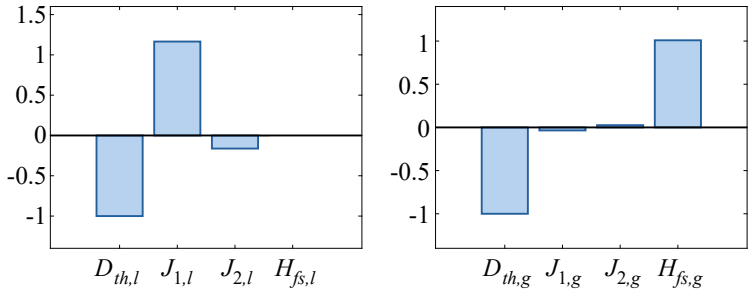

(b) Thermal energy budget for $\mathrm{Re}_c = 731$

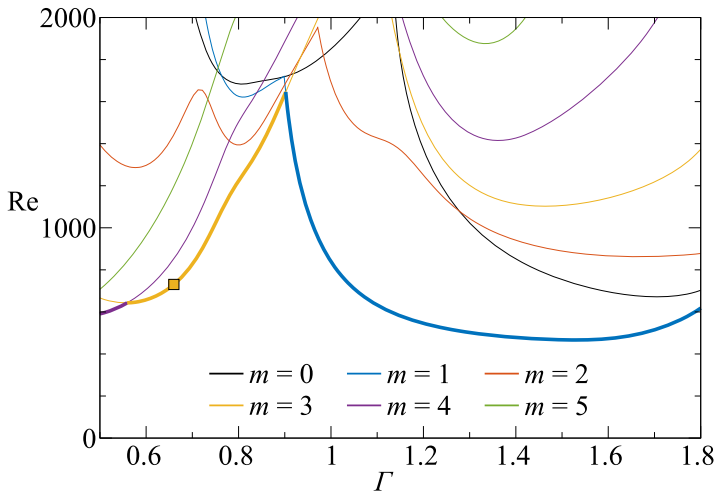

(c) Neutral and critical stability curves

Figure 2.5: (a) Critical conditions for $\Gamma = 0.66$, $\mathcal{V} = 1$, $\mathrm{Bd} = 0.41$, $\mathrm{Pr} = 28$, $\mathrm{Re}_c = 731$, and $m_c = 3$. The top-left panel shows a cross section at $z = 0.2$, the top-right panel is a three-dimensional reconstruction in the liquid phase, and the bottom panel considers the free surface. The perturbation temperature $\tilde{\theta}$ in plotted in colors, $\tilde{\boldsymbol{u}}$ as black arrows, and the gray arrow denotes the direction of rotation of the most critical perturbation. In the top-left panel, $j_1 + j_2$ is shown by black contour lines ($J_i = \int_V j_i \, \mathrm{d}V$), while the magenta line denotes the interface. (b) Thermal energy budget in the liquid (left) and in the gas (right) for corresponding critical conditions. (c) Stability diagram for $\mathcal{V} = 1$, $\mathrm{Pr} = 28$, $\Gamma \in [0.5,\ 1.8]$, and $\mathrm{Bd} = 0.41 \times (\Gamma/0.66)^2$.

wave traveling at constant rotational rate $\Omega = -4.15$ emerges as fully developed state for the flow, in agreement with the experimental observations of [207, 200] ($|\Omega_{\text{exp}}| = 4.27$).

The fully-developed supercritical flow is found to be organized around three fixed points and three limit cycles, which is a robust feature also observed for Re = 1750, 1850, and 1950 [200]. These invariant topological elements in the rotating frame are sketched in fig. 2.6(a). The figure also sketches the stable and unstable manifolds of the fixed points and limit cycles. The singular points on the cold and hot walls, denoted s_1 and s_2, respectively, are degenerate, since the wall-normal flow field in their vicinity vanishes at linear order. They are degenerate spiralling-out saddle foci whose unstable manifolds lie on the respective solid wall and up to computational accuracy, they are located on the axis of symmetry. The limit cycles w_1 and w_2 at the contact lines in the cold and the hot corner, as well as the line of flow separation w_c on the cold wall, are saddle limit cycles and likewise degenerate. Since the unstable manifolds of the saddle foci s_1 and s_2 are located on a solid boundary the heteroclinic connection of s_1 and s_2 with the saddle limit cycles w_c and w_2, respectively, must be understood in a degenerate sense. The third singular point s' is a free spiralling-in saddle focus located in close proximity of the z axis. Within the given numerical accuracy, s' is heteroclinically connected with s_2 on the hot wall, but disconnected from s_1 on the cold wall. The two saddle limit cycles located in the cold and hot corners w_1 and w_2 are heteroclinically connected with each other along the cylindrical liquid–gas interface. While the stable manifold of w_2 is connected with the saddle focus s_2, the unstable manifold of w_1 is connected to the saddle limit cycle w_c on the cold wall (fig. 2.6(a)). Along w_c the flow separates from the cold wall via a stream surface into the bulk. The broken connection together with the feedback mechanism provided by the axisymmetric part of the flow is responsible for the chaotic streamlines present in the liquid bridge. Regular and chaotic streamlines can co-exist in this steady three-dimensional incompressible flow [132, 208]. Owing to their relevance for FSCS, the analysis of the streamline topology is focused to the regular streamlines inside of the KAM tori in the rotating frame of reference. Figure 2.6(b) shows Poincaré section at $z = 0$. A three-dimensional reconstruction of the outermost KAM surface is depicted in 2.6(c). For a similar topological characterization at different Prandtl numbers, we refer to [209, 210, 211, 212].

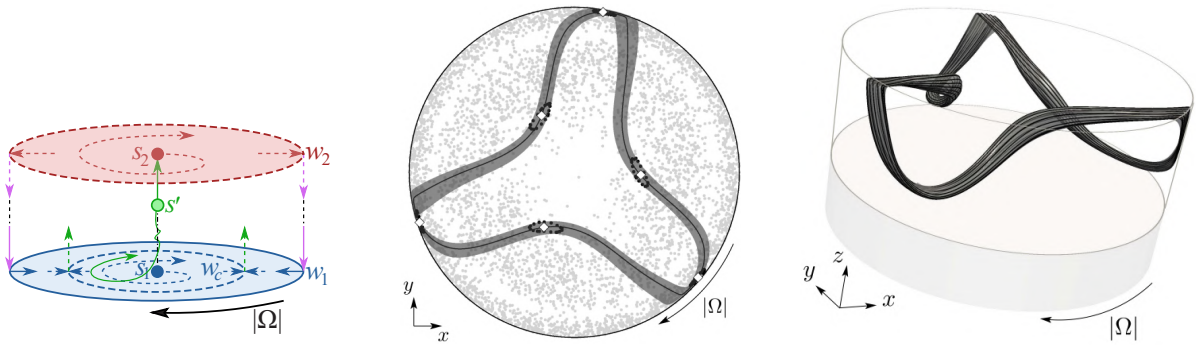

(a) Topology sketch (b) Poincaré section (c) KAM torus

Figure 2.6: Lagrangian topology of the flow streamlines. (a) Sketch of critical points, limit cycles, and their stable/unstable manifolds. (b) Poincaré section at $z = 0$: Poincaré returns of chaotic streamlines in light gray, Poincaré returns of regular streamlines as black dots, projection of the largest reconstructible KAM torus in gray shading, and projection of the periodic orbit as full line, while its Poincaré section is denoted by white diamonds. (c) Three-dimensional reconstruction of the outermost KAM surface.

2.3.1.3 Finite-Size Coherent Structures

The KAM tori analyzed above are properties of the flow field alone. The fluid inside of KAM tori does not mix with the fluid outside of the KAM tori. Their importance for particle accumulation [213] has been first explained by [164], and further generalized by [182] who described how particles moving in the region of chaotic streamlines can be transferred to the region of the KAM tori by way of the particle–surface interaction caused by, and depending on, the finite size of the particles. Once moving in the region of the KAM tori of the flow field the particles are prevented to leave this region by repeated collisions with the interface if the deviation of the particle trajectories from the streamlines is sufficiently small. In this respect, the KAM tori are templates for particle motion attractors (see fig. 2.7).

Owing to its Hamiltonian character [121], the fluid flow alone does not provide any dissipative mechanism that could drive the particle accumulation. Therefore we consider the motion of finite-size rigid spherical particles using the one-way coupling approach and including drag-, lift-, buoyancy- and viscous forces due to particle–free-surface interactions. Such simulations are capable of reproducing the rapid accumulation of particles well-established by experimental evidence (cf. fig. 2.7(b,c)). FSCS is found for various a, ϱ, Re, Γ, Bd, and Pr in experimental realizations [214, 215, 207, 216, 217] and numerical simulations [164, 210, 209, 218, 200, 212].

As for the mechanism leading to the particle trapping, one shall notice that the KAM tori closely approach the free surface. The repeated particle–boundary interaction is responsible of transfering the particles from the chaotic regions of the flow to the KAM tori, where the particles get trapped. This interpretation is further confirmed by two numerical counter proofs: (i) no particle accumulation is found by including all the dissipative mechanisms of the unbounded MRG equation and excluding the viscus forces near the free-surface, and (ii) a particle accumulation almost indistinguishable from fig. 2.7 is found excluding all the dissipative mechanisms except for the viscus forces near the free-surface [182], which corresponds to the use of a one-way coupling with perfect tracer in the bulk and the PSI model near the free surface (see fig. 1.9(b)). Hence, the particle–free-surface interactions provide the key dissipative mechanism for the FSCS.

(a) FSCS and flow topology (b) Simulations (c) Experiments

Figure 2.7: (a,b) Finite-size coherent structures for $\Delta_p/H = 0.00552$ corresponding to the experimental particles in (c) at $t = 25$ from an initially random distribution of 1000 particles using $\dot{\boldsymbol{x}}_p = \boldsymbol{u}$ supplemented by the PSI model. (a) Three-dimensional view in the rotating frame showing the outermost KAM torus (dark-gray), the temperature isosurface $\theta = 0.5$ (light-gray transparent surface) and particles (dark spherical markers). (b) Axial projection of (a) without the temperature field. (c) Experimental observation from the top view in the liquid bridge.

2.3.2 Antiparallel two-sided lid-driven cavity

2.3.2.1 Linear stability analysis

The incompressible two-dimensional flow in a two-sided lid-driven cavity offers a remarkably rich set of scenarios for the qualitatively different basic states and instabilities that can emerge upon a change of the two Reynolds numbers characterizing the two sliding walls. Here we focus on equal antiparallel motion, i.e. the left wall slides upward and the right wall slides downward at the same velocity U. This reduces the control parameters to one Reynolds number $\mathrm{Re} = HU/\nu$.

For long cavities where $\Gamma = L/H \gtrsim 2$, each moving wall can induce its own nearly square vortex. Examining one of these vortices: Downstream from the trailing edge of the corresponding moving wall, a wall jet forms. This jet separates from the downstream stationary wall and reconnects with the opposite (upstream) stationary wall of the same moving lid, driven by the significant underpressure at the upstream corner of the moving wall. This flow mirrors that of a one-sided lid-driven cavity. However, under sufficiently high Reynolds numbers, the wall jet from each of the two downstream corners remains attached and can extend to the opposite moving wall. Here, it becomes entrained by the upstream corner flow of the opposing moving wall, which now induces suction on the wall jet. Additional flow patterns arise for antiparallel wall motion due to the breakdown of point reflection symmetry concerning the center of the cavity [219].

Interest in double-lid-driven cavities stems not only from the nonuniqueness of the two-dimensional flow but also from providing insights into flow instabilities resulting from the interaction of two vortices confined to a rectangular domain. An interesting phenomenon is the elliptic instability, which occurs when a vortex experiences strain, causing the streamlines within the vortex core to become elliptical. Within a certain range of aspect ratios Γ, the co-rotating vortices generated by the antiparallel motion of the lids either fully coalesce into a vortex with elliptical streamlines at the center (as depicted by the black lines, representing streamlines of the basic state, in the top panel of fig. 2.8(a)), or they partially merge, resulting in a free hyperbolic stagnation point at the cavity's center, surrounded by closed streamlines beyond the separatrix. Both flow configurations exhibit a bipolar strain field, with the strain rate either smaller (elliptic point) or larger (hyperbolic point) than the rotation rate of the flow at the cavity's center.

The mechanism of the instability can be explained in terms of a resonance among two different three-dimensional Kelvin waves traveling about the vortex, where the resonant amplification is communicated by the strain field as part of the two-dimensional basic flow [220, 221]. This same mechanism also occurs for a single strained vortex in an unbounded domain [222].

The linear stability of the two-dimensional antiparallel lid-driven cavity flow as function of Γ was investigated by [223], who reported three distinct unstable mechanisms:

(i) the elliptic instability mechanism, characterized by a perturbation energy production at the merged vortex core (see top panel of fig. 2.8(a)) or at the cat's-eye vortices core if $\Gamma > 1$ and due to lift up effects (see left panel of fig. 2.8(b)),

(ii) the quadripolar instability mechanism (not shown),

(iii) the centrifugal instability mechanism, still promoted by lift up effects (see right panel of fig. 2.8(b)) but concentrating the energy production (see bottom panel of fig. 2.8(a)) in regions of the basic state prone to destabilization by Rayleigh's centrifugal criterion [224, 225].

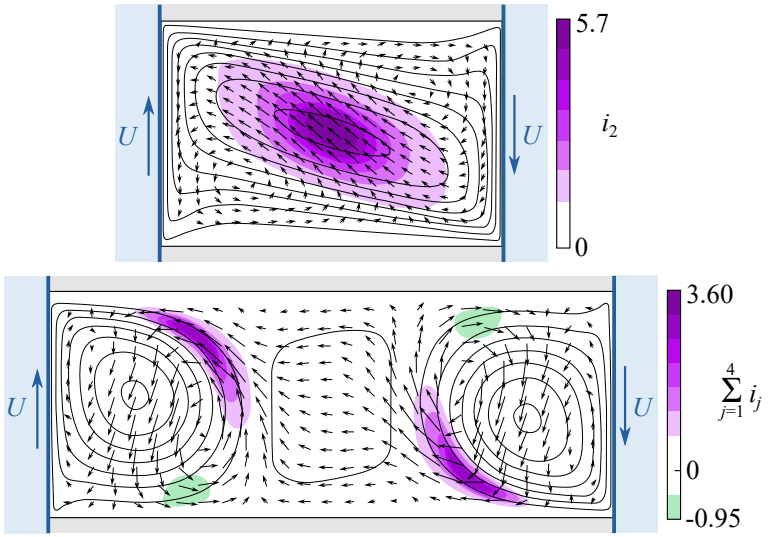

(a) Perturbatuion energy production

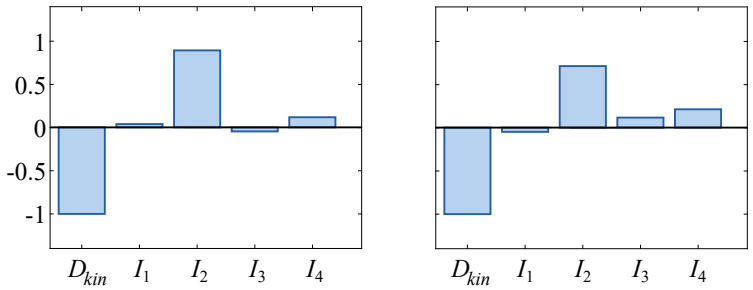

(b) Kinetic energy budget

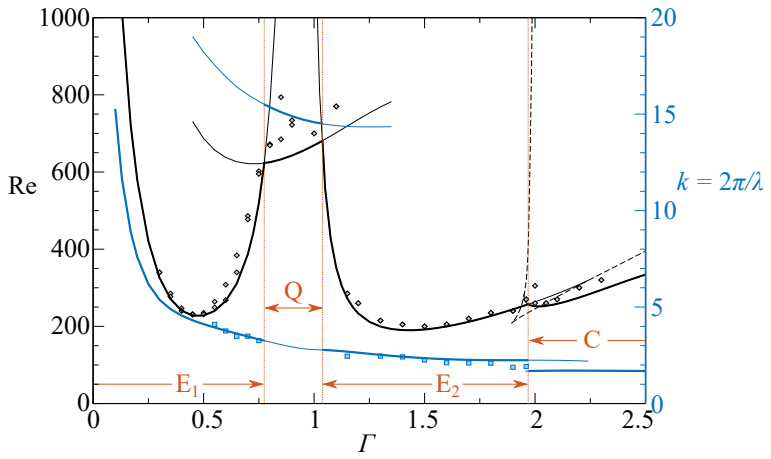

(c) Critical stability curves

Figure 2.8: (a) Critical conditions for $(\Gamma,\ \mathrm{Re}_c) = (1.5,\ 191.9)$ and $(2.5,\ 334.3)$ depicted at the top and bottom panel, respectively. The basic-state streamlines are shown as solid lines, the velocity perturbation $\tilde{\boldsymbol{u}}$ is depicted as black arrows. The energy production for i_2 and $\sum_j i_j$ are shown in color for the top and bottom panels, respectively, with $I_j = \int_V i_j \, \mathrm{d}V$. (b) Kinetic energy budget for $(\Gamma,\ \mathrm{Re}_c) = (1.5,\ 191.9)$ and $(2.5,\ 334.3)$ for the left and right panels, respectively. (c) Stability diagram for $\Gamma \in [0,\ 2.5]$. See [223] for the numerical data (lines) and [226] for the experimental ones (markers).

The critical curve shown in fig. 2.8(c) (black line) summarizes all the scenarios reported in [223]. All instabilities are stationary. The aspect ratio ranges for which the elliptic instability mechanism (E_1,E_2), the centrifugal mechanism (C), and the quadripolar (Q) instability mechanism dominate are indicated by orange lines. In addition to the critical wave numbers (blue lines) experimental results of [226] are shown as symbols. The stability analysis is complicated by the existence of multiple basic states. Their range of existence is indicated by dashed lines in fig. 2.8(c).

2.3.2.2 Streamline topology of the three-dimensional flow

As discussed for the thermocapillary liquid bridge, also for the two-dimensional steady two-sided lid-driven cavity, the three-dimensional most dangerous mode is needed for chaos to set in. Such a perturbation is steady, which is also confirmed by simulating the supercritical conditions without linearizing the convective term of the Navier–Stokes equations. Therefore, to investigate finite-size coherent structures in laminar, chaotic, antiparallel lid-driven cavities, we focus on $\Gamma = 1.7$, which implies an elliptic instability onset at low critical Reynolds number $\mathrm{Re}_c = 211.53$. Periodic boundary conditions are enforced to simulate the critical wavelength $\lambda_c = 2.73H$. To ease the notation, all the lengths are scaled by H and the center of the periodic cell is assumed to be at $z = 0$.

For the current aspect ratio $\Gamma = 1.7$, which exceeds 1.58, the strain rate at the center of the cavity cross-section slightly surpasses the rate of rotation. Consequently, the center forms a hyperbolic point $\check{h}$, while two elliptic points $\check{e}_{1,2}$ surround it, shaping a cat's-eye flow pattern (see left panel of fig. 2.9(a), $\mathrm{Re} = \mathrm{Re}_c$). Beyond the critical Reynolds number, translational invariance in z breaks due to a critical mode, manifested as steady convection cells periodic in z, each period containing two cells [223, 227]. The flow field of this critical mode exhibits point symmetry with respect to the centers $\boldsymbol{x}_c = (0, 0, \pm n\lambda_c/2)$, where $n \in \mathbb{N}_0$, of each convection cell, with the origin of the coordinate system defined at $n = 0$. Additionally, the critical mode displays mirror-symmetry planes at $z_n = \pm(1 + 2n)\lambda_c/4$, where the spanwise velocity w becomes zero. These point and mirror symmetries persist in the full finite-amplitude supercritical flow.

As translational invariance in z breaks beyond $\mathrm{Re} > \mathrm{Re}_c$, the periodic lines of fixed points in the two-dimensional flow are disrupted. Only four discrete fixed point types persist, with three located on the cell boundary (visible in the left panel of fig. 2.9(a)). Hyperbolic points at cell centers and boundaries retain their hyperbolic nature only within a narrow range of slightly supercritical Reynolds numbers. The fixed point at the cell center remains stationary due to flow symmetry. Fixed points $\check{e}_{1,2}$ on periodic lines at $\mathrm{Re} = \mathrm{Re}_c$ vanish for $\mathrm{Re} > \mathrm{Re}_c$, except on cell boundaries. Only on these mirror-symmetry planes do the two elliptic points smoothly transition into weak saddle foci, one spiraling inward (s_2') and the other outward (s_2). These four fixed points per cell undergo further alterations within a small range of supercritical Reynolds numbers, with s_2' disappearing already for $\mathrm{Re} > 1.0127 \times \mathrm{Re}_c$. Further insights into the merger of elliptic with hyperbolic points in two-dimensional incompressible flow are available in [228].

In the right panel of fig. 2.9(a), a depiction of supercritical flow for Reynolds numbers exceeding Re_c by more than 1.3% is presented. The remaining saddle points, namely s', s_1, and s_2, have been characterized based on their eigenvalues and stable/unstable manifolds. Analysis reveals

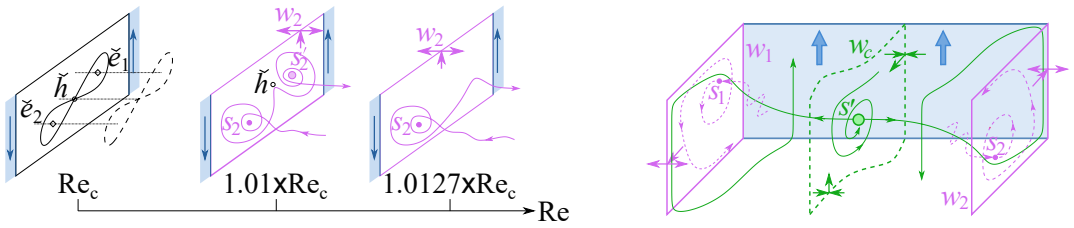

(a) Topology sketch

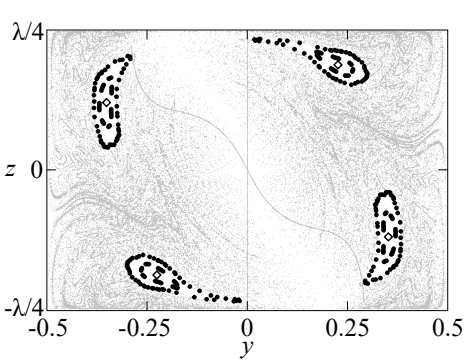

(b) Poincaré section

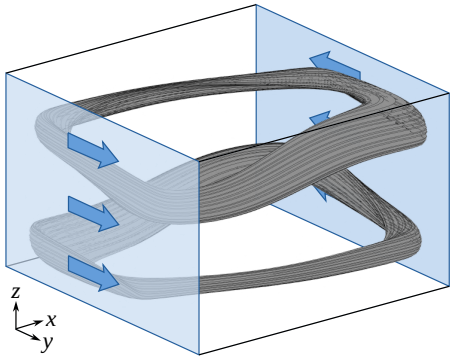

(c) KAM torus

Figure 2.9: Lagrangian topology of the flow streamlines. (a,left) Evolution of the critical points on the mirror-symmetric planes at $z_n = \pm(1+2n)\lambda_c/4$. (a,right) Sketch of critical points, limit cycles, and their stable/unstable manifolds. (b) Poincaré section at $x = 0$. (c) Three-dimensional reconstruction of the outermost KAM surface. Color coding consistent with fig. 2.6.

that s_1 and s_2 on the cell boundaries act as simple saddle foci, attracting along one-dimensional stable manifolds from the bulk and repelling along two-dimensional unstable manifolds spiraling outward on the respective cell boundary [229]. Conversely, s' represents a complex Shilnikov saddle with a stable two-dimensional spiraling-in manifold and a one-dimensional unstable manifold ejecting fluid elements from s' into the bulk, with a discontinuous connection to the stable manifolds of s_1 and s_2 (indicated by solid green and dashed magenta lines in the right panel of Fig. 2.9(a)). Alongside fixed points, degenerate saddle limit cycles are also observed. Two types of limit cycles exist on the walls. One type, labeled $w_{1,2}$, forms rectangles at the intersection of each cell boundary with the walls. These wall limit cycles are saddle limit cycles, attracting along the cell boundary and repelling in close proximity to the walls. The two unstable manifolds of w_1 and w_2 converge on the walls midway between both cell boundaries, representing the stable manifolds of another non-trivial degenerate saddle limit cycle w_c. Motion on the four walls is thus degenerate, with velocity being step-wise constant at magnitude Re or zero.

Since the one-dimensional manifolds of s', s_1, and s_2 are not connected their further evolution is of interest. All the one-dimensional manifolds originating by such saddle foci are found to alternate a spiral motion near the cell boundary to the one near the stable two-dimensional manifold of s'. During their evolution all streamlines approach the central saddle limit cycle w_c (dashed green in the right panel of fig. 2.9(a)) very closely or eventually terminate on the wall before coming even closer to the wall limit cycle. The close approach of all one-dimensional manifolds to the saddle limit cycle w_c signals its importance for the flow. The existence of a

degenerate heteroclinic tangle between the two-dimensional stable manifold of s' and the two-dimensional unstable manifold of w_c has indeed been found to be at the origin of chaos in the antiparallel lid-driven cavity [229].

The Lagrangian topology of the two-sided lid-driven cavity is demonstrated by a Poincaré section for a representative Reynolds number $\mathrm{Re} = 400$ (see fig. 2.9(b)). Two pairs of point-symmetric KAM tori are found to co-exist with the chaotic sea surrounding them. The corresponding reconstruction of the KAM tori is depicted in fig. 2.9(c).

2.3.2.3 Finite-Size Coherent Structures

As already observed for the thermocapillary liquid bridge, also the KAM tori in a two-sided lid-driven cavity approach closely the moving boundary. This implies that they can potentially serve as template for particle Finite-Size Coherent Structures if the particle–boundary interaction allows to transfer the particle centroid from the chaotic to the regular regions of the flow. An experimental confirmation is provided by fig. 2.10(a) for slightly different flow parameters, i.e. two-sided lid-driven cavity with $\Gamma = 1.6$ and slightly curved driving walls [230]. All experiments are carried out with a single particle, at initial random location in the domain. To experimentally confirm that inertial dissipation is not essential to the physical mechanism, particles are almost density matched to the flow, i.e. the experimental density ratio is $\varrho = 1.0001$. By adjusting the particle radius, one can regulate the minimum distance at which the particle is released after interacting with the moving wall. For $a = a_\mathrm{p}/H = 0.025$ (cyan), the particle is released on the outermost KAM surface identified through numerical simulations (depicted by black dots in fig. 2.10(a)). As the particle radius increases to $a = 0.39$ (red) and $a = 0.50$ (yellow), the distance from the wall increases, intersecting narrower KAM surfaces that align closely with the closed periodic orbit (black cross, computed numerically). Further enlarging the particle radius prevents the particle from being released precisely on the periodic orbit; however, it remains trapped in the KAM torus. This leads to a displacement of the periodic particle attractor (illustrated by maroon $a = 0.059$ and brown $a = 0.071$ Poincaré returns in fig. 2.10(a)). Due to the presence of a second (5-periodic) KAM torus discovered for $\Gamma = 1.6$ (visible as black dots around the largest KAM torus in fig. 2.10(a)), the smallest particle ($a = 0.025$) is also compatible with this second KAM torus, wherein it can become trapped (as indicated by blue Poincaré returns).

To further provide experimental evidence that bulk dissipative effects are negligible to the phenomenon and the transfer of particles from the chaotic sea to the regular region is at the core of the physical explanation of FSCS in laminar chaotic flows, we consider a particle of radius $a = 0.004$. The particle–boundary interaction is not sufficient to keep such particle far enough to the wall and transfer it inside the KAM torus. Therefore, we observe that the particle that was initially in the chaotic region, keeps producing random Poincaré returns (gray dots in fig. 2.10(a)), therefore bulk dissipation effects are not providing the necessary mechanism to produce a particle attractor compatible with the location and time scales of the previously demonstrated periodic and quasi-periodic particle coherent structures. This is a further confirmation that the observed phenomenon falls in the category of FSCS.

A further numerical proof of the essential role of particle–boundary interaction is given in

figs. 2.10(b,c). We initialize the particle on the periodic streamline at the center of the KAM torus for $\Gamma = 1.7$ (black line). The particle-to-fluid density ratio $\varrho = 1 \pm 0.1$ is selected such to either promote centrifugation of the particle outside of the regular region by inertial effects ($\varrho > 1$, green), or attraction ($\varrho < 1$, red) of the particle towards the KAM core. If particle–boundary interaction is included in the modeling equation for the particle dynamics, a line-like FSCS is found regardless of the sign of inertial effects, i.e. for $\varrho \lessgtr 1$ (see fig. 2.10(b)). This is in agreement with the experimental observations of [230]. On the contrary, if we neglect the particle–boundary interaction, and keep inertial effects in the particle motion model, the heavy particle gets centrifuged out of the regular region (see green line in fig. 2.10(c)). As expected, the lighter particle gets attracted to a periodic attractor near the closed streamline (see red line in fig. 2.10(c)), but the attraction rate is much slower that what observed in the experiments (see fig. 2.10(d) [160, 230]). For further details about the effect of inertia, gravity and particle size, we refer to [160, 230].

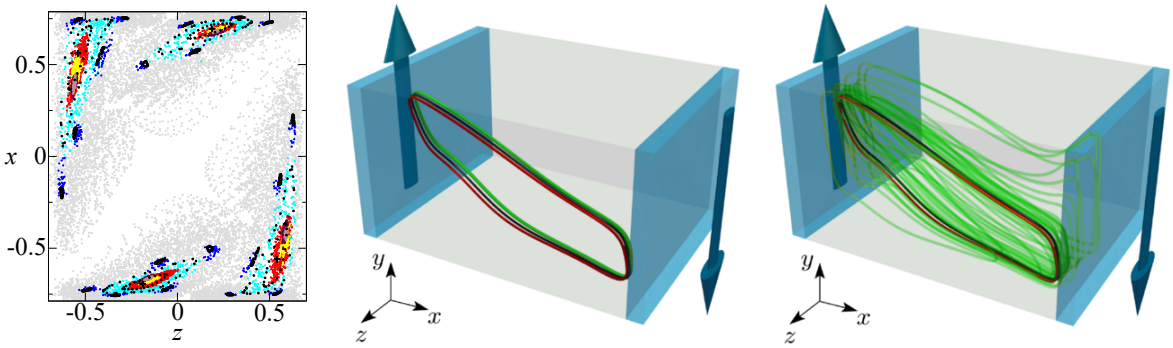

(a) Experiments (b) MRG + near-wall correction (c) Unbounded MRG

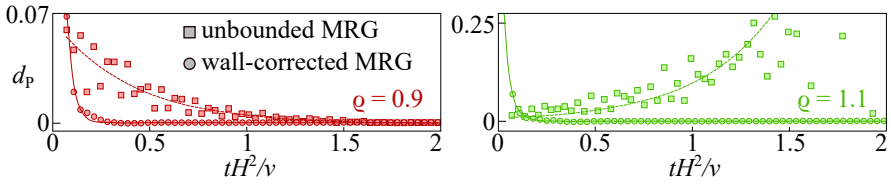

(d) Distance from the particle attractor

Figure 2.10: (a) Poincaré section at $y = 0$ of experimental particle trajectories of nearly neutrally-buoyant ($\varrho = 1.0001$) spherical particle after convergence on their respective attractor in a two-sided lid-driven cavity for $(\Gamma,\ \mathrm{Re}) = (1.6,\ 400)$. The colour indicates the particle radius: $a_\mathrm{p} =$ 0.15mm (grey), 0.45mm (cyan and blue), 1.00mm (red), 1.58mm (yellow), 2.00mm (brown), and 2.37mm (maroon). Particles with $a_\mathrm{p} = 0.15$mm (grey) move chaotically in the chaotic sea. For comparison, the Poincaré section of KAM tori and of closed streamlines are shown as black dots and crosses, respectively (see [230] for more details). (b,c) Trajectories of inertial particles with $\varrho = 0.9$ (red) and $\varrho = 1.1$ (green) for $a_\mathrm{p}/H = 0.05$ computed integrating a simplified MRG equation without Basset–Boussinesq history force and Faxén correction in a two-sided lid-driven cavity for $(\Gamma,\ \mathrm{Re}) = (1.7,\ 400)$. (b) Includes the near-wall correction of [155] (see fig. 1.9(a)). (c) Does not include any near-wall correction, hence makes use of the unbounded MRG equation. (d) Attraction to the limit cycle for $a_\mathrm{p}/H = 0.058$ expressed by the distance between the fixed-point attractor and of the Poincaré returns for the particle trajectory d_P at $x = 0$. See [160] for more details about (b–d).

2.3.3 Cuboidal lid-driven cavity

2.3.3.1 Linear stability analysis

The last example of laminar chaotic flows considered in this manuscript is the one-sided lid-driven cavity for which the sole top lid slides from left to right. The two-dimensional setup is depicted in fig. 2.2(a). For $\mathrm{Re} = LU/\nu \to 0$ the streamlines are symmetrical, due to the symmetries of Stokes flow. By increasing the Reynolds number, the streamlines tend to crowd near the moving lid, where the largest velocities arise, and two separated eddies in the bottom corners can be seen. For even larger Reynolds, the separated vortices at the bottom become stronger, even a second separated vortex can be found in the bottom right corner, and a third separated region is created, for $\mathrm{Re} \gtrsim 1000$, close to the upstream corner of the moving lid near $(x,\ y)/H = (-0.5,\ 0.5)$. For even higher Reynolds numbers the core of the vortex approaches a solid-body rotation with circular streamlines and constant vorticity [231].

While the two-dimensional flow for small and moderate Reynolds numbers is steady, it undergoes a Hopf bifurcation and becomes time-dependent for higher Reynolds numbers when inertia effects become larger. The breaking of the time translation symmetry for two-dimensional square lid-driven cavities occurs at critical Reynolds number $\mathrm{Re}_c(\Gamma = 1) = 8018.2 \pm 0.6$ [232]. Even though the time-periodic two-dimensional flow resulting from the Hopf bifurcation admits chaotic mixing, owing to the high Reynolds number, the flow configuration is unlikely to allow regular regions near the boundaries, hence is not a suitable candidate to study FSCS. On the other hand, allowing for three-dimensional instabilities, the critical Reynolds number reduces of one order of magnitude. In fact, considering $\Gamma = 1$, the one-sided lid-driven cavity undergoes a steady centrifugal instability for $\mathrm{Re}_c = 786.3 \pm 6$ and $k_c = 15.43 \pm 0.06$ in form of Taylor–Görtler vortices (see fig. 2.11(a), [233]). The dominant destabilizing interaction mechanism between the basic flow and the critical mode is due to the term lift-up mechanism (see i_2 in fig. 2.11(b)). For other aspect ratios the instability is also centrifugal in nature, but can have different flow structures, wave numbers and time dependence. In total, four different critical modes are destabilized across all the unstable branches (see 2.11(c)), typically having smaller critical wave numbers than the Taylor–Görtler vortices, C_2^e for $\Gamma = 1$.

2.3.3.2 Streamline topology of the three-dimensional flow

The Lagrangian topology of such a supercritical flow has been investigated by [139] for $\mathrm{Re} = 800$, 850 and 900. Despite the moderate Reynolds number and the co-existence of regular and chaotic streamlines, they pointed out that none of the KAM tori closely approaches the moving lid except for a narrow regular region identified at $\mathrm{Re} = 800$. The steady three-dimensional supercritical flow of an infinitely deep, square one-sided lid-driven cavity does not provide therefore a robust flow template for FSCS.

Rather than driving a two-dimensional flow beyond its stability limits for inducing a three-dimensional perturbation that could allow chaos to set in, one can consider an intrinsically three-dimensional flow. The origin of the reference frame is taken at the front-bottom-left corner of the cavity and all lengths are non-dimensionalized by H. The three dimensionality of the flow is therefore produced by considering no-slip walls at $z = \pm\lambda/2 = \pm W/2H$, where W denotes the

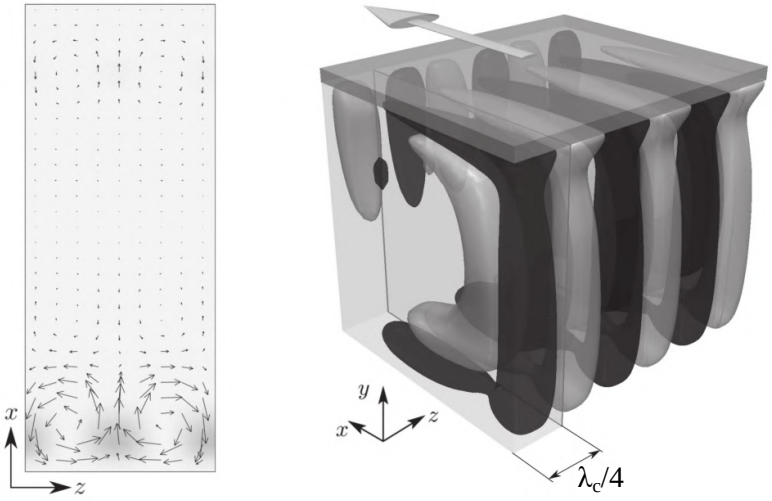

(a) Most dangerous perturbation and supercritical conditions

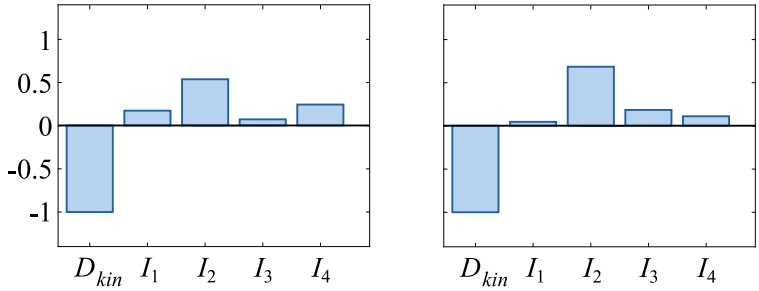

(b) Kinetic energy budget

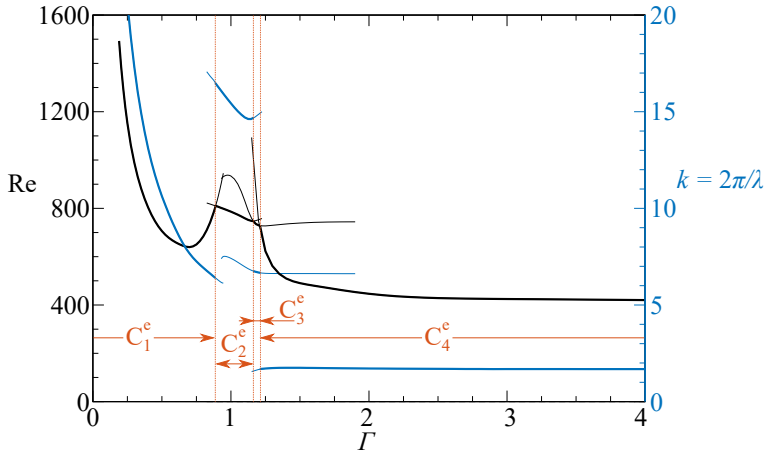

(c) Critical stability curves

Figure 2.11: (a,left) Critical conditions for $(\Gamma,\ \mathrm{Re}_c,\ k_c) = (1,\ 786.3,\ 15.43)$: The velocity perturbation $\tilde{\boldsymbol{u}}$ is depicted as black arrows, and the energy production for i_2 are shown in gray scale. (a,right) Isosurfaces of the spanwise velocity for $w = 0.01$ (light grey) and $w = -0.01$ (dark grey) for $(\Gamma,\ \mathrm{Re},\ \lambda_c) = (1,\ 900,\ 0.40678)$. (b) Kinetic energy budget for $(\Gamma,\ \mathrm{Re}_c) = (0.25,\ 288.2)$ and $(1.0,\ 786.3)$ for the left and right panels, respectively. (c) Stability diagram for $\Gamma \in [0,\ 4]$. See [233] for more details.

cavity depth. Let us consider a cubic one-sided lid-driven cavity, i.e. $\Gamma = \lambda = 1$ for $\mathrm{Re} = 200$. The fluid transport is mainly organized between the saddle focus in the midplane (s_2) and those on the end walls (s_1) (fig. 2.12(a)). Fluid originating from the vicinity of the half-saddle foci s_1 on the end walls moves in z direction towards s_2 in a spiralling fashion. From there it moves radially away from s_2, being separated into two streams. One of them is approaching the half saddle s_3, while the other one is approaching the saddle focus s_4. Near the edges $(x, y) = (0, 0)$ and $(1, 0)$ each of the two streams symmetrically splits into two and leaves the midplane in positive and negative z directions to reach the two end walls, near which they are again interwoven in the vicinity of the stable manifold of s_1. This three-dimensional splitting and merging provides the basic mechanism for chaotic mixing in the three-dimensional cavity. The chaotic (grey dots) and regular (black dots) Poincaré returns on the plane $x = 1/2$ are depicted in fig. 2.12(b). They demonstrate the rich variety of KAM tori found for such a moderate Reynolds number and resulting from a sequence of topological resonance phenomena. The outermost KAM surface for T_1 and T_7 is depicted in fig. 2.12(c), together with the closed streamline L_4 at the core of T_4.

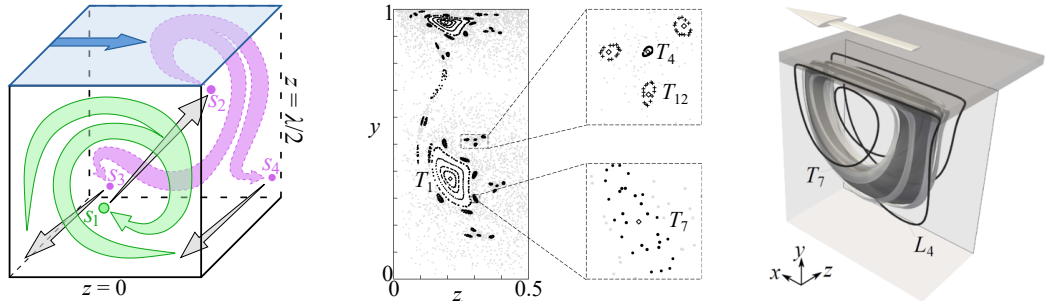

(a) Topology sketch (b) Poincaré section (c) KAM torus

Figure 2.12: Streamline topology for $(\Gamma,\ \lambda,\ \mathrm{Re}) = (1,\ 1,\ 200)$ [139]. See fig. 2.6 for color coding.

2.3.3.3 Finite-Size Coherent Structures

Equivalent KAM tori are found numerically for the cuboidal cavity with slightly curved walls used in the experiments of [161]. Their study further strengthens the experimental evidence of FSCS forming in correlation to the template provided by the KAM tori of the flow. The particle size determines the attractor, potentially more than one if multiple KAM tori are compatible with the δ due to a and ϱ, in agreement with the experimental evidence [230] and the numerical simulations for the two-sided lid-driven cavity (see fig. 2.13(b), [160]). The rapid attraction rate of a particle initially located in the chaotic sea to the corresponding attracting periodic orbit is not compatible with inertial attraction rates, but rather determined by the dissipation due to repeated particle–boundary interaction. This further confirms that the FSCS mechanism detailed in §2.3.1 and §2.3.2 applies also for the cuboidal one-sided lid-driven cavity (see fig. 2.13(a)).

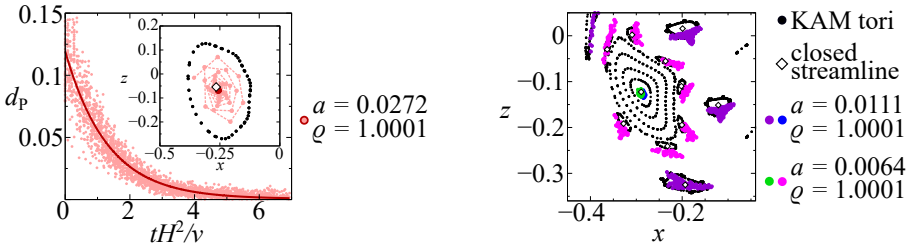

(a) $\mathrm{Re} = 100$ (b) $\mathrm{Re} = 200$

Figure 2.13: Poincaré section and d_P for $(\Gamma,\ \lambda) = (1,\ 1)$: (a) $\mathrm{Re} = 100$ and (b) $\mathrm{Re} = 200$ [139].

2.4 Summary and conclusions

In this chapter we presented an overview of Finite-Size Coherent Structures occurring in a variety of fluid dynamic set-ups. They are all single-particle attractors that rely on a mechanism capable of repeatedly bringing the particle near an impenetrable boundary. The viscous forces due to the particle's finite size are responsible of the intense dissipation experienced by the particulate dynamical system when the particle–boundary distance is small, i.e. $\delta \ll 1$. We stress that the inherent multiscale nature of such phenomenon presents three characteristic scales that are well separated among each other such that a sequence of asymptotic approaches can be used to explain the leading-order physics. Indeed, the largest scale L is due to the carrier fluid flow. As the particulate phase is here assumed to be dilute and formed by small particles $a_\mathrm{p} \ll L$, the fluid flow is not perturbed by the particles. This represents the leading-order asymptotic expansion for the carrier fluid flow (first outer expansion at $|\boldsymbol{x} - \boldsymbol{x}_\mathrm{p}|/a_\mathrm{p} \gg 1$). To match such expansion with the dynamics of the particulate flow (first inner expansion at $|\boldsymbol{x} - \boldsymbol{x}_\mathrm{p}|/a_\mathrm{p} = \mathcal{O}(1)$), the MRG equation is used, which consists of a leading-order correction for the trajectories of small particles ($a_\mathrm{p} \ll L$) far from the boundaries ($\delta \gg 1$). A second asymptotic matching between the far- (second outer expansion $\delta \gg 1$) and the near-boundary (second inner expansion $\delta \ll 1$) dynamics is then required to correctly take into account the leading-order particle–boundary interaction that is responsible of the emergence of the FSCS in two- and three-dimensional systems.

At first, FSCS in two-dimensional non-chaotic systems have been considered, demonstrating the occurrence of such phenomenon in confined oscillatory vortices, shear-driven cavities and near singular dihedral corners:

- The FSCS in oscillatory vortices are expected to hold significance for microfluidic systems that involve the centrifugal movement of particles. In fact, as OSC applies to heavy and light particles, FSCS could help sorting particles for a wide range of $\varrho \lessgtr 1$. Such applications encompass systems like confined cavities mounted on rotating disks, which are widely employed for automating life science analysis and synthesis protocols [234]. Indeed, as emphasized by [187], the phenomenon of counter-centrifugation in inertial particles becomes apparent when dealing with oscillatory frequencies and rotation rates that align with conventional bead beating protocols. Another pertinent domain for the OSC phenomenon is the realm of microscale centrifugation devices, with the potential for integration into lab-on-a-chip devices [235]. It is worth noting that utilizing FSCS as a result of the OSC phenomenon for the separation of stem cells with varying densities could complement other density-based separation methods, including density gradient centrifugation [236, 237] or density gradient centrifugation with negative selection [238].
- The FSCS in shear-driven cavities are observed in several microfluidic applications, such as microchannels with a meniscus subject to Marangoni stresses [180], and microbubbles attached to a locally heated channel wall [239]. Other applications involve microcavities mounted on a microchannel for cells capturing [178, 240] or size sorting [178, 241]. They are novel (bio)particle-focusing platforms developed for efficient cell/particle separation in bio-fluids, offering continuous high-throughput processing without the need for sheath fluids

or external forces. The mechanism at the core of FSCS allows to overcome the limits of traditional methods that rely on centrifugal effects [242, 243, 244] or external forces [245], and often lead to bulkier equipment and increased energy consumption.

- The FSCS near a singular corner have potential implications for microfluidic applications characterized by Stokesian flow and the presence of non-interacting, density-mismatched particles. Specifically, we find that the orientation of the device relative to gravity and the wall velocities can control the positioning of the particle attractor near the singular corner in a free stationary point or in a cavity [196]. Similar attractors are expected near the separatrix of a microfluidic T-junction [246]. In another relevant configuration, i.e. a channel flow past an open microcavity, the shear layer between the channel flow and the recirculating flow within the cavity induces particle clustering reminiscent of our identified corner attractor, as observed experimentally by [247]. Likewise, [248] observed particle clustering near a corner with an active surface in D-junction configurations. Additionally, due to the Stokesian nature of the attractor, reversing the velocity vectors and the corner's orientation results in a particle repellent effect. This hints at a novel approach for corner-cleaning in microfluidic devices.

The second part of this chapter dealt with FSCS in steady three-dimensional chaotic systems. The distinct feature of such class of particle coherent structures is that they do not rely on bulk forces, hence their occurrence can be understood as a result of the particle–boundary interaction and the transfer of the particles from the chaotic to the regular regions of the flow. It follows that after a relatively short time, the chaotic sea is depleted of particles and the KAM tori closest to the boundaries become a template for the attracting manifolds. As such mechanism does not rely on inertia or buoyancy, it could become a strong candidate for particle segregation in micron-sized cavities. Experimental evidence proving the robustness and generality of such a phenomenon are reported for: (i) thermocapillary liquid bridges [249, 250, 251, 252, 218, 200, 253, 217] over a wide range of aspect ratios, Prandtl and Reynolds numbers, (ii) single- and two-sided lid-driven cavities [254, 182, 230, 161], and (iii) thermocapillary droplets [255]. Equivalently, two-dimensional time-dependent flows can lead to chaotic mixing, hence they can experience the formation of FSCS conceptually similar to the ones we studied for steady three-dimensional flows [177, 178].

Chapter 3

Instability and Flow Control in Rotating Machines

Summary

Two types of turbomachines will be considered, namely a centrifugal pump and an axial compressor, focusing on the instabilities observed upon a variation of the flow rate. It will be discussed how a small radial gap ΔR can strongly affect the onset of rotating instabilities at the large flow scale R (i.e. impeller or carter radius), leading to rotating stalls that affect the safety margine and impact the operating conditions of the machine. We stress the significance of flows with well-separated length scales as the performance for optimal turbomachine design is contingent to employing $\Delta R/R \ll 1$. Finally, flow control specialized to affect the flow in the radial gap will be briefly discussed, demonstrating the effectiveness of active flow control in an axial compressor by employing air jets for suppressing an instability generated in the radial gap.

Contents

3.1 Introduction

Turbomachines serve to transfer energy between a rotating component, known as the rotor, and the fluid that flows across it. Their designs vary based on their specific functions, such as turbines (which transfer energy from the fluid to the rotor), compressors (which transfer energy from the rotor to the fluid), jet aircraft engines, pumps, turbochargers, etc [256]. Despite their diverse applications, most turbomachines share common features, with rotors comprising wheels mounted on a common shaft connected to a stationary housing through bearings. While it is essential to maintain a small clearance between rotor and housing to prevent leakage and optimize machine efficiency, this clearance introduces the risk of contact during rotation. Efficient and safe turbomachine operation necessitates therefore effective risk control for potential contacts. For a comprehensive review on rotor-to-stator contacts in turbomachines, we recommend consulting [257].

In axial and centrifugal compressors, minimizing the clearance between blade tips and the surrounding statoric elements enhances aerodynamic efficiency. As a consequence, the strive for improving turbomachinery performance tends to promote the separation of characteristic length scales between the bulk and the blade tip leakage flow between rotoric and statoric components. The bulk flow has typical coherent structures characterized by the radial dimension of the rotor R, as well as by the blade chord c. On the other hand, the leakage flow between statoric and rotoric components is established in radial gaps of characateristic size ΔR that is typically hundreds times smaller than R, i.e. $\Delta R/R \ll 1$. This motivates the importance of multiscale flows with well-separated length scales for turbomachinery applications.

Despite the significance of the clearance between rotoric and statoric components in terms of turbomachinery performance, a first optimal design of the rotor and stator blades is normally obtained under the simplifying assumption that the two-dimensional core flow far from the casing and the shaft is representative for estimating the mean turbomachinery performance. Such a simplification has been (and often still is) standard practice as it provides a leading-order guidance to designers [258, 259, 260]. Thereafter, blade-to-blade two-to-three-dimensional inverse methods have been implemented [261, 262, 263, 264, 265, 266], eventually integrating optimization algorithms with three-dimensional (or computationally cheaper quasi-3D) numerical simulations [267, 268, 269], and recently with genetic [270], adjoint [271], and machine learning [272] algorithms.

Due to the intricate nature of internal flows in turbomachinery, numerous flow characteristics are inherently three-dimensional, and quasi-3D approaches may fall short in predicting them [273, 259]. In the following sections, we will consider the intrinsically multiscale three-dimensional flows in turbomachinery, emphasizing the significance of the smallest scales, with a special focus on the importance of considering leakage flows when explaining, predicting and potentially controlling hydrodynamic instabilities. Our focus will center on two configurations: a centrifugal pump and an axial compressor.

3.2 Instabilities in centrifugal pump vaneless diffuser

Radial compressors or pump vaneless diffusers often encounter performance limitations in pressure recovery. Typical scenarios involve either dynamic or static stall, the former being far more complex to characterize compared to the latter. Unlike static stall, dynamic stall patterns are not stationary relative to a given reference frame; instead, they rotate within the machine system at a fraction of the machine's rotational speed. Such dynamic conditions can arise across various components in all types of turbomachines, contingent upon the specific speed and design. However, in radial flow machines like pumps, fans, and compressors, they are predominantly observed in configurations featuring a vaneless diffuser, which emerges as the component most susceptible to such instabilities. Given their potential to induce vibrations and trigger or amplify surge conditions throughout the machine system, controlling or mitigating these instabilities is crucial.

This is particularly evident when operating at partial flow rates, meaning rates below the design flow rate. The performance limitations stem from flow separation phenomena, as outlined by [274], which are typically categorized as singular and ordinary flow separations. Singular flow separation occurs when the vaneless diffuser induces excessive mean deceleration, while ordinary flow separation is more frequently caused by local streamline overturning near the wall.

The primary cause of separation is attributed to the local decrease in kinetic energy, as elucidated by various authors (see, for instance, [275]). Both forms of performance constraints pertain to static stall configurations that manifest in particular fixed positions within the machine. Nevertheless, they can trigger distinctive rotating instabilities, commonly referred to as rotating stall, to underscore the dynamic nature of the stall phenomenon.

Building upon insights from [275], critical evaluations of reverse flow onset in a vaneless diffuser were conducted by [276, 277]. In their initial work, [278] performed dynamic measurements within a vaneless diffuser, shedding light on the flow features of dynamic stall phenomena. They noted a gradual development of dynamic stall conditions throughout the diffuser as the machine flow rate decreased. This investigation was expanded to consider variations in diffuser geometry [279]. Theoretical inquiries into these unforced rotating instabilities have employed two distinct approaches: a three-dimensional wall boundary layer stability analysis [280] and a two-dimensional inviscid approach, assuming a core flow region within the hub-to-shroud sections of the vaneless diffuser [281, 282], particularly for wide diffuser ratios, i.e. for $(R_4 - R_3)/H \lesssim \mathcal{O}(1)$, where H denotes the diffuser height and $R_4 - R_3$ the outlet-to-inlet diffuser radius difference. See fig. 3.1 for an illustration of the pump schematic.

The findings indicate that the stability boundary for wide vaneless diffusers can be defined by the critical flow angle at the diffuser inlet. Moreover, this critical flow angle is noted to be influenced by the diffuser radius ratio and the number of stall cells. Within the framework of the core flow assumption, the impact of wall boundary layers appears negligible. However, it is anticipated that integrating wall boundary layer effects into the two-dimensional inviscid model proposed by [281] could alter the characteristics of the most critical mode predicted by their model. Such alterations might manifest in terms of the specific unstable pattern, and conceivably, in the number or propagation speed of stall cells, if not solely in the expression of instability onset

through the critical flow angle. Additionally, within similar two-dimensional assumptions, another investigation by [283] suggests that the typical *jet and wake* pattern generated by impellers does not influence the emergence of these rotating instabilities at low flow rates.

Previous investigations have identified an instability in the radial vaneless diffuser through numerical simulations and experiments [284] conducted for two partial flow rates. Depending on operational conditions, either a single-mode rotating stall or two competing modes leading to intermittency were observed [285]. However, it remains unclear whether a specific mechanism triggers the transition between these modes, or if the system's phase space at low flow rates is organized chaotically around two interconnected attractors (the two modes). In the latter scenario, no distinct mechanism would be necessary for mode switching, and intermittency would arise from the system's heightened sensitivity to minor perturbations near saddle or hyperbolic points in phase space. Additionally, [284] noted that capturing the instability accurately required considering the effect of leakage flow between the diffuser and the impeller, even with small radial gaps between them. Consequently, the instability is highly sensitive to the flow conditions at the diffuser inlet. In particular, [286, 287, 288, 289] explored three leakage flow configurations: (i) sealing the impeller-to-diffuser gap (zero-leakage), (ii) leaving a radial gap open to the surroundings for airflow into the diffuser (positive-leakage), or (iii) incorporating a fixed carter that connects the diffuser inlet to the section just before the impeller inlet, allowing air leakage from the diffuser to the impeller inlet through a small radial gap (negative-leakage). The first two configurations will be discussed in §3.2.1 for examining instabilities at the design flow rate.

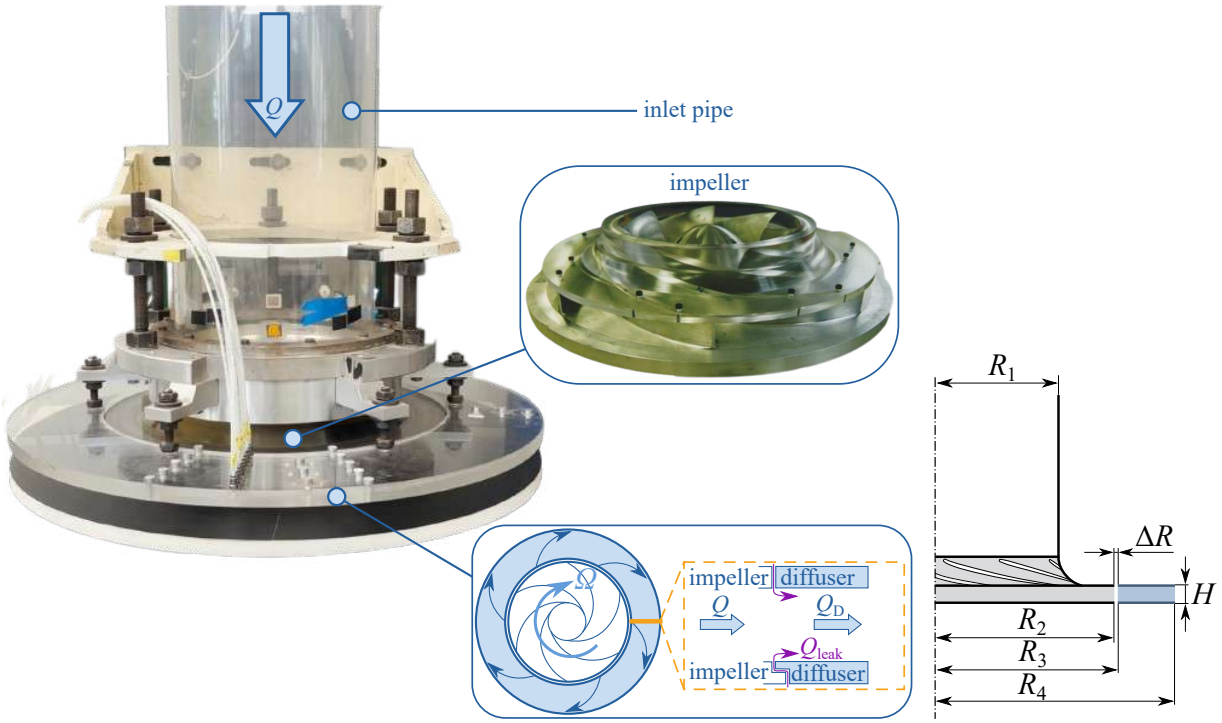

Figure 3.1: Experimental setup of the centrifugal pump operated at Arts et Métiers, Lille. The components of the pump are shown, together with a schematic of the flow (top view) and of the pump (side view). The inset in the orange dashed box shows the leakage flow.

3.2.1 Rotating instability about the design flow rate

The centrifugal pump depicted in fig. 3.1 is considered for zero- and positive-leakage cases, and its impeller rotates at constant rate $\Omega = f_{\text{imp}}/2\pi$. The 7-periodic spatially-modulated inlet due to the pump impeller leads to $\text{Re}_\Omega = \Omega R_3^2/\nu = 5.52 \times 10^5$ for all cases we consider hereinafter, where Re_Ω is a first Reynolds number that characterizes the flow based on the nominal tangential velocity at the diffuser inlet. A second Reynolds number is defined based on a volumetric flow rate Q entering the pump (see fig. 3.1), i.e. $\text{Re}_Q = Q/2\pi H\nu$. We employ a reference value $\tilde{\text{Re}}_Q = \tilde{Q}/2\pi H\nu = 6.46 \times 10^4$ and vary the parameter $\alpha_Q = \text{Re}_Q/\tilde{\text{Re}}_Q = Q/\tilde{Q} \in [0.75,\ 1.25]$ to investigate the turbulent flow instabilities in the diffuser with radial aspect ratio $\Gamma = R_4/R_3 = 1.5$ and a cross-sectional aspect ratio $(R_4 - R_3)/H = 3.325$ kept constant throughout. These parameters are selected to match with values used in the literature for carrying out numerical simulations [287, 284] and experiments [285, 282] in our same configuration.

3.2.1.1 Evidence of a rotating instability

At design flow rate, the static pressure cross-power spectrum experimentally measured at the diffuser hub shows the expected spectrum dominated by the blade passing frequency, i.e. $\hat{f}_{\text{blade}} = f_{\text{blade}}/f_{\text{imp}} = 7$ as there are 7 blades in the impeller (see fig. 3.2(a)). A qualitative equivalent spectrum (see fig. 3.2(b)) is retrieved when Unsteady Reynolds-Averaged Navier–Stokes (URANS) simulations are carried out for the same flow conditions and assuming a radial gap between the impeller and the diffuser of $\Delta R/R_3 = 1\%$, i.e. slightly larger than for the corresponding experiments [287]. When investigating the idealized case of null radial gap ($\Delta R = 0$, zero-leakage case), however, a remarkable difference is observed in the fast Fourier transform (FFT) of the cross-power spectrum computed for the corresponding URANS simulations. As demonstrated by [287], an instability (see $\hat{f}_{\text{inst}}$ in fig. 3.2(c)) can potentially occur at large flow rates due to the jet-wake features of the inflow, i.e. the intensity of the jet-wake, the mode of the periodic modulation in the azimuthal direction, and the inlet flow angle. The reason why the large-flow-rate instability gets suppressed for $\Delta R/R_3 = 1\%$ relies on the weakening of the jet-wake intensity due to more realistic inflow conditions (positive-leakage case). This is in agreement with the instability mechanism reported and discussed by [283] in a two-dimensional flow model.

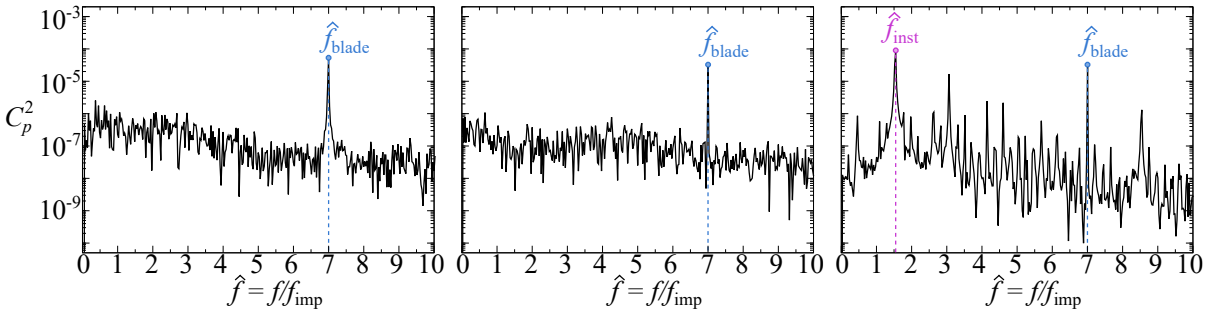

(a) Experiments: positive leakage (b) URANS: $\Delta R/R_3 = 1\%$ (c) URANS: $\Delta R = 0$

Figure 3.2: FFT of the cross-power spectrum for the pressure signal measured by pressure probe located on the shroud of the vaneless diffuser at midway between the inlet and the outlet [287].

3.2.1.2 Instabilities in the idealized configuration for $\Delta R = 0$

The flow dynamics within the vaneless diffuser with $\Delta R = 0$ have been investigated by [287, 289, 290]. They report azimuthal arithmetic-averaged color maps at the meridian section of the diffuser and instantaneous color maps at the mid-height of the diffuser for the velocity magnitude at three flow-rate Reynolds numbers with $\alpha_Q \in \{0.75,\ 1,\ 1.25\}$ (see fig. 3.3(a)). The azimuthally-averaged instantaneous color maps (see the top panels of fig. 3.3(a)) reveal that at the highest flow-rate Reynolds number, $\alpha_Q = 1.25$, the bulk flow in the radial diffuser passage is predominantly influenced by inviscid effects. The spatially-modulated swirling inflow induces partial blockage of the system, resulting in flow separation and reverse flow near the outlet of the hub wall. At the mid-height of the diffuser (see the bottom panels of fig. 3.3(a)), the velocity distribution appears regular, with main flow streamlines forming quasi-logarithmic spiral curves. Additionally, the jet-wake pattern is self-evident in the velocity magnitude distribution color map, characterized by seven high-velocity jets due to the 7-periodic inflow modulation. As the flow-rate Reynolds number decreases to the reference conditions $\alpha_Q = 1$, the reverse flow region over the hub becomes surface-filling, occupying almost half of the diffuser passage in the z-direction (see the top panels of fig. 3.3(a)). A clear 7-periodic instability flow pattern is observed at the mid-height of the diffuser (see the bottom panels of fig. 3.3(a)). The significant reverse flow observed at the meridian section of the diffuser is attributed to a core-flow rotating instability, consistent with the findings of [283], and further reinforced by the instability, as explained by [287]. As the flow-rate Reynolds number decreases further, i.e., for $\alpha_Q = 0.75$, the inflow velocity weakens (see the top panels of fig. 3.3(a)), and no rotating instability is observed (see the bottom panels of fig. 3.3(a)). This aligns with the interpretation of the rotating instability being responsible for the azimuthally-averaged reverse flow region, in accordance with the mechanism discussed by [283].

To investigate the characteristics of the core-flow instability, a quantitative analysis was conducted using an FFT of the cross-power spectrum from two numerical probes positioned at the mid-radial distance of the diffuser hub with an angular phase shift of 60° (see top panel of fig. 3.3(a-iv)). A wavelet analysis for $\Delta R = 0$ at $\alpha_Q = 1$ (see bottom panel of fig. 3.3(a-iv)) illustrates the presence of the 7-periodic blade passing frequency $\hat{f}_{\text{blade}} = 7$ in the FFT. Additionally, a low frequency $\hat{f}_{\text{r},m=7} = f_{\text{r},m=7}/f_{\text{imp}} = 1.543$ has been identified as the frequency of a 7-periodic pattern arising from the primary instability, rotating with an angular velocity $\omega_{\text{r},m=7}/\Omega = 0.22$ [287, 288, 289]. A summary of the instability scenario for $\Delta R = 0$ is presented in fig. 3.3(b). The jet wake generated by the impeller is depicted in fig. 3.3(b-i) in terms of the static pressure field at mid-height, portrayed by phase-averaging in a reference frame rotating with Ω. By subtracting this field from the instantaneous pressure field and phase-averaging in a reference frame rotating with $\omega_{\text{r},m=7}$, the 7-periodic instability pattern is discerned (see fig. 3.3(b-ii)). In a reference frame rotating with Ω, this instability propagates in the counter-clockwise direction (indicated by the arrow $\omega_{\text{r},m=7} - \Omega$ in fig. 3.3(b-ii)). The wavelet analysis validates the FFT results and indicates the presence of a pulsating signal, attributable to a secondary instability. This secondary instability, also 7-periodic, exhibits a frequency twice that of the primary instability $f_{\text{r},m=7}$. In a reference frame rotating with the primary instability ($\omega_{\text{r},m=7}$), the secondary instability transports the perturbation pattern radially (see fig. 3.3(b-iii)). Other frequencies

observed in the FFT and the wavelet analysis stem from more complex nonlinear interactions and are not discussed further.

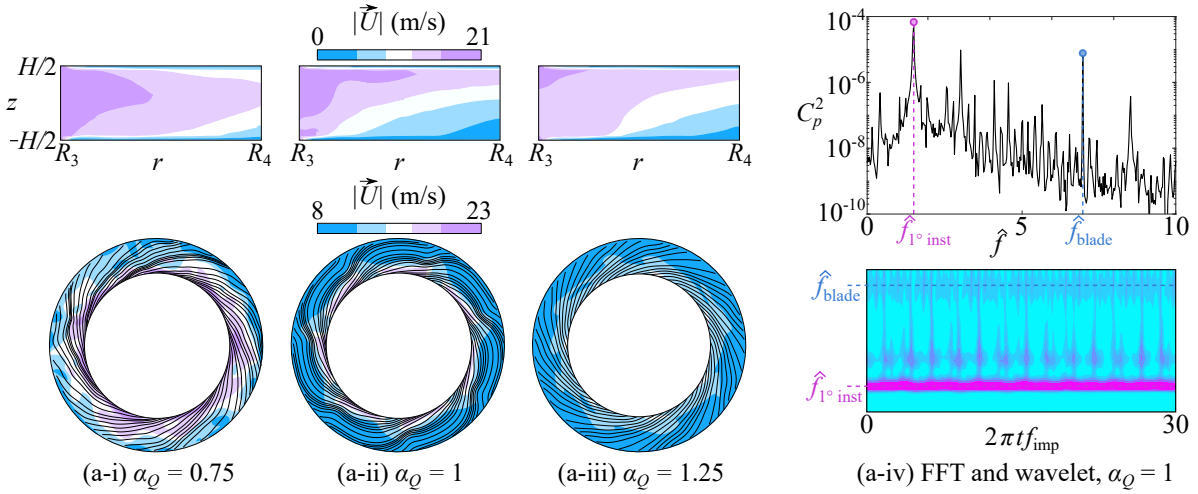

(a-i) $\alpha_Q = 0.75$ (a-ii) $\alpha_Q = 1$ (a-iii) $\alpha_Q = 1.25$ (a-iv) FFT and wavelet, $\alpha_Q = 1$

(a) Flow maps, FFT and wavelet analysis for $\Delta R = 0$

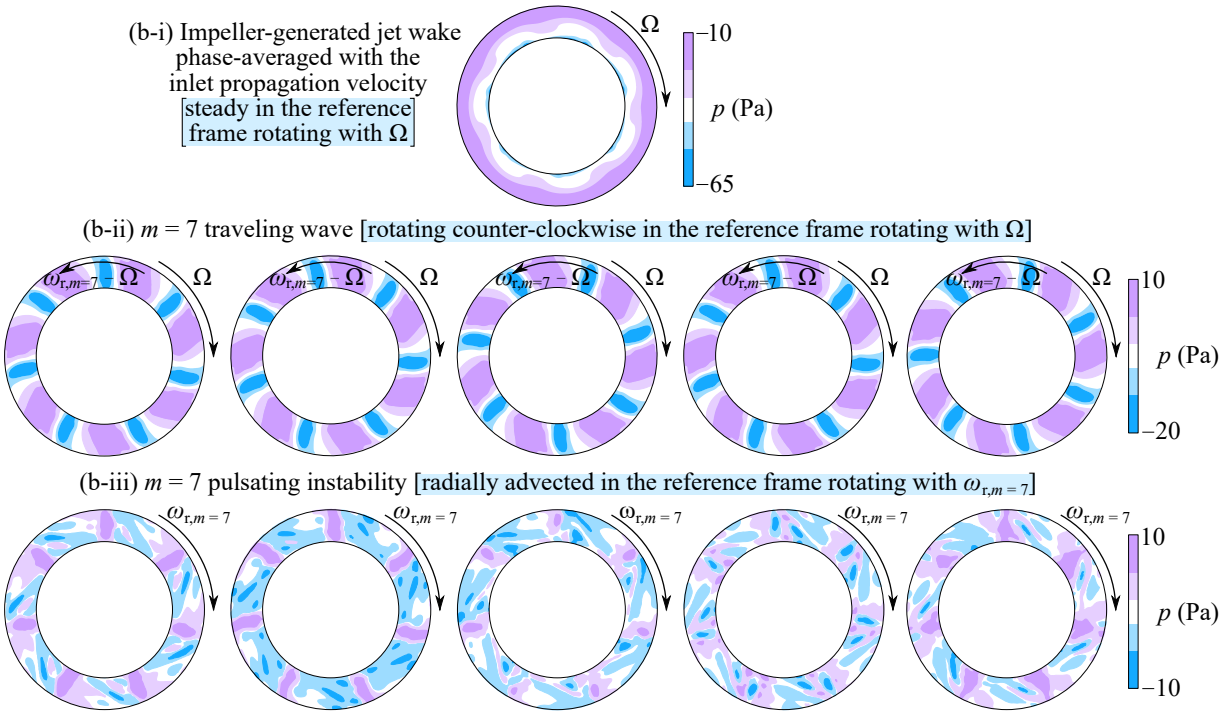

(b) Instability scenario for $\Delta R = 0$ at mid-height of the vaneless diffuser for $\alpha_Q = 1$

Figure 3.3: (a) Velocity magnitude at $\alpha_Q = 0.75$ (a-i), $\alpha_Q = 1$ (a-ii), and $\alpha_Q = 1.25$ (a-iii). Top panels: Azimuthal arithmetic-average fields at the meridian section. Bottom panels: Instantaneous fields at the mid-height of the diffuser and streamlines (black). (a-iv) FFT and wavelet analyses. (b-i) Phase-averaged static pressure distribution in a reference frame rotating with the inlet propagation velocity. (b-ii) Traveling wave depicted in the reference frame rotating with Ω and computed by subtracting the phase-averaged wake (b-i) to the instantaneous static pressure and phase-averaging with $\omega = \Omega + \omega_{r,m=7}$. (b-iii) Pulsating instability traveling in the reference frame rotating with $\Omega + \omega_{r,m=7}$ and computed with respect to the difference between the phase-averaged wake (b-i), the traveling wave (b-ii), and the instantaneous static pressure.

3.2.1.3 Effect of the leakage flow for $\Delta R > 0$

To explore the influence of leakage between rotating and steady walls on the flow field, azimuthal arithmetic-averaged color maps are presented at the meridian section of the diffuser, along with instantaneous color maps at the mid-height of the diffuser for the velocity magnitude, considering $\Delta R/R_3 = 1\%$ and three flow-rate Reynolds numbers with $\alpha_Q \in \{0.75,\ 1,\ 1.25\}$ (see fig. 3.4(a)). At the highest flow-rate Reynolds number ($\alpha_Q = 1.25$), the effect of leakage flow leads to a significantly enlarged reverse flow region compared to the ideal case (cf. top panels of figs. 3.4(a-iii) and 3.3(a-iii)). For $\Delta R/R_3 = 1\%$ at $\alpha_Q = 1.25$, the azimuthally-averaged flow field demonstrates features akin to those observed in the unstable zero-leakage case at $\alpha_Q = 1$ (see fig. 3.3(a-ii)), manifesting a 7-periodic flow pattern at the mid-height of the positive-leakage diffuser (see the bottom panels of fig. 3.4(a)). As the flow Reynolds number decreases to $\alpha_Q = 1$ and 0.75, the boundary layer thickness increases due to the effect of leakage flow. Consequently, the inflow velocity becomes more symmetrically distributed (see the top panels of fig. 3.4(a)), and no coherent 7-periodic pattern is observed (see the bottom panels of fig. 3.4(a)). We stress that no substantial flow separation is observed for $\Delta R/R_3 = 1\%$ when the 7-periodic pattern is absent, consistent with observations in the zero-leakage case, albeit occurring at different α_Q. The instability mechanism identified by [283] in two-dimensional flows and confirmed by [287] in three-dimensional conditions hinges on the intensity of the inlet modulation. The positive leakage flow attenuates the intensity of the jet-wake at the diffuser inlet, suggesting a tendency for the core-flow instability to shift towards higher flow Reynolds numbers. These observations suggest a potentially unstable scenario even for $\Delta R/R_3 = 1\%$, with an unstable boundary shifted to higher α_Q.

To validate this hypothesis, [288] conducted the same quantitative analyses (FFT and wavelet) as performed for $\Delta R = 0$. Figure 3.4(a-iv) illustrates the corresponding results for $\Delta R/R_3 = 1\%$ at the highest flow Reynolds number $\alpha_Q = 1.25$. The FFT still clearly depicts the 7-periodic inlet condition $\hat{f}_{\text{imp}} = 7$. However, no prominent instability frequencies are evident in the FFT, despite clear observation of two-dimensional jet-wake instability patterns in the snapshot of the instantaneous flow field (see fig. 3.4(a)). This discrepancy is clarified by the wavelet analysis, which reveals several low-frequency patterns intermingling throughout the simulation period. Consequently, identifying a distinct peak in the Fourier transform (other than the impeller frequency) is challenging, as any existing rotating instability is expected to manifest as a non-normal wave rather than a harmonic, unlike the case for $\Delta R = 0$. This feature complicates the identification of potential rotating instabilities in pumps with leakage flow.

Conducting a cross-correlation analysis of the two probe signals at $\Delta\varphi = 60°$, several distinct propagation velocities are captured. Phase-averaging the flow field with such velocities revealed the presence of three distinct rotating patterns. First, a 1-periodic rotating pattern with a normalized frequency $\hat{f}_{\text{r},m=1-} = 0.514$ was identified, rotating at an angular velocity $\omega_{\text{r},m=1-}/\Omega = 0.514$. Second, another 1-periodic rotating pattern corresponding to $\hat{f}_{\text{r},m=1+,7} = 1.486$ was found, rotating at $\omega_{\text{r},m=1+}/\Omega = 1.486$. Third, a 7-periodic rotating pattern was revealed, rotating at $\omega_{\text{r},m=7}/\Omega = 0.21$, a rotation rate similar to that observed for the 7-periodic harmonic produced by the rotating instability for $\Delta R = 0$. This analysis confirms the persistence of the two-dimensional

jet-wake instability for $\Delta R/R_3 = 1\%$, with the entrained leakage flow interacting with this instability to produce the observed 1-periodic traveling patterns. Figure 3.4(b) summarizes the instability scenario for $\Delta R/R_3 = 1\%$. Figure 3.4(b-i) illustrates the jet-wake pattern produced by the 7-periodic inlet, obtained by phase-averaging in a reference frame rotating with Ω. By subtracting this pattern from the instantaneous pressure field and phase-averaging in a reference frame rotating with $\omega_{r,m=1-}$, the 1-periodic traveling wave is identified. Further subtracting the phase-averaged jet-wake pattern and the 1-periodic instability pattern from the instantaneous pressure field, and phase-averaging again in a reference frame rotating with $\omega_{r,m=1+}$, reveals the field of the other (weaker) 1-periodic traveling wave. Notably, the two 1-periodic waves propagate in opposite circumferential directions and rotate with the same propagation velocity magnitude in a reference frame rotating with Ω. Their superposition results in a 1-periodic traveling wave and a 1-periodic standing wave in a reference frame rotating with Ω. This elucidates the main features introduced by the complex leakage flow inside the vaneless diffuser. Moreover, we stress that the propagation velocity of the 1-periodic patterns is approximately half of the inlet rotating velocity $R_3\Omega$, suggesting that the traveling velocity of these waves is primarily determined by the leakage flow between the steady (diffuser) and rotating (impeller) walls.

After subtracting the phase-averaged two 1-periodic instabilities and the jet-wake patterns from the instantaneous pressure field, a phase-average is performed again in a reference frame rotating with $\omega_{r,m=7}$, revealing the 7-periodic traveling pattern resulting from the jet-wake instability, which manifests as a non-Fourier mode. The qualitative and quantitative similarities with the instability found for $\Delta R = 0$ are evident (compare figs. 3.4(b-ii) and 3.3(b-ii)). However, the secondary instability observed for $\Delta R = 0$ (see fig. 3.3(b)) is absent for $\Delta R/R_3 = 1\%$. Instead, for the positive-leakage case, intermittent nonlinear interaction between mode $m = 7$ and modes $m = 1$ leads to the chaotic dynamics observed in the wavelet analysis (see fig. 3.4(a)).

To understand the origin of the $m = 1$ traveling wave, additional simulations have been conducted by [288] with two different radial gaps between the impeller and the diffuser, namely $\Delta R/R_3 = 0.\overline{3}\%$ and $0.\overline{6}\%$ for $\alpha_Q = 1$ and 1.25. Figure 3.5(a) illustrates the results for $\alpha_Q = 1$. Up to $\Delta R/R_3 = 0.\overline{6}\%$, the $m = 7$ jet-wake instability persists, as evidenced by the corresponding mean flow separation shown in fig. 3.5(a). Consequently, the critical radial gap lies within $(\Delta R/R_3)_{c,\alpha_Q=1} \in [0.\overline{6},\ 1]\%$ (see bottom panel of fig. 3.5(a)). No indication of the $m = 1$ traveling wave is observed for any of the simulations at $\alpha_Q = 1$, as confirmed by the FFT depicted in the top panel of fig. 3.5(a). This suggests that the jet-wake instability serves as a primary mechanism, but its interaction with the leakage flow does not necessarily lead to the $m = 1$ traveling wave. When the jet-wake instability dominates (as indicated by the amplitudes in the Fourier spectra of fig. 3.5(a)), the leakage flow may be too weak relative to the primary instability, preventing the onset of the $m = 1$ traveling wave. However, our simulations underscore the significance of the leakage flow, as evidenced by the transition of the jet-wake instability from $m = 7$ for $\Delta R/R_3 = 0$ and $\alpha_Q = 1$, to $m = 8$ for $\Delta R/R_3 = 0.\overline{3}\%$, and to $m = 6$ for $\Delta R/R_3 = 0.\overline{6}\%$ (see stability diagram in fig. 3.5(a)). As previously noted, the flow remains stable for $\Delta R/R_3 = 1\%$ at $\alpha_Q = 1$.

Increasing the flow rate to $\alpha_Q = 1.25$, the zero-leakage scenario ($\Delta R = 0$) remains stable

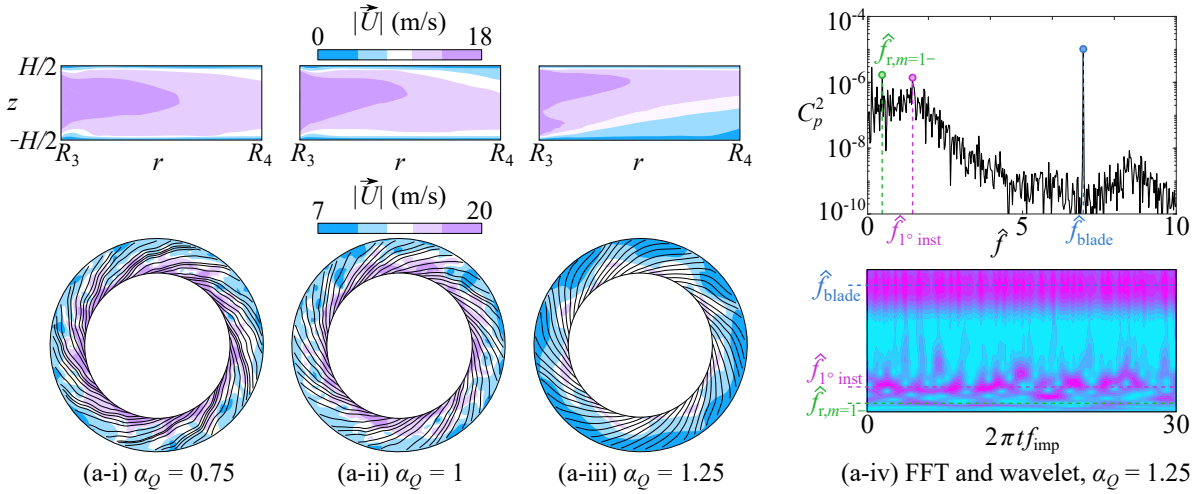

(a-i) $\alpha_Q = 0.75$ (a-ii) $\alpha_Q = 1$ (a-iii) $\alpha_Q = 1.25$ (a-iv) FFT and wavelet, $\alpha_Q = 1.25$

(a) Flow maps, FFT and wavelet analysis for $\Delta R/R_3 = 1\%$

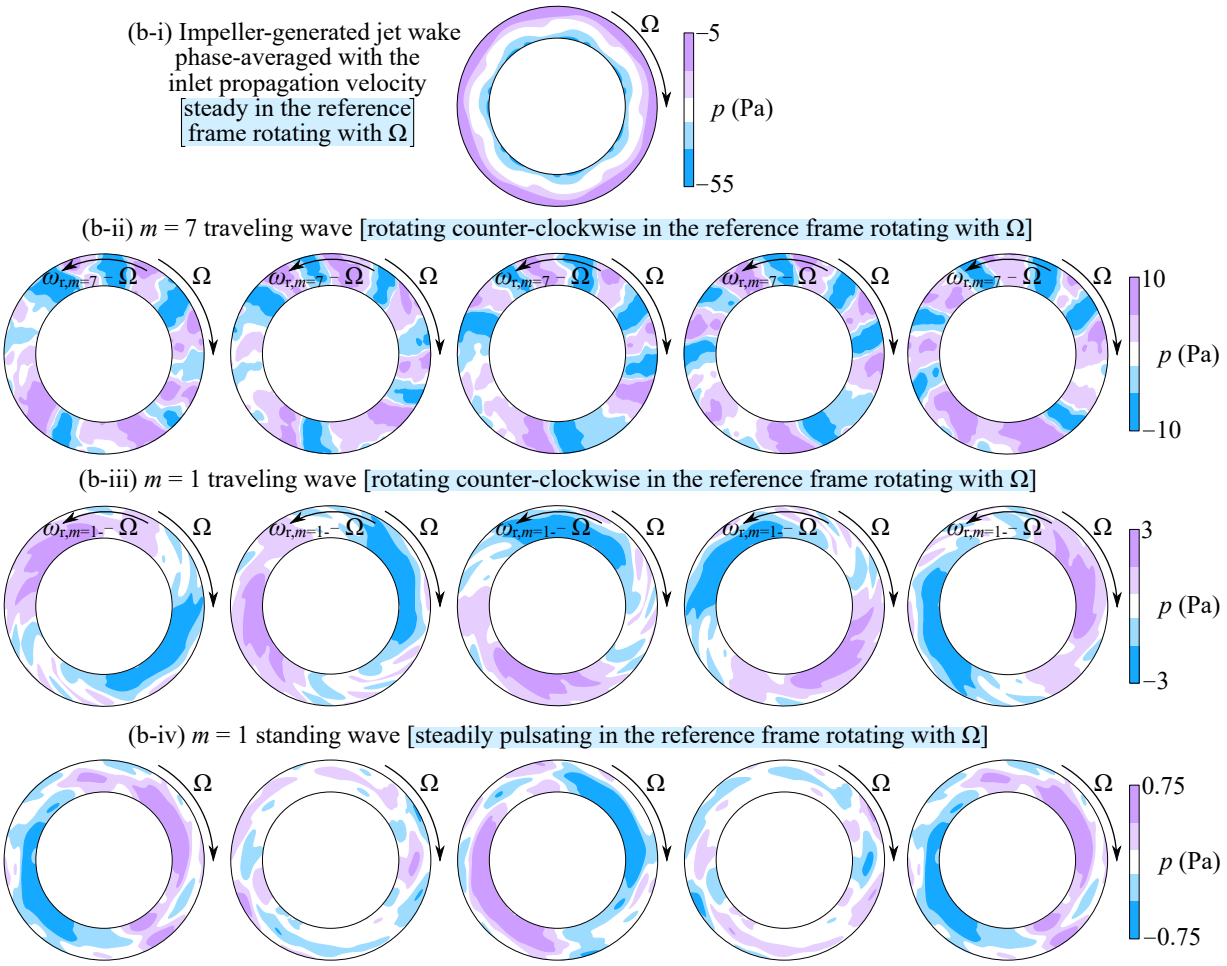

(b) Instability scenario for $\Delta R/R_3 = 1\%$ at mid-height of the vaneless diffuser for $\alpha_Q = 1.25$

Figure 3.4: See caption of fig. 3.3 for (a) and (b-i)–(b-ii). For (b-iii) see (b-ii) with $\omega = \omega_{r,m=1}$ instead of $\omega = \omega_{r,m=7}$. (b-iv) Standing wave steady in the reference frame rotating with Ω and computed with respect to the difference between the phase-averaged wake (b-i), the traveling wave (b-iii), and the instantaneous static pressure and phase-averaging with $\omega = \Omega$. All figures refer to $\Delta R/R_3 = 1\%$ at the mid-height of the annular ring for $\alpha_Q = 1.25$.

against the core-flow instability, exhibiting a broad range of frequencies in its Fourier spectrum (see fig. 3.5(b)). This dynamical behavior arises from the complex interplay between the inflow and the mean-flow separation occurring on the diffuser hub (see fig. 3.5(b) and [288]). With an augmentation in the radial gap, the jet-wake instability manifests at $\Delta R/R_3 = 0.\overline{3}\%$, establishing the critical gap size for the primary instability as $(\Delta R/R_3)_{c,1°,\alpha_Q=1.25} \in [0,\ 0.\overline{3}]\%$ for $\alpha_Q = 1.25$ (see stability diagram in fig. 3.5(b)). Despite the weakened jet-wake instability compared to $\alpha_Q = 1$, the radial gap $\Delta R/R_3 = 0.\overline{3}\%$ remains insufficient for the interaction between the corresponding leakage flow and the primary instability to trigger the $m = 1$ traveling wave. Conversely, for comparable jet-wake instability amplitudes (FFT in fig. 3.5(b)), the radial gap $\Delta R/R_3 = 0.\overline{6}\%$ induces a more intense leakage flow capable of triggering the secondary traveling-wave instability — as indicated by the presence of the $m = 1+$ frequency in the corresponding Fourier spectrum — a trend further amplified for $\Delta R/R_3 = 1\%$ as the primary instability diminishes in amplitude. Consequently, the critical radial gap for the secondary instability lies within $(\Delta R/R_3)_{c,2°,\alpha_Q=1.25} \in [0.\overline{3},\ 0.\overline{6}]\%$ for $\alpha_Q = 1.25$. Notably, for $\Delta R/R_3 = 0.\overline{6}\%$, the $m = 1$ traveling wave rotates clockwise in a reference frame synchronized with the inlet Ω. Once more, the leakage flow influences the dominant mode of the primary instability, transitioning the jet-wake instability from $m = 6$ for $\Delta R/R_3 = 0.\overline{3}\%$ to $m = 9$ for $\Delta R/R_3 = 0.\overline{6}\%$ and back to $m = 7$ for $\Delta R/R_3 = 1\%$ at $\alpha_Q = 1.25$ (see stability diagram in fig. 3.5(b)). A similar investigation into the core-flow instability at low flow rates reveals a comparable sensitivity to leakage flow, particularly evident for short diffuser aspect ratios, e.g., $\Gamma = 1.25$. For further details, refer to [290].

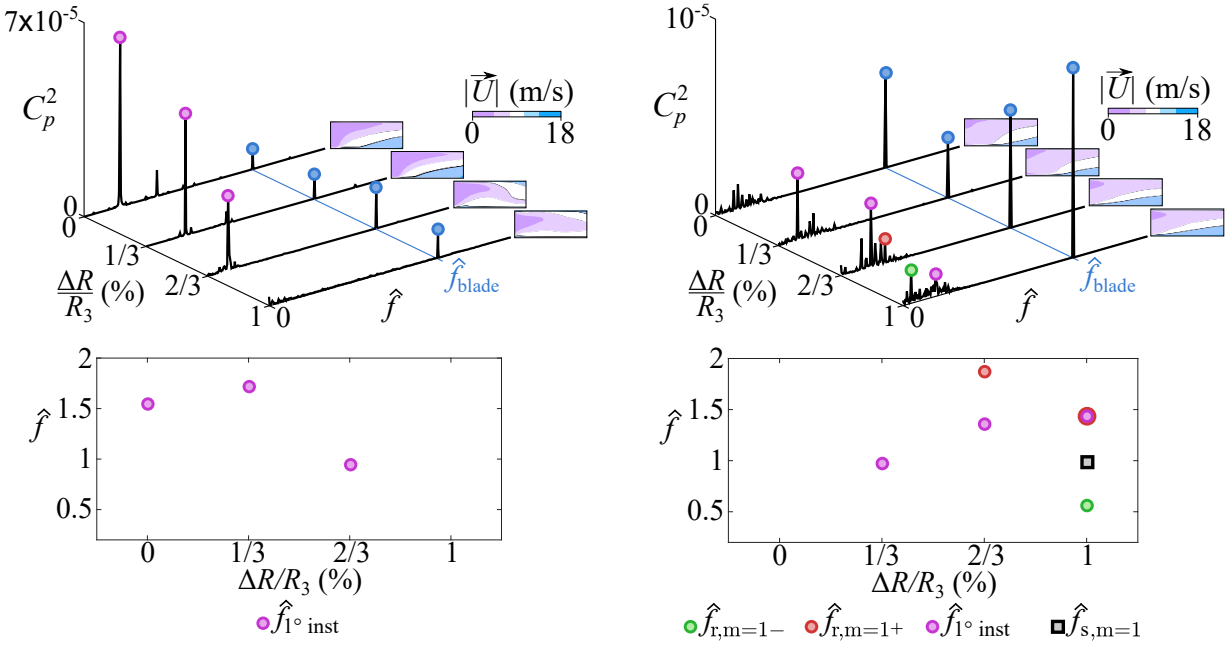

(a) $\alpha_Q = 1$ (b) $\alpha_Q = 1.25$

Figure 3.5: FFT, stability diagram, and azimuthal arithmetic-average velocity fields at the meridian section of the diffuser for (a) $\alpha_Q = 1$ and (b) $\alpha_Q = 1.25$ with different radial gaps: $\Delta R/R_3 = 0$, $0.\overline{3}\%$, $0.\overline{6}\%$, and 1%.

3.3 Instabilities and flow control in an axial compressor

Axial compressors play crucial roles across various industrial sectors, including power generation and aircraft engines. Among the challenges they face, maintaining stability becomes particularly difficult as the compressor pressure ratio increases. In the specific context of aeronautical applications, where reducing engine emissions is essential, extending compressor operating ranges and pushing for higher pressure ratios offer promising solutions, but not without risks. Rotating stall [291] emerges as a critical issue, disrupting the stability and advancement of modern axial compressors. This phenomenon arises from flow instabilities that worsen with perturbation intensity, ultimately compromising compressor efficiency when instability patterns spread azimuthally. In severe cases, rotating stall can lead to catastrophic machine failure. Despite these challenges, progress has been made in understanding the underlying instability mechanisms. Various routes to stall have been identified [292], including *modal* [293] and *spike*-type [294] rotating stalls. Detailed flow mechanisms for each process have been proposed in the literature through a combination of experimental and numerical research, and a brief summary of such two mechanisms will be presented in the following subsections.

The postponement of the onset of rotating stall becomes increasingly crucial, particularly in the context of future-generation engines with smaller cores and boundary layer ingestion, where this issue poses an even greater limitation. Aiming at delaying the onset of rotating instabilities, dedicated efforts have thus been devoted to designing and implementing effective flow control strategies, including both passive [295] and active [296] methods. In particular, the latter flow control technique is characterized by two small scales, i.e. the radial tip gap ΔR and the control jet thickness δ_j (see fig. 3.6). Their interaction determines the effective impact of the control strategy on the largest scale of the flow R, hence the performance of the compressor Ψ (normalized total-to-static pressure raise) upon a variation of the flow coefficient $\Phi = U/\Omega R$ (see fig. 3.6).

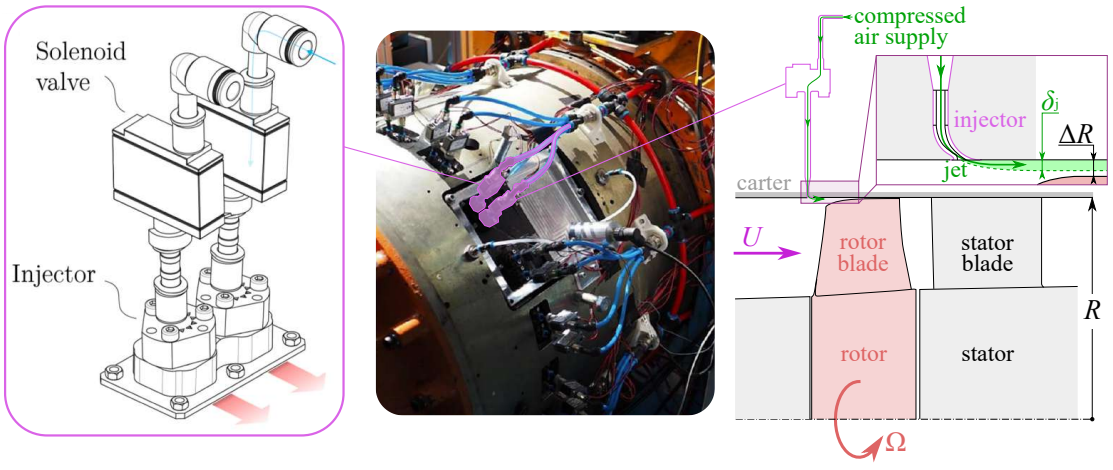

Figure 3.6: Experimental setup of the CME2 axial compressor operated at Arts et Métiers, Lille. A schematic of the compressor and the active flow control is depicted on the right, together with an inset that depicts the flow across the injector. A couple of the 40 injectors used to control the compressor flow is highlighted in magenta on the experimental setup (middle). A corresponding schematic is depicted in the magenta box on the left.

3.3.1 Spike instability

The understanding of the spike-type instability leading to rotating stall introduces challenges related, in particular, to the identification of the phenomenon itself. Moreover, in certain instances, the use of the term *spike* can be ambiguous, necessitating a more nuanced analysis of the stall inception mechanisms. The term *spike* denotes a peaked signature observed in local velocity or pressure measurements (see fig. 3.7). The presence of such a peak has initially been interpreted as a precursor of the rotating stall, which normally occurs a few revolutions after the spike. The large-scale rotating cells induced by the rotating stall travel at slower, yet comparable propagation rate with respect to the rotor rotation rate Ω.

Initial observations revealed a robust correlation between the spike onset and the upstream displacement of the interface between the Tip Leakage Flow (TLF) and the incoming flow [297]. As the operational point approaches the stability limit, the reduction in mass flow weakens the incoming flow relative to the TLF, potentially resulting in the occurrence of surge for the axial compressor. Recent investigations, both experimental [298] and numerical [299], have elucidated a direct linkage between the spike and the TLF. A criterion involving the simultaneous satisfaction of two conditions has been proposed by [299], even though recent investigations have introduced novel insights:

I) The interface between the TLF and the main flow must be aligned parallel to the leading-edge plane. This condition induces a disturbance in the rotor leading-edge region caused by the Tip Leakage Vortex (TLV) and sets the stage for the subsequent condition.

II) The spillage of tip leakage in front of the leading edge of a blade and the backflow at the trailing edge of the preceding blade are simultaneously observed, with the backflow augmenting the spillage.

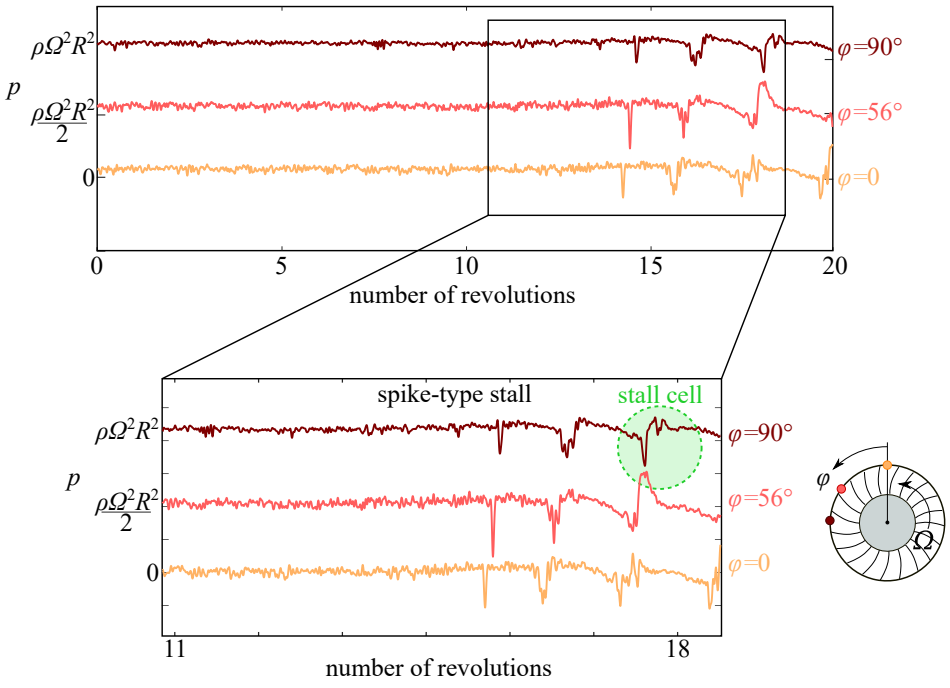

Figure 3.7: Static pressure measurements shifted by $\rho\Omega^2R^2/2$ at three azimuthal locations on the compressor carter. The figure demonstrates the spike-type stall for critical flow rate.

Distinctive pressure spikes have been observed in the numerical simulations conducted by [300] on configurations devoid of tip gaps, hence lacking tip leakage and backward spillage. They identified the formation of radial vortices extending from the suction side of blades to the casing, associating these structures with the observed spike. Notably, these radial vortices were previously documented by [301, 302, 303] in a large tip gap configuration parallel to tip leakage vortex breakdown, just before stall formation. These findings contribute additional insights to the understanding of the intricate mechanisms underlying the conditions leading to the spike type rotating stall.

More recently, these findings have been complemented by a numerical investigation into the influence of tip gap size on the flow mechanisms implicated during stall inception, revealing a robust correlation between the two [304]. Notably, the analysis demonstrates that for small tip clearances (below a critical value of $\Delta R/c = 0.5\%$), no spillage occurs, and the rotating stall is triggered by an increase in incidence due to blockages at the exit of the blade passage. Conversely, in cases of larger tip clearances, the leakage momentum hinders the formation of these blockages, but backflows may manifest. These distinct modes of *spike* type rotating stall are denoted as *casing corner separation dominated* and *tip leakage jet dominated*, respectively (see fig. 3.8 [304]).

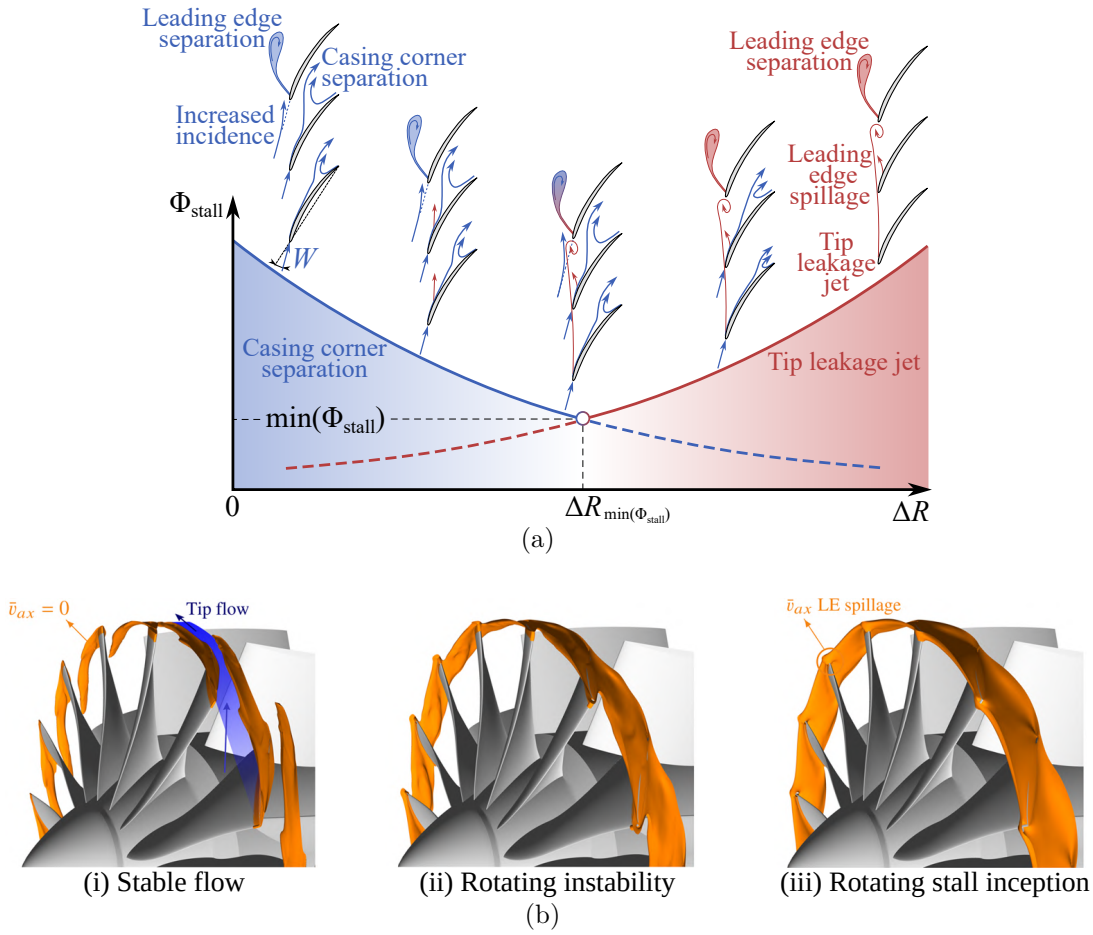

Figure 3.8: (a) Schematic of the two regimes identified for the TLF by [304]. (b) Visualization of the TLF and leading edge spillage at blade tip. Three regimes are depicted: (i) stable regime, (ii) inception of a rotating instability localized near the blade tip, (iii) rotating stall produced by the intensification of the rotating instability at blade tip. See [305] for more details.

3.3.2 Modal instability

For modal instabilities, the stall cells exhibit progressive growth, originating from small perturbations with high wavelengths compared to the blade channel. Figure 3.9 depicts a typical representation of the schematics of the incoming velocity perturbation (fig. 3.9(a)), and the experimental pressure signals (fig. 3.9(b)) exhibiting signatures characteristic of modal stall in the CME2 compressor operating at Arts et Métiers, Lille, upon the introduction of an inlet perturbation produced by a weakly-porous grid [306].

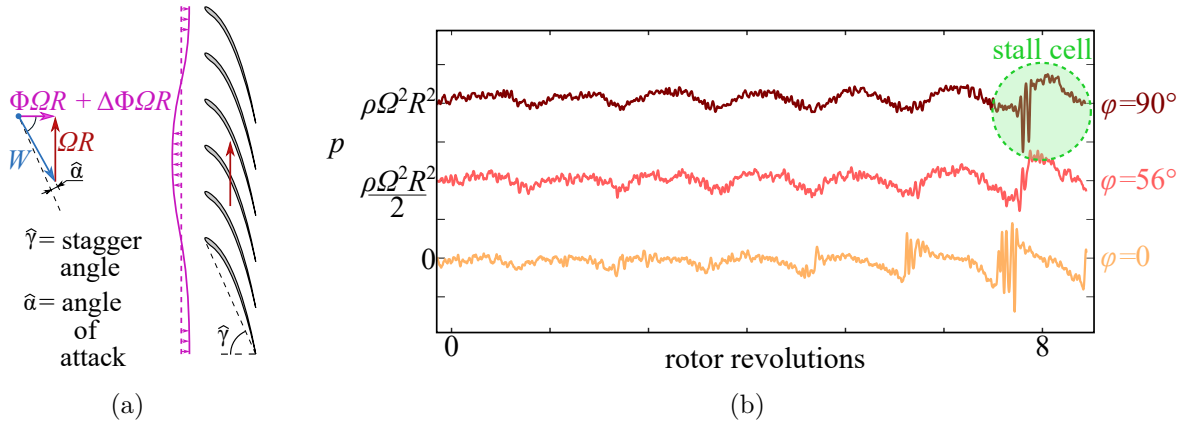

Figure 3.9: (a) Schematic of the inflow perturbation for modal instability. (b) Static pressure measurements shifted by $\rho\Omega^2R^2/2$ at three azimuthal locations for modal-type stall.

The modal instability is based on a linear mechanism, which can be elucidated by examining the meridian flow far from the blade tip. Various dedicated reduced-order models have been developed to investigate modal instabilities in axial compressors, with consideration given to azimuthal instabilities that may arise from boundary layer ingestion or upstream external asymmetries. One such model, proposed by Hynes–Greitzer ([307], see fig. 3.10), employs a concentration parameter approach. This approach assumes that the compressor's behavior can be replicated through the linear superposition of the time-averaged total-to-static $\Delta p_{\text{ts}} = (p_t - p)$ characteristic curve $\Psi = 2\Delta p_{\text{ts}}/\rho R^2\Omega^2$, a plenum of volume V_p concentrating all compressibility effects, and a throttle valve T_Φ to regulate the flow rate $\Phi = U/R\Omega$. Despite its simplicity, the model has demonstrated success in identifying the onset of modal instability observed in experimental conditions [307, 308, 309]. Additionally, this model has proven effective in accounting for the impact of an inlet pressure perturbation $p_{\text{in}}(\varphi)$ on the stability of a compressor [310, 306].

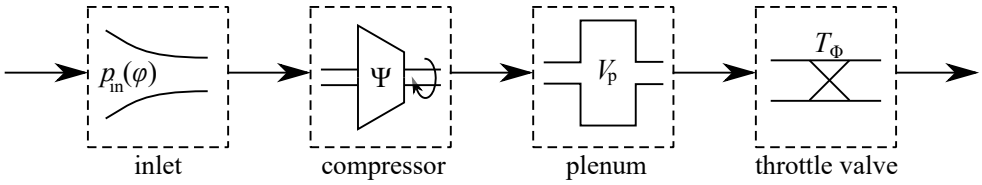

Figure 3.10: Schematic of the model proposed by Hynes–Greitzer [307]. Each box represents an effect included in the model. From left to right: inlet pressure perturbation in azimuthal direction, performance curve, compressibility effects, and flow rate control via a throttle valve.

3.3.3 Active flow control

Active control techniques, particularly for near-tip injection (see fig. 3.11(a)), have demonstrated their efficacy in enhancing compressor stability by displacing the surge line [311, 312, 313, 314]. Noteworthy successes have been achieved in practical applications, including real aircraft engines [315, 316]. While understanding the effects of active flow control is of primary importance, it is surprising that few studies have delved into the mechanisms involved when employing this technique and its impact on flow patterns in the tip gap. This stands in contrast to the extensive body of work focused on casing treatments [317, 318, 319, 320]. Active flow control methods have the added advantage of being switched on only when control is needed, thus leading to an overall reduced energy consumption. Previous studies [321, 296] have demonstrated the effectiveness of air jets in postponing the onset of rotating stall in the axial compressor CME2 installed at Arts et Métiers, Campus of Lille. Such a control strategy relies on the injection of high-momentum fluid flow near the tip leading edge of the rotor blades (see fig. 3.11(a) [322]) by a discrete set of air jets positioned circumferentially upstream of the compressor.

The implementation of active flow control through momentum injection at the blade tip has proven successful in expanding the operating range of the compressor (see fig. 3.11(b), [296]). This success is attributed to its ability to counteract *spike* inception mechanisms and bring the last stability point close to the maximum of the performance curve, where *mode*-type rotating stall may occur before the onset of rotating stall. The active control system offers a dual enhancement, reducing the stalling mass flow rate and increasing the pressure rise for a given operating point. The first effect is achieved by eliminating leading-edge separations at the tip, as evidenced by the absence of radial vortices. The second effect stems from a reduction in losses associated with secondary flows and the instability of the tip leakage vortex. This observation suggests however that overcoming the limitation by active flow control system designed to address spike mechanisms, will be constrained by modal-type stall.

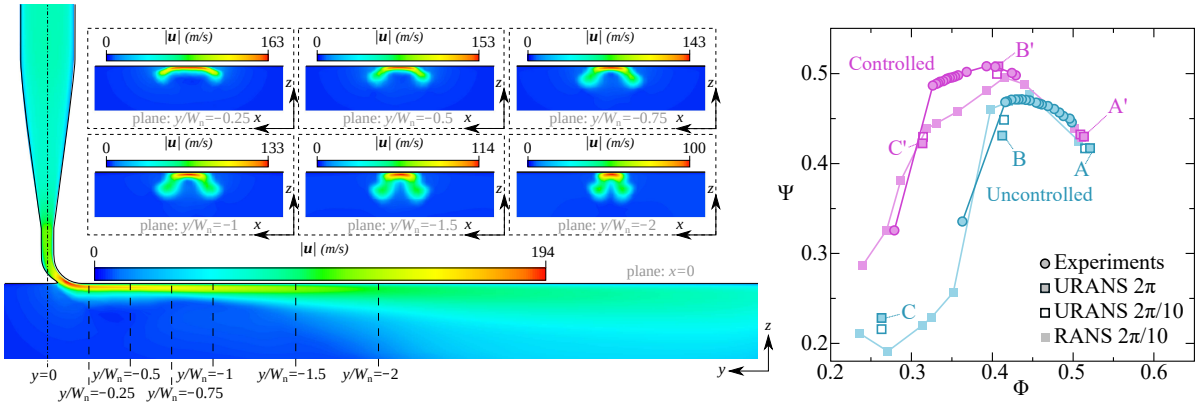

(a) Simulation of single injector

(b) CME2 performance curve

Figure 3.11: (a) Numerical simulations of the injector in quiescent air for inlet mass flow rate $\dot{m} = 1$g/s [322]. (b) Performance curves of the CME2 compressor for uncontrolled (light blue) and controlled conditions with 40 continuously blowing (magenta) injectors. The points A and A' refer to the flow rate Φ for uncontrolled nominal operating conditions, B and B' to the flow rate for the last stable point for uncontrolled CME2, while C and C' refer to stalled conditions.

3.4 Summary and conclusions

Two examples of rotating machines have been considered for demonstrating the significance of fluid dynamic systems in which two or more well-separated characteristic length scales are significant for determining the leading-order flow. In §3.2 a centrifugal pump has been considered focusing on the effect of a small leakage between the impeller and the radial diffuser. We demonstrated that the instability onset, as well as the secondary instability scenario are impacted by a leakage gap that is about a hundred times smaller than the diffuser inlet radius. This consideration is robust for both the kinds of instabilities identified in the vaneless diffuser, i.e. the high-flow-rate instability discussed in §3.2 and the low-flow-rate instability, as reported in [290].

This consideration suggests that the radial gap between impeller and diffuser inlet is a key parameter in designing a centrifugal pump. Moreover, owing to the sensitivity of hydrodynamic instabilities to the leakage flow, it could be envisaged an flow control device that actively regulates the radial gap according to the required leakage needed to suppress the instability inside the radial gap. A preliminary numerical investigation in this regards has been recently carried out by [289], who considered an instantaneous partial closure of the radial gap, demonstrating a suppression of the fully-developed instability mode ($m = 7$) for the larger gap of $\Delta R/R_3 = 1\%$, before triggering the instability mode specific of $\Delta R/R_3 = 0.\overline{6}\%$ ($m = 9$) or $0.\overline{3}\%$ ($m = 6$).

The second rotating machine considered is an axial compressor, namely CME2, operating at Arts et Métiers, Campus of Lille. The two well-separated characteristic lengths that one can identify in this case are the carter radius R and the blade-tip-to-carter gap ΔR, which is normally of the order of $\Delta R/R \approx 1\%$. The leading-order dynamics of CME2 is significantly affected by the tip-leakage vortices (at characteristic scale ΔR) that may lead to spike instabilities and potentially to rotating stall (at characteristic scale R) for low-enough flow rate. This instability scenario is representative of several aeronautical engines, hence controlling and potentially suppressing it is a long-lasting goal of the turbomachinery community.

In §3.3.3 we discussed the potential of suppressing the spike instability by active flow control. The experiments carried out in CME2 by blowing with either twenty or forty injectors [321, 296] demonstrate that the interaction of tip-leakage vortices leading to the spike instability can be annihilated by injecting high momentum and localizing it at the scale of $\delta_j/\Delta R = \mathcal{O}(1)$. In fact, the Coanda jet currently used on CME2 has a thickness of about 2 mm at the rotor leading edge and the blade-tip-to-carter gap used by [296] is 1.45 mm. We further stress that recent numerical simulations and experiments [323] in the same actively controlled configuration for $\Delta R = 3.48$ mm shows that active flow control can significantly improve the axial compressor performance, beyond the sole suppression of the instability. This opens to a future prospective in which a detailed multiscale analysis of the interaction between the jet and the gap flow at blade tip could explain such a significant performance enhancement. Furthermore, this would potentially drive a perspective for simultaneously designing axial compressors and their active control system. Indeed, if injecting momentum near the carter can remarkably affect the compressor performance for thick blade tip gaps, then one could expect that new optimal designs are possible when considering the rotor blades and the active flow control as the system to optimize as a whole.

Chapter 4

Pulmonary Flows

Summary

The complex multiphysics of distal airways occlusion is tackled by characterizing the effects of capillary stresses, multi-layer coating, surfactant dispersion, and non-Newtonian rheology of mucus. A standalone approach is used, including one of such modeling elements at a time, baring in mind that predictive simulations should finally combine the whole complexity of the airway fluid mechanics, included the complex fluid-structure interaction still neglected in the presented models. The occlusion considered in the bronchioles is due to a Rayleigh–Plateau instability occurring in the liquid film of thickness H lining the airways. The occlusion of the airways is predicted to occur for $H/a_n \approx 0.12 \ll 1$, where a_n is the airway radius at generation n. This therefore justifies the importance of well-separated length scales for the potential hindering of gas exchange at distal airways.

Contents

4.1 Introduction

The multiscale nature of the lungs network is exemplified in fig. 4.1. Starting from the trachea, which is considered to be the generation zero of radius $a_0 \in [1.5,\ 2]$cm, the respiratory tree bifurcates in bronchi first and bronchioles after with a morphological power-2 correlation, i.e. $a_n = a_0 \times 2^{-n/3}$, where n is the generation number and a_n the radius of the n-th generation. This holds true for the first 17 generations of adult human lungs.

The first 15 or 16 airway generations of adult human lungs are lined with a two-layer airway surface liquid (ASL, see fig. 4.1) [324] of thickness H. The corresponding flow involves three phases, i.e. air, mucus and serous liquid, while it transitions to a two-phase system (air and a waterish fluid) from the 16th or 17th generation on. In healthy patients, the ASL is thin ($\delta = H/a_n \approx 2-4\%$), while pathologies involving hypersecretion of mucus can lead to a ten-times thickening of the ASL in the bronchioles, i.e. $\delta \approx 20-40\%$ [325]. In the idealized case of a cross section (see inset of the bronchiole in fig. 4.1) subject to minimal airway wall deformations, two well-separated length scales allow investigating the problem asymptotically, as done by using the thin film approximation ($\delta \ll 1$, see [326, 327, 328, 329, 330, 331, 332, 333]). Reviews of respiratory airway closure, liquid plug propagation and rupture appear in [334, 335, 336, 337, 338].

Beside the intrinsic multiscale nature of the problem, respiratory fluid mechanics is further complexified by the non-Newtonian rheology of mucus [339], the highly non-linear mechanical behaviour of the lung walls [340], as well as the presence of surfactant [341]. Including the resulting multiphysics would be essential to the accurate prediction of lung pathologies. However, current experimental and numerical investigations are far from simulating all multiphysical non-linear interactions either by in-vitro/on-chip experiments [342, 343, 344, 345] or by numerical solvers [346, 347, 348] under controlled conditions. Viceversa, in vivo experiments [349, 350] can tackle the multiphysics complexity, but without assuring controlled conditions.

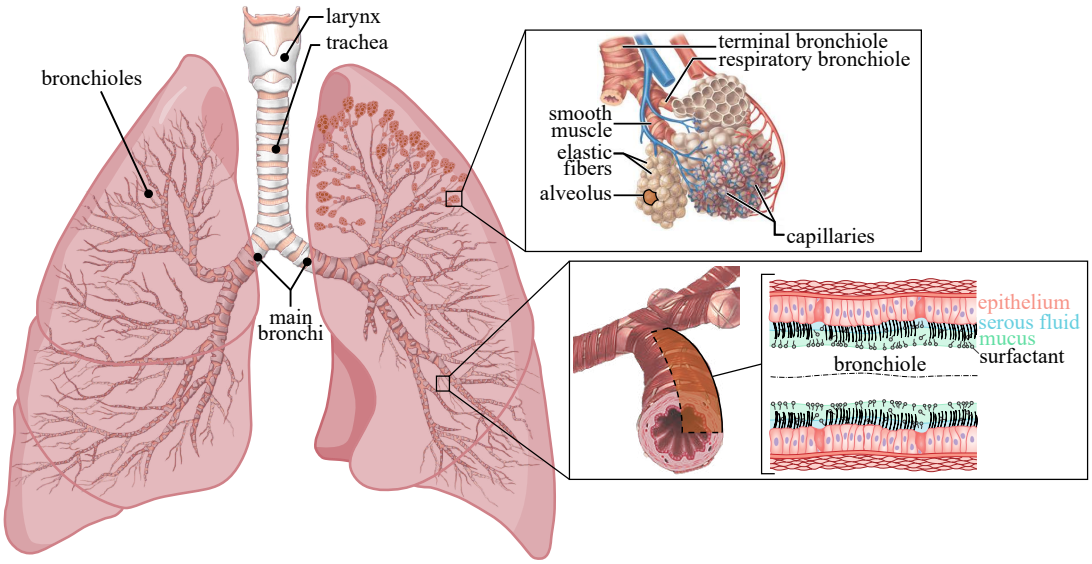

Figure 4.1: Schematic of the lung network (left), a distal bronchiole coated by mucus and serous layer (bottom-right panel), and three alveolar sacs, including the capillaries to oxygenate. The left figures in the insets are adapted from [351] and [352].

4.2 Airway closure models

Airway closure is usually associated with surfactant deficiency or dysfunction, accumulation of liquid from infections or edema, or mucus hypersecretion along the airway. Typical lung diseases involved include: asthma [353], pneumonia [354], bronchiolitis [355], cystic fibrosis [356], chronic obstructive pulmonary disease (COPD [357]), and acute respiratory distress syndrome (ARDS [358]), just to name a few. The so-called airway closure generally occurs in small airways near the end of expiration. The lung volume at which closure initiates is called the closing volume, which varies with disease, age, and sex [359, 360]. For an upright lung in gravity, the lower regions have compressed airway diameters from the weight of the lung above, so closure tends to occur there initially. It is therefore expected that, under microgravity conditions, airway closure occurs more homogeneously posing an additional risk, see [361, 362, 335].

For a clean interface in a rigid pipe, the critical film thickness is $\delta_c = H_c/a_n \approx 0.12$ [328]. This is the minimum film thickness such that the interfacial instability forms a liquid plug. Several studies have investigated models of the pre-coalescence closure instability under additional circumstances, including the effects of surfactant, viscoelasticity, non-axisymmetry, and wall flexibility. The effects of surfactants have been experimentally studied in capillary tubes by [363], who pointed out that surfactant can increase δ_c and decrease the growth rate, hence increase closure time, t_c. Theoretical and computational models based on lubrication theory [363, 364] and full Navier–Stokes equations [365] also confirm these findings. The Marangoni stresses induced by uneven distribution of interfacial surfactant concentration oppose the closure flow [366]. Moreover, it has been shown that viscoelasticity does not strongly affect the critical film thickness δ_c, and for $\delta < 0.119$ airway closure does not occur according to bifurcation theory [367]. On the other hand, if $14\% \leq \delta \leq 18\%$, increasing the Weissenberg number We speeds up the growth rate. The effect of wall compliance has been studied by [330, 364]. They showed that the airway wall deforms to narrow the tube and reduce the radius of curvature for the air–liquid interface, thereby enhancing the instability. Non-axisymmetric mechanical and hydrodynamic instabilities may further lead to the formation of a plug at lower δ_c than predicted by the axisymmetric models [368]. Prevention of closure by oscillating the core fluid axially was explored in [332], where non-linear saturation of the instability is reached when the growth in the turnaround phase balances the decay in the stroke phase and fluid is deposited back onto the wall.

These previous studies motivate extending the investigation to the analysis of coalescence and post-coalescence phases, not included when the lubrication theory is employed. The approach presented in this chapter aims to investigate standalone effects within the context of an airway closure model that neglects fluid-structure interactions. The ultimate goal is to identify some purely fluid mechanical features that would guide the understanding of the flow, provided that non-linear effects must be tested rather than relying on the models superposition.

As airway closure is due to a capillary instability, all the results in the following subsections make use of a capillary scaling, i.e. length, time, pressure, and velocity are non-dimensionalized with a_n, $\mu_{\mathrm{L}} a_n/\sigma_0$, σ_0/a_n, $\sigma_0/\mu_{\mathrm{L}}$, respectively, where μ_{L} the dynamic viscosity of the liquid phase (mucus for two-layer coating), and σ_0 is the reference surface tension at clean interface conditions.

4.2.1 Clean single-layer Newtonian airway closure

The simplest airway closure model allowing to retain the key features of the primary capillary instability is depicted in fig. 4.2. The airway walls are assumed to be rigid, the two-liquid coating is homogenized in one Newtonian layer lining the airway model, and no surfactant is included in the model. Despite the assumption that the surface tension is constant, two values are considered to model healthy conditions ($\sigma_0 = 26$ dyn cm^{-1}) and the mean effect of surfactant deficiency ($\sigma_0 = 52$ dyn cm^{-1}), which is mainly affecting the airway closure phenomenon.

A typical scenario observed during an airway closure is depicted in fig. 4.3(a) characterizing the coalescence process for La $= 100$, $\mu = 1.5 \times 10^{-3}$, $\varrho = 10^{-3}$, $\lambda = 6$, $\delta = 0.25$ in terms of pressure field and interface location (see fig. 4.3(b) for a definition of the non-dimensional groups). In the initial growth phase of the instability, the cross-sectional curvature of the interface $1/R_\mathrm{I}$ expands the flow in the liquid film at the location where the bulge is. This curvature effect dominates over the in-plane compression due to a thicker liquid film at the bulge, hence the lowest relative pressure is observed at the axial location of the bulge tip (see fig. 4.3(a)). Since the selected initial thickness of the film is greater than the critical thickness $\delta_c \approx 0.12$, the airway closure occurs. The capillary instability drains the liquid from the film (see pressure in fig. 4.3(a)) to supply the bulge up to the liquid plug formation. After the coalescence, the pressure field has its minimum at the liquid-gas interface near the centerline of the tube (light pink area). The flow is then pushed away from the plane of symmetry and drains even more liquid from the wall coating film to grow the liquid plug. In this phase the air–liquid interface advances with its two fronts in opposite directions leading to *bi-frontal plug growth* [369, 370]. The process occurs in a very short time and is characterized by high axial accelerations. Such a quick post-coalescence phase is comparable to the receding of two air fingers, whose fronts are moving in opposite directions. As pointed out by [369], during closure and also shortly afterwards, the pressure and the shear stress experience a sharp increase which is comparable to the one observed during propagation of liquid plugs and receding of air fingers. Few instants after closure, the stresses relax in magnitude down to a stationary state, which is achieved when the plug stops growing and the pressure field

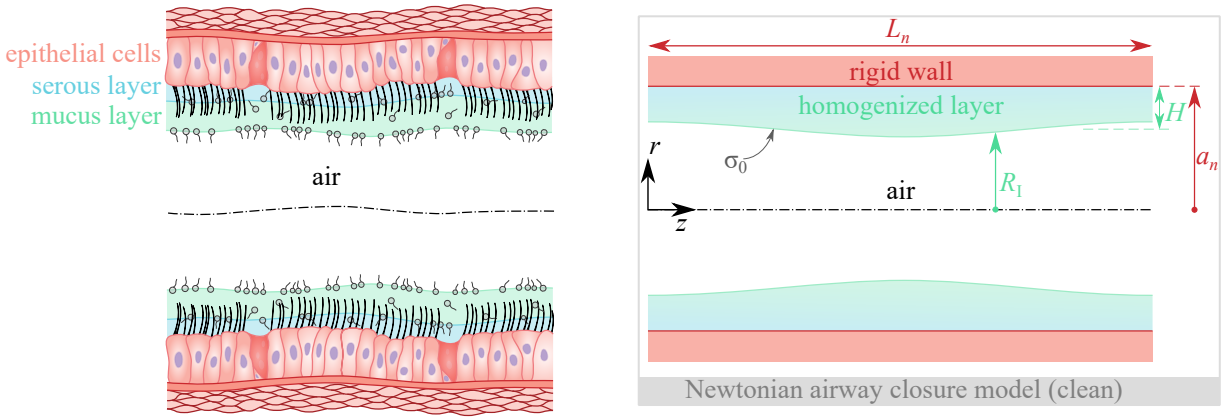

Figure 4.2: Schematic of an airway (left) and the corresponding model (right) for homogenized Newtonian liquid lining a rigid wall without surfactant.

is solely determined by the equilibrium Laplace pressure across the interface.

As it can be seen from fig. 4.3(b), the rapid growth of the shear stress in time, which is associated with the capillary instability, does not experience a maximum at the closure time, but keeps growing even after coalescence, reaches the maximum value at $t = t_m > t_c$, and then relaxes toward the final equilibrium value. The bi-frontal plug growth actually appears to be the most relevant and critical phase for the wall shear stresses, hence it may lead to the severe damage of epithelial cells [371]. This feature can be inferred also by the experimental measurements [372] and further implies the importance for numerical simulations to be able to handle a topological change of the liquid film.

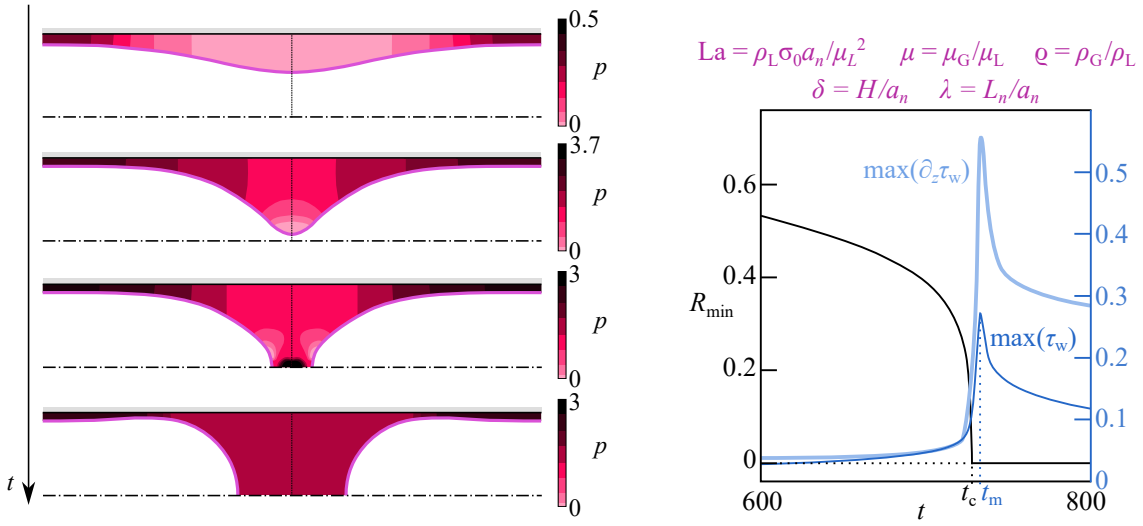

(a) Bifrontal plug growth

(b) Wall shear stress

Figure 4.3: (a) Pressure field in the liquid phase at two pre-coalescence ($t = 600$ and $t = 727$) and two post-coalescence instants ($t = 728$ and $t = 800$). The magenta line denotes the interface location. (b) Minimum of the interface radial location $R_{\min} = \min(R_I)$ (solid black line), maximum wall shear stress τ_w and shear stress gradient $\partial_z \tau_w$ (blue and light blue, respectively). All data refer to La $= 100$, $\mu = 1.5 \times 10^{-3}$, $\varrho = 10^{-3}$, $\lambda = 6$, $\delta = 0.25$ [369].

A second mechanism for pressure gradients at the wall has further been uncovered by [369]. The left panel of fig. 4.4 shows that the maximum wall pressure gradient $|\partial_z p_w|_{\max}$ can experience a monotonically growing trend in time, qualitatively different from the one reported for the shear stress and its gradient (cf. fig. 4.3(b)). The formation of the liquid plug, its bi-frontal growth, the consequent compression of the liquid film on the pipe wall and the propagation of the capillary wave are responsible for this effect. Figure 4.4(b) depicts the time evolution of the interface and the maximum wall pressure gradient for La $= 100$, $\mu = 1.5 \times 10^{-3}$, $\varrho = 10^{-3}$, $\lambda = 6$, $\delta = 0.25$. After the closure event, the bi-frontal plug growth forms a capillary wave on the shoulder of each of the two interface fronts. These waves compress the liquid film against the airway wall and slowly propagate symmetrically in axial direction. The correlation between the capillary ripples and the peaks of $|\partial_z p_w|_{\max}$ provide the evidence that the thin film dynamics is responsible for local pressure gradients that could potentially damage the epithelial cells.

One of the primary focuses of our study is to quantify the stress level exerted on the airway

wall, given its potential implications for epithelial response, which could range from lethal to sub-lethal, as discussed by [373]. While [374] previously speculated on this scenario using a single set of parameters and three initial film thicknesses, it was not until [369] that the actual stress level on cells throughout the entire pre- and post-coalescence process was numerically quantified. In their research, [369] demonstrated that both wall normal and tangential stresses on the cells, along with their gradients, attain maximum values of approximately $\max_{t,z}(|\tau_w|) \approx 250$ dyn cm^{-2} (300 to 600% of the pre-coalescence values), $\max_{t,z}(|\partial_z p_w|) \approx 4.50 \times 10^4$ dyn cm^{-3} and $\max_{t,z}(|\partial_z \tau_w|) \approx 8 \times 10^3$ dyn cm^{-3} for parameters commonly observed in adult lung airways, such as La $= 200$, $\mu = 1.5 \times 10^{-3}$, $\varrho = 10^{-3}$, $\lambda = 6$, and $\delta = 0.20$. These stress levels significantly surpass the thresholds known to severely damage epithelial cells. In fact, according to the findings of [375], cell damage occurs if $\max_{t,z}(|\tau_w|) > 12.9$ dyn cm^{-2}, $\max_{t,z}(|\partial_z \tau_w|) > 2.1 \times 10^3$ dyn cm^{-3}, and $\max_{t,z}(|\partial_z p_w|) > 3.21 \times 10^4$ dyn cm^{-3}. Furthermore, [343] also confirms the potentially lethal effect of wall stresses on epithelial cells, noting that a hazardous condition for cells arises when shear stress exceeds $\max_{t,z}(|\tau_w|) > 98.58$ dyn cm^{-2}. The threshold considered hazardous for epithelial cells is notably less than half of the peak value of tangential stresses predicted by the airway closure model proposed by [369]. In a comparative analysis with experimentally estimated damaging conditions by [372], [374] concluded that while the level of shear stress during the pre-coalescence process might be sufficient to cause cell damage, pressures and gradients fall below experimentally determined threshold values. However, within the airway closure model simulated by [369], it was demonstrated that peaks in wall stresses and their gradients occur during the post-coalescence phase, far surpassing the experimentally established damaging thresholds. Finally, an increase in the initial film thickness H is observed to accelerate the formation of a liquid plug, consistent with predictions by [374, 372]. Furthermore, while tangential and normal wall stresses, along with shear stress gradients, show relatively little sensitivity to δ, the initial film thickness significantly influences the wall pressure gradient, which markedly increases as δ decreases [369]. This phenomenon is attributed to the bi-frontal plug growth resulting from the propagation of the capillary wave, as depicted in the right panel of fig. 4.4, and is indicative of thin-film dynamics near the wall inducing a pressure gradient $\partial_z p_w \sim -\delta \partial_z^3 (1 - R_I/a_n)$ due to Laplace pressure.

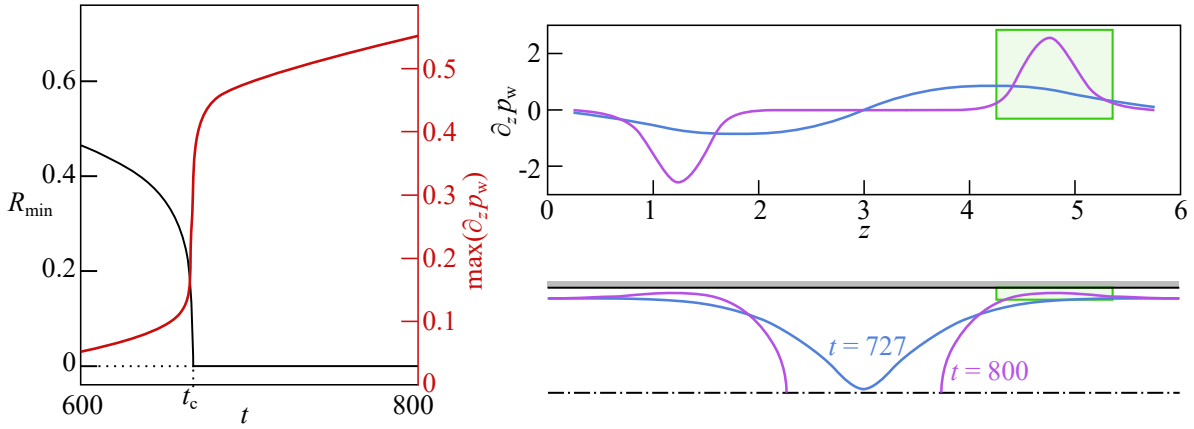

Figure 4.4: (a) Time evolution of the minimum radius of the interface, R_{min} (black line) and the maximum wall pressure gradient $\max(\partial_z p)$ (red). (b) Correlation between the capillary wave (green box for interface at $t = 800$, bottom panel) and the maximum wall pressure gradient (green box, top panel). All data refer to La $= 100$, $\mu = 1.5 \times 10^{-3}$, $\varrho = 10^{-3}$, $\lambda = 6$, $\delta = 0.25$ [369].

4.2.2 Clean two-layers Newtonian airway closure

The model of §4.2.1 is here generalized including two Newtonian liquid layers (see fig. 4.5). A linear stability analysis is performed using the lubrication theory in the thin-film limit. By employing the same methodology of [327] and [330], an evolution equation for the air-mucus interface is derived where curvature effects do not enter the leading order in the lubrication limit $\delta \to 0$. Introducing the local wall-normal coordinate ξ, together with the subscripts 's' for serous layer and 'm' for mucus layer, the momentum and continuity equations yield

$$\frac{\partial p_\mathrm{s}}{\partial z} = \tilde{\mu}\frac{\partial^2 w_\mathrm{s}}{\partial \xi^2}, \qquad \frac{\partial p_\mathrm{m}}{\partial z} = \frac{\partial^2 w_\mathrm{m}}{\partial \xi^2}, \qquad \frac{\partial p_\mathrm{s,m}}{\partial \xi} = 0, \qquad \frac{\partial u_\mathrm{s,m}}{\partial \xi} + \frac{\partial w_\mathrm{s,m}}{\partial z} = 0, \tag{4.1}$$

where $\tilde{\mu} = \mu_\mathrm{s}/\mu_\mathrm{m}$ and $(u,\ w)$ denote the wall-normal and axial velocity components in the thin films coating the airway. The no-slip boundary conditions at the wall require that $(u_\mathrm{s},\ w_\mathrm{s}) = (0,\ 0)$ at $\xi = 0$. The serous-mucus interface at $\eta = 1 - R_\mathrm{II}(z)$ is assumed to neglect the jump in the normal stress since the surface tension between the serous and mucus interface $\sigma_\mathrm{0,s\text{-}m}$ is small [376].

Integrating the continuity equations across the liquid layers and using the kinematic and stress boundary conditions, an evolution equation for the air-mucus interface $\zeta = 1 - R_\mathrm{I}(z)$ yields

$$\begin{aligned}\frac{\partial \zeta}{\partial t} + \frac{1}{3}\frac{\partial}{\partial z}\left[\zeta^3\left(\frac{\partial \zeta}{\partial z} + \frac{\partial^3 \zeta}{\partial z^3}\right)\right] - \left(1-\tilde{\mu}^{-1}\right)\frac{\partial}{\partial z}\left[\eta\zeta^2\left(\frac{\partial \zeta}{\partial z} + \frac{\partial^3 \zeta}{\partial z^3}\right)\right] \\ + \left(1-\tilde{\mu}^{-1}\right)\frac{\partial}{\partial z}\left[\zeta\eta^2\left(\frac{\partial \zeta}{\partial z} + \frac{\partial^3 \zeta}{\partial z^3}\right)\right] - \frac{\left(1-\tilde{\mu}^{-1}\right)}{3}\frac{\partial}{\partial z}\left[\eta^3\left(\frac{\partial \zeta}{\partial z} + \frac{\partial^3 \zeta}{\partial z^3}\right)\right] = 0.\end{aligned} \tag{4.2}$$

The linear stability of the air-mucus interface is investigated by using the method of normal modes. As discussed in §1.3, the ansatz for small perturbations is developed in normal modes as follows

$$\zeta = \delta\left(1 + \epsilon\sum_j \hat{\zeta}_j e^{\gamma_j t + ik_j z}\right), \qquad \eta = \delta_\mathrm{s}\left(1 + \epsilon\sum_j \hat{\eta}_j e^{\gamma_j t + ik_j z}\right), \tag{4.3}$$

where $|\hat{\zeta}_j| = \mathcal{O}(1)$ and $|\eta_j| = \mathcal{O}(1)$ are the coefficients of the Fourier mode expansion (4.3),

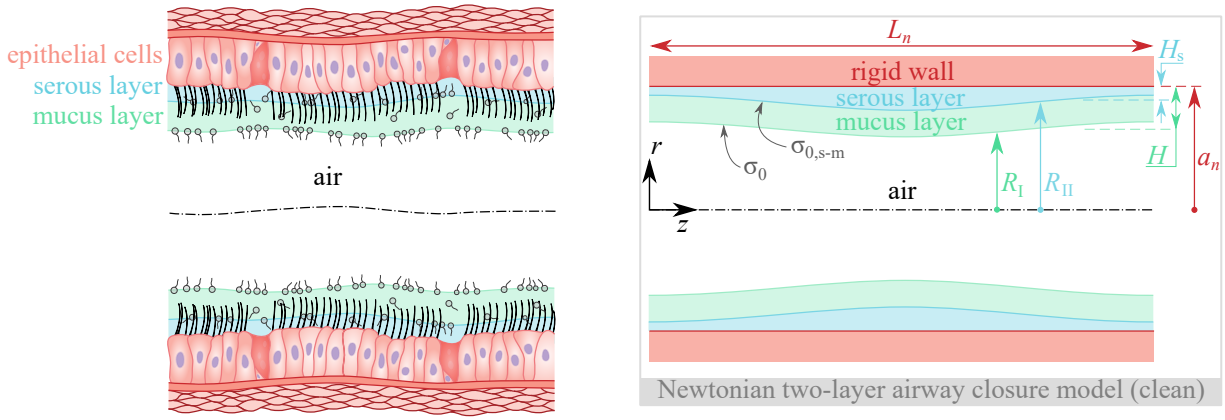

Figure 4.5: Schematic of an airway (left) and the corresponding model (right) for two Newtonian liquid layers lining a rigid wall without surfactant.

k_j is the wave number and γ_j is the growth rate of the small perturbation and $\delta_s = H_s/a_n$. Substituting (4.3) into (4.2) and neglecting the higher order terms, the dispersion relation for the most dangerous growth rate $\check{\gamma}$ corresponding to the most dangerous wavenumber $\check{k}$ is obtained as

$$\check{\gamma} = \frac{1}{3}\check{k}^2\left(1-\check{k}^2\right)\delta^3\left\{1+3\left(\tilde{\mu}^{-1}-1\right)\left[\frac{\delta_\mathrm{s}}{\delta}-\left(\frac{\delta_\mathrm{s}}{\delta}\right)^2+\frac{1}{3}\left(\frac{\delta_\mathrm{s}}{\delta}\right)^3\right]\right\}. \tag{4.4}$$

Upon increasing the total ASL thickness δ, the most-dangerous growth rate $\check{\gamma}$ also increases, thereby promoting airway closure (see fig. 4.6(a)). We stress that the terms in the square bracket on the right-hand side of (4.4) represent additional effects due to the two-layer model, reducing to its one-layer counterpart for $\tilde{\mu} = 1$ or $\delta_\mathrm{s} = 0$. Since $\delta_\mathrm{s} > 0$ and $\tilde{\mu}^{-1} > 1$ for the mucus and the serous layers, the last group of terms in (4.4) is always positive, indicating that the serous layer has a destabilizing effect, facilitating airway closure. This remains true even if the total thickness is kept constant and δ_s is increased (see fig. 4.6(b)). The impact of the serous-to-mucus viscosity ratio $\tilde{\mu}$ is illustrated in fig. 4.6(c), demonstrating a decrease in $\check{\gamma}$ with a decrease in $\tilde{\mu}$. This may seem counter-intuitive, as a less viscous serous layer would be expected to promote airway closure by aiding mucus drainage into the interfacial bulges. However, when plotting the dimensional growth rate $\check{\gamma}^*$, the expected trend is observed (see right panel of fig. 4.6(c)).

By carrying out time-marching simulations, one can remark that running into a Plateau–Rayleigh instability does not necessarily lead to airway closure. The increased resistance of draining the thin liquid film before formation of a liquid plug can saturate the growth rate of the instability up to preventing the closure event. This is depicted in fig. 4.7 for several two-layer thicknesses δ, keeping constant the serous layer thickness to $\delta_\mathrm{s} = 0.05$.

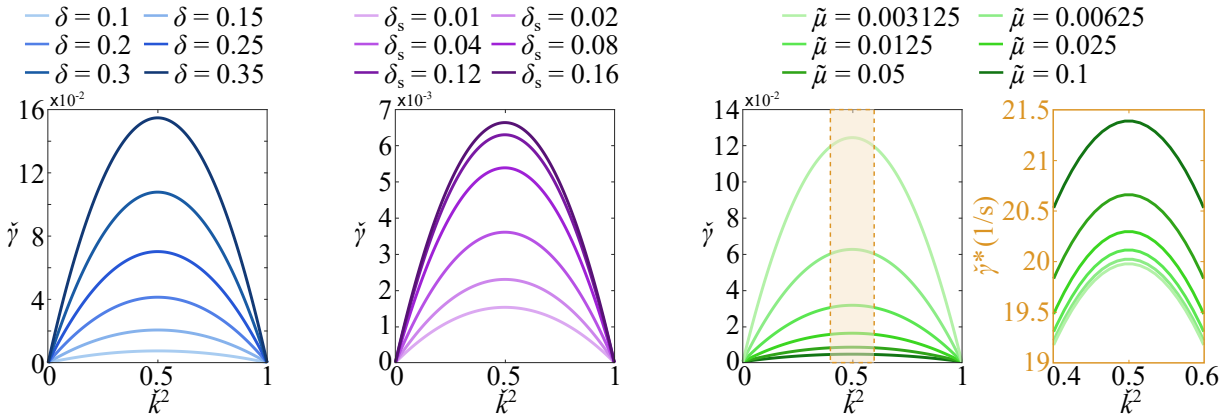

(a) varying δ (b) varying δ_s (c) varying $\tilde{\mu}$

Figure 4.6: Most dangerous growth rate $\check{\gamma}$ plotted against the square of the wave number $\check{k}^2$ upon a variation of: (a) the total non-dimensional airway surface liquid thickness δ with $\tilde{\mu} = 0.1$ and $\delta_\mathrm{s} = 0.05$, (b) the serous layer non-dimensional thickness δ_s with $\tilde{\mu} = 0.1$ and $\delta = 0.20$ and (c) the serous-to-mucus viscosity ratio $\tilde{\mu}$ with $\delta = 0.20$ and $\delta_\mathrm{s} = 0.05$. The inset in (c) shows the dimensional most dangerous growth rate $\check{\gamma}^*$ plotted against $\check{k}^2$. The serous-to-mucus density ratio is defined as $\tilde{\rho} = \rho_\mathrm{s}/\rho_\mathrm{m} = 1$ and the ratio between the mucus–serous layer $\sigma_{0,\text{s-m}}$ and mucus–air layer σ_0 is set to $\tilde{\sigma} = \sigma_{0,\text{s-m}}/\sigma_0 = 0$.

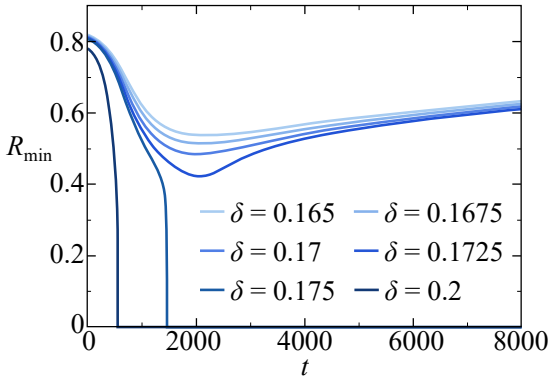

Figure 4.7: Time evolution of the minimum interface radius, $R_{min} = \min(R_I)$, is plotted for $\delta = 0.1650, 0.1675, 0.17, 0.1725, 0.1750$ and 0.2. The serous film thickness is kept constant at $\delta_s = 0.05$. All simulations are performed for La $= 174$, $\lambda = 6$, $\tilde{\mu} = 0.1$, $\tilde{\rho} = 1$, and $\tilde{\sigma} = 0.1$.

The simulations of the whole dynamics also confirm the remarkable speed up of the airway closure predicted by the linear stability analysis for the two-layer model. Quantifying it, by considering the two-layer dynamics can lead to closure up to 6 times faster than the corresponding one-layer case (see fig. 4.8). This means that airway closure may occur far more frequently, hence it can be cumulatively more dangerous that what predicted by the single-layer model. The lower viscosity of the serous layer has however a protective effect on the stresses experienced by the epithelium, as observed by the reduced stress level of the two-layer case (see fig. 4.8).

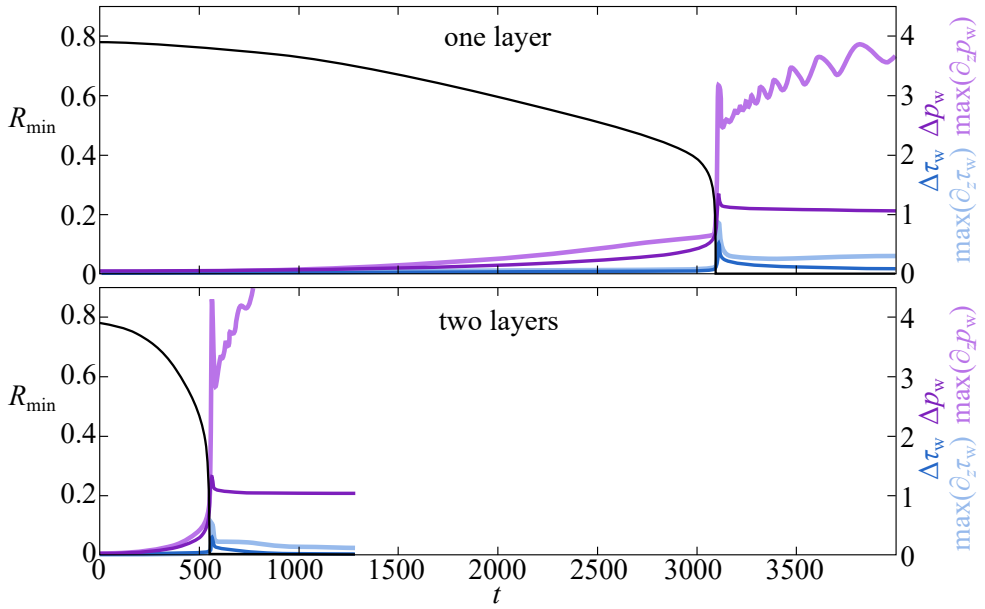

Figure 4.8: Time evolution of the minimum core radius R_{min}, wall pressure excursion $\Delta p_w = \max(p_w)$ - $\min(p_w)$, wall shear stress excursion $\Delta\tau_w = \max(\tau_w)$ - $\min(\tau_w)$, maximum absolute value of the wall pressure gradient $|\partial_z p_w|_{max}$, and maximum absolute value of the wall shear stress gradient $|\partial_z \tau_w|_{max}$ for (a) the one-layer and (b) the two-layer cases. All simulations are carried out for La $= 174$, $\lambda = 6$, and $\delta = 0.2$, while $\delta_s = 0.05$, $\tilde{\mu} = 0.1$, $\tilde{\rho} = 1$, and $\tilde{\sigma} = 0.1$ are used for the two-layer model.

4.2.3 Single-layer Newtonian airway closure with surfactant

Building on the approach aimed to study standalone effects, the single-layer Newtonian model with clean interface is enriched by including surfactant and modeling their dynamics as proposed by [377] (see fig. 4.9). The relevance of a corresponding parametric study is motivated either by pathological conditions corresponding to a surfactant deficiency, or by surfactant replacement therapies commonly in use as medical treatments to favour airway reopening and inhibit successive liquid plug formation.

With an increase in the bulk surfactant concentration C_0, the surface tension σ decreases when averaged along the interface $\langle\sigma\rangle$, resulting in a net decrease of the average local Laplace number $\langle \mathrm{La}\rangle = \mathrm{La}\langle\sigma\rangle/\sigma_0$, where we recall that σ_0 is the surface tension for a clean interface. Since the surfactant is not uniformly distributed, surface tension gradients induce Marangoni stresses. However, for the given parameters, the reduction in average capillary stresses outweighs the impact of Marangoni stresses [366], which are of minor importance for the dynamics of the liquid plug immediately before and after closure. Consequently, as shown in fig. 4.10, increasing C_0 decelerates the Plateau–Rayleigh instability, resulting in a longer closure time t_c. We stress that the relative increase in closure time is highly nonlinear. For instance, with small bulk surfactant concentrations, a five-fold increase in C_0 — from $C_0 = 10^{-5}$ to $C_0 = 5 \times 10^{-5}$ — leads to a relative increase in t_c of approximately 10%. Conversely, for the highest surfactant concentrations considered, a five-fold increase in C_0 — from $C_0 = 10^{-4}$ to $C_0 = 5\times10^{-4}$ — nearly doubles the closure time, resulting in a relative increase in t_c of about 100%. This behavior can be attributed to the nonlinear decrease in surface tension with an increase in interfacial surfactant concentration $\varpi(z)$ (see fig. 4.10).

The impact of the bulk surfactant concentration on wall stresses, however, appears less significant. Monitoring the tangential wall stress excursions, $\Delta\tau_w(t) = \max_z \tau(r=1) - \min_z \tau(r=1)$, fig. 4.10 shows only minor changes in stress peaks for $C_0 \leq 10^{-4}$. Increasing the bulk surfactant concentration to $C_0 = 5 \times 10^{-4}$ reduces the tangential stress peak by approximately 20% compared to $C_0 = 10^{-4}$. The quantitative characterization of this nonlinear process is influenced by the model (see fig. 4.10, [378]). Consistent observations are made for the maximum tangential

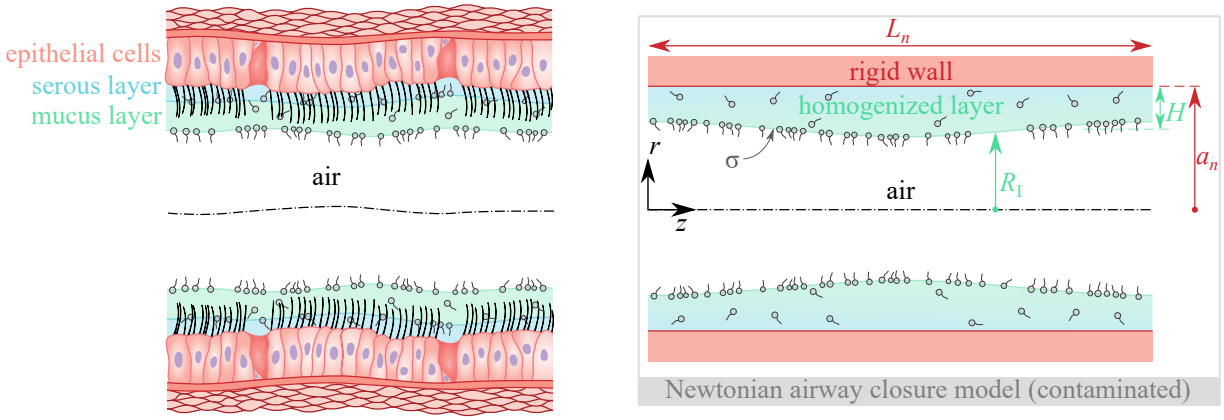

Figure 4.9: Schematic of an airway (left) and the corresponding model (right) for homogenized Newtonian liquid lining a rigid wall with dispersed surfactant.

stress gradients $\max|\partial_z \tau_w|$, while the peak normal wall stress excursions, $\Delta p_w = \max_z p(r = 1) - \min_z p(r = 1)$, are essentially unaffected by C_0 even for the highest bulk surfactant concentrations considered. A more noticeable impact is demonstrated in fig. 4.10 for the maximum axial wall pressure gradient $\max|\partial_z p(r = 1)|$. This aligns with the observations of [369], who linked the peak of $\max|\partial_z p_w|$ to the capillary wave originating near the wall right after the bi-frontal plug growth, which enlarges the liquid plug. The net decrease in the local Laplace number $\langle La \rangle$ due to the increase in surfactant concentration results in weaker capillary stresses, hence weaker $\max|\partial_z p_w|$.

The same qualitative impact on the airway closure process observed upon an increase of the initial bulk concentration C_0, is also reproduced by an increase of the elasticity number β, while the penetration depth χ, the adsorption and desorption coefficients, K_a and K_d, respectively, and the Schmidt number at the interface and in the bulk, Sc_s and Sc, respectively, have a minor impact on the dynamics of airway closure (see fig. 4.10 for a definition of such non-dimensional groups). These conclusions are robust upon a change of the Laplace number (see [366]).

For pathological cases at the 8th and 9th generation, the order of magnitude of the capillary frequency $\sigma_0/\mu_L a_n$ is 500/s and 1000/s, respectively. Including healthy cases for the 10th and 11th generation, the capillary frequency increases to 2000/s and 5000/s, respectively, for healthy individuals, and to 3000/s and 8500/s for pathological patients [366]. Considering that for healthy

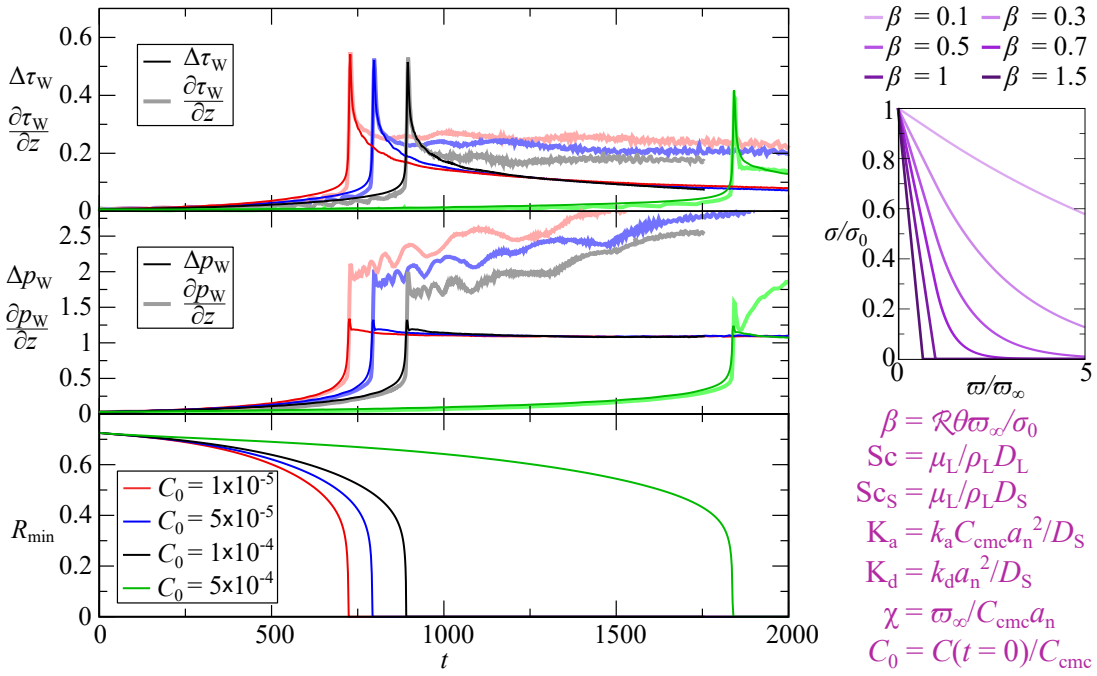

Figure 4.10: Effect of the bulk surfactant concentration. Bottom: $R_I(t)$ (solid line). Middle: $\Delta p_w(t)$ (light-colored bold line) and $\max|\partial_z p(r = 1)|$ (dark-colored line). Top: $\Delta\tau_w(t)$ (light-colored bold line) and $\max|\partial_z \tau(r = 1)|$ (dark-colored line). The bulk surfactant concentration C_0 is varied between 10^{-5} and 5×10^{-4}, whereas the other simulation parameters are fixed: La = 100, $\beta = 0.7$, Sc = 10, $Sc_s = 100$, $K_a = 10^4$, $K_d = 10^2$, $\chi = 0.01$, and $\delta = 0.25$. The surface surfactant concentration is ϖ, ϖ_∞ its asymptotic matching level for σ/σ_0 passing from a linear to an exponential law in ϖ/ϖ_∞ at $\varpi/\varpi_\infty = 1$, k_a and k_d are the adsorption and desorption coefficients, D_L and D_S the surfactant diffusions in the bulk and the surface, $\mathcal{R}$ is the ideal gas constant, and C_{cmc} the critical micelle concentration [366, 379].

patients the respiratory frequency is about 20/min (one breath every 3 seconds, [380]), the airway closure predicted in our model is considered physiologically relevant if t_c occurs before $t_c \lesssim 3 \times 2000 = 6000$ capillary time units at the 10th generation, and $t_c \lesssim 3 \times 5000 = 15000$ capillary time units at the 11th generation. The respiratory rate increases up to about 30/min for pathological conditions (one breath every 2 seconds, [380]), hence the critical time threshold for pathological cases reduces to $t_c \lesssim 2 \times 500 = 1000$ capillary time units at the 8th generation, $t_c \lesssim 2 \times 1000 = 2000$ at the 9th generation, while it increases to $t_c \lesssim 2 \times 3000 = 6000$ at the 10th generation, and $t_c \lesssim 2 \times 8500 = 17000$ capillary time units at the 11th generation.

The stability diagram for the airway closure model is presented in light of the previous considerations regarding the timescales of the corresponding biological system. We define as *physiologically unstable* all conditions leading to the formation of a liquid plug *within a breathing cycle*. If the liquid plug does not form (stable) or forms too late (finite-time stable), we assume that airway closure would not occur in a corresponding physiological system, and we denote such cases as *physiologically stable*.

The stability threshold for airway closure is examined using parameters La $= 100$, $\beta = 0.7$, Sc $= 10$, Sc$_s = 100$, $K_a = 10^4$, $K_d = 10^2$, $\chi = 0.01$, $C_0 \in [0,\ 5 \times 10^{-4}]$, and $\delta \in [0.125,\ 0.25]$. A summary of the physiological stability conditions is illustrated in three diagrams in fig. 4.11. In the case of fast-breathing pathological patients, occlusion of distal airways may occur at generation 8 for a critical average thickness $\delta_c \in [0.2,\ 0.225]$ if $C_0 \in [0,\ 10^{-4}]$ (see fig. 4.11(a)). Increasing the initial surfactant concentration to $C_0 = 5 \times 10^{-4}$ in such scenarios induces an unconditionally stable condition, preventing airway closure for $\delta \in [0.2,\ 0.225]$ and shifting the critical film thickness to $\delta_c \in [0.225,\ 0.25]$.

When examining 9th-generation bronchioles of fast-breathing pathological patients (see fig. 4.11(b)), the physiologically critical average thickness decreases to $\delta_c \in [0.175,\ 0.2]$ if $C_0 \in [0,\ 5 \times 10^{-5}]$ and $\delta_c \in [0.2,\ 0.225]$ if $C_0 \in [10^{-5},\ 5 \times 10^{-5}]$. This reduction in system stability is understandable as higher generations correspond to smaller bronchioles, where capillary forces become more dominant. Consequently, the Plateau–Rayleigh instability originating airway closure more frequently leads to airway occlusion in distal airways compared to lower-generation bronchioles. This loss of physiological stability is further evident in fig. 4.11(c), where 10th and higher generations are considered. Here, the critical average film thickness decreases to $\delta_c \in [0.175,\ 0.2]$ if $C_0 \in [0,\ 10^{-4}]$ and $\delta_c \in [0.2,\ 0.225]$ if C_0 is 5×10^{-5}. It is important to note that these critical values are notably higher than the value predicted by [328], i.e., $\delta_c = 0.12$.

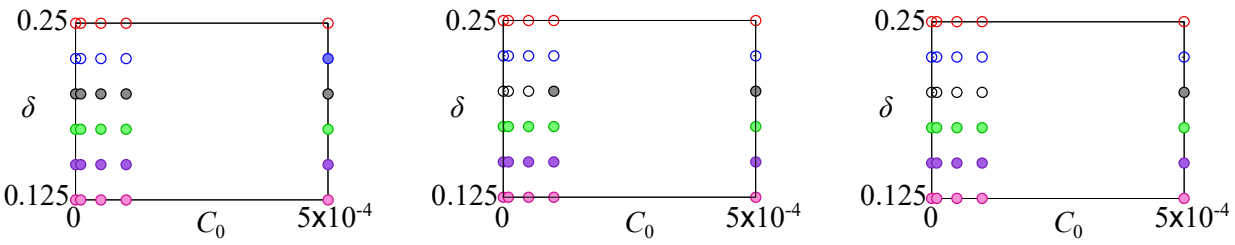

(a) 8-th generation (b) 9-th generation (c) 10-th generation

Figure 4.11: Physiological stability diagram for bronchioles of: (a) 8th generation in fast-breathing pathological patients, (b) 9th generation in fast-breathing pathological patients, and (c) 10th and higher generations in all patients: • = *physiologically* stable, ∘ = *physiologically* unstable.

4.2.4 Clean single-layer viscoelastic airway closure

A further variation on the Newtonian single-layer case takes into account the viscoelastic properties of mucus. The homogenized layer is modeled by using the Oldroyd-B constitutive law, whose extra stresses $\boldsymbol{S}$ are due to the feedback of the polymers on the solvent matrix at molecular scale. A corresponding schematic is depicted in fig. 4.12. The comparison between the viscoelastic (solid lines) and the Newtonian (dashed lines) airway closure models is presented in fig. 4.13 in terms of the excursion of the wall shear stress as a function of time, $\Delta\tau_{\mathrm{w}}(t) = \max_z \tau(r=1) - \min_z \tau(r=1)$. All the results in fig. 4.13 are obtained for $\mu = 1.5\times10^{-4}$, $\varrho = 10^{-3}$, $\epsilon = 0.25$, $\lambda = 6$ and three different Laplace numbers, i.e. La = 200, 20, and 2. For the Oldroyd-B model, the solvent-to-total viscosity ratio $\mu_{\mathrm{S}} = \mu_{\mathrm{L,S}}/\mu_{\mathrm{L}} = 0.5$ and the Weissenberg number $\mathrm{We} = \Lambda\sigma_0/a_n\mu_L = 100$ are used, where $\mu_{\mathrm{L,S}}$ denotes the solvent viscosity, μ_L the total liquid viscosity, and Λ the polymeric relaxation time. Consequently, the polymeric-to-total viscosity ratio $\mu_{\mathrm{P}} = \mu_{\mathrm{L,P}}/\mu_{\mathrm{L}} = 1 - \mu_{\mathrm{S}}$.

For both constitutive models, an increase in the Laplace number leads to a higher peak in shear stress level, rising from approximately $\max(\Delta\tau_{\mathrm{w}}) \approx 0.4$ for La = 2 to $\max(\Delta\tau_{\mathrm{w}}) \approx 0.6$ for La = 200. As discussed by [381], the peak shear stress level at the wall shows little sensitivity to the viscoelastic properties of the fluid. This is due to the fact that the initial peak observed in tangential stress results from the immediate response of the fluid to bi-frontal plug growth. Therefore, the sharp peak in the curves primarily stems from the Newtonian component of the liquid, with extra stresses playing a minor role immediately after coalescence. Further analysis of wall stresses for the Oldroyd-B model, including the impact of We and μ_{S} on the Newtonian component of tangential stress, viscoelastic extra stresses, and pressure, is detailed in [381].

The viscoelasticity also affects airway closure by reducing the closure time by approximately 20%, in line with the theoretical prediction by [367]. However, the most significant role of mucus's viscoelastic properties emerges sometime after the coalescence event. Figure 4.13 illustrates the qualitative disparity between Newtonian and viscoelastic scenarios: In a Newtonian liquid, tangential stresses relax to around $\Delta\tau_{\mathrm{w}} \approx 0.1$ after a rapid transient caused by bi-frontal plug growth. Conversely, when considering viscoelastic effects, the elastic response of the polymeric

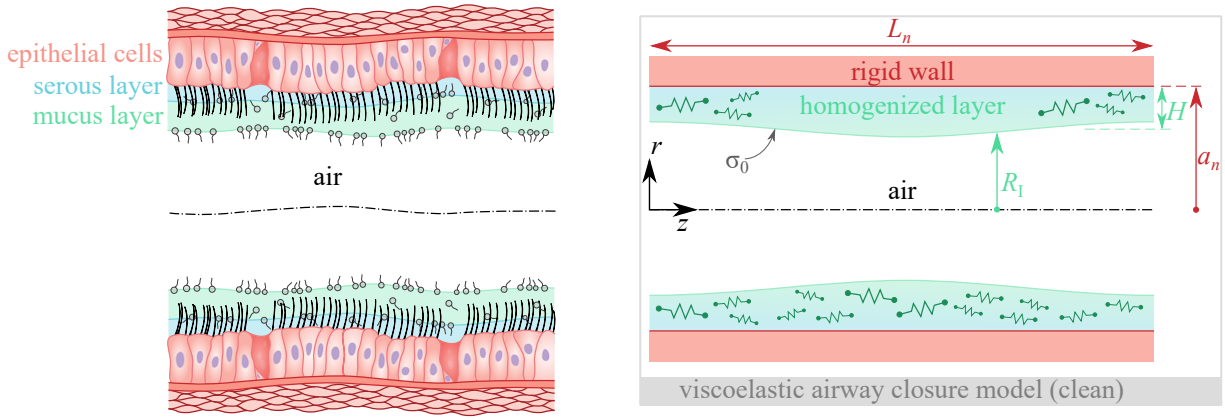

Figure 4.12: Schematic of an airway (left) and the corresponding model (right) for homogenized viscoelastic liquid lining a rigid wall without surfactant.

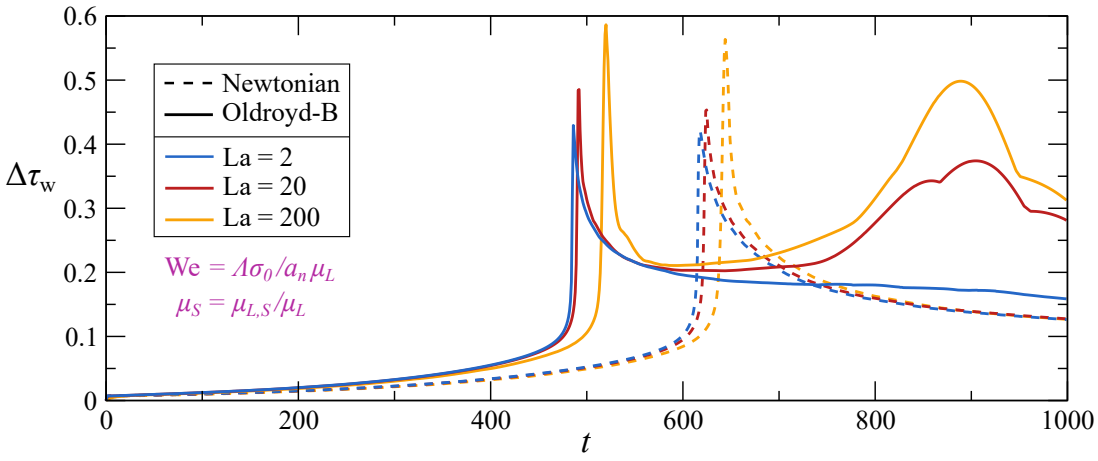

Figure 4.13: Excursion of the tangential stress distribution along the wall, $\Delta\tau_w(t) = \max_z \tau(r = 1) - \min_z \tau(r = 1)$ for $\mu = 1.5 \times 10^{-4}$, $\varrho = 10^{-3}$, $\delta = 0.25$, $\lambda = 6$. Three Laplace numbers are considered: La = 200 (black), 20 (red) and 2 (blue). Two constitutive models for the liquid phase, i.e. the Newtonian (dashed lines) and the Oldroyd-B model (solid lines, $\mu_S = 0.5$ and We = 100), are compared.

phase induces a secondary increase in wall shear stress excursion, potentially reaching the same magnitude as the initial Newtonian peak. This distinct post-coalescence dynamics, both qualitatively and quantitatively, was first reported by [381] and warrants special attention.

The post-coalescence stability properties of the viscoelastic flow are evaluated by examining the excursion of the wall extra stress, ΔS_w. To quantify the growth rate of the elasto-inertial instability, $\Delta S_w(t)$ is fitted using a local exponential function, $\Delta S_w(t) \approx A_0 + A_1 \exp(\check{\gamma} t)$. A least-squares fit is performed along with a pattern recognition algorithm to identify the best match between ΔS_w and the fitting function over the largest time interval with a minimum confidence level of 90%. Three examples are presented in the right panels of fig. 4.14 for $\mu_S = 0.25$, La = 200, and We = 10 (bottom), We = 100 (middle), and We = 1000 (top). The black lines represent the numerical simulation results of ΔS_w, while the thick lines depict the local exponential fit for stable ($\check{\gamma} < 0$, red) or unstable ($\check{\gamma} > 0$, blue) conditions. The exponential growth rates $\check{\gamma}$ are then quantified and plotted against a modified elasticity number $\mathrm{El}_m = \mathrm{We}\sqrt{1-\mu_S}/\mathrm{La}$. An example is shown in the inset of the left panel of fig. 4.14 for La = 200, $\mu_S \in [0.25,\ 0.9]$, and We $\in [5, 2000]$. The neutral conditions (violet markers) $\mathrm{El}_{m,n}$ are determined by finding the zeros of $\check{\gamma}(\mathrm{El}_m)$ at constant La. The neutral stability curve is then approximated using spline interpolation of the three neutral stability points (dashed violet line). As depicted in fig. 4.14, both inertial (La) and elastic ($\mathrm{We}\sqrt{1-\mu_S}$) effects influence the neutral stability curve, and utilizing the modified elasticity number El_m proves effective in characterizing the onset of the elasto-inertial instability.

It is worth noting that the flow oscillations induced by instability are observed across different constitutive models employed for the extra-stress tensor. This is evidenced by viscoelastic models used in studies such as [382] and [383], and further supported by simulations conducted in [381] using the FENE-CR model proposed by [384]. Results indicate that the elasto-inertial instability also manifests in the FENE-CR model for polymer extensibility values that are physically relevant. Thus, it can be concluded that the instability is not an artifact of the viscoelastic model being

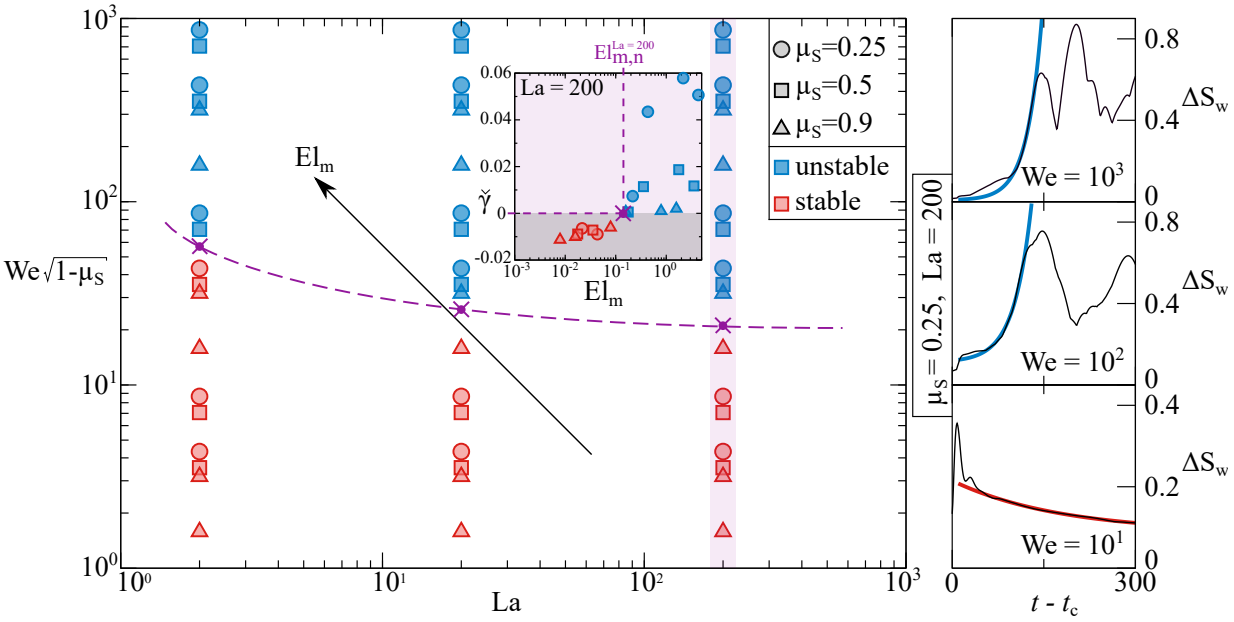

Figure 4.14: Stability diagram for the post-coalescence elasto-inertial instability. The left panel represents the stable (red) and unstable (blue) conditions for $\mu_S = 0.25$ (circles), $\mu_S = 0.5$ (squares) and $\mu_S = 0.9$ (triangles). The violet markers denote the neutral conditions extrapolated in terms of the modified elastic parameter El_m. An example of such an extrapolation is reported in the inset for La = 200. The dashed violet line denotes the neutral stability curve approximated by spline interpolation of the three neutral stability points (violet markers). The three right panel shows the local exponential fit $\Delta S_w(t) \approx A_0 + A_1 \exp(\check{\gamma} t)$ for $\mu_S = 0.25$, La = 200 and three Weissenberg numbers, i.e. We = 10 (bottom), We = 100 (middle), and We = 1000 (top). The black lines denote the extra-stress excursion and the thick lines denote the local exponential fit, either for stable ($\check{\gamma} < 0$, red) or unstable ($\check{\gamma} > 0$, blue) conditions.

used. However, it is important to emphasize that when the extensibility of polymers is limited, the elasto-inertial instability is suppressed, underscoring the significance of stretching polymeric chains to support the elastic nature of the instability mechanism [381].

In summary, the Newtonian peak of wall stresses resulting from rapid bi-frontal plug growth shows minimal sensitivity to the viscoelastic parameters of the Oldroyd-B model, including the Weissenberg number We and the solvent-to-total dynamic viscosity ratio μ_S. This emphasizes that bi-frontal plug growth could potentially cause severe damage to epithelial cells, irrespective of mucus's viscoelastic properties. Moreover, under conditions where We, La, We/La, and $\mu_P = 1 - \mu_S$ are sufficiently high, the elastic instability in the viscoelastic fluid generates additional shear stresses, further contributing to epithelial cell damage and inducing ΔS_w of comparable magnitude to that observed during the Newtonian peak. Additionally, these results remain robust concerning the airway aspect ratio. Doubling the periodic domain ($\lambda = 12$) in simulations shows no significant alteration in instability mechanisms or stress peak amplitudes. The only notable difference is a shorter closure time and a corresponding time shift in the elasto-inertial instability when transitioning from $\lambda = 6$ to $\lambda = 12$.

4.2.5 Clean single-layer elastoviscoplastic airway closure

A last variation on the simplest Newtonian model of §4.2.1 is here considered generalizing the viscoelastic constitutive Oldroyd-B model to the elastoviscoplastic (EVP) Saramito-HB model [385] (see schematic depicted in fig. 4.15). The additional non-dimensional groups introduced by the EVP constitutive model are the flow coefficient n and the Bingham number $\mathrm{Bi} = \tau_y a_n/\sigma_0$, where τ_y denotes the yield stress. The Weissenberg number is computed by using the polymeric relaxation time $\Lambda = \mu_{\mathrm{L,P}}/G$, where the polymeric viscosity $\mu_{L,P}$ is defined as $\mu_{L,P} = K\,|\dot{\boldsymbol{\gamma}}|^{1-n}$, $|\dot{\boldsymbol{\gamma}}|$ is a reference strain rate, G denotes the elastic modulus, and K the consistency factor. Table 4.1 shows that healthy, asthma, COPD and CF mucus have significantly different EVP characteristics. Elastic modulus G and yield stress τ_y of COPD and CF mucus samples are almost an order of magnitude larger than those of the healthy and asthma cases. Therefore the yielded zones for healthy and CF mucus are compared in fig. 4.16 during an airway closure process of these cases (see [386] for more details). The determination of unyielded regions employs a criterion based on $\max\left[0, (|\boldsymbol{S}_{\mathrm{d}}| - \mathrm{Bi})\,/\,(\mu_{\mathrm{P}}|\boldsymbol{S}_{\mathrm{d}}|)\right] < 10^{-3}$, where $|\boldsymbol{S}_{\mathrm{d}}|$ is the norm of the non-dimensional deviatoric extra stress.

The comparison is conducted for $\delta = 0.35$ and $\mathrm{La} = 300$, specifically chosen to induce airway closure for CF. In cases where strong elasto-plastic characteristics hinder the growth of capillary instability leading to airway closure, these parameters are crucial. Figure 4.16 shows how yielded and unyielded zones evolve with airway closure. In each figure, the top half of each panel is the healthy case, and the bottom half is the CF case. Air is located at the core of the airway (white

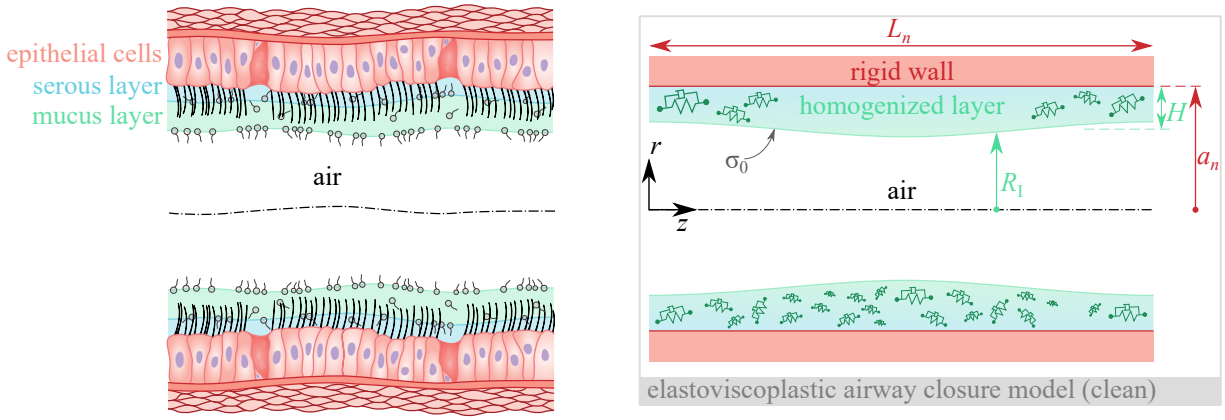

Figure 4.15: Schematic of an airway (left) and the corresponding model (right) for homogenized elastoviscoplastic liquid lining a rigid wall without surfactant.

	Healthy	Asthma	COPD	CF
G (Pa)	0.094	0.105	1.155	2.109
τ_y (Pa)	0.476	1.186	11.77	6.830
n (-)	0.552	0.331	0.752	0.513
K (Pa·s^n)	0.124	1.037	1.056	1.701

Table 4.1: The parameters of the Saramito-HB model reported in [386] and determined by performing a rheological fitting procedure to the experimental measurements of [339].

in fig. 4.16), while yielded and unyielded zones in the EVP liquid layer are depicted by light-green and light-blue colors, respectively. Snapshots are taken to show how yielded zones evolve with the deformation of the air-liquid interface (magenta), so there are three snapshots before and three after the closure event for comparing healthy and CF conditions. As the rheological parameters result in twice smaller We for CF mucus than healthy mucus, the smaller We of CF mucus explains the difference between the non-dimensional closure times Δt_c of these cases due to increased stiffness of the mucus as a result of viscoelastic net effects (see §4.2.4). Furthermore, the order-of-magnitude-larger Bi of CF mucus induces smaller yielded zones, located at the bulge tip and just behind the shoulder, since shear stresses are larger in these regions.

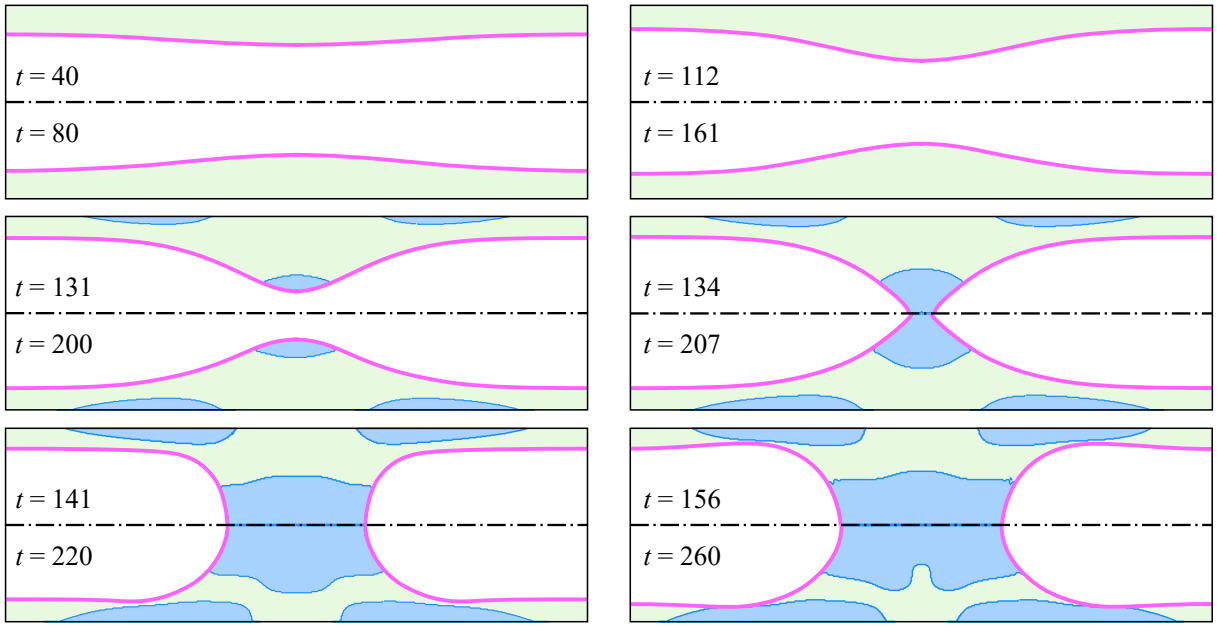

Figure 4.16: Comparison of yield zones between healthy (top half of each panel) and CF (bottom half of each panel) mucus for $\lambda = 6$, $\delta = 0.35$ and La $= 300$. The other non-dimensional parameters for the healthy case are $n = 0.552$, We $= 203.8$ and Bi $= 3.967 \times 10^{-3}$, while for cystic fibrosis they yield $n = 0.513$, We $= 87.26$ and Bi $= 5.692 \times 10^{-2}$. Air is embedded at the core (white) of the interface (magenta). Yielded and unyielded regions of the liquid layer represented by light-green and light-blue, respectively. For EVP parameters of the liquid layer refer to table 4.1.

Figure 4.17 illustrates a comparison of various rheological conditions for mucus. The excursion of tangential wall stress is analyzed by decomposing it into its Newtonian and extra stress components. In cases with lower elastoviscoplastic character, such as healthy and asthma, the contribution of extra stress to the total $\Delta\tau_w$ is minimal. However, for COPD mucus, the initial peak increases by nearly 30% due to the heightened contribution of extra stress to the total tangential stress excursion on the wall. This suggests that in highly EVP mucus, stress peaks may not solely result from the Newtonian contribution but also from the extra stress component. Additionally, the extra stress continues to grow as the Newtonian component relaxes post-closure. Notably, for COPD closure, extra stress persists after closure, reaching magnitudes comparable to the Newtonian peak. This implies that highly EVP mucus continuously damages cells on

the respiratory wall, in contrast to the Newtonian case where stresses relax to lower levels after reaching their peaks. For a broader understanding of the Saramito model, [348] examined the impact of residual stress and kinematic hardening on the closure problem. A summary of the difference in airway closure time predicted by the two rheological models is presented in fig. 4.18.

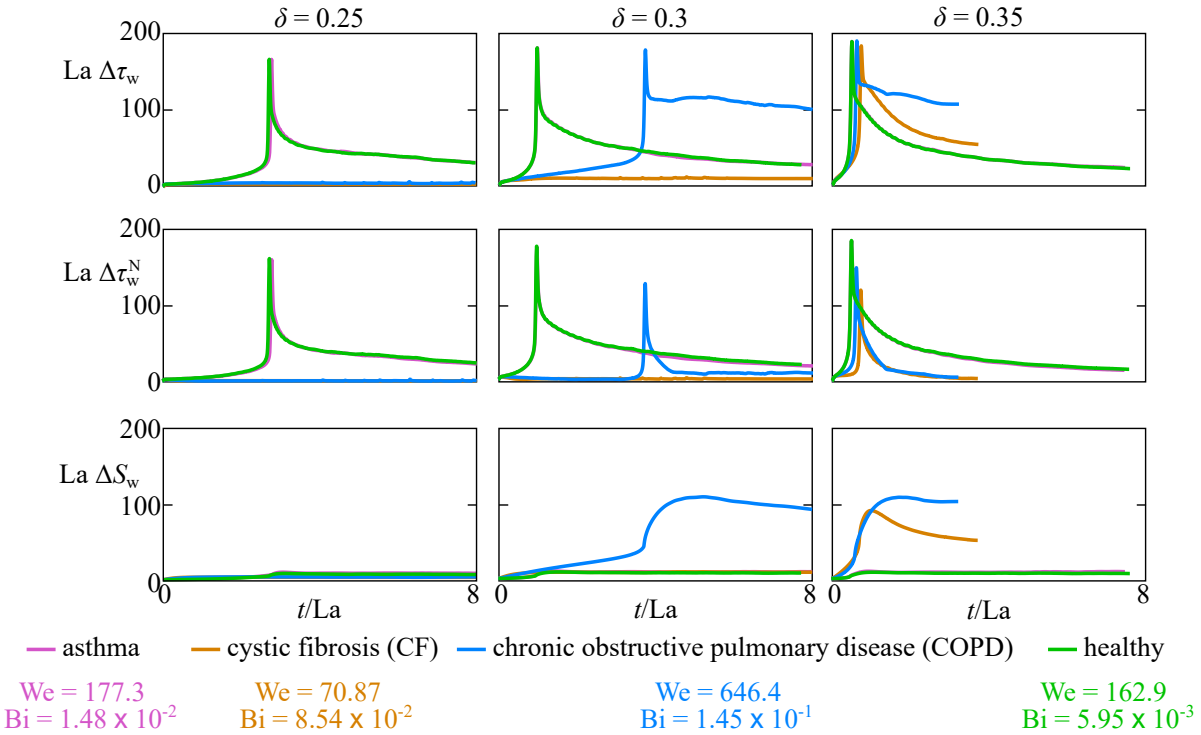

Figure 4.17: Evolution of wall tangential stress excursion, $\Delta\tau_w$ = max(τ_w) - min(τ_w), which consists of Newtonian ($\Delta\tau^N$) and extra-stress (ΔS) components, for La = 200 and δ = 0.25 (top), δ = 0.30 (middle), and δ = 0.35 (bottom). Note that the non-dimensional time, t, is divided by La to eliminate the effect of surface tension, σ_0, on the time scaling for a better interpretation of the results. Stess excursions are also multiplied by La for the same purpose.

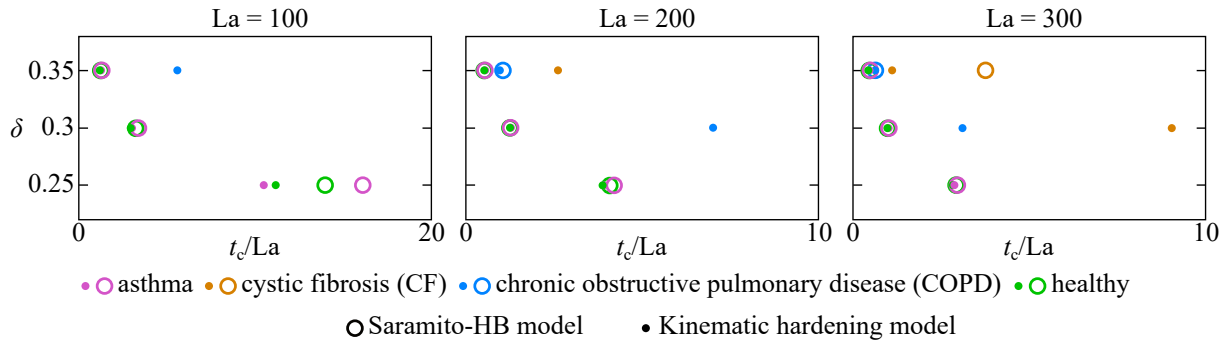

Figure 4.18: Closure time for the Saramito-HB model (○) and the kinematic hardening model (●) for three Laplace numbers and three average film thicknesses. The four rheologies of mucus corresponding to asthma (pink), CF (orange), COPD (blue), and healthy (green) conditions are depicted.

4.3 Summary and conclusions

The range of scales to deal with when simulating human lungs, as well as their solid and fluid mechanics complexity, do not allow for a direct simulation of the whole respiratory tree. Not even simulating a single bronchiole including three dimensional effects, two-layer liquid lining, non-Newtonian rheology, surfactant, realistic wall model, and fluid structure interactions has yet been done. In this chapter several efforts have been reported to build upon standalone effects capable of guiding the phenomenological understanding of airway closure in distal airways, focusing on the sole fluid mechanical aspects.

By studying a single-liquid-layer clean Newtonian model (see §4.2.1), it results that the capillary instability that leads to a fluid-mechanically-driven airway closure carries two sources of mechanical stresses on the epithelium: (i) the tangential and normal stresses produced by the sudden topological change termed bifrontal-plug growth, and (ii) the normal stress gradients due to the capillary wave propagation in the thin film during the post-coalescence phase.

The generalization of this model to a two-liquid lining, yet clean and Newtonian (see §4.2.2), has demonstrated the protective effect of the serous layer by an increase of the critical film thickness needed to induce airway closure. On the other hand, the presence of the serous layer is also associated to a detrimental effect on the characteristic time of closure, which can speed up the airway occlusion event up of a factor six due to an enhanced drainage of the thin mucus film.

Upon the introduction of surfactant (see §4.2.3), we showed that the Newtonian dynamics does not undergo remarkable qualitative changes. A small surfactant concentration can however significantly postpone the closure and reduce the wall stresses, hence the damage of the epithelium. On the other hand, whenever non-Newtonian effects are considered (see §4.2.4), a secondary instability of elasto-inertial nature is robustly predicted by multiple viscoelastic models. This can induce a significant source of post-coalescence stresses on the airway walls. Such an instability seems confirmed by extending the rheological model to elastoviscoplastic fluids (see §4.2.5, [386, 348]), however the viscoplastic character of mucus tends to further postpone or even to tame down the secondary instability in some cases.

Our same conceptual approach that wants to build a core understanding by investigating standalone effects in airway closure and reopening has been followed by several authors in the literature. Some of them focused on the fluid-structure interaction that leads to an elasto-capillary closure [368] in which the complex wall dynamics may play a significant role [67]. Others focused either on the effect of surfactant [387, 388, 389], or on the sole viscoelasticy [390, 367] or viscoplasticity [391, 392, 393] of mucus, or even on the effect of the metachronal waves on the mucus transport [394, 395]. Most of such investigations are carried out numerically or by employing thin film approximations that have been proven successful to predict the Plateau–Rayleigh instability for $\delta = \mathcal{O}(0.1)$. As reported in the literature for viscoplastic mucus properties in the presence of surfactant [396], and for the interaction of flow on a viscoelastic/Newtonian mucus/serous bi-layer model [397], non-linear interactions can trigger unexpected phenomena, which leads to conclude that the standalone approach requires robustness tests to the inherent superposition assumption.

Chapter 5

Research Vision

Summary

Five avenues for future research in multiscale flows with well-separated length scales are discussed, ranging from (i) active to (ii) passive flow control, (iii) cavitation near a solid boundary, (iv) small particles in elastic turbulence and (v) multiphysics respiratory flows. The corresponding research vision is shaped by combining theory, numerical simulations, machine-learning, reduced-order models and scale-matching approaches. Finally, a brief conclusion is aimed at summarizing the achievements, perspectives and limits of the approach proposed in this manuscript for dealing with flows characterized by well-separated length scales.

Contents

5.1 Introduction

Multiscale systems with two or more well-separated length scales can lead to striking phenomena, as demonstrated for the illustrative examples of (i) particle-laden flows at small and moderate Reynolds numbers in §2, (ii) instabilities and control in turbomachinery in §3, and (iii) airway closure in human lungs in §4. Identifying leading-order effects and achieving a corresponding matching between the length scales that dominate the considered phenomenon is an essential part of the understanding of such systems and can further lead to the determination of an approximation capable of predicting the critical features of the dynamics within a satisfactory degree of accuracy.

Except for a few cases, some of which already discussed in this manuscript, modeling the multiscale systems of interest in this work cannot always be achieved employing solely theoretical approaches such as asymptotic expansions. A sophisticated combination of asymptotic theory, numerical simulations, heuristic modeling, and machine learning is therefore at the core of the research vision presented in chapter. Five research problems will be discussed, in which most if not all of the aforementioned methods of investigations will be put in place to tackle the challenges due to well-separated length scales.

The rationale followed to combine theoretical, numerical, model reduction and machine learning approaches is as follows:

- Numerical simulations of a part of the system or a limited range of scales provides the main prediction tool where asymptotics, machine learning, and reduced-order modeling shall be embedded.
- Asymptotic theory forms the basis for understanding system behavior as length scales (and control parameters, in general) approach extremes. The emphasis is on extracting leading-order effects at different scales to reveal essential information governing large-scale dynamics. Alternatively, asymptotic-inspired heuristic models are proposed.
- To bridge scale gaps and enhance asymptotic/heuristic models accuracy, machine learning algorithms are employed. These algorithms will be used to learn relationships between variables at different scales, ensuring compatibility between asymptotic/heuristic approximations and facilitating scale matching consistency.
- Considering computational complexity, ad-hoc reduced order modeling is introduced to simplify representations. This involves leveraging insights by asymptotic theory and feeding the corresponding asymptotic physics into machine learning tools to create accurate reduced-order models, significantly limiting the computational demand. Moreover, experimental measurements can be used to further supply data to the machine learning algorithms.

In the following sections we will discuss how this strategy will shape the research vision for dealing with a handful of research topics, i.e.: (i) active control in axial compressors in §5.2, (ii) mixing and passive flow control by weakly-porous grids in §5.3, (iii) bubble cavitation near a wall in §5.4, (iv) finite-size coherent structures in elastic turbulence in §5.5, and (v) multiphysics in pulmonary flows in §5.6.

5.2 Stability onset and active control in axial compressors

Despite the effectiveness of air jets for active flow control, devising efficient and tailored control strategies remains a challenge. A significant factor contributing to this challenge is the absence of efficient and precise predictive models for control design. To address this limitation, a common approach is to employ *surrogate models*. These models, constructed from data, can effectively approximate the relationship between input parameters and the output of a given process. Examples of surrogate models encompass the response surface methodology [398], Kriging (also referred to as Gaussian process regression [399]), and artificial neural networks [400]. Leveraging such surrogate models enables the handling of local optimization using gradient-based techniques or global optimization employing methods such as the Nelder-Mead's simplex method [401] or genetic algorithms [402]. Within turbomachinery, surrogate models find applications in various domains including aerodynamic design optimization [400], flow modeling [403], performance predictions [404], and flow control strategies [405], among others [406].

In the domain of flow control, data-driven techniques have gained increasing attention [407, 408]. Two prominent avenues include evolutionary algorithms [402, 409, 410, 411] and deep reinforcement learning (DRL) [412, 413, 414, 415, 416]. Deep reinforcement learning relies on *deep neural networks* to approximate the optimal state-action combination through repeated interactions with the experimental or numerical environment. Conversely, genetic algorithms draw inspiration from natural selection and genetic principles to iteratively evolve a population of potential control strategies. Experimental applications of evolutionary algorithms include optimizing the control parameters of dielectric barrier discharge actuators for managing flow separation downstream of a backward-facing step [417]. Similarly, genetic algorithms have been integrated with artificial neural networks to optimize parameters of suction/blowing strategies for controlling separation over the SD7003 airfoil [418]. For a comprehensive overview, interested readers can refer to [408, 419] or the comprehensive book on *machine learning control* [420].

In a recent study, [421] successfully trained a shallow neural network to capture the relationship between the control parameters of the compressor and the active control system in CME2 (see §3.3.3) and two performance indices that characterize the effectiveness of the control strategy in terms of the margins in the flow rate and the total pressure ratio between the nominal and the critical operating points. The first performance index is the *power balance* (PB):

$$\mathrm{PB} = \left[\frac{(Q_{\mathrm{s,b}} + Q_{\mathrm{inj}}) \times p_{\mathrm{tt,c}}}{\rho_{\mathrm{c}}} - \frac{Q_{\mathrm{s,b}} \times p_{\mathrm{tt,b}}}{\rho_{\mathrm{b}}}\right] \times \frac{100}{P_{\mathrm{nom}}}, \tag{5.1}$$

where $Q_{\mathrm{s,b}}$ and Q_{inj} are the flow rate in the baseline configuration and the flow rate injected by the actuators, respectively, $p_{\mathrm{tt,b}}$ and $p_{\mathrm{tt,c}}$ are the total-to-total pressure raise in the baseline and controlled configurations, respectively, ρ_{b} and ρ_{c} are the fluid density in the two configurations, and P_{nom} is the nominal power of the compressor. The second performance index is the *surge margin improvement* (SMI) defined as follows:

$$\mathrm{SMI} = \frac{\mathrm{SM_c} - \mathrm{SM_b}}{\mathrm{SM_b}} \times 100, \tag{5.2}$$

where SM_b and SM_c are the surge margins of baseline and controlled configurations, respectively:

$$\mathrm{SM_b} = \left(\frac{p_{\mathrm{tt,b}}}{Q_{\mathrm{s,b}}} \times \frac{Q_{\mathrm{nom}}}{P_{\mathrm{nom}}} - 1 \right) \times 100, \qquad \mathrm{SM_c} = \left(\frac{p_{\mathrm{tt,c}}}{Q_{\mathrm{s,c}}} \times \frac{Q_{\mathrm{nom}}}{P_{\mathrm{nom}}} - 1 \right) \times 100. \tag{5.3}$$

The control parameters include the rotational velocity and three air jets related parameters: the absolute injection angle, the number of injectors pairs, and the absolute injection velocity (see top-right panel of fig. 5.1). Moreover, they employed a genetic algorithm to solve the optimization problem for actual controlling configurations, retrieving the pareto curve for three rotation rates of the CME2 compressor, i.e. $\Omega = 3200\,\mathrm{rpm}$, $4500\,\mathrm{rpm}$ and $6000\,\mathrm{rpm}$ (see fig. 5.1).

Future researches will focus on generalizing such an approach to other axial compressors, such as the Larzac engine [316] in order to test its applicability for transonic compressors. This ongoing research is in continuation with the scope of the ACONIT project [422], for which corresponding data are already available. The current surrogate model, however, does not provide an interpretable framework for understanding the physical limits and potentials of optimal control configurations. Making use of asymptotic approaches will therefore help identifying the mechanisms responsible for the stall inception and the predicted optima. In particular, as recent studies pointed out [323], active flow control has a drastic impact on the performance curve when the tip gap ΔR is comparable to the thickness of the controlling jet δ_{j}, whereas it is of more limited use if ΔR is significantly smaller than δ_{j}. This suggests that two dedicated asymptotic analyses can elucidate on the stall prediction and the corresponding optimal control for $\Delta R/\delta_{\mathrm{j}} = \mathcal{O}(1)$ and $\Delta R/\delta_{\mathrm{j}} = \mathcal{O}(\epsilon)$ for various regimes of applications in terms of compressibility effects, e.g. for $\mathrm{Ma} < 0.3$ and $\mathrm{Ma} \sim 0.8$. Clearly, such considerations must rely on an advancement of the understanding of the spike- and modal-type instability mechanisms.

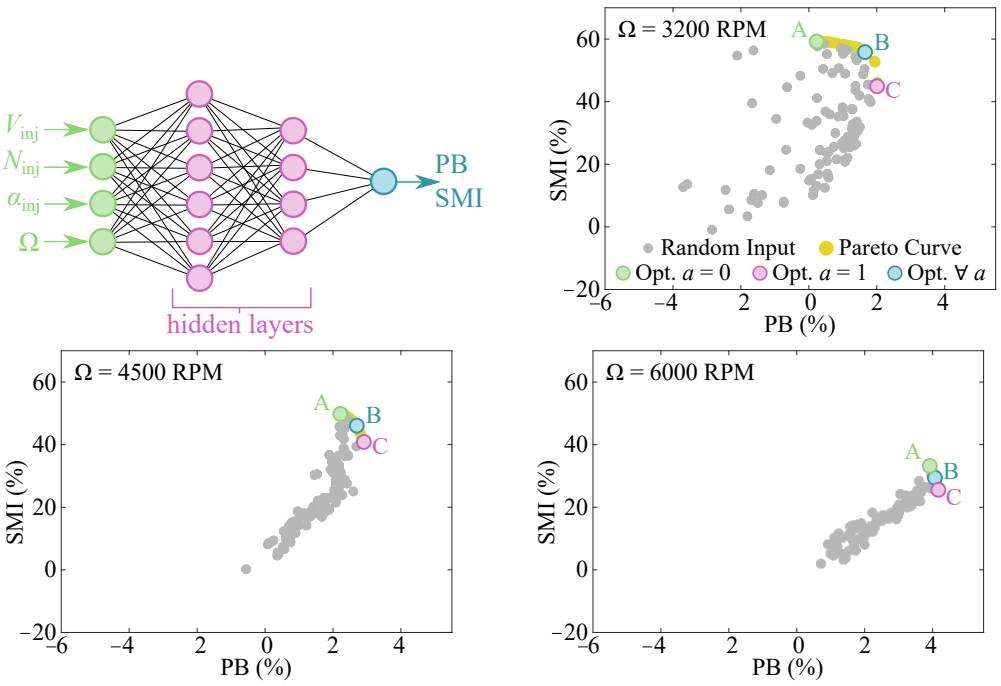

Figure 5.1: Neural network bi-objective optimization of the flow control for the axial compressor CME2 operating at Arts et Métiers, Lille. The inputs to the neural network are denoted in green, while the outputs are listed in blue. Two neural networks are used, one for PB and the other for SMI. The bi-objective optimization is carried out for the following cost function $f = a\ \mathrm{PB} + (a-1)\ \mathrm{SMI}$, where $a \in [0,\ 1]$ is a weighting parameter (see [421] for details).

5.3 Weakly-porous grids for mixing and passive flow control

Grids and screens are normally designed for two distinct targets: (i) enhancing mixing by increasing the production of stirring downstream of the grid or the screen and (ii) controlling the flow by a pressure drop distortion of arbitrary complexity [423]. The former is usually achieved by employing uniform or fractal grids with high porosities that only marginally affect the pressure drop, while the latter involves complicated pressure patterns generated by very low porosities $\Phi_g \lesssim 0.3$ (void-to-whole-volume ratio of the porous domain). We aim to bridge the gap between the two regimes by investigating weakly-porous grids and their potentials to passively control the flow and enhance chaotic mixing not necessarily involving turbulence.

Several modelling approaches have been proposed for estimating the loss coefficient of uniform grids, i.e. the pressure difference normalized with the dynamic pressure $\rho U^2/2$. A first comprehensive review of loss coefficients for wire gauze is reported in [424], who models the screen as an isentropic contraction followed by a sudden enlargement of the streamtube resulting in the loss coefficient $K_{\Delta p} = (1 - \Phi_g)^{-2}$. A similar result has been previously obtained by [425], who models the wire gauze as an ensemble of isolated cylinders placed across the flow, which results in a loss coefficient $K_{\Delta p} = \Phi_g(1 - \Phi_g)^{-2}$. This latter form, with the introduction of an experimental correction factor, is also reported in [426], while a Reynolds number correction was proposed by [427], $K_{\Delta p} = \alpha_{\Phi_g} + \beta_{\Phi_g}(\Phi_g Re)^{-1}$. The first term accounts for the pressure drop due to inertial forces (Forchheimer term) and it dominates for $\mathrm{Re} \gtrsim 2000$, while the second term considers the losses due to shear forces (Darcy term) and it dominates for $\mathrm{Re} \lesssim 200$ [428]. Such relations have been confirmed for square mesh grids or flow normal to a bank of cylindrical tubes, and corresponding generalization to non-uniform grids have been proposed. Further generalizations to include effects of the grid thickness and complex holes patterns for perforated plates are reported in [429, 427, 430].

Despite the experimental confirmations, such models suffer of serious limitations due to the several assumptions that reduce their applicability and the accuracy of their prediction [431, 310]. Such models hold true if the curvature of the grid-deflected streamlines is small, hence they do not apply to recirculating flows and weakly-porous grids. In terms of $K_{\Delta p}$, these models are valid for small loss coefficients. Moreover, they neglect the interaction of turbulent fluctuations and mean flow, as well as the transfer of energy from the mean flow to the fluctuating part of the flow. Moreover, they also neglect the turbulent diffusion in the mixing layer between differently distorted regions generally inducing different turbulence intensities. Finally, they assume that the grid spans over the whole cross section, hence sectorial grids cannot be tackled with such theoretical approaches. This latter limitation is partially overcome by the modelling approach proposed by [432] and extended by [433], who represents the grid as a source density distribution, or by the approach of [434], who computes the mass and momentum balance for each streamtube flowing through a grid pore enforcing conservation of mass and momentum upstream of the grid. Still, such theoretical models (see [435] for a review of classic approach) cannot accurately tackle small porosities $\Phi_g \lesssim 0.3$ [436].

To fill the gap present in the current modeling, we will consider laminar and transitional flows

strongly perturbed by the presence of a weakly-porous rigid grid. A variety of scales is involved in such flows, ranging from the largest convective scales of the incoming flow down to the small grid-pore-diameters scale. Our future researches will develop a first-principle approach to deal with weakly-porous grids by exploiting the separation of scales between the large-scale flow far from the grid and the small-scale flow at the grid's pores' scale. A novel scale-matching approach will be derived by making use of theoretical analysis, numerical simulations, and recent machine learning advancements following the conceptual scheme reported in fig. 5.2.

Such a multi-scale matching algorithm will be derived within the framework of the ANR-JCJC project MultiMatchGrid in order to model and carry out predictive simulations of grid flows. The long-term goal of such an approach is improving the robustness and security of grid-based flow controls and avoiding undesired flow instabilities. The resulting methodology will be spendable by the industry for designing grid-based passive control systems that will allow an efficient and robust design of potentially ground-breaking mixing enhancers. Other potential extensions include turbulence control in pipes and inflow control for turbomachinery. Future generalizations may include the extension of our methodology to deformable and moving grids, with potential applications to typical textile design problems and complex membrane dynamics.

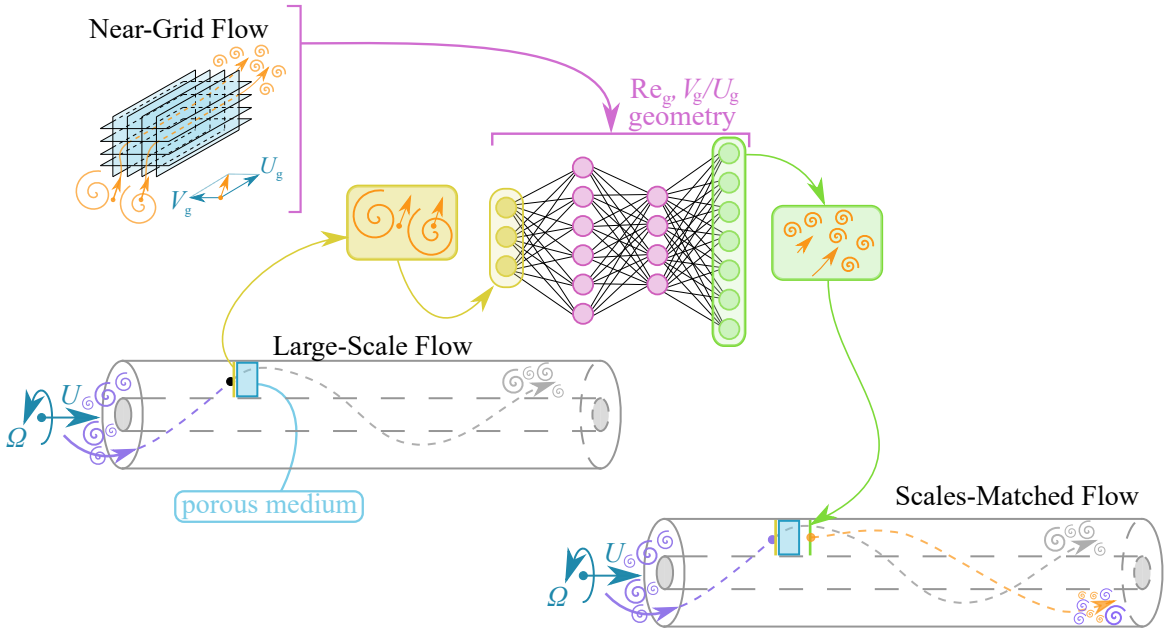

Figure 5.2: Schematic of the first-principle approach to deal with weakly-porous grids by exploiting the separation of scales between the large-scale flow far from the grid and the small-scale flow at the grid's pores' scale. The conceptual workflow of such scale-matching approach makes use of parametric near-grid simulations (top-left figure, *small-scale flow*, orange) employed as database to train a reduced-order model (neural network). The *large-scale flow* (bottom-left figure, violet) is computed by replacing the grid with a porous medium, in order to take into account the leading-order resistance of the grid for the flow far from the grid. The matching of the two well-separated scales of the flow (bottom-right figure) will be carried out by employing the large-scale flow as input (violet) to the machine learning model trained on the pores' scale flow to correct for near-grid leading-order effects (orange). This is expected to provide a leading-order correction of the flow downstream of the grid (orange plus violet).

5.4 Cavitation near a wall

Cavitation is among the most studied phenomena in classic and modern fluid mechanics. It strongly affects the performance of engineering designs such as hydraulic turbomachineries and pumps [437], is used in numerous biomedical applications [438], and it encompasses a complex physics that is fundamentally investigated by studying the behaviour of a cavitating bubble near a wall. In general, the study of collapsing bubbles near a wall is of great interest for industrial applications. In fact, cavitating bubbles occur in diesel injection nozzles [439] and high speed flows past hydrofoils [440], just to mention a few fields of application.

Several theoretical approaches have been proposed in the literature to tackle this problem, based on the different regimes involved in the bubble collapse. Classic approaches make use of asymptotic expansions carried out on interfacial flows. They do not include the full range of scales, but rather rely on asymptotic limits of the Navier–Stokes equations, complemented, where necessary, by moving contact line models or simplified boundary conditions for the fluid slipping along the wall [441, 442, 48]. By means of leading-order analyses, successive-order corrections and asymptotic matching, their ultimate goal is an analytic solution which could describe the flow field in closed form, valid within the asymptotic limit of the small parameters tending to zero [37]. It is not always possible to find a closed-form solution to the asymptotic problem, however, asymptotic analyses that manage to characterize the correct scaling of various non-dimensional groups involved in the problem (Reynolds, Prandtl, Bond number, etc.) provide a great contributions to the understanding of the physics, as well as a reduced-order differential problem which can then be more easily tackled by numerical simulations [45, 443].

Rather than solving the asymptotic problems, most of the numerical investigations focus on the discretization of the Navier–Stokes system. The majority of them maintains the assumption of moving contact line models or relies on simplified slip conditions tuned to experimental measurements [444]. This approach has the advantage of not being limited to considering asymptotically small parameters, and can enter in regimes in which several different effects are of comparable importance. Phenomena including the whole complexity of the continuum scales can be studied by numerical simulations which employ the Navier–Stokes system. Numerical techniques such as adaptive time-stepping and numerical mesh refining [445], multigrid methods [446] and chimera meshes [447] lead to expensive simulations that are incompatible with the detailed flow characterization pursued for large parametric spaces.

In our on-going researches, two types of scales are currently considered for the cavitation problem of a simple bubble near a wall, and each of them is tackled, at best, by one of the two approaches presented below:

- the large-scale flow that involves the whole bubble dynamics far from the wall should be solved numerically by discretizing the Navier–Stokes system or characterized experimentally (see two leftmost panels of fig. 5.3);
- the small-scale flow that tackles the near-wall region can enjoy the simplification provided by asymptotic expansions that analytically solve or at least reduce the Navier–Stokes system to a simplified set of leading-order equations (thin film approximation, see right panel of fig. 5.3).

It is therefore natural to exploit both these approaches and match them across the boundaries between large and small scales (see dashed box in fig. 5.3). Fundamental reference small-scale problems will thereafter be solved numerically or analytically. The study of the matching regimes of our flows is a major focus of our future researches, where scaling arguments will provide the theoretical justification to simplify the flow whenever some or all the required non-dimensional parameters (Ma, Re, H/R, ...) are small enough. For instance, if we focus on a subdomain very close to a wall, the characteristic length scale H of such subdomain is given by the distance from the wall at which the matching condition is applied. Hence, close enough to the wall, i.e. for $H \ll R$, diffusive effects dominate. If also the reference velocity given by the matching conditions is low due to the presence of the wall, i.e. $\mathrm{Ma} \ll 1$, also the compressibility of the flow can be neglected. This is just one of the possible scenarios considered in such a matching problem, which will then benefit of analytic solutions and asymptotic models defined in such small-scale subdomains.

Further research will focus on a thorough characterization of the kinematic template of the flow [448] for the collapsing bubble problem. Most of the in-depth analysis carried out so far about bubbles collapsing near a wall is provided in the Eulerian reference frame [449]. Major attention is paid to the measurement of pressure and temperature inside the bubble [450, 451], and relatively little attention is paid on the effect of mixing and material transport. It is however clear that the convective transport of small particles, eventually resulting from cavitation erosion, is best understood by characterizing the kinematic template of the flow. Owing to the compressible mass conservation equation, sinks and sources play a major role in the flow topology, however, whenever the phase transition is considered, also incompressible flows can admit them. Moreover the interaction of transport barriers with the shock waves which can occur inside the cavitating bubble is still a largely unexplored field despite its important implications on the cavitation erosion.

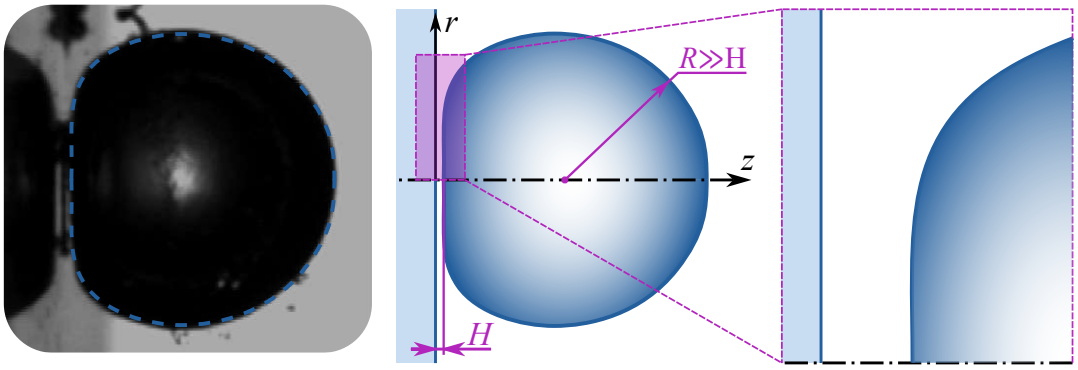

Figure 5.3: Experimental visualization of a cavitation bubble near a wall (left). The interface is fitted with the axisymmetric function $(z-a_1)^2 \times (1+a_2/z^{a_3}) + r^2 - a_4^2 = 0$, where z and r are the axial and radial coordinates, while a_i for $i = 1,\ 2,\ 3,\ 4$ are fitting coefficients. The problem is schematically reproduced (middle), where two well-separated length scales are identified, i.e. the characteristic radius of the bubble R and the lubrication gap H between the bubble interface and the wall. A blow up of the problem near the wall is depicted in the inset on the right.

5.5 Finite-Size Coherent Structures in elastic turbulence

The mechanism at the core of elastic turbulence (ET) relies on the occurrence of elastic instabilities caused by the interplay between the elastic properties of the suspension, its macroscopic viscosity, and the bulk force due to pressure gradients. Such instabilities are controlled by the Weissenberg number $\mathrm{We} = |\dot{\gamma}|\Lambda$, which is the product of a characteristic rate of deformation in the flow $|\dot{\gamma}|$ and the largest polymer relaxation time Λ. In curvilinear shear flow, such as Couette flow between rotating cylinders, normal stress difference creates a volume force acting on the fluid in the direction of the radius of curvature, known as *hoop stress*, which is responsible for elastic instability. The idea that an elastic instability could occur in Couette flow was first proposed by [452] and later confirmed through experimentation by [453]. This instability has also been studied extensively in other curvilinear geometries, as the streamline curvature is a required feature to initiate the hoop stress positive-feedback loop.

The study of ET characterized by irregular flow patterns at Weissenberg numbers largely above the threshold for purely elastic instability, was conducted in various flow geometries such as Taylor–Couette flow between cylinders, swirling flow between two disks, and flow in a curvilinear channel. It was observed that in dilute polymer solutions, at $\mathrm{We} \gg 1$ and $\mathrm{Re} \ll 1$, a chaotic flow similar to inertial turbulence could be excited. This was first observed in both Taylor-Couette and von Kármán swirling flows [454] and was characterized by an increase in flow resistance, algebraic decay of velocity power spectra across a wide range of scales, and more efficient mixing than in regular (laminar) flow. These properties are similar to those of inertial turbulence, and have been observed at polymer concentrations as low as 7 ppm [454], i.e. in very dilute solutions. Note, however, that the elastic energy is proportional to the polymer concentration, so it is expected that ET cannot be generated at concentrations below a certain threshold.

While elastic turbulence shares similarities with inertial turbulence, the physical mechanisms behind the two types of chaotic motion are ınherently different. Unlike inertial turbulence at high Reynolds numbers, which is caused by large Reynolds stresses, elastic stress, $\boldsymbol{S}$, is the primary source of non-linearity and the cause of elastic turbulence in low-Reynolds-number flows of polymer solutions. An early key experimental observation in the study of ET is the power-law decay of velocity power spectra E in a large majority of flow geometries, with an exponent $\alpha_{\mathrm{ET}} < -3$ (typically $\alpha_{\mathrm{ET}} \in [-3.6,\ -3.3]$). The sharp decay of the velocity spectrum means that ET is a spatially smooth, temporally random flow, dominated by strong nonlinear interactions among a few large-scale modes. This type of random flow is also present in inertial turbulence below the dissipation scale and is referred to as the Batchelor flow regime.

Theoretical studies were prompted by the early experimental results of ET. The onset of this phenomenon at the molecular level is attributed to a coil-stretch transition in the presence of a fluctuating velocity field when $\mathrm{We} > 1$. The idea that polymers stretch in a random flow was first suggested by [455, 456] in relation to turbulent drag reduction in inertial turbulence. Theory predicts that at $\mathrm{We} > 1$, there is a significant change in the statistics of polymer stretching, with most molecules becoming strongly stretched up to their full length. This prediction has been recently experimentally verified [457] and has significant implications at macroscopic scale

because it leads the coil-stretch transition to produce a non-Newtonian response of the polymer solution. Theoretical arguments, in homogeneous isotropic conditions, also suggest steep spectra of exponent larger than 3 in absolute value [458].

Numerical simulations of viscoelastic flow at high Weissenberg numbers have been challenging for decades, due to the difficulty to control numerical instabilities arising at large elasticity values. However, the introduction of the log-conformation transformation by [459] revealed successful to circumvent the numerical blowup in such a parameter range. The implementation of this approach under OpenFOAM by [460] has been used to obtain our preliminary results in the Taylor–Couette setup (see fig. 5.4) that align with previous experimental and numerical [461] results. Specifically, it is observed a seemingly random fluctuating flow field, as well as an algebraic decay in the spectra of velocity fluctuations with a power law characterized by $\alpha_{\mathrm{ET}} \approx -3$ (see fig. 5.4(b)). Further work is needed to validate the simulation results, including systematic comparison with experiments, implementation and testing of a passive tracer solver, and studying the dynamics of stirring and mixing. Owing to the chaotic character of the flow, this system represents an excellent candidate to study Finite-Size Coherent Structures for small particles that could be led to accumulate by the kinetic energy dissipation provided by the interaction of the particles either with the outer or with the inner cylinder.

The viscoelastic Taylor–Couette flow could represent an efficient particle sorting set-up at microscale. Moreover, owing to the small stresses and slow velocities, the same set-up could be used for mixing and potentially sorting swimmers without the risk of damaging their biological structure.

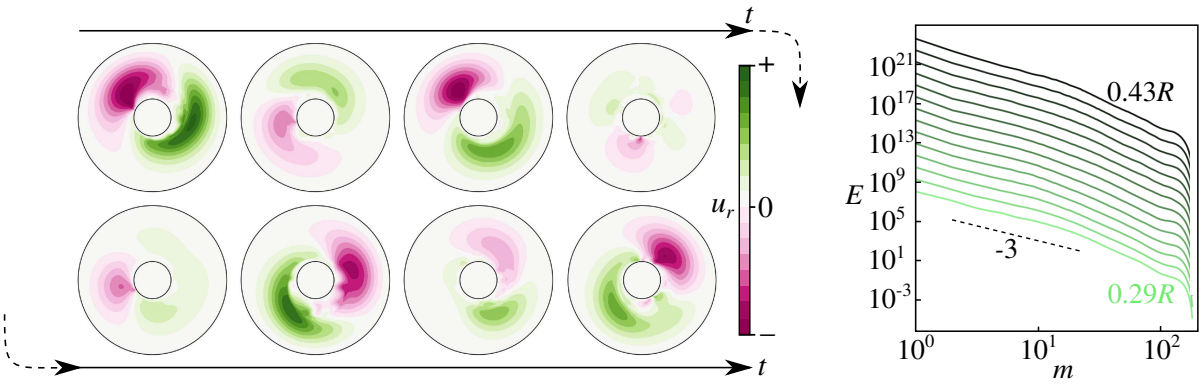

(a) Time evolution of elastic turbulence

(b) Spatial spectra

Figure 5.4: (a) Preliminary numerical results for the radial velocity field, representative of the secondary flow, at a 8 evenly spaced times in a 2D micron-scale Taylor–Couette geometry for $\Gamma = R_{\mathrm{in}}/R = 1/4$, $\mathrm{Re} = \Omega R^2/\nu = 10^{-4}$ and $\mathrm{We}/(1-\Gamma) = \Lambda\Omega = 25$, where R_{in} and R denote the inner and outer radii, respectively, Ω is the rotation rate of the outer cylinder (the inner one is kept at rest), and Λ is the polymeric relaxation time. (b) Spatial power spectra E of the secondary flow in radial direction at different radial positions presented with an arbitrarily offset to ease their reading. The spectra show the ET features identified near the inner cylinder with a clear exponent $\alpha_{\mathrm{ET}} \approx -3$. Similar results are obtained upon a variation of $\mathrm{We}/(1-\Gamma) \in [12.5,\ 100]$.

5.6 Multiphysics in pulmonary flows

According to the pre-pandemic studies conducted by the Organization for Economic Cooperation and Development (OECD) all over Europe, North and Central America, and in a few South-American and Asian countries, the 8% of preventable causes of mortality for premature deaths in 2019 is due to the respiratory system [462]. The same holds true for the 9% of treatable causes of mortality for premature deaths in 2019 [462]. Respectively, this means that: (a) an accurate diagnosis of respiratory diseases could have prevented ≈ 152k people to end up in intensive care or even to die before it, and (b) a correct treatment of the hospitalized patients could have saved ≈ 99k lives in OECD countries during 2019. This proves that even the most advanced medical diagnoses and treatments have significant room for improvement. On top of such statistics, the recent years further worsened the impact of pulmonary-induced deceases especially due to the COVID-19 pandemics.

Recent numerical tools to assist pulmonologists implement machine learning for tomographic image recognition in lungs [463, 464]. Their diagnostic capabilities are limited by the resolution of the images (≈ 2 mm^3 [465]), hence they are accurate up to the first seven airway generations and successful at classifying diseases only when they are already apparent. Other computational approaches use simulations capable of tackling the complex geometry of patient-specific lungs, simplifying, however, the distal airways and/or alveoli by means of 0D/1D models [466, 346] and neglecting the complex rheology of the airway surface liquid (ASL, mucus and serous fluid coating the airways). As a major drawback, these models cannot accurately predict the occlusion of airways, frequently occurring under pathological conditions.

In future researches, we will rather propose to overcome both such limitations by employing a first-principle approach capable of tackling resolutions down to 0.1μm scale, and accurately embedding the complex multiphysics of the lungs. As reported in §4, the successful implementation of such first-principle models helped simulating the whole topological change of the air-mucus interface leading to airway closure/reopening of distal airways including surfactant [379, 366], non-Newtonian [381] and three-phase effects [376]. These first-principle models could predict the inflammatory state of airway epithelium, as well as indicators of edema in the interstitium (≈ 1 μm in thickness) between an alveolus and a capillary (see fig. 5.5, [467]). The main drawback of first-principle simulations is however their computational cost.

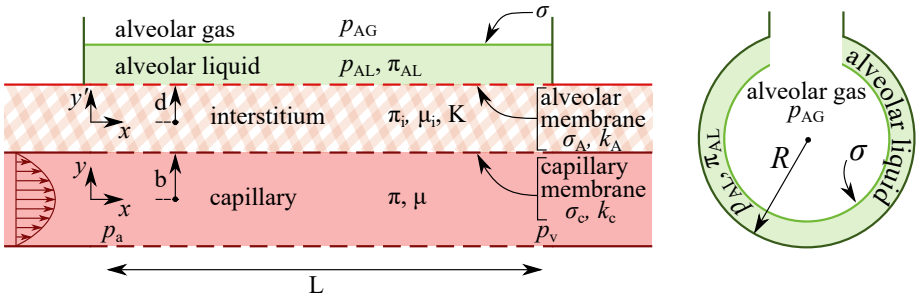

Figure 5.5: Two-dimensional model of a septal tract with capillary, interstitium, and alveolar compartments (left), and schematics of a spherical alveolus (right). For the definition of the parameters indicated in the schematics we refer to [467].

This is further complexified by the fact that the total number of generations in the human lungs of an adult is 24, starting from the trachea (≈ 1.5 cm) down to the alveolar sacs (≈ 200 μm). Morphometrical studies in healthy lungs report that there are about 8×10^6 airways [468] and about 5×10^8 alveoli [469]. The corresponding range of scales makes each direct first-principle numerical simulation of the whole lungs network far from being feasible. So far, simplified network simulations [470] and 3D+0D/1D coupling strategies of distal airways [466, 346] have been used to account for Newtonian fluid dynamic resistance, lung compliance and liquid coating. None of the existing network models includes an adequate representation of the multiphysics, which precludes from accurately accounting for the frequent instabilities induced by lung diseases.

In future works we will match the local dynamics of airways/alveoli simulated by first-principle physics with the global dynamics of the lung network simulated by one-dimensional network models. We therefore aim to reliably solve the multiphysics of the local flow over the physiologically-relevant parameter space for healthy and pathological conditions, accounting for: (i) the complex rheology of mucus [471, 348], (ii) the active effect of helical fibres and collagen in the lung walls [340, 472], (iii) the effect of cilia beating [394, 473], and (iv) soluto-capillary effects due to the surfactant naturally produced by the lungs [396, 379]. Special attention will be paid to reliably predict the formation and rupture of mucus plugs in distal airways, the wall stress for airways and alveoli, and the impact of mucus rheology on lung pathologies.

We expect that the approach proposed in §5.1 and here specialized for respiratory fluid dynamics will be capable of tackling currently inaccessible scales (down to 0.1 μm, excellent candidate for thin-film theory [467]) and instability phenomena which are essential for predicting the development of respiratory diseases in human lungs. Our ultimate goal will be forecasting: (i) the blockage of gas exchange at distal airways, (ii) the collapse of the alveoli, (iii) relevant medical indicators pointing to epithelium inflammation along the airway/alveolar walls, and (iv) risks of edema in the interstitium between an alveolus and a surrounding capillary.

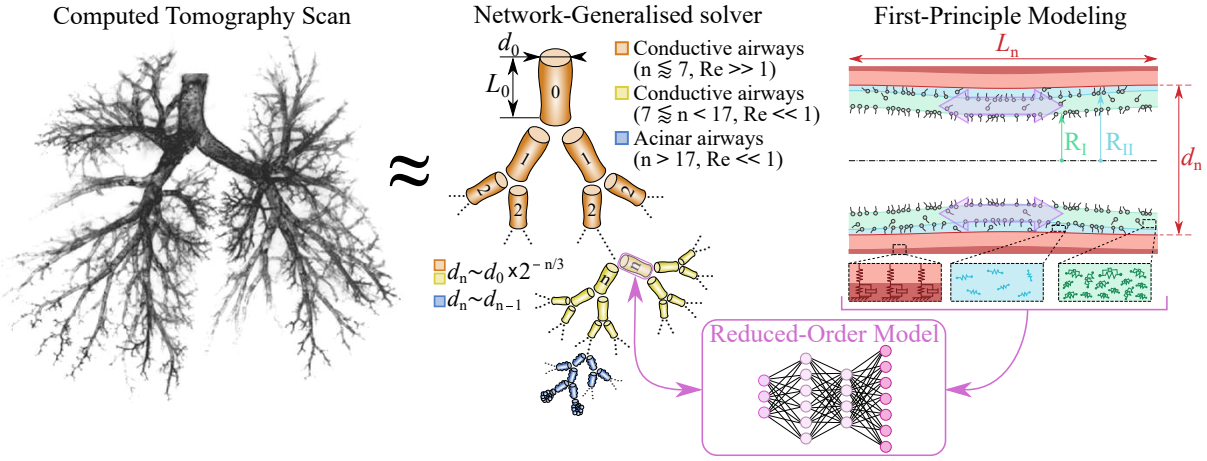

Figure 5.6: Schematic of the first-principle approach to deal with the lung network by combining a 0D/1D network approach (middle) with multiphysics first-principle simulations of single distal airways (right). The conceptual workflow of such scale-matching approach makes use of parametric 2D/3D simulations in the bronchioles that will be used to train a reduced-order model (magenta box). The flow conditions computed by the network solver for each distal airway will provide the local input parameters to the reduced-order model in order to predict the bronchiole dynamics. This is expected to provide a leading-order approximation that could be adapted to tackle patient-specific lung networks (left [465]).

5.7 Conclusions

A conceptually consistent approach to a variety of problems has been demonstrated effective throughout this manuscript and will be further pursued for future researches. The limit of such an approach is that it cannot apply whenever a continuous spectrum of scales is phenomenologically important for the system dynamics. For instance, whenever turbulence is considered, the energy cascade relies on a continuous transfer of kinetic energy among contiguous scales down to dissipation at Kolmogorov scale. Evidently, we cannot apply the approach pursued in this work for most of the turbulent flows as they cannot be reduced to the interaction of a few and even well-separated scales.

On the other hand, whenever the system dynamics is sensitive to small localized areas, such as unpenetrable boundaries (see §2), small gaps (see §3), or coating regions (see §4), a separation of scales is expected and remarkably intriguing phenomena may be observed owing to the interplay between small and large scales of the flow. We stress that the relevance of such systems is predominant in entire fluid mechanics domains such as microfluidics, interfacial flows at moderate and small Reynolds numbers, and biological applications. Moreover, as demonstrated under multiple circumstances, such systems with well-separated length scales are excellent candidates for flow control, as a localized minimal effort can produce remarkable flow modifications.

Summary of Research Contribution

Owing to the variety of topics dealt with in this manuscript, and for the seek of presenting and discussing them within their large context, the contribution of the author may not have clearly emerged. Hereinafter, we summarize the role of the author's research for the presented results.

Starting from §2, the author has delved into the characterization of all the FSCS discussed in details, contributing to the theoretical conceptualization of the phenomenon, its numerical simulation and the corresponding mathematical modeling. The presented experimental validations have been obtained either in collaboration with the teams of H. C. Kuhlmann (TU Wien) and I. Ueno (Tokyo University of Science), or independently by the latter. All the results concerning the kinematic template of the flows constitute an original contribution of the author's research, while among the stability analyses presented in §2.3, he contributed to the ones about the thermocapillary liquid bridge.

All the results about the instability in the vaneless diffuser discussed in details in §3 emerged from an internal collaboration at Arts et Métiers within the framework of the PhD thesis of M. Fan, co-supervised together with A. Dazin. Most of the concepts concerning the stall in axial compressors are a review of the scientific literature that serves to establish the context for discussing the research activity on the CME2 compressor operated at Arts et Métiers, Lille. The experimental measurements presented in §3.3, as well as the performance curves have been obtained within the framework of the PhD theses of A. Baretter and C. Rannou, with whom the author collaborates to shed light on the physical mechanisms and reduced-order modeling of stall inception, as well as its transition from spike-type to modal-type stall.

The airway closure models presented in §4 constitute a core activity of the author's research that emerged as a collaboration with J. B. Grotberg (University of Michigan) and M. Muragoglu (Koç University). All the discussed results have been obtained as original contributions either due to the author's simulations, or to the simulations by O. Erken and B. Fazla, whom the author contributed to supervise in collaboration with M. Muragoglu (Koç University) and D. Izbassarov (Finnish Meteorological Institute).

Finally, the future research projects sketched in §5 result either from an original conceptualization of the author (see §5.3 and §5.6) or from the collaborations between the author and: (i) the team at Arts et Métiers (A. Dazin, P. Joseph, and J. C. Loiseau, see §5.2), (ii) O. Coutier-Delgosha at VirginiaTech (see §5.4), (iii) S. Berti and E. Calzavarini at University of Lille, T. Burghelea at University of Nantes, and V. Bertola at University of Liverpool (see §5.5).

References

[1] N Peters. "Multiscale combustion and turbulence". *Proc. Combust. Inst.* 32.1 (2009), pp. 1–25 (cit. on p. 2).

[2] HA Stone, AD Stroock, and A Ajdari. "Engineering flows in small devices: microfluidics toward a lab-on-a-chip". *Annu. Rev. Fluid Mech.* 36 (2004), pp. 381–411 (cit. on p. 2).

[3] A Moreau, F Yaya, H Lu, A Surendranath, A Charrier, B Dehapiot, E Helfer, A Viallat, and Z Peng. "Physical mechanisms of red blood cell splenic filtration". *Proc. Natl. Acad. Sci.* 120.44 (2023), e2300095120 (cit. on p. 2).

[4] E Nader, S Skinner, M Romana, R Fort, N Lemonne, N Guillot, A Gauthier, S Antoine-Jonville, C Renoux, M-D Hardy-Dessources, E Stauffer, P Joly, Y Bertrand, and P Connes. "Blood rheology: key parameters, impact on blood flow, role in sickle cell disease and effects of exercise". *Front. Physiol.* 10 (2019), p. 1329 (cit. on p. 2).

[5] AR Pries, TW Secomb, and P Gaehtgens. "Biophysical aspects of blood flow in the microvasculature". *Cardiovasc. Res.* 32.4 (1996), pp. 654–667 (cit. on p. 2).

[6] LE Scriven. "Physics and applications of dip coating and spin coating". *MRS Proc.* 121 (1988), pp. 717–729 (cit. on p. 2).

[7] L Prandtl. "Neue Untersuchungen über die strömende Bewegung der Gase und Dämpfe". *Phys. Zeits.* 8.1 (1907), pp. 23–30 (cit. on p. 3).

[8] T Meyer. "Über zweidimensionale Bewegungsvorgänge in einem Gas, das mit Überschallgeschwindigkeit strömt". PhD thesis. Göttingen, 1908 (cit. on p. 3).

[9] A Busemann. "Drücke auf kegelförmige Spitzen bei Bewegung mit Überschallgeschwindigkeit". *ZAMM* 9.6 (1929), pp. 496–498 (cit. on p. 3).

[10] GI Taylor and JW Maccoll. "The air pressure on a cone moving at high speeds". *Proc. R. Soc. Lond. A* 139.838 (1933), pp. 298–311 (cit. on p. 3).

[11] O Janzen. "Beitrag zu einer Theorie der stationären Strömung kompressibler Flüssigkeiten". *Phys. Zeits.* 14.1 (1913), pp. 639–643 (cit. on pp. 3, 4).

[12] Lord Rayleigh. "On the flow of compressible fluid past an obstacle". *Philos. Mag.* 32.187 (1916), pp. 1–6 (cit. on pp. 3, 4).

[13] EF Toro. *Riemann solvers and numerical methods for fluid dynamics: a practical introduction*. Springer Science & Business Media, 2013 (cit. on p. 3).

[14] DD Joseph. *Stability of fluid motions I*. Vol. 27. Springer Science & Business Media, 2013 (cit. on pp. 3, 17).

[15] K Stewartson. "On the impulsive motion of a flat plate in a viscous fluid, I". *Q. J. Mech. Appl. Math.* 4.2 (1951), pp. 182–198 (cit. on p. 3).

[16] K Stewartson. “On the impulsive motion of a flat plate in a viscous fluid. II”. *Q. J. Mech. Appl. Math.* 26.2 (1973), pp. 143–152 (cit. on p. 3).

[17] LD Landau and EM Lifshitz. *Course of Theoretical Physics*. Vol. 6. Elsevier, 2013 (cit. on p. 3).

[18] M Van Dyke. “Perturbation methods in fluid mechanics/Annotated edition”. *NASA STI/Recon Tech. Rep. A* 75 (1975), p. 46926 (cit. on pp. 3, 4, 9, 10).

[19] PJ Schmid. “Dynamic mode decomposition of numerical and experimental data”. *J. Fluid Mech.* 656 (2010), pp. 5–28 (cit. on p. 3).

[20] PJ Schmid. “Dynamic mode decomposition and its variants”. *Annu. Rev. Fluid Mech.* 54 (2022), pp. 225–254 (cit. on p. 3).

[21] JL Lumley. “The structure of inhomogeneous turbulent flows”. *Atmospheric turbulence and radio wave propagation*. Ed. by AM Yaglom and VI Tartarsky. Nauka, 1967, pp. 166–178 (cit. on p. 3).

[22] G Berkooz, P Holmes, and JL Lumley. “The proper orthogonal decomposition in the analysis of turbulent flows”. *Annu. Rev. Fluid Mech.* 25.1 (1993), pp. 539–575 (cit. on p. 3).

[23] BO Koopman. “Hamiltonian systems and transformation in Hilbert space”. *Proc. Natl. Acad. Sci.* 17.5 (1931), pp. 315–318 (cit. on p. 3).

[24] I Mezić. “Analysis of fluid flows via spectral properties of the Koopman operator”. *Annu. Rev. Fluid Mech.* 45 (2013), pp. 357–378 (cit. on p. 3).

[25] SL Brunton, JL Proctor, and JN Kutz. “Discovering governing equations from data by sparse identification of nonlinear dynamical systems”. *Proc. Natl. Acad. Sci.* 113.15 (2016), pp. 3932–3937 (cit. on p. 3).

[26] W Chester. “The quasi-cylindrical shock tube”. *Philos. Mag.* 45.371 (1954), pp. 1293–1301 (cit. on p. 3).

[27] RF Chisnell. “The motion of a shock wave in a channel, with applications to cylindrical and spherical shock waves”. *J. Fluid Mech.* 2.3 (1957), pp. 286–298 (cit. on p. 3).

[28] GB Whitham. “On the propagation of shock waves through regions of non-uniform area or flow”. *J. Fluid Mech.* 4.4 (1958), pp. 337–360 (cit. on p. 3).

[29] T von Kármán. “Compressibility effects in aerodynamics”. *J. Spacecr. Rockets* 40.6 (2003), pp. 992–1011 (cit. on p. 3).

[30] H-S Tsien. “Two-dimensional subsonic flow of compressible fluids”. *J. Spacecr. Rockets* 40.6 (2003), pp. 983–991 (cit. on p. 3).

[31] JR Spreiter. “The local linearization method in transonic flow theory”. *Symposium Transsonicum: Aachen, 3.–7. September 1962*. Springer. 1964, pp. 152–183 (cit. on p. 3).

[32] MR Maxey and JJ Riley. “Equation of motion for a small rigid sphere in a nonuniform flow”. *Phys. Fluids* 26.4 (1983), pp. 883–889 (cit. on pp. 4, 24, 25).

[33] R Gatignol. “The Faxén formulae for a rigid particle in an unsteady non-uniform Stokes flow”. *J. Mec. Theor. Appl.* 1.2 (1983), pp. 143–160 (cit. on pp. 4, 24).

[34] CW Oseen. “Über die Stokes’sche Formel und über eine verwandte Aufgabe in der Hydrodynamik”. *Arkiv Mat., Astron. och Fysik* 6 (1910), p. 1 (cit. on p. 4).

[35] PG Saffman. “The lift on a small sphere in a slow shear flow”. *J. Fluid Mech.* 22.2 (1965), pp. 385–400 (cit. on p. 4).

[36] L Prandtl. *Applications of modern hydrodynamics to aeronautics*. Tech. rep. 1923 (cit. on p. 4).

[37] M Van Dyke. "Lifting-line theory as a singular-perturbation problem". *ZAMM* 28.1 (1964), pp. 90–102 (cit. on pp. 4, 94).

[38] JF Brady and G Bossis. "Stokesian dynamics". *Annu. Rev. Fluid Mech.* 20.1 (1988), pp. 111–157 (cit. on p. 4).

[39] J Happel and H Brenner. *Low Reynolds number hydrodynamics: with special applications to particulate media*. Springer Science & Business Media, 2012 (cit. on p. 4).

[40] H Schlichting and K Gersten. *Boundary-layer theory*. springer, 2016 (cit. on p. 4).

[41] LN Trefethen, AE Trefethen, SC Reddy, and TA Driscoll. "Hydrodynamic stability without eigenvalues". *Science* 261.5121 (1993), pp. 578–584 (cit. on pp. 4, 16).

[42] PJ Schmid and DS Henningson. *Stability and Transition in Shear Flows*. Springer, 2001 (cit. on p. 4).

[43] FP Bretherton. "The motion of long bubbles in tubes". *J. Fluid Mech.* 10.2 (1961), pp. 166–188 (cit. on p. 4).

[44] P Aussillous and D Quéré. "Quick deposition of a fluid on the wall of a tube". *Phys. Fluids* 12.10 (2000), pp. 2367–2371 (cit. on p. 4).

[45] A Oron, SH Davis, and SG Bankoff. "Long-scale evolution of thin liquid films". *Rev. Mod. Phys.* 69.3 (1997), p. 931 (cit. on pp. 5, 94).

[46] RV Craster and OK Matar. "Dynamics and stability of thin liquid films". *Rev. Mod. Phys.* 81.3 (2009), p. 1131 (cit. on p. 5).

[47] J Eggers and E Villermaux. "Physics of liquid jets". *Rep. Prog. Phys.* 71.3 (2008), p. 036601 (cit. on p. 5).

[48] D Bonn, J Eggers, J Indekeu, J Meunier, and E Rolley. "Wetting and spreading". *Rev. Mod. Phys.* 81.2 (2009), p. 739 (cit. on pp. 5, 94).

[49] S Kalliadasis, C Ruyer-Quil, B Scheid, and MG Velarde. *Falling liquid films*. Vol. 176. Springer Science & Business Media, 2011 (cit. on p. 5).

[50] O Reynolds. "On the theory of lubrication and its application to Mr. Beauchamp tower's experiments, including an experimental determination of the viscosity of olive oil". *Philos. Trans. R. Soc.* 177 (1886), pp. 157–234 (cit. on p. 8).

[51] J Eggers and MA Fontelos. *Singularities: formation, structure, and propagation*. Vol. 53. Cambridge University Press, 2015 (cit. on p. 9).

[52] J Eggers. "Nonlinear dynamics and breakup of free-surface flows". *Rev. Mod. Phys.* 69.3 (1997), p. 865 (cit. on pp. 9, 11).

[53] L Prandtl. "Über Flüssigkeitsbewegung bei sehr kleiner Reibung". *Math-Kongr, Heidelberg* (1904), p. 3 (cit. on p. 9).

[54] H Blasius. *Grenzschichten in Flüssigkeiten mit kleiner Reibung*. Druck von BG Teubner, 1907 (cit. on p. 9).

[55] S Kaplun. "The role of coordinate systems in boundary-layer theory". *ZAMP* 5 (1954), pp. 111–135 (cit. on p. 9).

[56] L Ting. "On the initial conditions for boundary layer equations". *J. Math. Phys.* 44 (1965), pp. 353–367 (cit. on p. 9).

[57] P Luchini and A Bottaro. “Görtler vortices: a backward-in-time approach to the receptivity problem”. *J. Fluid Mech.* 363 (1998), pp. 1–23 (cit. on pp. 9, 18).

[58] MJ Lighthill. “On boundary layers and upstream influence II. Supersonic flows without separation”. *Proc. R. Soc. Lond. A* 217.1131 (1953), pp. 478–507 (cit. on p. 9).

[59] K Stewartson and PG Williams. “Self-induced separation”. *Proc. R. Soc. Lond. A* 312.1509 (1969), pp. 181–206 (cit. on p. 9).

[60] JAF Plateau. *Statique expérimentale et théorique des liquides soumis aux seules forces moléculaires*. Vol. 2. Gauthier-Villars, 1873 (cit. on p. 11).

[61] Lord Rayleigh. “On the capillary phenomena of jets”. *Proc. R. Soc. London* 29.196-199 (1879), pp. 71–97 (cit. on p. 11).

[62] Lord Rayleigh. “On the instability of a cylinder of viscous liquid under capillary force”. *Philos. Mag.* 34.207 (1892), pp. 145–154 (cit. on p. 11).

[63] Lord Rayleigh. “On the instability of cylindrical fluid surfaces”. *Philos. Mag.* 34.207 (1892), pp. 177–180 (cit. on p. 11).

[64] D Quéré. “Fluid coating on a fiber”. *Annu. Rev. Fluid Mech.* 31.1 (1999), pp. 347–384 (cit. on p. 11).

[65] Y Geng, S Ling, J Huang, and J Xu. “Multiphase microfluidics: fundamentals, fabrication, and functions”. *Small* 16.6 (2020), p. 1906357 (cit. on p. 11).

[66] B Derby. “Inkjet printing of functional and structural materials: fluid property requirements, feature stability, and resolution”. *Annu. Rev. Mater. Res.* 40 (2010), pp. 395–414 (cit. on p. 11).

[67] JB Grotberg and OE Jensen. “Biofluid mechanics in flexible tubes”. *Annu. Rev. Fluid Mech.* 36 (2004), pp. 121–147 (cit. on pp. 11, 87).

[68] PG Drazin and LN Howard. “Hydrodynamic stability of parallel flow of inviscid fluid”. *Adv. Appl. Mech.* 9 (1966), pp. 1–89 (cit. on p. 11).

[69] PG Baines and H Mitsudera. “On the mechanism of shear flow instabilities”. *J. Fluid Mech.* 276 (1994), pp. 327–342 (cit. on p. 11).

[70] H Luce, T Mega, MK Yamamoto, M Yamamoto, H Hashiguchi, S Fukao, N Nishi, T Tajiri, and M Nakazato. “Observations of Kelvin-Helmholtz instability at a cloud base with the middle and upper atmosphere (MU) and weather radars”. *J. Geophys. Res. Atmos.* 115.D19 (2010) (cit. on p. 11).

[71] G Baumgarten and DC Fritts. “Quantifying Kelvin–Helmholtz instability dynamics observed in noctilucent clouds: 1. Methods and observations”. *J. Geophys. Res. Atmos.* 119.15 (2014), pp. 9324–9337 (cit. on p. 11).

[72] DC Fritts, G Baumgarten, K Wan, J Werne, and T Lund. “Quantifying Kelvin–Helmholtz instability dynamics observed in noctilucent clouds: 2. Modeling and interpretation of observations”. *J. Geophys. Res. Atmos.* 119.15 (2014), pp. 9359–9375 (cit. on p. 11).

[73] MD Cann, K Friedrich, JR French, and D Behringer. “A case study of cloud-top Kelvin–Helmholtz instability waves near the dendritic growth zone”. *J. Atmos. Sci.* 79.2 (2022), pp. 531–549 (cit. on p. 11).

[74] BJ Bayly, SA Orszag, and T Herbert. “Instability mechanisms in shear-flow transition”. *Annu. Rev. Fluid Mech.* 20.1 (1988), pp. 359–391 (cit. on p. 11).

[75] S Grossmann. “The onset of shear flow turbulence”. *Rev. Mod. Phys.* 72.2 (2000), p. 603 (cit. on p. 11).

[76] FP Bertolotti, T Herbert, and PR Spalart. “Linear and nonlinear stability of the Blasius boundary layer”. *J. Fluid Mech.* 242 (1992), pp. 441–474 (cit. on p. 11).

[77] SA Maslowe. “Shear flow instabilities and transition”. *Hydrodynamic instabilities and the transition to turbulence*. Springer, 2005, pp. 181–228 (cit. on p. 11).

[78] M Sano and K Tamai. “A universal transition to turbulence in channel flow”. *Nat. Phys.* 12.3 (2016), pp. 249–253 (cit. on p. 11).

[79] B Eckhardt, TM Schneider, B Hof, and J Westerweel. “Turbulence transition in pipe flow”. *Annu. Rev. Fluid Mech.* 39 (2007), pp. 447–468 (cit. on p. 11).

[80] H Bénard. “Ètude expérimentale des courants de convection dans une nappe liquide. - Régime permanent : tourbillons cellulaires”. *J. Phys. Theor. Appl.* 9.1 (1900), pp. 513–524 (cit. on p. 11).

[81] Lord Rayleigh. “On convection currents in a horizontal layer of fluid, when the higher temperature is on the under side”. *Phil. Mag.* 32.192 (1916), pp. 529–546 (cit. on p. 11).

[82] S Chandrasekhar. *Hydrodynamic and hydromagnetic stability*. Clarendon Press, 1968 (cit. on p. 11).

[83] AE Gill and A Davey. “Instabilities of a buoyancy-driven system”. *J. Fluid Mech.* 35.4 (1969), pp. 775–798 (cit. on p. 11).

[84] B Gebhart. “Instability, transition, and turbulence in buoyancy-induced flows”. *Annu. Rev. Fluid Mech.* 5.1 (1973), pp. 213–246 (cit. on p. 11).

[85] RW Griffiths and PF Linden. “The stability of buoyancy-driven coastal currents”. *Dyn. Atmos. Oceans* 5.4 (1981), pp. 281–306 (cit. on p. 11).

[86] B Qiu, N Imasato, and T Awaji. “Baroclinic instability of buoyancy-driven coastal density currents”. *J. Geophys. Res. Oceans* 93.C5 (1988), pp. 5037–5050 (cit. on p. 11).

[87] AJ Wells and MG Worster. “A geophysical-scale model of vertical natural convection boundary layers”. *J. Fluid Mech.* 609 (2008), pp. 111–137 (cit. on p. 11).

[88] C Gladstone and AW Woods. “On buoyancy-driven natural ventilation of a room with a heated floor”. *J. Fluid Mech.* 441 (2001), pp. 293–314 (cit. on p. 11).

[89] J Kim, A Tzempelikos, and JE Braun. “Review of modelling approaches for passive ceiling cooling systems”. *J. Build. Perform. Simul.* 8.3 (2015), pp. 145–172 (cit. on p. 11).

[90] A Oberbeck. “Über die Wärmeleitung der Flüssigkeiten bei Berücksichtigung der Strömungen infolge von Temperaturdifferenzen”. *Ann. Phys.* 243.6 (1879), pp. 271–292 (cit. on p. 13).

[91] J Boussinesq. *Théorie analytique de la chaleur mise en harmonic avec la thermodynamique et avec la théorie mécanique de la lumière: Refroidissement et échauffement par rayonnement, conductibilité des tiges, lames et masses cristallines, courants de convection, théorie mécanique de la lumière*. Vol. 2. Gauthier-Villars, 1903 (cit. on p. 13).

[92] A Galántai. “The theory of Newton’s method”. *J. Comput. Appl. Math.* 124.1-2 (2000), pp. 25–44 (cit. on p. 14).

[93] E Åkervik, L Brandt, DS Henningson, J Hœpffner, O Marxen, and P Schlatter. “Steady solutions of the Navier-Stokes equations by selective frequency damping”. *Phys. Fluids* 18.6 (2006) (cit. on p. 14).

[94] J Bechhoefer, V Ego, S Manneville, and B Johnson. “An experimental study of the onset of parametrically pumped surface waves in viscous fluids”. *J. Fluid Mech.* 288 (1995), pp. 325–350 (cit. on p. 15).

[95] T Besson, WS Edwards, and LS Tuckerman. "Two-frequency parametric excitation of surface waves". *Phys. Rev. E* 54.1 (1996), p. 507 (cit. on p. 15).

[96] M Stojanović, F Romanò, and HC Kuhlmann. "Instability of axisymmetric flow in thermocapillary liquid bridges: Kinetic and thermal energy budgets for two-phase flow with temperature-dependent material properties". *Eur. J. Appl. Math.* (2023), pp. 1–27 (cit. on pp. 15, 37).

[97] PJ Schmid. "Nonmodal stability theory". *Annu. Rev. Fluid Mech.* 39 (2007), pp. 129–162 (cit. on p. 15).

[98] SA Orszag. "Accurate solution of the Orr–Sommerfeld stability equation". *J. Fluid Mech.* 50.4 (1971), pp. 689–703 (cit. on p. 16).

[99] PJ Schmid, DS Henningson, MR Khorrami, and MR Malik. "A study of eigenvalue sensitivity for hydrodynamic stability operators". *Theor. Comput. Fluid Dyn.* 4 (1993), pp. 227–240 (cit. on p. 16).

[100] RR Kerswell. "Nonlinear nonmodal stability theory". *Annu. Rev. Fluid Mech.* 50 (2018), pp. 319–345 (cit. on p. 17).

[101] MR Jovanović. "From bypass transition to flow control and data-driven turbulence modeling: an input–output viewpoint". *Annu. Rev. Fluid Mech.* 53 (2021), pp. 311–345 (cit. on p. 18).

[102] LN Cattafesta III and M Sheplak. "Actuators for active flow control". *Annu. Rev. Fluid Mech.* 43 (2011), pp. 247–272 (cit. on p. 18).

[103] WS Saric, HL Reed, and EJ Kerschen. "Boundary-layer receptivity to freestream disturbances". *Annu. Rev. Fluid Mech.* 34.1 (2002), pp. 291–319 (cit. on p. 18).

[104] P Luchini and A Bottaro. "Adjoint equations in stability analysis". *Annu. Rev. Fluid Mech.* 46 (2014), pp. 493–517 (cit. on p. 18).

[105] JHM Fransson and A Talamelli. "On the generation of steady streamwise streaks in flat-plate boundary layers". *J. Fluid Mech.* 698 (2012), pp. 211–234 (cit. on p. 18).

[106] JC Lin, SK Robinson, RJ McGhee, and WO Valarezo. "Separation control on high-lift airfoils via micro-vortex generators". *J. Aircr.* 31.6 (1994), pp. 1317–1323 (cit. on p. 18).

[107] S Shahinfar, SS Sattarzadeh, JHM Fransson, and A Talamelli. "Revival of classical vortex generators now for transition delay". *Phys. Rev. Lett.* 109.7 (2012), p. 074501 (cit. on p. 18).

[108] AY Turk. "Heat transfer enhancement downstream of vortex generators on a flat plate". PhD thesis. Iowa State University, 1984 (cit. on p. 18).

[109] J Kim and TR Bewley. "A linear systems approach to flow control". *Annu. Rev. Fluid Mech.* 39 (2007), pp. 383–417 (cit. on p. 18).

[110] SL Brunton and JN Kutz. *Data-driven science and engineering: Machine learning, dynamical systems, and control*. Cambridge University Press, 2019 (cit. on p. 18).

[111] B Moya, I Alfaro, D Gonzalez, F Chinesta, and E Cueto. "Physically sound, self-learning digital twins for sloshing fluids". *PLoS One* 15.6 (2020), e0234569 (cit. on p. 18).

[112] A Barkanyi, T Chovan, S Nemeth, and J Abonyi. "Modelling for digital twins—potential role of surrogate models". *Processes* 9.3 (2021), p. 476 (cit. on p. 18).

[113] EN Lorenz. "Deterministic nonperiodic flow". *Int. J. Atmos. Sci.* 20.2 (1963), pp. 130–141 (cit. on p. 19).

[114] SH Strogatz. *Nonlinear dynamics and chaos with student solutions manual: With applications to physics, biology, chemistry, and engineering*. CRC press, 2018 (cit. on pp. 19, 20).

[115] S Wiggins. *Global bifurcations and chaos: analytical methods*. Vol. 73. Springer Science & Business Media, 2013 (cit. on p. 19).

[116] M Hénon and C Heiles. "The applicability of the third integral of motion: some numerical experiments". *Astron. J.* 69 (1964), p. 73 (cit. on p. 19).

[117] VI Arnol'd and A Avez. *Ergodic problems of classical mechanics*. The mathematical physics monograph series. Benjamin, 1968 (cit. on p. 19).

[118] MV Berry. "Regular and irregular motion". *Hamiltonian Dynamical Systems*. CRC Press, 2020, pp. 27–53 (cit. on p. 19).

[119] J Moser. *Stable and random motions in dynamical systems: With special emphasis on celestial mechanics*. Vol. 1. Princeton university press, 2001 (cit. on p. 19).

[120] AJ Lichtenberg and MA Lieberman. *Regular and stochastic motion*. Vol. 38. Springer Science & Business Media, 2013 (cit. on p. 19).

[121] K Bajer. "Hamiltonian formulation of the equations of streamlines in three-dimensional steady flows". *Chaos Soliton Fract.* 4.6 (1994), pp. 895–911 (cit. on pp. 19, 21, 35, 40).

[122] M Shub. "Communications-WHAT IS... a Horseshoe?" *Not. Am. Math. Soc.* 52.5 (2005), pp. 516–517 (cit. on p. 19).

[123] S Smale. "Differentiable dynamical systems". *Bull. Am. Math. Soc.* 73.6 (1967), pp. 747–817 (cit. on p. 19).

[124] S Smale. "Finding a horseshoe on the beaches of Rio". *Math. Intell.* 20.1 (1998), pp. 39–44 (cit. on p. 19).

[125] J Guckenheimer and P Holmes. *Nonlinear oscillations, dynamical systems, and bifurcations of vector fields*. Vol. 42. Springer Science & Business Media, 2013 (cit. on pp. 19, 20).

[126] S Wiggins. *Chaotic transport in dynamical systems*. Vol. 2. Springer Science & Business Media, 2013 (cit. on pp. 19, 20).

[127] JM Ottino. "Mixing, chaotic advection, and turbulence". *Annu. Rev. Fluid Mech.* 22.1 (1990), pp. 207–254 (cit. on p. 19).

[128] P Holmes. "Some remarks on chaotic particle paths in time-periodic, three-dimensional swirling flows". *Contemp. Math* 28 (1984), pp. 393–404 (cit. on p. 19).

[129] A Leonard, V Rom-Kedar, and S Wiggins. "Fluid mixing and dynamical systems". *Nucl. Phys.* 2 (1987), pp. 179–190 (cit. on p. 19).

[130] DS Broomhead and Susan C Ryrie. "Particle paths in wavy vortices". *Nonlin.* 1.3 (1988), p. 409 (cit. on p. 19).

[131] V Rom-Kedar, A Leonard, and S Wiggins. "An analytical study of transport, mixing and chaos in an unsteady vortical flow". *J. Fluid Mech.* 214 (1990), pp. 347–394 (cit. on p. 19).

[132] JM Ottino. *The kinematics of mixing: stretching, chaos, and transport*. Vol. 3. Cambridge university press, 1989 (cit. on pp. 19, 21, 39).

[133] JM Ottino. "The mixing of fluids". *Sci. Am.* 260.1 (1989), pp. 56–67 (cit. on p. 19).

[134] H Aref. "Stirring by chaotic advection". *J. Fluid Mech.* 143 (1984), pp. 1–21 (cit. on pp. 19, 21).

[135] H Aref, JR Blake, M Budišić, SSS Cardoso, JHE Cartwright, HJH Clercx, K El Omari, U Feudel, R Golestanian, E Gouillart, GJF van Heijst, TS Krasnopolskaya, Y Le Guer, RS MacKay, VV Meleshko, G Metcalfe, I Mezić, APS de Moura, O Piro, MFM Speetjens, R Sturman, J-L Thiffeault, and I Tuval. "Frontiers of chaotic advection". *Rev. Mod. Phys.* 89.2 (2017), p. 025007 (cit. on pp. 19, 21, 22).

[136] T Tél, A de Moura, C Grebogi, and G Károlyi. "Chemical and biological activity in open flows: A dynamical system approach". *Phys. Rep.* 413.2-3 (2005), pp. 91–196 (cit. on p. 22).

[137] RS MacKay and JD Meiss. *Hamiltonian Dynamical Systems: a reprint selection*. CRC Press, 2020 (cit. on p. 22).

[138] RS MacKay, JD Meiss, and IC Percival. "Transport in Hamiltonian systems". *Physica D* 13.1-2 (1984), pp. 55–81 (cit. on p. 22).

[139] F Romanò, T Türkbay, and HC Kuhlmann. "Lagrangian chaos in steady three-dimensional lid-driven cavity flow". *Chaos* 30.7 (2020), p. 073121 (cit. on pp. 22, 47, 49).

[140] L Brandt and F Coletti. "Particle-laden turbulence: progress and perspectives". *Annu. Rev. Fluid Mech.* 54 (2022), pp. 159–189 (cit. on p. 23).

[141] JJ Stickel and RL Powell. "Fluid mechanics and rheology of dense suspensions". *Annu. Rev. Fluid Mech.* 37 (2005), pp. 129–149 (cit. on p. 23).

[142] CM Tchen. "Mean value and correlation problems connected with the motion of small particles suspended in a turbulent fluid". PhD thesis. TU Delft, 1947 (cit. on p. 24).

[143] SE Corrsin and J Lumley. "On the equation of motion for a particle in turbulent fluid". *Appl. Sci. Res.* 6.2-3 (1956), pp. 114–116 (cit. on p. 24).

[144] YA Buevich. "Motion resistance of a particle suspended in a turbulent medium". *Fluid Dyn.* 1.6 (1966), pp. 119–119 (cit. on p. 24).

[145] JJ Riley. "Computer simulations of turbulent dispersion". PhD thesis. 1971 (cit. on p. 24).

[146] MH Kobayashi and CFM Coimbra. "On the stability of the Maxey–Riley equation in nonuniform linear flows". *Phys. Fluids* 17.11 (2005) (cit. on p. 24).

[147] M Farazmand and G Haller. "The Maxey–Riley equation: Existence, uniqueness and regularity of solutions". *Nonlinear Anal. Real World Appl.* 22 (2015), pp. 98–106 (cit. on p. 24).

[148] GP Langlois, M Farazmand, and G Haller. "Asymptotic dynamics of inertial particles with memory". *J. Nonlin. Sci.* 25 (2015), pp. 1225–1255 (cit. on p. 24).

[149] SG Prasath, V Vasan, and R Govindarajan. "Accurate solution method for the Maxey–Riley equation, and the effects of Basset history". *J. Fluid Mech.* 868 (2019), pp. 428–460 (cit. on p. 24).

[150] J Boussinesq. "Sur la résistance qu'oppose un fluide indéfini au repos, sans pesanteur, au mouvement varié d'une sphère solide qu'il mouille sur toute sa surface, quand les vitesses restent bien continues et assez faibles pour que leurs carrés et produits soient négligeables". *CR Acad. Sc. Paris* 100 (1885), pp. 935–937 (cit. on p. 25).

[151] AB Basset. *A treatise on hydrodynamics: with numerous examples*. Vol. 2. Deighton, Bell and Company, 1888 (cit. on p. 25).

[152] Z Zhang, V Bertin, MH Essink, H Zhang, N Fares, Z Shen, T Bickel, T Salez, and A Maali. "Unsteady drag force on an immersed sphere oscillating near a wall". *J. Fluid Mech.* 977 (2023), A21 (cit. on pp. 25, 30).

[153] F-L Yang. "A formula for the wall-amplified added mass coefficient for a solid sphere in normal approach to a wall and its application for such motion at low Reynolds number". *Phys. Fluids* 22.12 (2010) (cit. on p. 25).

[154] S Schubert and T Rung. "On the relation of added mass and added resistance due to wall interference". *Sh. Technol. Res.* 66.2 (2019), pp. 117–134 (cit. on p. 25).

[155] H Brenner. "The slow motion of a sphere through a viscous fluid towards a plane surface". *Chem. Eng. Sci.* 16.3-4 (1961), pp. 242–251 (cit. on pp. 25, 30, 34, 46).

[156] AJ Goldman, RG Cox, and H Brenner. "Slow viscous motion of a sphere parallel to a plane wall—I Motion through a quiescent fluid". *Chem. Eng. Sci.* 22.4 (1967), pp. 637–651 (cit. on pp. 25, 34).

[157] RG Cox and H Brenner. "The slow motion of a sphere through a viscous fluid towards a plane surface—II Small gap widths, including inertial effects". *Chem. Eng. Sci.* 22.12 (1967), pp. 1753–1777 (cit. on pp. 25, 34).

[158] M Chaoui and F Feuillebois. "Creeping flow around a sphere in a shear flow close to a wall". *Q. J. Mech. Appl. Math.* 56.3 (2003), pp. 381–410 (cit. on pp. 25, 30).

[159] J Magnaudet and M Abbas. "Near-wall forces on a neutrally buoyant spherical particle in an axisymmetric stagnation-point flow". *J. Fluid Mech.* 914 (2021), A18 (cit. on pp. 25, 30).

[160] F Romanò, P Kunchi Kannan, and HC Kuhlmann. "Finite-size Lagrangian coherent structures in a two-sided lid-driven cavity". *Phys. Rev. Fluids* 4.2 (2019), p. 024302 (cit. on pp. 25, 46, 49).

[161] H Wu, F Romanò, and HC Kuhlmann. "Attractors for the motion of a finite-size particle in a cuboidal lid-driven cavity". *J. Fluid Mech.* 955 (2023), A16 (cit. on pp. 25, 49, 51).

[162] C Kuehn, F Romanò, and HC Kuhlmann. "Tracking particles in flows near invariant manifolds via balance functions". *Nonlin. Dyn.* 92 (2018), pp. 983–1000 (cit. on p. 25).

[163] JC Lasheras and K-K Tio. "Dynamics of a small spherical particle in steady two-dimensional vortex flows". *Appl. Mech. Rev.* 47.6S (1994), S61–S69 (cit. on p. 25).

[164] E Hofmann and HC Kuhlmann. "Particle accumulation on periodic orbits by repeated free surface collisions". *Phys. Fluids* 23.7 (2011), p. 072106 (cit. on pp. 25, 29, 40).

[165] AF Filippov. *Differential equations with discontinuous righthand sides: control systems*. Vol. 18. Springer Science & Business Media, 2013 (cit. on p. 25).

[166] N-S Cheng. "Simplified settling velocity formula for sediment particle". *J. Hydraul. Eng.* 123.2 (1997), pp. 149–152 (cit. on p. 29).

[167] J Peng and R Peterson. "Attracting structures in volcanic ash transport". *Atmos. Environ.* 48 (2012), pp. 230–239 (cit. on p. 29).

[168] MJ Olascoaga and G Haller. "Forecasting sudden changes in environmental pollution patterns". *Proc. Natl. Acad. Sci.* 109.13 (2012), pp. 4738–4743 (cit. on p. 29).

[169] CT Crowe, JD Schwarzkopf, M Sommerfeld, and Y Tsuji. *Multiphase flows with droplets and particles*. CRC press, 2011 (cit. on p. 29).

[170] S Holmberg and Y Li. "Modelling of the indoor environment–particle dispersion and deposition". *Indoor Air* 8.2 (1998), pp. 113–122 (cit. on p. 29).

[171] M Parsi, K Najmi, F Najafifard, S Hassani, BS McLaury, and SA Shirazi. "A comprehensive review of solid particle erosion modeling for oil and gas wells and pipelines applications". *J. Nat. Gas Sci. Eng.* 21 (2014), pp. 850–873 (cit. on p. 29).

[172] Z Liu, K Chen, C Davis, S Sherlock, Q Cao, X Chen, and H Dai. "Drug delivery with carbon nanotubes for in vivo cancer treatment". *Cancer Res.* 68.16 (2008), pp. 6652–6660 (cit. on p. 29).

[173] G Haller. "Lagrangian coherent structures". *Annu. Rev. Fluid Mech.* 47 (2015), pp. 137–162 (cit. on p. 29).

[174] MW Reeks. "The transport of discrete particles in inhomogeneous turbulence". *J. Aerosol Sci.* 14.6 (1983), pp. 729–739 (cit. on p. 29).

[175] S Goto and JC Vassilicos. "Sweep-stick mechanism of heavy particle clustering in fluid turbulence". *Phys. Rev. Lett.* 100.5 (2008), p. 054503 (cit. on p. 29).

[176] P Singh and DD Joseph. "Fluid dynamics of floating particles". *J. Fluid Mech.* 530 (2005), pp. 31–80 (cit. on p. 29).

[177] S Yazdi and AM Ardekani. "Bacterial aggregation and biofilm formation in a vortical flow". *Biomicrofluidics* 6.4 (2012) (cit. on pp. 29, 51).

[178] A Karimi, S Yazdi, and AM Ardekani. "Hydrodynamic mechanisms of cell and particle trapping in microfluidics". *Biomicrofluidics* 7.2 (2013) (cit. on pp. 29, 50, 51).

[179] Z Wang and J Zhe. "Recent advances in particle and droplet manipulation for lab-on-a-chip devices based on surface acoustic waves". *Lab on a Chip* 11.7 (2011), pp. 1280–1285 (cit. on p. 29).

[180] M Orlishausen, L Butzhammer, D Schlotbohm, D Zapf, and W Köhler. "Particle accumulation and depletion in a microfluidic Marangoni flow". *Soft Matter* 13.39 (2017), pp. 7053–7060 (cit. on pp. 29, 50).

[181] F Romanò. "Particle accumulation in incompressible laminar flows due to particle-boundary interaction". PhD thesis. Wien, 2016 (cit. on pp. 29, 33).

[182] F Romanò, H Wu, and HC Kuhlmann. "A generic mechanism for finite-size coherent particle structures". *Int. J. Multiph. Flow* 111 (2019), pp. 42–52 (cit. on pp. 29, 40, 51).

[183] KD Squires and JK Eaton. "Preferential concentration of particles by turbulence". *Phys. Fluids* 3.5 (1991), pp. 1169–1178 (cit. on p. 30).

[184] N Raju and E Meiburg. "Dynamics of small, spherical particles in vortical and stagnation point flow fields". *Phys. Fluids* 9.2 (1997), pp. 299–314 (cit. on p. 30).

[185] A Babiano, JHE Cartwright, O Piro, and A Provenzale. "Dynamics of a small neutrally buoyant sphere in a fluid and targeting in Hamiltonian systems". *Phys. Rev. Lett.* 84.25 (2000), p. 5764 (cit. on p. 30).

[186] G Segre and A Silberberg. "Radial particle displacements in Poiseuille flow of suspensions". *Nature* 189.4760 (1961), pp. 209–210 (cit. on p. 30).

[187] S Xu and A Nadim. "Oscillatory counter-centrifugation". *Phys. Fluids* 28.2 (2016) (cit. on pp. 31, 50).

[188] G Verhille and P Le Gal. "Aggregation of fibers by waves". *Nonlinear Waves and Pattern Dynamics*. Ed. by N Abcha, E Pelinovsky, and I Mutabazi. Cham: Springer International Publishing, 2018, pp. 127–136 (cit. on p. 31).

[189] F Romanò. "Oscillatory switching centrifugation: dynamics of a particle in a pulsating vortex". *J. Fluid Mech.* 857 (2018), R3 (cit. on p. 31).

[190] F Romanò. "Particle coherent structures in confined oscillatory switching centrifugation". *Crystals* 11.2 (2021), p. 183 (cit. on p. 31).

[191] F Romanò and HC Kuhlmann. "Numerical investigation of the interaction of a finite-size particle with a tangentially moving boundary". *Int. J. Heat Fluid Flow* 62 (2016), pp. 75–82 (cit. on p. 33).

[192] F Romanò and HC Kuhlmann. "Particle–boundary interaction in a shear-driven cavity flow". *Theor. Comput. Fluid Dyn.* 31.4 (2017), pp. 427–445 (cit. on p. 33).

[193] F Romanò, HC Kuhlmann, M Ishimura, and I Ueno. "Limit cycles for the motion of finite-size particles in axisymmetric thermocapillary flows in liquid bridges". *Phys. Fluids* 29.9 (2017), p. 093303 (cit. on p. 33).

[194] F Romanò, P-E des Boscs, and HC Kuhlmann. "Forces and torques on a sphere moving near a dihedral corner in creeping flow". *Eur. J. Mech. B/Fluids* 84 (2020), pp. 110–121 (cit. on p. 34).

[195] GB Jeffery. "On the steady rotation of a solid of revolution in a viscous fluid". *Proc. Lond. Math. Soc.* 2.1 (1915), pp. 327–338 (cit. on p. 34).

[196] F Romanò, P-E des Boscs, and HC Kuhlmann. "Stokesian motion of a spherical particle near a right corner made by tangentially moving walls". *J. Fluid Mech.* 927 (2021), A41 (cit. on pp. 34, 51).

[197] L Babor and HC Kuhlmann. "Lagrangian transport in the time-periodic two-dimensional lid-driven square cavity". *Phys. Fluids* 35.3 (2023) (cit. on p. 35).

[198] CW Leong and JM Ottino. "Experiments on mixing due to chaotic advection in a cavity". *J. Fluid Mech.* 209 (1989), pp. 463–499 (cit. on p. 35).

[199] M Wanschura, HC Kuhlmann, and HJ Rath. "Linear stability of two-dimensional combined buoyant-thermocapillary flow in cylindrical liquid bridges". *Phys. Rev. E* 55.6 (1997), p. 7036 (cit. on pp. 36, 37).

[200] F Romanò and HC Kuhlmann. "Finite-size Lagrangian coherent structures in thermocapillary liquid bridges". *Phys. Rev. Fluids* 3.9 (2018), p. 094302 (cit. on pp. 36, 37, 39, 40, 51).

[201] M Stojanović, F Romanò, and HC Kuhlmann. "Stability of thermocapillary flow in liquid bridges fully coupled to the gas phase". *J. Fluid Mech.* 949 (2022), A5 (cit. on pp. 36, 37).

[202] M Wanschura, VM Shevtsova, HC Kuhlmann, and HJ Rath. "Convective instability mechanisms in thermocapillary liquid bridges". *Phys. Fluids* 7.5 (1995), pp. 912–925 (cit. on pp. 36, 37).

[203] MK Smith and SH Davis. "Instabilities of dynamic thermocapillary liquid layers. Part 1. Convective instabilities". *J. Fluid Mech.* 132 (1983), pp. 119–144 (cit. on p. 36).

[204] M Stojanović, F Romanò, and HC Kuhlmann. "High-Prandtl-number thermocapillary liquid bridges with dynamically deformed interface: effect of an axial gas flow on the linear stability". *J. Fluid Mech.* 978 (2024), A27 (cit. on p. 37).

[205] M Stojanović, F Romanò, and HC Kuhlmann. "Flow instability in high-Prandtl-number liquid bridges with fully temperature-dependent thermophysical properties". *J. Fluid Mech.* 978 (2024), A17 (cit. on p. 37).

[206] F Romanò, M Stojanović, and HC Kuhlmann. "Scaling and modeling of the heat transfer across the free surface of a thermocapillary liquid bridge". *Int. J. Num. Meth. Heat Fluid Flow* (2024) (cit. on p. 37).

[207] A Toyama, M Gotoda, T Kaneko, and I Ueno. "Existence conditions and formation process of second type of spiral loop particle accumulation structure (SL-2 PAS) in half-zone liquid bridge". *Microgravity Sci. Technol.* 29 (2017), pp. 263–274 (cit. on pp. 39, 40).

[208] HG Schuster and W Just. *Deterministic chaos: an introduction*. John Wiley & Sons, 2006 (cit. on p. 39).

[209] FH Muldoon and HC Kuhlmann. "Coherent particulate structures by boundary interaction of small particles in confined periodic flows". *Physica D* 253 (2013), pp. 40–65 (cit. on pp. 39, 40).

[210] RV Mukin and HC Kuhlmann. "Topology of hydrothermal waves in liquid bridges and dissipative structures of transported particles". *Phys. Rev. E* 88 (2013), p. 053016 (cit. on pp. 39, 40).

[211] I Barmak, F Romanò, P Kunchi Kannan, and HC Kuhlmann. "Coherent particle structures in high-Prandtl-number liquid bridges". *Microgravity Sci. Technol.* 33 (2021), pp. 1–10 (cit. on p. 39).

[212] I Barmak, F Romanò, and HC Kuhlmann. "Finite-size coherent particle structures in high-Prandtl-number liquid bridges". *Phys. Rev. Fluids* 6.8 (2021), p. 084301 (cit. on pp. 39, 40).

[213] F Romanò and HC Kuhlmann. "Finite-size coherent structures in thermocapillary liquid bridges". *Int. J. Microgravity Sci. Appl.* 36.2 (2019), p. 360201 (cit. on p. 40).

[214] S Tanaka, H Kawamura, I Ueno, and D Schwabe. "Flow structure and dynamic particle accumulation in thermocapillary convection in a liquid bridge". *Phys. Fluids* 18.6 (2006) (cit. on p. 40).

[215] M Gotoda, DE Melnikov, I Ueno, and V Shevtsova. "Experimental study on dynamics of coherent structures formed by inertial solid particles in three-dimensional periodic flows". *Chaos* 26.7 (2016) (cit. on p. 40).

[216] M Gotoda, A Toyama, M Ishimura, T Sano, M Suzuki, T Kaneko, and I Ueno. "Experimental study of coherent structures of finite-size particles in thermocapillary liquid bridges". *Phys. Rev. Fluids* 4.9 (2019), p. 094301 (cit. on p. 40).

[217] S Noguchi and I Ueno. "Spatial-temporal behaviors of low-Stokes-number particles forming coherent structures in high-aspect-ratio liquid bridges by thermocapillary effect". *Phys. Rev. Fluids* 8.11 (2023), p. 114002 (cit. on pp. 40, 51).

[218] DE Melnikov and V Shevtsova. "Different types of Lagrangian coherent structures formed by solid particles in three-dimensional time-periodic flows". *Eur. Phys. J.* 226 (2017), pp. 1239–1251 (cit. on pp. 40, 51).

[219] S Albensoeder, HC Kuhlmann, and HJ Rath. "Multiplicity of steady two-dimensional flows in two-sided lid-driven cavities". *Theor. Comp. Fluid Dyn.* 14 (2001), pp. 223–241 (cit. on p. 41).

[220] W Thomson. "On gravitational oscillations of rotating water". *Proc. R. Soc. Edinb.* 10 (1880), pp. 92–100 (cit. on p. 41).

[221] C Eloy and S Le Dizes. "Stability of the Rankine vortex in a multipolar strain field". *Phys. Fluids* 13.3 (2001), pp. 660–676 (cit. on p. 41).

[222] F Waleffe. "On the three-dimensional instability of strained vortices". *Phys. Fluids* 2.1 (1990), pp. 76–80 (cit. on p. 41).

[223] S Albensoeder and HC Kuhlmann. "Linear stability of rectangular cavity flows driven by anti-parallel motion of two facing walls". *J. Fluid Mech.* 458 (2002), pp. 153–180 (cit. on pp. 41–43).

[224] Lord Rayleigh. "On the dynamics of revolving fluids". *Proc. R. Soc. Lond. A* 93.648 (1917), pp. 148–154 (cit. on p. 41).

[225] D Sipp and L Jacquin. “Three-dimensional centrifugal-type instabilities of two-dimensional flows in rotating systems”. *Phys. Fluids* 12.7 (2000), pp. 1740–1748 (cit. on p. 41).

[226] C Blohm, S Albensoeder, HC Kuhlmann, M Broda, and HJ Rath. “The two-sided lid-driven cavity: Aspect-ratio dependence of the flow stability”. *ZAMM* 81.S3 (2001), pp. 781–782 (cit. on pp. 42, 43).

[227] CH Blohm and HC Kuhlmann. “The two-sided lid-driven cavity: experiments on stationary and time-dependent flows”. *J. Fluid Mech.* 450 (2002), pp. 67–95 (cit. on p. 43).

[228] M Brøns and JN Hartnack. “Streamline topologies near simple degenerate critical points in two-dimensional flow away from boundaries”. *Phys. Fluids* 11 (1999), pp. 314–324 (cit. on p. 43).

[229] F Romanò, S Albensoeder, and HC Kuhlmann. “Topology of three-dimensional steady cellular flow in a two-sided anti-parallel lid-driven cavity”. *J. Fluid Mech.* 826 (2017), pp. 302–334 (cit. on pp. 44, 45).

[230] H Wu, F Romanò, and HC Kuhlmann. “Attractors for the motion of a finite-size particle in a two-sided lid-driven cavity”. *J. Fluid Mech.* 906 (2021), A4 (cit. on pp. 45, 46, 49, 51).

[231] GK Batchelor. “On steady laminar flow with closed streamlines at large Reynolds number”. *J. Fluid Mech.* 1.2 (1956), pp. 177–190 (cit. on p. 47).

[232] F Auteri, N Parolini, and L Quartapelle. “Numerical investigation on the stability of singular driven cavity flow”. *J. Comput. Phys.* 183.1 (2002), pp. 1–25 (cit. on p. 47).

[233] S Albensoeder, HC Kuhlmann, and HJ Rath. “Three-dimensional centrifugal-flow instabilities in the lid-driven cavity problem”. *Phys. Fluids* 13 (2001), pp. 121–135 (cit. on pp. 47, 48).

[234] J Ducrée, S Haeberle, S Lutz, S Pausch, F Von Stetten, and R Zengerle. “The centrifugal microfluidic Bio-Disk platform”. *J. Micromech. Microeng.* 17.7 (2007), S103 (cit. on p. 50).

[235] D Mark, S Haeberle, G Roth, F Von Stetten, and R Zengerle. “Microfluidic lab-on-a-chip platforms: requirements, characteristics and applications”. *Microfluidics Based Microsystems*. Dordrecht: Springer Netherlands, 2010, pp. 305–376 (cit. on p. 50).

[236] H Pertoft. “Fractionation of cells and subcellular particles with Percoll”. *J. Biochem. Biophys. Methods* 44.1-2 (2000), pp. 1–30 (cit. on p. 50).

[237] JP Smith, AC Barbati, SM Santana, JP Gleghorn, and BJ Kirby. “Microfluidic transport in microdevices for rare cell capture”. *Electrophoresis* 33.21 (2012), pp. 3133–3142 (cit. on p. 50).

[238] T Tondreau, L Lagneaux, M Dejeneffe, A Delforge, M Massy, C Mortier, and D Bron. “Isolation of BM mesenchymal stem cells by plastic adhesion or negative selection: phenotype, proliferation kinetics and differentiation potential”. *Cytotherapy* 6.4 (2004), pp. 372–379 (cit. on p. 50).

[239] K Tatsumi, T Atsumi, K Namura, R Kuriyama, M Suzuki, and K Nakabe. “Marangoni convection around a microbubble attached to a locally heated channel wall”. *Heat Transf. Res.* 51.12 (2020) (cit. on p. 50).

[240] R Khojah, R Stoutamore, and D Di Carlo. “Size-tunable microvortex capture of rare cells”. *Lab on a Chip* 17.15 (2017), pp. 2542–2549 (cit. on p. 50).

[241] H Haddadi and D Di Carlo. “Inertial flow of a dilute suspension over cavities in a microchannel”. *J. Fluid Mech.* 811 (2017), pp. 436–467 (cit. on p. 50).

[242] AAS Bhagat, SS Kuntaegowdanahalli, and I Papautsky. "Enhanced particle filtration in straight microchannels using shear-modulated inertial migration". *Phys. Fluids* 20.10 (2008) (cit. on p. 51).

[243] D Di Carlo. "Inertial microfluidics". *Lab on a Chip* 9.21 (2009), pp. 3038–3046 (cit. on p. 51).

[244] J Zhang, W Li, M Li, G Alici, and N-T Nguyen. "Particle inertial focusing and its mechanism in a serpentine microchannel". *Microfluid. Nanofluidics* 17 (2014), pp. 305–316 (cit. on p. 51).

[245] M Madou, J Zoval, G Jia, H Kido, J Kim, and N Kim. "Lab on a CD". *Annu. Rev. Biomed. Eng.* 8 (2006), pp. 601–628 (cit. on p. 51).

[246] D Vigolo, S Radl, and HA Stone. "Unexpected trapping of particles at a T junction". *Proc. Natl. Acad. Sci.* 111.13 (2014), pp. 4770–4775 (cit. on p. 51).

[247] SC Hur, AJ Mach, and D Di Carlo. "High-throughput size-based rare cell enrichment using microscale vortices". *Biomicrofluidics* 5.2 (2011) (cit. on p. 51).

[248] A Volpe, P Paiè, A Ancona, R Osellame, PM Lugarà, and G Pascazio. "A computational approach to the characterization of a microfluidic device for continuous size-based inertial sorting". *J. Phys. D* 50.25 (2017), p. 255601 (cit. on p. 51).

[249] D Schwabe, P Hintz, and S Frank. "New features of thermocapillary convection in floating zones revealed by tracer Particle Accumulation Structures (PAS)". *Microgravity Sci. Technol.* 9 (1996), pp. 163–168 (cit. on p. 51).

[250] D Schwabe, S Tanaka, A Mizev, and H Kawamura. "Particle Accumulation Structures in time-dependent thermocapillary flow in a liquid bridge under microgravity conditions". *Microgravity Sci. Technol.* 18 (2006), pp. 117–127 (cit. on p. 51).

[251] D Schwabe, AI Mizev, M Udhayasankar, and S Tanaka. "Formation of dynamic Particle Accumulation Structures in oscillatory thermocapillary flow in liquid bridges". *Phys. Fluids* 19 (2007), pp. 072102-1–072102-18 (cit. on p. 51).

[252] I Ueno, Y Abe, K Noguchi, and H Kawamura. "Dynamic Particle Accumulation Structure (PAS) in half-zone liquid bridge–reconstruction of particle motion by 3-D PTV". *Adv. Space Res.* 41.12 (2008), pp. 2145–2149 (cit. on p. 51).

[253] T Sakata, S Terasaki, H Saito, S Fujimoto, I Ueno, T Yano, K Nishino, Y Kamotani, and S Matsumoto. "Coherent structures of m = 1 by low-Stokes-number particles suspended in a half-zone liquid bridge of high aspect ratio: Microgravity and terrestrial experiments". *Phys. Rev. Fluids* 7.1 (2022), p. 014005 (cit. on p. 51).

[254] HC Kuhlmann, F Romanò, H Wu, and S Albensoeder. "Particle-motion attractors due to particle-boundary interaction in incompressible steady three-dimensional flows". 20th Australasian Fluid Mechanics Conference. Ed. by Greg Ivey, Tongming Zhou, Nicole Jones, and Scott Draper. Australasian Fluid Mechanics Society, 2016, 102, Paper no. 449 (cit. on p. 51).

[255] T Takakusagi and I Ueno. "Flow patterns induced by the thermocapillary effect and resultant structures of suspended particles in a hanging droplet". *Langmuir* 33.46 (2017), pp. 13197–13206 (cit. on p. 51).

[256] SL Dixon and C Hall. *Fluid mechanics and thermodynamics of turbomachinery*. Butterworth-Heinemann, 2013 (cit. on p. 53).

[257] G Jacquet-Richardet, M Torkhani, P Cartraud, F Thouverez, TN Baranger, M Herran, C Gibert, S Baguet, P Almeida, and L Peletan. "Rotor to stator contacts in turbomachines. Review and application". *Mech. Syst. Signal Process.* 40.2 (2013), pp. 401–420 (cit. on p. 53).

[258] RA Van den Braembussche. "Numerical optimization for advanced turbomachinery design". *Optimization and computational fluid dynamics*. Springer, 2008, pp. 147–189 (cit. on p. 53).

[259] B Chen and X Yuan. "Advanced aerodynamic optimization system for turbomachinery". *J. Turbomach.* 130.2 (2008), p. 021005 (cit. on p. 53).

[260] A Safari, HG Lemu, S Jafari, and M Assadi. "A comparative analysis of nature-inspired optimization approaches to 2D geometric modelling for turbomachinery applications". *Math. Probl. Eng.* 2013 (2013) (cit. on p. 53).

[261] W Schwering. "Design of cascades for incompressible plane potential flows with prescribed velocity distribution". *J. Eng. Power.* 93.3 (1971), pp. 321–331 (cit. on p. 53).

[262] C Lecomte. "Calculation of cascade profiles from the velocity distribution". *J. Eng. Power.* 96 (1974), pp. 407–412 (cit. on p. 53).

[263] G Meauze. "An inverse time marching method for the definition of cascade geometry". *J. Eng. Power.* 104.3 (1982), pp. 650–656 (cit. on p. 53).

[264] O Leonard and RA Van den Braembussche. "Design method for subsonic and transonic cascade with prescribed Mach number distribution". *ASME J. Turbomach.* 114.3 (1992), pp. 553–560 (cit. on p. 53).

[265] T Dang and V Isgro. "Euler-based inverse method for turbomachinery blades, Part 1: Two-dimensional cascades". *AIAA Journal* 33.12 (1995), pp. 2309–2315 (cit. on p. 53).

[266] T Dang, S Damle, and X Qiu. "Euler-based inverse method for turbomachinery blades, Part 2: Three-dimensional flows". *J. Eng. Power.* 38.11 (2000), pp. 2007–2013 (cit. on p. 53).

[267] S Goel, JI Cofer IV, and H Singh. *Turbine airfoil design optimization*. Vol. 78729. ASME, 1996 (cit. on p. 53).

[268] Y Niizeki. "Optimization system for compressor aerodynamic design". Vol. 475. 1999 (cit. on p. 53).

[269] K Ashihara and A Goto. "Turbomachinery blade design using 3-D inverse design method, CFD and optimization algorithm". *Turbo Expo: Power for Land, Sea, and Air*. Vol. 78507. ASME. 2001, V001T03A053 (cit. on p. 53).

[270] CM Chan, HL Bai, and DQ He. "Blade shape optimization of the Savonius wind turbine using a genetic algorithm". *Appl. Energy* 213 (2018), pp. 148–157 (cit. on p. 53).

[271] J Luo, C Zhou, and F Liu. "Multipoint design optimization of a transonic compressor blade by using an adjoint method". *J. Turbomach.* 136.5 (2014), p. 051005 (cit. on p. 53).

[272] M Ghalandari, A Ziamolki, A Mosavi, S Shamshirband, K-W Chau, and S Bornassi. "Aeromechanical optimization of first row compressor test stand blades using a hybrid machine learning model of genetic algorithm, artificial neural networks and design of experiments". *Eng. Appl. Comput. Fluid Mech.* 13.1 (2019), pp. 892–904 (cit. on p. 53).

[273] JD Denton and WN Dawes. "Computational fluid dynamics for turbomachinery design". *Proc. Inst. Mech. Eng. C* 213.2 (1998), pp. 107–124 (cit. on p. 53).

[274] D Japikse. “Stall, stage stall, and surge”. *Proceedings of the Tenth Turbomachinery Symposium*. 1981 (cit. on p. 54).

[275] W Jansen. “Rotating stall in a radial vaneless diffuser”. *J. Basic Eng.* 86 (1964), pp. 750–758 (cit. on p. 54).

[276] Y Senoo and Y Kinoshita. “Influence of inlet flow conditions and geometries of centrifugal vaneless diffusers on critical flow angle for reverse flow”. *J. Fluids Eng.* 99.1 (1977), pp. 98–102 (cit. on p. 54).

[277] Y Senoo, Y Kinoshita, and I Ishida. “Asymmetric flow in vaneless diffusers of centrifugal blowers”. *J. Fluids Eng.* 99.1 (1977), pp. 104–114 (cit. on p. 54).

[278] AN Abdelhamid, WH Colwill, and JF Barrows. “Experimental investigation of unsteady phenomena in vaneless radial diffusers”. *J. Eng. Power* 101 (1979), pp. 52–59 (cit. on p. 54).

[279] AN Abdelhamid. “Effects of vaneless diffuser geometry on flow instability in centrifugal compression systems”. *Turbo Expo: Power for Land, Sea, and Air*. Vol. 101. 1981, 79610, p. V001T03A008 (cit. on p. 54).

[280] P Frigne and R Van den Braembussche. “A theoretical model for rotating stall in the vaneless diffuser of a centrifugal compressor”. *J. Eng. Gas Turbine. Power* 107.2 (1985), pp. 507–513 (cit. on p. 54).

[281] Y Tsujimoto, Y Yoshida, and Y Mori. “Study of vaneless diffuser rotating stall based on two-dimensional inviscid flow analysis”. *J. Fluids Eng.* 118.1 (1996), pp. 123–127 (cit. on p. 54).

[282] YG. Heng, A Dazin, and MN Ouarzazi. “Linear stability analysis of rotating stall in a wide vaneless diffuser”. *12th European Conference on Turbomachinery Fluid Dynamics and Thermodynamics, ETC 2017 - Conference Proceedings*. 2017 (cit. on pp. 54, 56).

[283] S Ljevar, HC de Lange, and AA van Steenhoven. “Two-dimensional rotating stall analysis in a wide vaneless diffuser”. *Int. J. Rotating Mach.* 2006 (2006), pp. 1–11 (cit. on pp. 55–57, 59).

[284] G Pavesi, A Dazin, G Cavazzini, G Caignaert, G Bois, and G Ardizzon. “Experimental and numerical investigation of unforced unsteadiness in a vaneless radial diffuser”. *9th European Conference on Turbomachinery: Fluid Dynamics and Thermodynamics, ETC 2011 - Conference Proceedings*. Vol. 1. 2011 (cit. on pp. 55, 56).

[285] A Dazin. “High-speed stereoscopic PIV study of rotating instabilities in a radial vaneless diffuser”. *Exp. Fluids* 51 (2011), pp. 83–93 (cit. on pp. 55, 56).

[286] M Fan, A Dazin, F Romanò, and G Bois. “Effect of leakage on the performance of the vaneless diffuser of a centrifugal pump model”. *Conference on Modelling Fluid Flow (CMFF’22), Budapest, Hungary*. 2022, pp. 51–58 (cit. on p. 55).

[287] M Fan, A Dazin, G Bois, and F Romanò. “Effect of inlet leakage flow on the instability in a radial vaneless diffuser”. *Phys. Fluids* 35.1 (2023) (cit. on pp. 55–57, 59).

[288] M Fan, A Dazin, G Bois, and F Romanò. “Instabilities in a turbulent swirling source flow between parallel rings”. *Phys. Fluids* 35.10 (2023) (cit. on pp. 55, 57, 59, 60, 62).

[289] M Fan, A Dazin, G Bois, and F Romanò. “Instabilities identification based on a new centrifugal 3D impeller outflow model”. *Aerosp. Sci. Technol.* (2023), p. 108466 (cit. on pp. 55, 57, 68).

[290] M Fan, A Dazin, G Bois, and F Romanò. “Effect of radius ratio on the instabilities in a vaneless diffuser”. *Eur. J. Mech. B/Fluids* 104 (2024), pp. 1–7 (cit. on pp. 57, 62, 68).

[291] CS Tan, I Day, S Morris, and A Wadia. "Spike-type compressor stall inception, detection, and control". *Annu. Rev. Fluid Mech.* 42 (2010), pp. 275–300 (cit. on p. 63).

[292] TR Camp and IJ Day. *A study of spike and modal stall phenomena in a low-speed axial compressor*. Vol. 78682. ASME, 1997 (cit. on p. 63).

[293] NM McDougall, NA Cumpsty, and TP Hynes. "Stall inception in axial compressors". *J. Turbomach.* 112.1 (1990), pp. 116–123 (cit. on p. 63).

[294] IJ Day. "Stall inception in axial flow compressors". *J. Turbomach.* 115.1 (1993), pp. 1–9 (cit. on p. 63).

[295] MD Hathaway. *Passive endwall treatments for enhancing stability*. Tech. rep. 2007 (cit. on p. 63).

[296] G Margalida, P Joseph, O Roussette, and A Dazin. "Active flow control in an axial compressor for stability improvement: on the effect of flow control on stall inception". *Exp. Fluids* 62.1 (2021), pp. 1–13 (cit. on pp. 63, 67, 68).

[297] DA Hoying, CS Tan, HD Vo, and EM Greitzer. "Role of blade passage flow structures in axial compressor rotating stall inception". *J. Turbomach.* 121.4 (1999), pp. 735–742 (cit. on p. 64).

[298] A Deppe, H Saathoff, and U Stark. "Spike-type stall inception in axial-flow compressors". *Proceeding of 6th Conference on Turbomachinery, Fluid Dynamics and Thermodynamics, Lille, France*. 2005 (cit. on p. 64).

[299] HD Vo, CS Tan, and EM Greitzer. "Criteria for spike initiated rotating stall". *J. Turbomach.* 130.1 (2008), p. 011023 (cit. on p. 64).

[300] G Pullan, AM Young, IJ Day, EM Greitzer, and ZS Spakovszky. "Origins and structure of spike-type rotating stall". *J. Turbomach.* 137.5 (2015), p. 051007 (cit. on p. 65).

[301] M Inoue, M Kuroumaru, T Tanino, S Yoshida, and M Furukawa. "Comparative studies on short and long length-scale stall cell propagating in an axial compressor rotor". *J. Turbomach.* 123.1 (2001), pp. 24–30 (cit. on p. 65).

[302] M Inoue, M Kuroumaru, S Yoshida, T Minami, K Yamada, and M Furukawa. "Effect of tip clearance on stall evolution process in a low-speed axial compressor stage". *Turbo Expo: Power for Land, Sea, and Air*. Vol. 41707. 2004, pp. 385–394 (cit. on p. 65).

[303] K Yamada, H Kikuta, M Furukawa, S Gunjishima, and Y Hara. "Effects of tip clearance on the stall inception process in an axial compressor rotor". *Turbo Expo: Power for Land, Sea, and Air*. Vol. 55249. ASME. 2013, V06CT42A035 (cit. on p. 65).

[304] M Hewkin-Smith, G Pullan, SD Grimshaw, EM Greitzer, and ZS Spakovszky. "The role of tip leakage flow in spike-type rotating stall inception". *J. Turbomach.* 141.6 (2019), p. 061010 (cit. on p. 65).

[305] VBC de Almeida, E Tüzüner, M Eck, and D Peitsch. "Numerical characterization of prestall disturbances in a compressor stage". *J. Turbomach.* 146.8 (2024), p. 081009 (cit. on p. 65).

[306] A Baretter, P Joseph, O Roussette, A Dazin, and F Romanò. "Scaling laws at stall in an axial compressor with an upstream perturbation". *AIAA Journal* submitted (2024) (cit. on p. 66).

[307] TP Hynes and EM Greitzer. "A method for assessing effects of circumferential flow distortion on compressor stability". *J. Turbomach.* 109.3 (1987), pp. 371–379 (cit. on p. 66).

[308] R Chue, TP Hynes, EM Greitzer, CS Tan, and JP Longley. "Calculations of inlet distortion induced compressor flow field instability". *Int. J. Heat Fluid Flow* 10.3 (1989), pp. 211–223 (cit. on p. 66).

[309] P Lin, C Wang, and Y Wang. "A high order model of rotaing stall in axial compressors with inlet distortion". *Chin. J. Aeronaut.* 30.3 (2017), pp. 898–906 (cit. on p. 66).

[310] A Baretter, P Joseph, O Roussette, F Romanò, and A Dazin. "Experimental analysis of an axial compressor operating under flow distortion". *Turbo Expo: Power for Land, Sea, and Air*. Vol. 86090. ASME. 2022, V10AT29A030 (cit. on pp. 66, 92).

[311] KL Suder, MD Hathaway, SA Thorp, AJ Strazisar, and MB Bright. "Compressor stability enhancement using discrete tip injection". *J. Turbomach.* 123.1 (2001), pp. 14–23 (cit. on p. 67).

[312] C Nie, G Xu, X Cheng, and J Chen. "Micro air injection and its unsteady response in a low-speed axial compressor". *J. Turbomach.* 124.4 (2002), pp. 572–579 (cit. on p. 67).

[313] M Kefalakis and KD Papailiou. "Active flow control for increasing the surge margin of an axial flow compressor". *Turbo Expo: Power for Land, Sea, and Air*. Vol. 4241. 2006, pp. 101–111 (cit. on p. 67).

[314] J Li, F Lin, Z Tong, C Nie, and J Chen. "The dual mechanisms and implementations of stability enhancement with discrete tip injection in axial flow compressors". *J. Turbomach.* 137.3 (2015), p. 031010 (cit. on p. 67).

[315] M Stößel, S Bindl, and R Niehuis. "Rotating stall inception inside the low pressure compressor of a twin-spool turbofan engine". *Turbo Expo: Power for Land, Sea, and Air*. Vol. 55225. ASME. 2013, V06AT35A003 (cit. on p. 67).

[316] M Stößel, S Bindl, and R Niehuis. "Ejector Tip Injection for Active Compressor Stabilization". *Turbo Expo: Power for Land, Sea, and Air*. Vol. 45608. ASME. 2014, V02AT37A004 (cit. on pp. 67, 91).

[317] H Takata and Y Tsukuda. "Stall margin improvement by casing treatment—its mechanism and effectiveness". *J. Eng. Power* 99.1 (1977), pp. 121–133 (cit. on p. 67).

[318] GDJ Smith and NA Cumpsty. "Flow phenomena in compressor casing treatment". *J. Eng. Gas Turbines Power* 106.3 (1984), pp. 532–541 (cit. on p. 67).

[319] H Fujita and H Takata. "A study on configurations of casing treatment for axial flow compressors". *Bulletin of JSME* 27.230 (1984), pp. 1675–1681 (cit. on p. 67).

[320] NA Cumpsty. *Part-circumference casing treatment and the effect on compressor stall*. Vol. 79139. ASME, 1989 (cit. on p. 67).

[321] J Moubogha Moubogha, G Margalida, P Joseph, O Roussette, and A Dazin. "Stall margin improvement in an axial compressor by continuous and pulsed tip injection". *Int. J. Turbomach. Propuls. Power* 7.1 (2022), p. 10 (cit. on pp. 67, 68).

[322] O El Mokkadem, X Chen, C Phan, J Delva, P Joseph, A Dazin, and F Romanò. "Small-width wall-attached Coandă jets for flow control". *Flow* 3 (2023), E17 (cit. on p. 67).

[323] C Rannou, J Marty, G Tanguy, and A Dazin. "Effect of tip gap size on the performance of an axial compressor stage with and without active flow control". *Int. J. Turbomach. Propuls. Power* 8.3 (2023), p. 30 (cit. on pp. 68, 91).

[324] JH Widdicombe, SJ Bastacky, DX Wu, and CY Lee. "Regulation of depth and composition of airway surface liquid". *Eur. Respir. J.* 10 (1997), pp. 2892–2897 (cit. on p. 70).

[325] MA Sackner and CS Kim. “Phasic flow mechanisms of mucus clearance”. *Eur. J. Respir. Dis.* 153 (1987), pp. 159–164 (cit. on p. 70).

[326] SL Goren. “The instability of an annular thread of fluid”. *J. Fluid Mech.* 12.2 (1962), pp. 309–319 (cit. on p. 70).

[327] PS Hammond. “Nonlinear adjustment of a thin annular film of viscous fluid surrounding a thread of another within a circular cylindrical pipe”. *J. Fluid Mech.* 137 (1983), pp. 363–384 (cit. on pp. 70, 75).

[328] PA Gauglitz and CJ Radke. “An extended evolution equation for liquid film breakup in cylindrical capillaries”. *Chem. Eng. Sci.* 43.7 (1988), pp. 1457–1465 (cit. on pp. 70, 71, 80).

[329] M Johnson, RD Kamm, LW Ho, A Shapiro, and TJ Pedley. “The nonlinear growth of surface-tension-driven instabilities of a thin annular film”. *J. Fluid Mech.* 233 (1991), pp. 141–156 (cit. on p. 70).

[330] D Halpern and JB Grotberg. “Fluid-elastic instabilities of liquid-lined flexible tubes”. *J. Fluid Mech.* 244 (1992), pp. 615–632 (cit. on pp. 70, 71, 75).

[331] PD Howell, SL Waters, and JB Grotberg. “The propagation of a liquid bolus along a liquid-lined flexible tube”. *J. Fluid Mech.* 406 (2000), pp. 309–335 (cit. on p. 70).

[332] D Halpern and JB Grotberg. “Nonlinear saturation of the Rayleigh instability due to oscillatory flow in a liquid-lined tube”. *J. Fluid Mech.* 492 (2003), pp. 251–270 (cit. on pp. 70, 71).

[333] JP White and M Heil. “Three-dimensional instabilities of liquid-lined elastic tubes: A thin-film fluid-structure interaction model”. *Phys. Fluids* 17.3 (2005) (cit. on p. 70).

[334] JB Grotberg. “Pulmonary flow and transport phenomena”. *Annu. Rev. Fluid Mech.* 26.1 (1994), pp. 529–571 (cit. on p. 70).

[335] JB Grotberg. “Respiratory fluid mechanics and transport processes”. *Annu. Rev. Biomed. Eng.* 3.1 (2001), pp. 421–457 (cit. on pp. 70, 71).

[336] DP Gaver and OE Jensen. “Surfactant and airway liquid flows”. *Lung Surfactant Function and Disorder*. Ed. by K Nag. CRC Press, 2005, pp. 192–220 (cit. on p. 70).

[337] SN Ghadiali and DP Gaver. “Biomechanics of liquid–epithelium interactions in pulmonary airways”. *Respir. Physiol. Neurobiol.* 163.1-3 (2008), pp. 232–243 (cit. on p. 70).

[338] JB Grotberg. “Respiratory fluid mechanics”. *Phys. Fluids* 23.2 (2011) (cit. on p. 70).

[339] J Patarin, E Ghiringhelli, G Darsy, M Obamba, P Bochu, B Camara, S Quétant, J-L Cracowski, C Cracowski, and MR de Saint Vincent. “Rheological analysis of sputum from patients with chronic bronchial diseases”. *Sci. Rep.* 10 (2020), pp. 1–10 (cit. on pp. 70, 84).

[340] JE Hiorns, OE Jensen, and BS Brook. “Nonlinear compliance modulates dynamic bronchoconstriction in a multiscale airway model”. *Biophys. J.* 107 (2014), pp. 3030–3042 (cit. on pp. 70, 99).

[341] LM Nogee. “Genetic mechanisms of surfactant deficiency”. *Neonatology* 85 (2004), pp. 314–318 (cit. on p. 70).

[342] U Savla and CM Waters. “Mechanical strain inhibits repair of airway epithelium in vitro”. *Am. J. Physiol. Lung Cell. Mol. Physiol.* 274.6 (1998), pp. L883–L892 (cit. on p. 70).

[343] D Huh, H Fujioka, YC Tung, N Futai, R Paine, JB Grotberg, and S Takayama. "Acoustically detectable cellular-level lung injury induced by fluid mechanical stresses in microfluidic airway systems". *Proc. Natl. Acad. Sci.* 104 (2007), pp. 18886–18891 (cit. on pp. 70, 74).

[344] HL Viola, V Vasani, K Washington, J-H Lee, C Selva, A Li, CJ Llorente, Y Murayama, JB Grotberg, F Romanò, and S Takayama. "Liquid plug propagation in computer-controlled microfluidic airway-on-a-chip with semi-circular microchannels". *Lab on a Chip* 24.2 (2024), pp. 197–209 (cit. on p. 70).

[345] SA Bahrani, S Hamidouche, M Moazzen, K Seck, C Duc, M Muradoglu, JB Grotberg, and F Romanò. "Propagation and rupture of elastoviscoplastic liquid plugs in airway reopening model". *J. Non-Newt. Fluid Mech.* 300 (2022), p. 104718 (cit. on p. 70).

[346] PG Koullapis, FS Stylianou, J Sznitman, B Olsson, and SC Kassinos. "Towards whole-lung simulations of aerosol deposition: A model of the deep lung". *J. Aerosol Sci.* 144 (2020), p. 105541 (cit. on pp. 70, 98, 99).

[347] H Ma, H Fujioka, D Halpern, JHT Bates, and DP Gaver III. "Full-lung simulations of mechanically ventilated lungs incorporating recruitment/derecruitment dynamics". *Front. Netw. Physiol.* 3 (2023), p. 1257710 (cit. on p. 70).

[348] B Fazla, O Erken, F Romanò, and M Grotberg JB Muradoglu. "Effects of kinematic hardening of mucus polymers in an airway closure model". submitted (2024) (cit. on pp. 70, 86, 87, 99).

[349] RH Brown and W Mitzner. "Airway closure with high PEEP in vivo". *J. Appl. Physiol.* 89.3 (2000), pp. 956–960 (cit. on p. 70).

[350] L Broche, P Pisa, L Porra, L Degrugilliers, A Bravin, M Pellegrini, JB Borges, G Perchiazzi, A Larsson, G Hedenstierna, and S Bayat. "Individual airway closure characterized in vivo by phase-contrast CT imaging in injured rabbit lung". *Crit. Care Med.* 47.9 (2019), e774–e781 (cit. on p. 70).

[351] URL: https://antranik.org/the-respiratory-system/ (cit. on p. 70).

[352] K Patrias. *Citing Medicine: The NLM Style Guide for Authors, Editors, and Publishers [Internet], 2nd edition*. Ed. by Wendling D. Bethesda (MD): National Library of Medicine (US), 2007 (cit. on p. 70).

[353] JCCM Veen, AJ Beekman, EH Bel, and PJ Sterk. "Recurrent exacerbations in severe asthma are associated with enhanced airway closure during stable episodes". *Am. J. Respir. Crit. Care Med.* 161 (2000), pp. 1902–1906 (cit. on p. 71).

[354] A Gunther, C Siebert, R Schmidt, S Ziegler, F Grimminger, M Yabut, B Temmesfeld, D Walmrath, H Morr, and W Seeger. "Surfactant alterations in severe pneumonia, acute respiratory distress syndrome, and cardiogenic lung edema". *Am. J. Respir. Crit. Care Med.* 153 (1996), pp. 176–184 (cit. on p. 71).

[355] PA Dargaville, M South, and PN McDougall. "Surfactant abnormalities in infants with severe viral bronchiolitis". *Arch. Dis. Child* 75 (1996), pp. 133–136 (cit. on p. 71).

[356] M Griese, R Essl, R Schmidt, E Rietschel, F Ratjen, M Ballmann, and K Paul. "Pulmonary surfactant, lung function, and endobronchial inflammation in cystic fibrosis". *Am. J. Respir. Crit. Care Med.* 170 (2004), pp. 1000–1005 (cit. on p. 71).

[357] C Guerin, S Lemasson, R de Varax, J Milic-Emili, and G Fournier. "Small airway closure and positive end-expiratory pressure in mechanically ventilated patients with chronic obstructive pulmonary disease." *Am. J. Respir. Crit. Care Med.* 155 (1997), pp. 1949–1956 (cit. on p. 71).

[358] CS Baker, TW Evans, BJ Randle, and PL Haslam. "Damage to surfactant-specific protein in acute respiratory distress syndrome". *The Lancet* 353.9160 (1999), pp. 1232–1237 (cit. on p. 71).

[359] FR Bode, J Dosman, RR Martin, H Ghezzo, and PT Macklem. "Age and sex differences in lung elasticity, and in closing capacity in nonsmokers". *J. Appl. Physiol.* 41.2 (1976), pp. 129–135 (cit. on p. 71).

[360] GB Drummond and J Milic-Emili. *Forty years of closing volume*. 2007 (cit. on p. 71).

[361] GK Prisk. "The lung in space". *Clin. Chest Med.* 26.3 (2005), pp. 415–438 (cit. on p. 71).

[362] JB West, AR Elliott, HJB Guy, and GK Prisk. "Pulmonary function in space". *J. Am. Med. Assoc.* 277.24 (1997), pp. 1957–1961 (cit. on p. 71).

[363] KJ Cassidy, D Halpern, BG Ressler, and JB Grotberg. "Surfactant effects in model airway closure experiments". *J. Appl. Physiol.* 87.1 (1999), pp. 415–427 (cit. on p. 71).

[364] D Halpern and JB Grotberg. "Surfactant effects on fluid-elastic instabilities of liquid-lined flexible tubes: a model of airway closure". *J. Biomechech. Eng.* 115 (1993), pp. 271–277 (cit. on p. 71).

[365] D Campana, J Di Paolo, and FA Saita. "A 2-D model of Rayleigh instability in capillary tubes–surfactant effects". *Int. J. Multiph. Flow* 30.5 (2004), pp. 431–454 (cit. on p. 71).

[366] F Romanò, M Muradoglu, and JB Grotberg. "Effect of surfactant in an airway closure model". *Phys. Rev. Fluids* 7.9 (2022), p. 093103 (cit. on pp. 71, 78, 79, 98).

[367] D Halpern, H Fujioka, and JB Grotberg. "The effect of viscoelasticity on the stability of a pulmonary airway liquid layer". *Phys. Fluids* 22 (2010), p. 011901 (cit. on pp. 71, 81, 87).

[368] M Heil, AL Hazel, and JA Smith. "The mechanics of airway closure". *Respir. Physiol. Neurobiol.* 163 (2008), pp. 214–221 (cit. on pp. 71, 87).

[369] F Romanò, H Fujioka, M Muradoglu, and JB Grotberg. "Liquid plug formation in an airway closure model". *Phys. Rev. Fluids* 4.9 (2019), p. 093103 (cit. on pp. 72–74, 79).

[370] NJ Douville, P Zamankhan, YC Tung, R Li, BL Vaughan, CF Tai, J White, PJ Christensen, JB Grotberg, and S Takayama. "Combination of fluid and solid mechanical stresses contribute to cell death and detachment in a microfluidic alveolar model". *Lab on a Chip* 11 (2011), pp. 609–619 (cit. on p. 72).

[371] H Tavana, P Zamankhan, PJ Christensen, JB Grotberg, and S Takayama. "Epithelium damage and protection during reopening of occluded airways in a physiologic microfluidic pulmonary airway model". *Biomed. Microdevices* 13 (2011), pp. 731–742 (cit. on p. 73).

[372] S Bian, CF Tai, D Halpern, Y Zheng, and JB Grotberg. "Experimental study of flow fields in an airway closure model". *J. Fluid Mech.* 647 (2010), pp. 391–402 (cit. on pp. 73, 74).

[373] JB Grotberg. "Crackles and wheezes: Agents of injury?" *Ann. Am. Thorac. Soc.* 16.8 (2019), pp. 967–969 (cit. on p. 74).

[374] CF Tai, S Bian, D Halpern, Y Zheng, M Filoche, and JB Grotberg. "Numerical study of flow fields in an airway closure model". *J. Fluid Mech.* 677 (2011), pp. 483–502 (cit. on p. 74).

[375] AM Bilek, KC Dee, and DP Gaver. "Mechanisms of surface-tension-induced epithelial cell damage in a model of pulmonary airway reopening". *J. Appl. Physiol.* 94 (2003), pp. 770–783 (cit. on p. 74).

[376] O Erken, F Romanò, JB Grotberg, and M Muradoglu. "Capillary instability of a two-layer annular film: an airway closure model". *J. Fluid Mech.* 934 (2022), A7 (cit. on pp. 75, 98).

[377] HA Stone. “A simple derivation of the time-dependent convective-diffusion equation for surfactant transport along a deforming interface”. *Phys. Fluids* 2.1 (1990), pp. 111–112 (cit. on p. 78).

[378] VG Levich and CW Tobias. “Physicochemical hydrodynamics”. *J. Electrochem. Soc.* 110.11 (1963), p. 251C (cit. on p. 78).

[379] M Muradoglu, F Romanò, H Fujioka, and JB Grotberg. “Effects of surfactant on propagation and rupture of a liquid plug in a tube”. *J. Fluid Mech.* 872 (2019), pp. 407–437 (cit. on pp. 79, 98, 99).

[380] MA Cretikos, R Bellomo, K Hillman, J Chen, S Finfer, and A Flabouris. “Respiratory rate: the neglected vital sign”. *Med. J. Aust.* 188.11 (2008), pp. 657–659 (cit. on p. 80).

[381] F Romanò, H Fujioka, M Muradoglu, and JB Grotberg. “The effect of viscoelasticity in an airway closure model”. *J. Fluid Mech.* 913 (2021), A31 (cit. on pp. 81–83, 98).

[382] J Kim, SO Hong, TS Shim, and JM Kim. “Inertio-elastic flow instabilities in a 90° bent microchannel”. *Soft Matter* 13.34 (2017), pp. 5656–5664 (cit. on p. 82).

[383] L Casanellas, MA Alves, RJ Poole, S Lerouge, and A Lindner. “The stabilizing effect of shear thinning on the onset of purely elastic instabilities in serpentine microflows”. *Soft Matter* 12.29 (2016), pp. 6167–6175 (cit. on p. 82).

[384] MD Chilcott and JM Rallison. “Creeping flow of dilute polymer solutions past cylinders and spheres”. *J. Non-Newt. Fluid Mech.* 29 (1988), pp. 381–432 (cit. on p. 82).

[385] P Saramito. “A new elastoviscoplastic model based on the Herschel–Bulkley viscoplastic model”. *J. Non-Newt. Fluid Mech.* 158.1-3 (2009), pp. 154–161 (cit. on p. 84).

[386] O Erken, B Fazla, M Muradoglu, D Izbassarov, F Romanò, and JB Grotberg. “Effects of elastoviscoplastic properties of mucus on airway closure in healthy and pathological conditions”. *Phys. Rev. Fluids* 8.5 (2023), p. 053102 (cit. on pp. 84, 87).

[387] D Halpern, H Fujioka, S Takayama, and JB Grotberg. “Liquid and surfactant delivery into pulmonary airways”. *Respir. Physiol. Neurobiol.* 163.1-3 (2008), pp. 222–231 (cit. on p. 87).

[388] OE Jensen, D Halpern, and JB Grotberg. “Transport of a passive solute by surfactant-driven flows”. *Chem. Eng. Sci.* 85 (1994), pp. 1107–1117 (cit. on p. 87).

[389] SL Waters and JB Grotberg. “The propagation of a surfactant laden liquid plug in a capillary tube”. *Phys. Fluids* 14.2 (2002), pp. 471–480 (cit. on p. 87).

[390] SH Hsu, KP Strohl, and AM Jamieson. “Role of viscoelasticity in tube model of airway reopening. I. non-Newtonian sols”. *J. Appl. Physiol.* 76.6 (1994), pp. 2481–2489 (cit. on p. 87).

[391] P Zamankhan, BT Helenbrook, S Takayama, and JB Grotberg. “Steady motion of Bingham liquid plugs in two-dimensional channels”. *J. Fluid Mech.* 705 (2012), pp. 258–279 (cit. on p. 87).

[392] P Zamankhan, S Takayama, and JB Grotberg. “Steady displacement of long gas bubbles in channels and tubes filled by a Bingham fluid”. *Phys. Rev. Fluids* 3.1 (2018), p. 013302 (cit. on p. 87).

[393] Y Hu, F Romanò, and JB Grotberg. “Effects of surface tension and yield stress on mucus plug rupture: a numerical study”. *J. Biomech. Eng.* 142.6 (2020), p. 061007 (cit. on p. 87).

[394] SM Mitran. “Metachronal wave formation in a model of pulmonary cilia”. *Comput. Struct.* 85 (2007), pp. 763–774 (cit. on pp. 87, 99).

[395] A Choudhury, M Filoche, NM Ribe, N Grenier, and GF Dietze. “On the role of viscoelasticity in mucociliary clearance: a hydrodynamic continuum approach”. *J. Fluid Mech.* 971 (2023), A33 (cit. on p. 87).

[396] JD Shemilt, A Horsley, OE Jensen, AB Thompson, and CA Whitfield. “Surface-tension-driven evolution of a viscoplastic liquid coating the interior of a cylindrical tube”. *J. Fluid Mech.* 944 (2022), A22 (cit. on pp. 87, 99).

[397] JA Moriarty and JB Grotberg. “Flow-induced instabilities of a mucus–serous bilayer”. *J. Fluid Mech.* 397 (1999), pp. 1–22 (cit. on p. 87).

[398] CM Jang and KY Kim. “Optimization of a stator blade using response surface method in a single-stage transonic axial compressor”. *Proc. Inst. Mech. Eng. A* 219.8 (2005), pp. 595–603 (cit. on p. 90).

[399] TW Simpson, TM Mauery, JJ Korte, and F Mistree. “Kriging models for global approximation in simulation-based multidisciplinary design optimization”. *AIAA Journal* 39.12 (2001), pp. 2233–2241 (cit. on p. 90).

[400] T Mengistu and W Ghaly. “Aerodynamic optimization of turbomachinery blades using evolutionary methods and ANN-based surrogate models”. *Optim. Eng.* 9.3 (2008), pp. 239–255 (cit. on p. 90).

[401] JA Nelder and R Mead. “A simplex method for function minimization”. *Comput. J.* 7.4 (1965), pp. 308–313 (cit. on p. 90).

[402] T Bäck and H-P Schwefel. “An overview of evolutionary algorithms for parameter optimization”. *Evol. Comput.* 1.1 (1993), pp. 1–23 (cit. on p. 90).

[403] Jichao Li, Xiaosong Du, and Joaquim RRA Martins. “Machine learning in aerodynamic shape optimization”. *Prog. Aerosp. Sci.* 134 (2022), p. 100849 (cit. on p. 90).

[404] Z Liu and IA Karimi. “Gas turbine performance prediction via machine learning”. *Energy* 192 (2020), p. 116627 (cit. on p. 90).

[405] J Yu, Z Wang, F Chen, J Yu, and C Wang. “Kriging surrogate model applied in the mechanism study of tip leakage flow control in turbine cascade by multiple DBD plasma actuators”. *Aerosp. Sci. Technol.* 85 (2019), pp. 216–228 (cit. on p. 90).

[406] Z Li and X Zheng. “Review of design optimization methods for turbomachinery aerodynamics”. *Prog. Aerosp. Sci.* 93 (2017), pp. 1–23 (cit. on p. 90).

[407] SL Brunton and BR Noack. “Closed-loop turbulence control: progress and challenges”. *Appl. Mech. Rev.* 67.5 (2015) (cit. on p. 90).

[408] F Ren, H-B Hu, and H Tang. “Active flow control using machine learning: A brief review”. *J. Hydrodyn.* 32.2 (2020), pp. 247–253 (cit. on p. 90).

[409] A Debien, KAFF von Krbek, N Mazellier, T Duriez, L Cordier, BR Noack, MW Abel, and A Kourta. “Closed-loop separation control over a sharp edge ramp using genetic programming”. *Exp. Fluids* 57.3 (2016), p. 40 (cit. on p. 90).

[410] R Li, BR Noack, L Cordier, J Borée, and F Harambat. “Drag reduction of a car model by linear genetic programming control”. *Exp. Fluids* 58.8 (2017), p. 103 (cit. on p. 90).

[411] Z Wu, D Fan, Y Zhou, R Li, and BR Noack. “Jet mixing enhancement using machine learning control”. *Exp. Fluids* 59.131 (2018), pp. 1–17 (cit. on p. 90).

[412] J Rabault, M Kuchta, A Jensen, U Réglade, and N Cerardi. “Artificial neural networks trained through deep reinforcement learning discover control strategies for active flow control”. *J. Fluid Mech.* 865 (2019), pp. 281–302 (cit. on p. 90).

[413] J Degrave, F Felici, J Buchli, M Neunert, B Tracey, F Carpanese, T Ewalds, R Hafner, A Abdolmaleki, D de Las Casas, C Donner, L Fritz, C Galperti, A Huber, J Keeling, M Tsimpoukelli, J Kay, A Merle, J-M Moret, S Noury, F Pesamosca, D Pfau, O Sauter, C Sommariva, S Coda, B Duval, A Fasoli, P Kohli, K Kavukcuoglu, D Hassabis, and M Riedmiller. "Magnetic control of Tokamak plasmas through deep reinforcement learning". *Nature* 602.7897 (2022), pp. 414–419 (cit. on p. 90).

[414] P Garnier, J Viquerat, J Rabault, A Larcher, A Kuhnle, and E Hachem. "A review on deep reinforcement learning for fluid mechanics". *Comput. Fluids* 225 (2021), p. 104973 (cit. on p. 90).

[415] R Paris, S Beneddine, and J Dandois. "Robust flow control and optimal sensor placement using deep reinforcement learning". *J. Fluid Mech.* 913 (2021), A25 (cit. on p. 90).

[416] H Tang, J Rabault, A Kuhnle, Y Wang, and T Wang. "Robust active flow control over a range of Reynolds numbers using an artificial neural network trained through deep reinforcement learning". *Phys. Fluids* 32.5 (2020), p. 053605 (cit. on p. 90).

[417] N Benard, J Pons-Prats, J Periaux, G Bugeda, P Braud, JP Bonnet, and E Moreau. "Turbulent separated shear flow control by surface plasma actuator: Experimental optimization by genetic algorithm approach". *Exp. Fluids* 57.2 (2016), pp. 1–17 (cit. on p. 90).

[418] DJ Kamari, M Tadjfar, and A Madadi. "Optimization of SD7003 airfoil performance using TBL and CBL at low Reynolds numbers". *Aerosp. Sci. Technol.* 79 (2018), pp. 199–211 (cit. on p. 90).

[419] SL Brunton, BR Noack, and P Koumoutsakos. "Machine learning for fluid mechanics". *Annu. Rev. Fluid Mech.* 52 (2020), pp. 477–508 (cit. on p. 90).

[420] T Duriez, SL Brunton, and BR Noack. *Machine learning control - taming nonlinear dynamics and turbulence*. Vol. 116. Fluid mechanics and its applications. Cham: Springer International Publishing, 2017 (cit. on p. 90).

[421] MA Elhawary, F Romanò, J-C Loiseau, and A Dazin. "Machine learning for optimal flow control in an axial compressor". *Eur. Phys. J. E* 46.4 (2023), pp. 1–13 (cit. on pp. 90, 91).

[422] A Dazin, P Joseph, F Romanò, Q Gallas, J Marty, G Aigouy, M Stößel, and R Niehuis. "The ACONIT project: an innovative design approach of active flow control for surge prevention in gas turbines". *IOP Conf. Series: Mat. Sci. Eng.* Vol. 1024. 1. IOP Publishing. 2021, p. 012068 (cit. on p. 91).

[423] S Zheng, PJK Bruce, JMR Graham, and JC Vassilicos. "Weakly sheared turbulent flows generated by multiscale inhomogeneous grids". *J. Fluid Mech.* 848 (2018), pp. 788–820 (cit. on p. 92).

[424] RA Pinker and MV Herbert. "Pressure loss associated with compressible flow through square-mesh wire gauzes". *J. Mech. Eng. Sci.* 9.1 (1967), pp. 11–23 (cit. on p. 92).

[425] KEG Wieghardt. "On the resistance of screens". *Aeronaut. Quart.* 4.2 (1953), pp. 186–192 (cit. on p. 92).

[426] JH McCarthy. "Steady flow past non-uniform wire grids". *J. Fluid Mech.* 19.4 (1964), pp. 491–512 (cit. on p. 92).

[427] JW Elder. "Steady flow through non-uniform gauzes of arbitrary shape". *J. Fluid Mech.* 5.3 (1959), pp. 355–368 (cit. on p. 92).

[428] JC Ward. "Turbulent flow in porous media". *J. Hydraul. Eng.* 90.5 (1964), pp. 1–12 (cit. on p. 92).

[429] IE Idelchik, MO Steinberg, and OG Martynenko. *Handbook of hydraulic resistance*. Vol. 2. Hemisphere publishing corporation New York, 1986 (cit. on p. 92).

[430] D.S. Miller. *Internal flow systems*. BHRA Fluid Engineering series. BHRA (Information Services), 1990 (cit. on p. 92).

[431] A Baretter, B Godard, P Joseph, O Roussette, F Romanò, R Barrier, and A Dazin. "Experimental and numerical analysis of a compressor stage under flow distortion". *Int. J. Turbomach. Propuls. Power* 6.4 (2021), p. 43 (cit. on p. 92).

[432] GI Taylor. "The aerodynamics of porous sheets". *Aeronaut. Res. Counc. Rep. Mem.* 2237 (1944), pp. 163–176 (cit. on p. 92).

[433] J-K Koo and DF James. "Fluid flow around and through a screen". *J. Fluid Mech.* 60.3 (1973), pp. 513–538 (cit. on p. 92).

[434] W Schneck, A Ferrar, J Bailey, K Hoopes, and W O'Brien. "Improved prediction method for the design of high-resolution total pressure distortion screens". *51st AIAA Journal Aerospace Sciences Meeting including the New Horizons Forum and Aerospace Exposition*. 2013, p. 1133 (cit. on p. 92).

[435] EM Laws and JL Livesey. "Flow through screens". *Annu. Rev. Fluid Mech.* 10.1 (1978), pp. 247–266 (cit. on p. 92).

[436] IP Castro. "Wake characteristics of two-dimensional perforated plates normal to an air-stream". *J. Fluid Mech.* 46.3 (1971), pp. 599–609 (cit. on p. 92).

[437] SC Li. *Cavitation of hydraulic machinery*. Vol. 1. World Scientific, 2000 (cit. on p. 94).

[438] W Mingxi, Y Feng, and G Ter Haar. *Cavitation in Biomedicine: Principles and Techniques*. Springer, 2015 (cit. on p. 94).

[439] C Badock, R Wirth, A Fath, and A Leipertz. "Investigation of cavitation in real size diesel injection nozzles". *Int. J. Heat Fluid Flow* 20.5 (1999), pp. 538–544 (cit. on p. 94).

[440] A Kubota, H Kato, and H Yamaguchi. "A new modelling of cavitating flows: a numerical study of unsteady cavitation on a hydrofoil section". *J. Fluid Mech.* 240 (1992), pp. 59–96 (cit. on p. 94).

[441] N Savva, G A Pavliotis, and S Kalliadasis. "Contact lines over random topographical substrates. Part 1. Statics". *J. Fluid Mech.* 672 (2011), pp. 358–383 (cit. on p. 94).

[442] N Savva, GA Pavliotis, and S Kalliadasis. "Contact lines over random topographical substrates. Part 2. Dynamics". *J. Fluid Mech.* 672 (2011), pp. 384–410 (cit. on p. 94).

[443] M Bestehorn, A Pototsky, and U Thiele. "3D large scale Marangoni convection in liquid films". *Eur. Phys. J. B* 33.4 (2003), pp. 457–467 (cit. on p. 94).

[444] M Ramiasa-MacGregor, A Mierczynska, R Sedev, and K Vasilev. "Tuning and predicting the wetting of nanoengineered material surface". *Nanoscale* 8.8 (2016), pp. 4635–4642 (cit. on p. 94).

[445] MJ Berger and P Colella. "Local adaptive mesh refinement for shock hydrodynamics". *J. Comput. Phys.* 82.1 (1989), pp. 64–84 (cit. on p. 94).

[446] P Wesseling. *Introduction to multigrid methods*. Edwards, 1995 (cit. on p. 94).

[447] JA Benek, P Buning, and J Steger. "A 3-D chimera grid embedding technique". *7th Computational Physics Conference*. 1985, p. 1523 (cit. on p. 94).

[448] H Aref. "Chaotic advection of fluid particles". *Philos. Trans. R. Soc. A* 333.1631 (1990), pp. 273–288 (cit. on p. 95).

[449] D Fuster and S Popinet. “An all-Mach method for the simulation of bubble dynamics problems in the presence of surface tension”. *J. Comput. Phys.* 374 (2018), pp. 752–768 (cit. on p. 95).

[450] MP Brenner, S Hilgenfeldt, and D Lohse. “Single-bubble sonoluminescence”. *Rev. Mod. Phys.* 74.2 (2002), p. 425 (cit. on p. 95).

[451] Y Saade, D Lohse, and D Fuster. “A multigrid solver for the coupled pressure-temperature equations in an all-Mach solver with VoF”. *J. Comput. Phys.* 476 (2023), p. 111865 (cit. on p. 95).

[452] RG Larson, ESG Shaqfeh, and SJ Muller. “A purely elastic instability in Taylor–Couette flow”. *J. Fluid Mech.* 218.1 (1990), p. 573 (cit. on p. 96).

[453] A Groisman and V Steinberg. “Mechanism of elastic instability in Couette flow of polymer solutions: Experiment”. *Phys. Fluids* 10.10 (1998), pp. 2451–2463 (cit. on p. 96).

[454] A Groisman and V Steinberg. “Elastic turbulence in curvilinear flows of polymer solutions”. *New J. Phys.* 6 (2004), pp. 29–29 (cit. on p. 96).

[455] JL Lumley. “Drag reduction by additives”. *Annu. Rev. Fluid Mech.* 1.1 (1969), pp. 367–384 (cit. on p. 96).

[456] JL Lumley. “On the solution of equations describing small scale deformation”. *Sym. Math.* 9 (1972), pp. 315–334 (cit. on p. 96).

[457] E Balkovsky, A Fouxon, and V Lebedev. “Turbulent dynamics of polymer solutions”. *Phys. Rev. Lett.* 84.20 (2000), pp. 4765–4768 (cit. on p. 96).

[458] A Fouxon and V Lebedev. “Spectra of turbulence in dilute polymer solutions”. *Phys. Fluids* 15.7 (2003), pp. 2060–2072 (cit. on p. 97).

[459] R Fattal and R Kupferman. “Constitutive laws for the matrix-logarithm of the conformation tensor”. *J. Non-Newt. Fluid Mech.* 123.2-3 (2004), pp. 281–285 (cit. on p. 97).

[460] F Pimenta and MA Alves. “Stabilization of an open-source finite-volume solver for viscoelastic fluid flows”. *J. Non-Newt. Fluid Mech.* 239 (2017), pp. 85–104 (cit. on p. 97).

[461] R van Buel, C Schaaf, and H Stark. “Elastic turbulence in two-dimensional Taylor-Couette flows”. *Europhys. Lett.* 124.1 (2018), p. 14001 (cit. on p. 97).

[462] OCDE. *Health at a Glance 2021*. 2021 (cit. on p. 98).

[463] F Zhang. “Application of machine learning in CT images and X-rays of COVID-19 pneumonia”. *Medicine* 100 (2021), e26855 (cit. on p. 98).

[464] B Wang and W Zhang. “MARnet: multi-scale adaptive residual neural network for chest X-ray images recognition of lung diseases”. *Math. Biosci. Eng.* 19 (2022), pp. 331–350 (cit. on p. 98).

[465] PA De Jong, FR Long, JC Wong, PJ Merkus, HA Tiddens, JC Hogg, and HO Coxson. “Computed tomographic estimation of lung dimensions throughout the growth period”. *Eur. Respir. J.* 27 (2006), pp. 261–267 (cit. on pp. 98, 99).

[466] CJ Roth, M Ismail, L Yoshihara, and WA Wall. “A comprehensive computational human lung model incorporating inter-acinar dependencies: Application to spontaneous breathing and mechanical ventilation”. *Int. J. Num. Meth. Biomed. Eng.* 33 (2017), e02787 (cit. on pp. 98, 99).

[467] JB Grotberg and F Romanò. “Computational pulmonary edema: A microvascular model of alveolar capillary and interstitial flow”. *APL Bioeng.* 7.3 (2023) (cit. on pp. 98, 99).

[468] N Pozin, S Montesantos, I Katz, M Pichelin, I Vignon-Clementel, and C Grandmont. "A tree-parenchyma coupled model for lung ventilation simulation". *Int. J. Num. Meth. Biomed. Eng.* 33 (2017), e2873 (cit. on p. 99).

[469] M Ochs, JR Nyengaard, A Jung, L Knudsen, M Voigt, T Wahlers, J Richter, and HJ Gundersen. "The number of alveoli in the human lung". *Am. J. Respir. Crit. Care Med.* 169 (2004), p. 120 (cit. on p. 99).

[470] H Ma, H Fujioka, D Halpern, and DP Gaver III. "Surfactant-mediated airway and acinar interactions in a multi-scale model of a healthy lung". *Front. Physiol.* 11 (2020), p. 941 (cit. on p. 99).

[471] SK Lai, YY Wang, D Wirtz, and J Hanes. "Micro-and macrorheology of mucus". *Adv. Drug Deliv. Rev.* 61 (2009), pp. 86–100 (cit. on p. 99).

[472] JE Hiorns, OE Jensen, and BS Brook. "Static and dynamic stress heterogeneity in a multiscale model of the asthmatic airway wall". *J. Appl. Physiol.* 121.1 (2016), pp. 233–247 (cit. on p. 99).

[473] M Bottier, M Peña Fernández, G Pelle, D Isabey, B Louis, JB Grotberg, and M Filoche. "A new index for characterizing micro-bead motion in a flow induced by ciliary beating: Part II, modeling". *PLoS Comput. Biol.* 13 (2017), e1005552 (cit. on p. 99).

Scientific Profile

Name	Francesco Romanò
Address	27 Rue Henri Dunant, 59000, Lille, France
Telephone	+33 6 45 20 18 89
E-mail	francesco.romano@ensam.eu
Skype	f.romano1988
Website	www.francescoromano.net
GitHub	github.com/fromano88
Nationality	Italian
Date of birth	December 15th, 1988
Marital status	Married, no children

Research Activity

Career

Period	October 2023 – present
Position	*Guest Professor,* Fluid Mechanics
Affiliation	National Research Center of Pumps, Jiangsu University, Zhenjiang, Jiangsu (China)

Period	September 2019 – present
Position	*Associate Professor,* Fluid Mechanics and Energetics
Affiliation	Lille Fluid Mechanics Laboratory, Arts et Métiers, Lille (France)

Period	April 2018 – August 2019
Position	*Post-Doctoral Fellow,* Biomedical Engineering
Affiliation	Dept. Biomedical Engineering, University of Michigan, Ann Arbor, MI (USA)

Period	October 2016 – March 2018
Position	*Post-Doctoral Fellow,* Mechanical Engineering
Affiliation	Inst. Fluid Mechanics and Heat Transfer, TU Wien, Vienna (Austria)

Period	October 2012 – September 2016
Position	*PhD Student,* Mechanical Engineering
Affiliation	Inst. Fluid Mechanics and Heat Transfer, TU Wien, Vienna (Austria)

Education

Period	October 2012 – September 2016
Degree	*PhD,* Mechanical Engineering, full marks and distinction
Defended on	September 27th, 2016
Ph.D. Committee	Michael Krommer (TU Wien, Austria), committee chair
	Hendrik C. Kuhlmann (TU Wien, Austria), examiner
	Cristian Marchioli (University of Udine, Italy), examiner and reviewer
	Eckart Meiburg (UC Santa Barbara, USA), reviewer
Thesis Title	*Particle accumulation structures in boundary-driven flows*
Supervisor	Hendrik C. Kuhlmann
Affiliation	Inst. Fluid Mechanics and Heat Transfer, TU Wien, Vienna (Austria)

Period	October 2010 – July 2012
Degree	*MSc,* Aerospace Engineering, full marks and highest honors
Defended on	July 10th, 2012
Thesis Title	*Analysis of some streaks generation method in a Blasius boundary layer*
Supervisor	Simone Camarri
Affiliation	Dept. Aerospace Engineering, University of Pisa, Pisa (Italy)

Period	September 2007 – October 2010
Degree	*BSc,* Aerospace Engineering, full marks
Defended on	October 12th, 2010
Thesis Title	*Transient of Poiseuille flow simulation using FreeFEM++*
Supervisor	Maria Vittoria Salvetti
Affiliation	Dept. Aerospace Engineering, University of Pisa, Pisa (Italy)

Projects

The following acronyms are used for funding agencies:

ANR	Agence Nationale de la Recherche, France (National Agency for Research)
CIFRE	Conventions Industrielles de Formation par la Recherche, France (Industrial Training Agreements through Research)
CNES	Centre National d'Études Spatiales, France (National Centre for Space Studies)
CSC	Chinese Research Council, China
ESA	European Space Agency, Europe
FFG	Förderagentur für die unternehmensnahe Forschung und Entwicklung, Austria (The Austrian Research Promotion Agency)
FWF	Österreichischer Wissenschaftsfonds, Austria (Austrian Science Fund)
GENCI	Grand Équipement National de Calcul Intensif, France (High Performance Computing National Facility)
NIH	National Institutes of Health, United States
TUBITAK	Türkiye Bilimsel ve Teknolojik araştırma Kurumunun, Türkiye (Scientific and Technological Research Council of Türkiye)

Project	Multiphase flow through converging nozzles
Role	Participant
Grant No.	FFG Innovation Check #847669 (≈ 10k€)

Project	Steam sterilisation
Role	Scientific Co-Coordinator
Grant No.	FFG Project #851030 (1 PhD student ≈ 160k€)

Project Dynamics of suspended particles in periodic vortex flows
Role Participant
Grant No. ESA-SciSpace #AO-2000-091

Project Thermocapillary oscillatory motion and interfacial heat exchange (JEREMI)
Role Participant
Grant No. ESA-SciSpace #AO-2004-097

Project Modelling Support to ESA-JAXA JEREMI project on ISS
Role Participant
Grant No. ESA-SciSpace #PO-4000121111 (1 PostDoc ≈ 250k€)

Project Microfluidic tissue engineering of small airway injuries
Role Participant
Grant No. NIH research Grant #1R01HL136141-01 (1 PostDoc ≈ 200k$)

Project Stability Analysis for the JEREMI Experiment
Role Participant
Grant No. FFG Project "SAJE", #866027 (1 PhD student ≈ 270k€)

Project Intricate bodies in the boundary layer – bridging fluid mechanics, morphology and ecology in larval Drusinae (Insecta: Trichoptera)
Role Contributor to the project proposal
Grant No. FWF Project #P30048-B29 (1 PhD student + 1 PostDoc ≈ 370k€)

Project Modelization of the turbulence
Role Scientific Co-Coordinator
Grant No. GENCI Project #A0062A01741 (0.5M CPU hours)

Project Stability analysis in a centrifugal pump
Role Scientific Co-Leader
Grant No. CSC-ParisTech 2018 (1 PhD student ≈ 140k€)

Project Modelization of the turbulence
Role Scientific Co-Coordinator
Grant No. GENCI Project #A0062A01741 (1.5M CPU hours)

Project Horizon2020: Design and control of an axial compressor
Role Participant
Grant No. CleanSky: ACONIT (≈ 1.6M€)

Project Numerical study of a cavitating bubble near a wall
Role Scientific Co-Leader
Grant No. CSC-ParisTech 2019 (1 PhD student ≈ 140k€)

Project Airway closure in human lungs
Role Participant
Grant No. TUBITAK #119M513 (1 PhD student ≈ 70k€)

Project Design of a pintle injector
Role Scientific Co-Leader
Grant No. CNES: PERSEUS

Project Design and simulation of an two-phase pipeline with a pump-turbine
Role Scientific Co-Leader
Grant No. SuperGrid/General Electric (1 PostDoc ≈ 200k€)

Project Modelization of turbulence
Role Scientific Co-Coordinator
Grant No. GENCI Project #A0062A01741 (5M CPU hours)

Project Numerical and experimental study of liquid plugs in human lungs
Role Scientific Co-Leader
Grant No. CSC-ParisTech 2020 (1 PhD student ≈ 140k€)

Project PINN for the physics of complex flows
Role Scientific Co-Leader
Grant No. ENSAM AAP PhD Theses 2021 (1 PhD student ≈ 110k€)

Project Multi-scale matching for flows with a grid
Role Scientific Leader
Grant No. ANR-JCJC 2021 (1 PhD student + 1 PostDoc ≈ 220k€)

Project Numerical study of multiple cavitating bubbles near a wall
Role Scientific Co-Leader
Grant No. CSC-ParisTech 2022 (1 PhD student ≈ 140k€)

Project Modelization of turbulence
Role Scientific Co-Coordinator
Grant No. GENCI Project #A0062A01741 (6M CPU hours)

Project	Life-cycle design and systemic approach for heating storage energy efficiency
Role	Participant
Grant No.	ANR-Chaire Industrielle (1 PostDoc ≈ 80k€)

Project	Elastic turbulence in curvilinear geometries
Role	Scientific Co-Leader
Grant No.	CSC-ParisTech 2023 (1 PhD student ≈ 140k€)

Project	Modeling of stall in axial compressors
Role	Scientific Co-Leader
Grant No.	CIFRE-Safran (1 PhD student ≈ 200k€)

Project	Modelization of the turbulence
Role	Scientific Co-Coordinator
Grant No.	GENCI Project #A0162A01741 (6M CPU hours)

Awards and Grants

Awards
Medal for graduation with honors, University of Pisa, 2012
Honorary Franklin Membership, Member #YG60806, 2018
Qualification as Maître de Conférences #19260330790, 2019
Featured Paper on *Chaos* **30**, 2020
Honorary Rosalind Member of London Journals Press, Member #WQ06394, 2020
Cover Page, *Int. J. Turbomach. Propuls. Power*, **6**(4), 2022
Guest Professorship, Jiangsu University, October 2023 – present

Grants
PostDoc Fellowship, Mech. Eng., TU Wien, Vienna, Austria, 2016–2018
Sponsorship for Computational Resources: cluster VSC at TU Wien, 2018–2022
PostDoc Fellowship, Biomedic. Eng., U-M, Ann Arbor, USA, 2018–2019
Sponsorship for Computational Resources: cluster Flux at U-M, 2019–2022
FFG Funding for 1 PhD Thesis, 2016
CSC Funding for 1 PhD Thesis, 2019
GENCI Computational Resources: cluster Jean-Zay/SKL/Rome, 2019 to present
CSC Funding for 1 PhD Thesis, 2020
SuperGrid/General Electric Funding for 1 PostDoc, 2020
CSC Funding for 1 PhD Thesis, 2021
ENSAM Funding for 1 PhD Thesis, 2021
ANR Funding for 1 M.Sc. Thesis, 1 PhD Thesis and 1 PostDoc, 2021
CSC Funding for 1 PhD Thesis, 2022
Collaboration: 1 PostDoc, ANR Chaire Industrielle "CORENSTOCK", 2023
CSC Funding for 1 PhD Thesis, 2023
Safran Funding for 1 PhD Thesis, 2023

Organizing, Editing and Reviewing Activity

Conferences

Org. Committee, International Marangoni Association (IMA7), Vienna, 2014
Org. Committee, European Fluid Mechanics Conference (EFMC12), Vienna, 2018
Sci. Committee, Conference on Modelling Fluid Flow (CMFF'18), Budapest, 2018
Chairman of the Session "Control and drag reduction 4", EFMC12, Vienna, 2018
Reviewer, Conference on Modelling Fluid Flow (CMFF'18), Budapest, 2018
Reviewer, International Conference on Multiphase Flow (ICMF2019), Rio de Janeiro, 2019
Reviewer, Conference of Mechanical, Electric and Industrial Eng. (MEIE 2019), China, 2018
Reviewer, International Conference on Physics, Mathematics and Statistics (ICPMS2019), China, 2019
Reviewer, European Conference on Turbomachinery (ECT14), Gdansk, 2021
Sci. Committee, Conference on Modelling Fluid Flow (CMFF'22), Budapest, 2022
Sci. Committee, Journées Scientifiques, Fluides et écoulements complexes, Nantes, 2023

Seminars

Organizer of Scientific Seminars at Laboratoire de Mécanique des Fluides de Lille, 2019–present
Organizer of the Multimedia Footage, LMFL Fluid Mechanics Webinars, YouTube, 2020–present
Responsible Arts et Métiers of the topic "Santé" (Health) for the Laboratoire de Mécanique des Fluides de Lille, 2024–present

Reviewer ($\approx$ 70 papers)

ACS Omega
Acta Mechanica
Applied Mathematics and Computation
ASME Journal of Verification, Validation and Uncertainty Quantification
Chemical Engineering Science
Chaos: An Interdisciplinary Journal of Nonlinear Science
Coatings
Dynamics of Atmospheres and Oceans
Energies
European Journal of Mechanics / B Fluids
Frontiers in Space Technologies, Microgravity
International Journal of Heat and Mass Transfer
International Journal of Multiphase Flow
International Journal of Non-Linear Mechanics
International Journal of Thermal Science
International Journal of Turbomachinery, Propulsion and Power
Journal of Applied Mathematics and Computational Mechanics

Journal of Engineering and Technological Sciences
Journal of Fluid Mechanics
Journal of Scientific Computing
Langmuir
Mathematics and Computers in Simulation
Meccanica
Microgravity Science and Technolology
Philosophical Transactions of the Royal Society A
Physics of Fluids
Science Progress
Scientific Reports
Springer Nature Applied Science
Symmetry
Theoretical and Computational Fluid Dynamics
The European Physical Journal Plus
Waves in Random and Complex Media
World Journal of Mechanics

Editor
Reviewer Editor for Frontiers in Space Technologies, Microgravity
Associate Editor for Journal of Drainage and Irrigation Machinery Engineering

PhD Theses
PhD Candidate Committee, Alberto Baretter, Arts et Métiers/ONERA
PhD Candidate Committee, Hui Wang, Arts et Métiers/VirginiaTech
PhD Candidate Committee, Shuo Liu, Arts et Métiers/VirginiaTech
PhD Candidate Committee, Ali Maghouli, Arts et Métiers/VirginiaTech
PhD Candidate Committee, Clémence Rannou, Arts et Métiers/ONERA
PhD Candidate Committee, Joe El Ghossein, VirginiaTech
PhD Thesis Reviewer, Lukas Babor, TUWien
PhD Defence Committee, Lukas Babor, TUWien
PhD Defence Committee, Antoine Charles, TUWien

Technical Competences

Software	Nek5000	Programming Languages	MATLAB
	FreeFEM++		C++
	FEniCS		Fortran
	OpenFoam		python
	basilisk		shell
	StarCCM+		

Teaching and Mentoring Activity

Teaching Experience

Period	September 2021 – to date (36 teaching hours in total)
Position	*Associate Professor*, Dept. Fluid Mechanics and Energetics
Course Title	*CFD applied to Automobile Engines* (1st year Master)
Affiliation	Arts et Métiers, Lille Fluid Mechanics Laboratory, Lille (France)

Period	March 2020 – to date (40 teaching hours in total)
Position	*Associate Professor*, Dept. Fluid Mechanics and Energetics
Course Title	*CFD applied to Turbomachinery* (1st year Master)
Affiliation	Centrale Lille, Lille Fluid Mechanics Laboratory, Lille (France)

Period	September 2020 – to date (48 teaching hours in total)
Position	*Associate Professor*, Dept. Fluid Mechanics and Energetics
Course Title	*CFD applied to Fluid Mechanics* (2nd year Master)
Affiliation	University of Lille, Lille Fluid Mechanics Laboratory, Lille (France)

Period	September 2020 – to date (21 teaching hours in total)
Position	*Associate Professor*, Dept. Fluid Mechanics and Energetics
Course Title	*Intermediate Energetics and Heat Transfer* (3rd year Bachelor)
Affiliation	Arts et Métiers, Lille Fluid Mechanics Laboratory, Lille (France)

Period	September 2020 – to date (92 teaching hours in total)
Position	*Associate Professor*, Dept. Fluid Mechanics and Energetics
Course Title	*Intermediate Fluid Mechanics* (3rd year Bachelor)
Affiliation	Arts et Métiers, Lille Fluid Mechanics Laboratory, Lille (France)

Period	September 2020 – to date (96 teaching hours in total)
Position	*Associate Professor*, Dept. Fluid Mechanics and Energetics
Course Title	*Design of Aeronautical Structures: CFD of an Airplane Wing* (3rd year Bachelor)
Affiliation	Arts et Métiers, Lille Fluid Mechanics Laboratory, Lille (France)

Period	September 2019 – to date (156 teaching hours in total)
Position	*Associate Professor*, Dept. Fluid Mechanics and Energetics
Course Title	*Finite Element Methods in Solid Mechanics* (3rd year Bachelor)
Affiliation	Arts et Métiers, Lille Fluid Mechanics Laboratory, Lille (France)

Period	September 2019 – to date (116 teaching hours in total)
Position	*Associate Professor*, Dept. Fluid Mechanics and Energetics
Course Title	*Heat Transfer and Thermal Science* (3rd year Bachelor)
Affiliation	Arts et Métiers, Lille Fluid Mechanics Laboratory, Lille (France)

Period	September 2019 – to date (200 teaching hours in total)
Position	*Associate Professor,* Dept. Fluid Mechanics and Energetics
Course Title	*Advanced Energetics and Turbomachinery* (1st year Master)
Affiliation	Arts et Métiers, Lille Fluid Mechanics Laboratory, Lille (France)

Period	October 2012 – January 2018 (176 teaching hours in total)
Position	*University Assistant,* Inst. Fluid Mechanics and Heat Transfer
Course Title	*Numerical Methods in Fluid Dynamics* (1st year Master)
Affiliation	TU Wien, Institute of Fluid Mechanics and Heat Transfer, Vienna (Austria)

Mentoring

Mentoring summary

	Internships	Exchange programs	Bachelor's theses	Master's theses
Total	17	2	2	21
at national scale	15	–	1	4
at international scale	2	2	1	17

Internships

Student	Shaimaa Hefny (2nd year Master's student)
Period	3-months internship, summer semester 2016
Project	Heat transfer for thermocapillary liquid bridges
Affiliation	TU Wien, Vienna (Austria)
	Alexandria University (Egypt)

Student	Tuğçe Türkbay (1st year Master's student)
Period	3-months internship, summer semester 2016
Project	Lagrangian topology in lid-driven cavities
Affiliation	TU Wien, Vienna (Austria)
	Çukurova University (Turkey)

Student	Joseph Cavataio (2nd year Bachelor's student)
Period	3-months internship, summer semester 2018
Project	Airway closure in human lungs
Affiliation	University of Michigan (USA)

Student	Samantha Rondeau (2nd year Bachelor's student)
Period	3-months internship, summer semester 2018
Project	Airway closure in human lungs
Affiliation	University of Michigan (USA)

Student	Pavithra Kalarani (1st year Master's student)
Period	2-months internship, summer semester 2020
Project	Deep learning approach applied to axial compressors
Affiliation	Arts et Métiers, Lille (France)
	École Centrale de Lille, Lille (France)

Student	Sufyan Shafi (1st year Master's student)
Period	2-months internship, summer semester 2020
Project	Projection of divergence-free flows
Affiliation	Arts et Métiers, Lille (France)
	École Centrale de Lille, Lille (France)

Student	Tarkash Siddique Munawar (1st year Master's student)
Period	2-months internship, summer semester 2020
Project	Stability analysis of a model for axial compressors
Affiliation	Arts et Métiers, Lille (France)
	École Centrale de Lille, Lille (France)

Student	Murukesh Muralidhar (1st year Master's student)
Period	2-months internship, summer semester 2021
Project	Experimental characterization of water droplet impinging on a wall
Affiliation	Arts et Métiers, Lille (France)
	École Centrale de Lille, Lille (France)

Student	Venkata Hari Charan Mulakaloori (1st year Master's student)
Period	2-months internship, summer semester 2021
Project	Linear stability analysis of an annular gap between rotor and carter
Affiliation	Arts et Métiers, Lille (France)
	École Centrale de Lille, Lille (France)

Student	Megan Dlima (1st year Master's student)
Period	2-months internship, summer semester 2021
Project	Turbulent flow through a grid in a pipe using OpenFOAM
Affiliation	Arts et Métiers, Lille (France)
	École Centrale de Lille, Lille (France)

Student	François Dottori (1st year Master's student)
Period	3-months, starting during summer semester 2021
Project	Study of non-Newtonian tubular exchanger-reactors
Affiliation	Arts et Métiers, Lille (France)
	École des Mines de Douai, Douai (France)

Student	Zhongxuan Huo (1st year Master's student)
Period	6-months, starting during summer semester 2022
Project	Elastic turbulence in the curvilinear geometry
Affiliation	Arts et Métiers, Lille (France)
	Polytech Lille, Lille (France)

Student	Aaron Gregorio Coutinho (1st year Master's student)
Period	6-months, starting during summer semester 2023
Project	Simulation of interacting Coandă-effect actuators for active flow control
Affiliation	Arts et Métiers, Lille (France)

Student	Parth Patel (1st year Master's student)
Period	5-months, starting during summer semester 2024
Project	Elastic turbulence in the curvilinear geometry
Affiliation	Arts et Métiers, Lille (France)
	Polytech Lille, Lille (France)

Student	Lucas Dupuis (1st year Master's student)
Period	5-months, starting during summer semester 2024
Project	Numerical study of oscillating grid turbulence
Affiliation	Arts et Métiers, Lille (France)
	École des Mines Nord-Europe, Douai (France)

Student	Alvaro Recio (1st year Master's student)
Period	3-months, starting during summer semester 2024
Project	Mechanical analogy of surge in axial compressors
Affiliation	Arts et Métiers, Lille (France)

Student	Sudhisha Echampati (1st year Master's student)
Period	3-months, starting during summer semester 2024
Project	Numerical simulation of rotor blade cascade
Affiliation	Arts et Métiers, Lille (France)

Exchange programs

Student	Takeru Oba (2nd year Master's student)
Period	3-months internship, winter semester 2017
Project	Finite-size Lagrangian coherent structures in liquid bridges
Affiliation	TU Wien, Vienna (Austria)
	Tokyo University of Science (Japan)

Student	Saeid Panahi (1st year Ph.D. student)
Period	3-months internship, winter semester 2017
Project	Stability of an annular flow in pipes
Affiliation	TU Wien, Vienna (Austria)
	Amirkabir University of Technology (Iran)

Bachelor's theses

Student	Faraz Beladi (3rd year Bachelor's student)
Period	3-months, starting during winter semester 2017
Project	Effect of non-divergence-free error in flow topology
Affiliation	TU Wien, Vienna (Austria)

Student	Parvathy K. K. (3rd year Bachelor's student)
Period	3-months, starting during summer semester 2016
Project	Finite-size Lagrangian coherent structures
Affiliation	TU Wien, Vienna (Austria)
	Birla Institute of Technology and Science (India)

Master's theses

Student	Michael Riedl (2nd year Master's student)
Period	6-months, starting during winter semester 2015
Project	Lagrangian topology in rotating-lid cavities
Affiliation	TU Wien, Vienna (Austria)

Student	Vincze Mihály (2nd year Master's student)
Period	6-months, starting during summer semester 2015
Project	Lagrangian topology in lid-driven cavities
Affiliation	TU Wien, Vienna (Austria)
	Budapest University of Technology and Economics, Budapest (Hungary)

Student	Arash Hajisharifi (2nd year Master's student)
Period	6-months, starting during winter semester 2016
Project	Lagrangian topology in rotating drums
Affiliation	TU Wien, Vienna (Austria)
	University of Pisa, Pisa (Italy)

Student	Sencer Yücesan (2nd year Master's student)
Period	6-months, starting during summer semester 2017
Project	Effect of wall curvature on flow stability in lid-driven cavities
Affiliation	TU Wien, Vienna (Austria)
	Fachhochschule Wiener Neustadt, Wiener Neustadt (Austria)

Student	Charlène Phan (2nd year Master's student)
Period	6-months, starting during summer semester 2020
Project	Flow control in an axial compressor
Affiliation	Arts et Métiers, Lille (France)
	Université de Lille, Lille (France)

Student	Venkata Sai Krishna Danda (2nd year Master's student)
Period	6-months, starting during summer semester 2020
Project	Impingement of a liquid droplet on a solid substrate
Affiliation	Arts et Métiers, Lille (France)
	Universität Rostock (Germany)

Student	Intissar Benjalila (2nd year Master's student)
Period	6-months, starting during summer semester 2020
Project	Airway reopening in human lungs
Affiliation	Arts et Métiers, Lille (France)
	École des Mines de Douai, Douai (France)

Student	Pierre Leroux (2nd year Master's student)
Period	6-months, starting during summer semester 2020
Project	Design of a pintle injector
Affiliation	Arts et Métiers, Lille (France)
	Centre national d'études spatiales, Paris (France)

Student	Raj Jayeshkumar Gandhi (2nd year Master's student)
Period	5-months, starting during summer semester 2021
Project	Elastic turbulence in the curvilinear geometry
Affiliation	Arts et Métiers, Lille (France)

Student	Oğuzhan Erken (2nd year Master's student)
Period	9-months, starting during starting during summer semester 2021
Project	Three-phase airway closure in human lungs
Affiliation	Koç Üniversitesi, Istanbul (Turkey)
	Arts et Métiers, Lille (France)

Student	Oussama El Mokkadem (2nd year Master's student)
Period	6-months, starting during summer semester 2021
Project	Numerical simulations of injectors for flow control
Affiliation	Arts et Métiers, Lille (France)

Student	Charles Carre (2nd year Master's student)
Period	5-months, starting during summer semester 2022
Project	Dynamics and rupture of non-Newtonian liquids plugs in bifurcated geometry
Affiliation	Arts et Métiers, Lille (France)
	École des Mines de Douai, Douai (France)

Student	Hossameldin Abdelaziz (2nd year Master's student)
Period	6-months, starting during summer semester 2022
Project	Multi-scale matching for flows with a grid
Affiliation	Arts et Métiers, Lille (France)

Student	Aditya Rathore (2nd year Master's student)
Period	6-months, starting during summer semester 2022
Project	Simulation of interacting Coandă-effect actuators for active flow control
Affiliation	Arts et Métiers, Lille (France)

Student	Romain Peron (2nd year Master's student)
Period	6-months, starting during summer semester 2022
Project	Fluid-structure interaction between a flat plate and an incoming flow
Affiliation	Arts et Métiers, Lille (France)

Student	Morteza Naeini (2nd year Master's student)
Period	6-months, starting during summer semester 2022
Project	Elasto-inertial instabilities in a two-phase Taylor-Couette flow
Affiliation	Arts et Métiers, Lille (France)
	École des Mines de Douai, Douai (France)

Student	Zhongxuan Huo (2nd year Master's student)
Period	6-months, starting during summer semester 2023
Project	Elastic turbulence in the curvilinear geometry
Affiliation	Arts et Métiers, Lille (France)
	Polytech Lille, Lille (France)

Student	Rami Janbeih (2nd year Master's student)
Period	5-months, starting during summer semester 2024
Project	Simulation of non-Newtonian centrifugal pumps
Affiliation	Arts et Métiers, Lille (France)

Student	Nesrine Tounsi (2nd year Master's student)
Period	6-months, starting during summer semester 2024
Project	Inlet condition sensitivity of Coandă-effect actuators for active flow control
Affiliation	Arts et Métiers, Lille (France)

Supervision of PhD Students and PostDoc researchers

PhD students

Student	Christian Schmidrathner
Period	9/2016–4/2018
Supervision	50% for 1.5 years together with H.C. Kuhlmann (50%)
Project	Steam sterilization
Funding	FFG project # 851030
Affiliation	TU Wien, Vienna (Austria)

Student	Meng Fan
Period	10/2019–12/2023 (defended in 12/2023)
Supervision	50% together with A. Dazin (50%)
Project	Stability and flow characterization in centrifugal pumps
Funding	CSC-ParisTech 2018
Affiliation	Arts et Métiers, Lille (France)

Student	Zhidian Yang
Period	10/2020–present
Supervision	30% together with O. Delgosha-Coutier (30%) and A. Dazin (40%)
Project	Numerical simulation, analysis, and prediction of a cavitating bubble near a wall
Funding	CSC-ParisTech 2019
Affiliation	Arts et Métiers, Lille (France)

Student	Renjie Hao
Period	7/2022–present
Supervision	30% together with A.S. Bahrani (30%) and M. Meldi (40%)
Project	Numerical and experimental study of liquid plugs in human lungs
Funding	CSC-ParisTech 2020
Affiliation	Arts et Métiers, Lille (France)

Student	Mohamed Elhawary
Period	10/2021–present
Supervision	30% together with J.-C. Loiseau (30%) and A. Dazin (40%)
Project	PINN for the physics of complex flows
Funding	ENSAM AAP PhD Theses 2021
Affiliation	Arts et Métiers, Lille (France)

Student	Hossameldin Abdelaziz
Period	10/2022–present
Supervision	50% together with M. Meldi (50%)
Project	Multi-scale matching for flows with a grid
Funding	ANR-JCJC 2021, "MultiMatchGrid"
Affiliation	Arts et Métiers, Lille (France)

Student	Bo Wang
Period	10/2022–present
Supervision	30% together with O. Delgosha-Coutier (30%) and A. Dazin (40%)
Project	Numerical study of multiple cavitating bubbles near a wall
Funding	CSC-ParisTech 2022
Affiliation	Arts et Métiers, Lille (France)

Student	Zhonxuan Hou
Period	10/2023–present
Supervision	30% together with S. Berti (30%) and A. Dazin (40%)
Project	Elastic turbulence in curvilinear geometries
Funding	CSC-ParisTech 2023
Affiliation	Arts et Métiers, Lille (France)

Student	Adou Francis Seka
Period	3/2024–present
Supervision	50% together with A. Dazin (50%)
Project	Modeling of stall in axial compressors
Funding	CIFRE-Safran
Affiliation	Arts et Métiers, Lille (France)

PostDoc researchers

Student	Meng Fan
Period	2/2024–present
Project	Numerical simulation of single- and multi-phase pumps
Funding	SuperGrid/General Electrics
Affiliation	Arts et Métiers, Lille (France)

Student	Marwane Elkarii
Period	9/2023–present
Project	Chaotic mixing, instabilities and transition in non-isothermal pipes
Funding	ANR Chaire Industrielle, "CORENSTOCK"
Affiliation	École des Mines Nord Europe, Douai (France)

Scientific Dissemination

Dissemination summary

	Book Chapters	Papers	Proceedings	Conferences	Invited Talks
Total	1	56	30	54	31
as sole author/speaker	–	5	–	2	31
with Ph.D. supervisor	1	25	12	29	–
with supervised Ph.D. students	–	5	3	5	–
since joining Arts et Métiers	–	42	14	24	23

Book chapters

B1. H. C. Kuhlmann, F. Romanò, *The lid-driven cavity* , Computational Modelling of Bifurcations and Instabilities in Fluid Dynamics, Springer, **50** (2019) 233–310.

Scientific papers

J1. F. Romanò, H. C. Kuhlmann, *Numerical investigation of the interaction of a finite-size particle with a tangentially moving boundary*, Int. J. Heat Fluid Fl., **62** (A) (2016) 75–82.

J2. F. Romanò, H. C. Kuhlmann, *Smoothed-profile method for momentum and heat transfer in particulate flows*, Int. J. Numer. Meth. Fluids, **83** (6) (2017) 485–512.

J3. F. Romanò, H. C. Kuhlmann, *Particle–boundary interaction in a shear-driven cavity flow*, Theor. Comp. Fluid Dyn., **31** (4) (2017) 427–445.

J4. F. Romanò, A. Hajisharifi, H. C. Kuhlmann, *Cellular flow in a partially filled rotating drum: regular and chaotic advection*, J. Fluid Mech., **825** (2017) 631–650.

J5. F. Romanò, S. Albensoeder, H. C. Kuhlmann, *Topology of three-dimensional steady cellular flow in a two-sided anti-parallel lid-driven cavity*, J. Fluid Mech., **826** (2017) 302–334.

J6. F. Romanò, H. C. Kuhlmann, M. Ishimura, I. Ueno *Limit cycles for the motion of finite-size particles in axisymmetric thermocapillary flows in liquid bridges*, Phys. Fluids, **29** (2017) 093303.

J7. C. Kuehn, F. Romanò, H. C. Kuhlmann, *Tracking particles in flows near invariant manifolds via balance functions*, Nonlinear Dyn., **92** (2018) 983–1000.

J8. F. Romanò, H. C. Kuhlmann, *Finite-size Lagrangian coherent structures in thermocapillary liquid bridges*, Phys. Rev. Fluids, **3** (2018) 094302.

J9. F. Romanò, *Oscillatory switching centrifugation: dynamics of a particle in a pulsating vortex*, J. Fluid Mech., **857** (2018) R3.

J10. F. Romanò, H. Wu, H. C. Kuhlmann, *A generic mechanism for finite-size coherent particle structures*, Int. J. Multiphase Flow, **111** (2019) 42–52.

J11. F. Romanò, H. C. Kuhlmann, *Heat transfer across the free surface of a thermocapillary liquid bridge*, Tech. Mech., **39** (2019) 72–84.

J12. F. Romanò, Parvathy K. K., H. C. Kuhlmann, *Finite-size Lagrangian coherent structures in a two-sided lid-driven cavity*, Phys. Rev. Fluids, **4** (2019) 024302.

J13. F. Romanò, H. C. Kuhlmann, *Finite-size coherent structures in thermocapillary liquid bridges: A review*, Int. J. Microgravity Sci. Appl., **36** (2019) 360201.

J14. M. Muradoglu, F. Romanò, H. Fujioka, J. B. Grotberg, *Effects of surfactant on propagation and rupture of a liquid plug in a tube.*, J. Fluid Mech., **872** (2019) 407–437.

J15. F. Romanò, H. Fujioka, M. Muradoglu, J. B. Grotberg, *Liquid plug formation in an airway closure model*, Phys. Rev. Fluids, **4** (2019) 093103.

J16. F. Romanò, *Reconstructing the unperturbed fluid flow by tracking of large particles*, Phys. Rev. Fluids, **4** (2019) 104301.

J17. Y. Hu, F. Romanò, J. B. Grotberg, *Effects of Surface Tension and Yield Stress on Mucus Plug Rupture: A Numerical Study*, J. Biomech. Eng., **142** (2020) 061007.

J18. F. Romanò, P.-E. des Boscs, H. C. Kuhlmann, *Forces and torques on a sphere moving near a dihedral corner in creeping flow*, Eur. J. Mech. - B/Fluids, **84** (2020) 110–121.

J19. F. Romanò, T. Türkbay, H. C. Kuhlmann, *Lagrangian chaos in lid-driven cavities*, Chaos, **30** (2020) 073121. **Featured Paper**

J20. F. Romanò, V. Suresh, P. A. Galie, J. B. Grotberg, *Peristaltic flow in the glymphatic system*, Nature – Sci. Rep., **10** (2020), 21065.

J21. I. Barmak, F. Romanò, P. Kunchi Kannan, H. C. Kuhlmann, *Coherent particle structures in high-Prandtl-number liquid bridges*, Micrograv. Sci. Tech., **33** (2021), 1-10.

J22. F. Romanò, M. Muradoglu, H. Fujioka, J. B. Grotberg, *The effect of viscoelasticity in an airway closure model*, J. Fluid. Mech., **913** (2021), A31.

J23. H. Wu, F. Romanò, H. C. Kuhlmann, *Attractors for the motion of a finite-size particle in a two-sided lid-driven cavity*, J. Fluid. Mech., **906** (2021), A4.

J24. F. Romanò, *Stability of generalized Kolmogorov flow in a channel*, Phys. Fluids, **33** (2021), 024106.

J25. F. Romanò, *Particle Coherent Structures in Confined Oscillatory Switching Centrifugation*, Crystals, **11** (2021), 183.

J26. F. Romanò, P.-E. des Boscs, H. C. Kuhlmann, *Stokesian motion of a spherical particle near a right corner made by tangentially moving walls*, J. Fluid Mech., **927** (2021), A41.

J27. I. Barmak, F. Romanò, H. C. Kuhlmann, *Finite-size coherent particle structures in high-Prandtl-number liquid bridges*, Phys. Rev. Fluids, **6** (2021), 084301.

J28. F. Romanò, A. Charles, F. Dottori, A. S. Bahrani, *Transition to turbulence in a heated non-Newtonian pipe flow*, Phys. Fluids, **33** (2021), 091702.

J29. A. Baretter, B. Godard, P. Joseph, O. Roussette, F. Romanò, R. Barrier, A. Dazin, *Experimental and numerical analysis of a compressor stage under flow distortion*, Int. J. Turbomach. Propuls. Power, **6** (2021), 43. **Cover Page**

J30. E. P. Beretta, F. Romanò, G. A. Sancini, J. B. Grotberg, G. F. Nieman, G. A. Miserocchi, *Pulmonary interstitial matrix and lung fluid balance from normal to the acutely injured lung*, Front. Physiol., **12** (2021), 781874.

J31. O. Erken, F. Romanò, J. B. Grotberg, M. Muradoglu, *Capillary instability of a two-layer annular film: An airway closure model*, J. Fluid Mech., **934** (2022), A7.

J32. S. A. Bahrani, S. Hamidouche, M. Moazzen, K. Seck, C. Duc, M. Muradoglu, J. B. Grotberg, F. Romanò, *Propagation and rupture of elastoviscoplastic liquid plugs in airway reopening model*, J. Non-Newt. Fluid Mech., **300** (2022), 104718.

J33. F. Romanò, *Reconstructing the neutrally-buoyant particle flow near a singular corner*, Acta Mech. Sinica, **38** (2022), 1-8.

J34. H. Fujioka, F. Romanò, M. Muradoglu, J. B. Grotberg, *Splitting of a three-dimensional liquid plug at an airway bifurcation*, Phys. Fluids, **34** (2022), 081907.

J35. F. Romanò, M. Muradoglu, H. Fujioka, J. B. Grotberg, *The effect of surfactant in an airway closure model*, Phys. Rev. Fluids, **7** (2022), 093103.

J36. A. Charles, F. Romanò, T. Ribeiro, S. Azimi, V. Rocher, J.-C. Baudez, S. A. Bahrani, *Laminar-turbulent intermittency in pipe flow for an Herschel-Bulkley fluid: Radial receptivity to finite-amplitude perturbations*, Phys. Fluids, **34** (2022), 111703.

J37. M. Stojanović, F. Romanò, H. C. Kuhlmann, *Stability of thermocapillary flow in liquid bridges fully coupled to the gas phase*, J. Fluid Mech., **949** (2022), A5.

J38. H. Wu, F. Romanò, H. C. Kuhlmann, *Attractors for the motion of a finite-size particle in a cubic lid-driven cavity*, J. Fluid Mech., **955** (2023), A16.

J39. O. Erken, B. Fazla, D. Izbassarov, F. Romanò, J. B. Grotberg, M. Muradoglu, *Effects of elastoviscoplastic properties of mucus on airway closure in healthy and pathological conditions*, Phys. Rev. Fluids, **8** (2023), 053102.

J40. M. Fan, A. Dazin, G. Bois, F. Romanò, *Effect of inlet leakage flow on the instability in a radial vaneless diffuser*, Phys. Fluids, **35** (2023), 014105.

J41. M. Fan, A. Dazin, G. Bois, F. Romanò, *Instabilities identification based on a new centrifugal 3D impeller outflow model*, Aerosp. Sci. Technol., **140** (2023), 108466.

J42. M. A. Elhawary, F. Romanò, J.-C. Loiseau, A. Dazin, *Machine learning for optimal flow control in an axial compressor*, The Europ. Phys. J. E, **46** (2023), 28.

J43. O. El Mokkadem, X. Chen, C. Phan, P. Joseph, A. Dazin, F. Romanò, *Small-width wall-attached Coandă jets for flow control*, Flow, **3** (2023), E17.

J44. Y. Hu, F. Romanò, J. B. Grotberg, *Entropic lattice Boltzmann model for surface tension effects on liquid plug rupture in two-and three-dimensional channels*, Phys. Rev. Fluids, **8** (2023), 073603.

J45. M. Stojanović, F. Romanò, H. C. Kuhlmann, *MaranStable: A linear stability solver for multiphase flows in canonical geometries*, SoftwareX, **23** (2023), 101405.

J46. J. B. Grotberg, F. Romanò, *Computational pulmonary edema: A microvascular model of alveolar capillary and interstitial flow*, APL Bioeng., **7** (2023), 036101.

J47. M. Fan, A. Dazin, G. Bois, F. Romanò, *Instabilities in a turbulent swirling source flow between parallel rings*, Phys. Fluids, **365** (2023), 101701.

J48. M. Fan, A. Dazin, G. Bois, F. Romanò, *Effect of radius ratio on the instabilities in a vaneless diffuser*, Europ. J. Mech. Fluids/B, **104** (2024), 1–7.

J49. M. Stojanović, F. Romanò, H. C. Kuhlmann, *Instability of axisymmetric flow in thermocapillary liquid bridges: Kinetic and thermal energy budgets for two-phase flow with temperature-dependent material properties*, European J. Appl. Math., **35** (2024), 267–293.

J50. H. Viola, V. Vasani, K. Washington, J. Hoon Lee, C. Selva, A. Li, C. J. Llorente, Y. Murayama, J. B. Grotberg, F. Romanò, S. Takayama, *Liquid plug propagation in computer-controlled microfluidic airway-on-a-chip with semi-circular microchannels*, Lab on a Chip, **24** (2024), 197–209.

J51. M. Stojanović, F. Romanò, H. C. Kuhlmann, *High-Prandtl-number thermocapillary liquid bridges with dynamically deformed interface: effect of an axial gas flow on the linear stability*, J. Fluid Mech., **978** (2024), A27.

J52. M. Stojanović, F. Romanò, H. C. Kuhlmann, *Flow instability in high-Prandtl-number liquid bridges with fully temperature-dependent thermophysical properties*, J. Fluid Mech., **978** (2024), A17.

J53. F. Romanò, M. Stojanović, H. C. Kuhlmann, *Scaling and modeling of the heat transfer across the free surface of a thermocapillary liquid bridge*, Int. J. Num. Meth. Heat Fluid Flow, **34** (2024), 1528–1566.

J54. A. Baretter, P. Joseph, O. Roussette, A. Dazin, F. Romanò, *Scaling laws at stall in an axial compressor with an upstream perturbation*, **submitted** (2023).

J55. B. Fazla, O. Erken, D. Izbassarov, F. Romanò, J. B. Grotberg, M. Muradoglu, *Effect of kinematic hardening of mucus polymers in an airway closure model*, **submitted** (2023).

J56. J. C. Grotberg, F. Romanò, J. B. Grotberg, *A novel model of pulmonary edema: mechanisms, insights, and puzzles*, **submitted** (2023).

Conference proceedings

P1. F. Romanò, H. C. Kuhlmann, *Interaction of a finite-size particle with the moving lid of a cavity*, PAMM, **15** (1) (2015) 519–520.

P2. F. Romanò, S. Albensoeder, H. C. Kuhlmann *Topology of three-dimensional steady cellular flow in a two-sided lid-driven cavity*, APS Bulletin (2015).

P3. H. C. Kuhlmann, F. Romanò, H. Wu, S. Albensoeder, *Particle-motion attractors due to particle–boundary interaction in incompressible steady three-dimensional flows*, The 20th Australasian Fluid Mechanics Conference (ed. G. Ivey, T. Zhou, N. Jones, S. Draper), Australasian Fluid Mechanics Society (2016), pp. 102, paper no. 449.

P4. F. Romanò, H. C. Kuhlmann *Topology of azimuthally travelling waves in thermocapillary liquid bridges*, APS Bulletin (2016).

P5. F. Romanò, H. C. Kuhlmann *Finite-size Lagrangian coherent particle structures in thermocapillary liquid bridges*, APS Bulletin (2017).

P6. H. Wu, F. Romanò, H. C. Kuhlmann, *Attractors for the motion of finite-size particles in a two-sided lid-driven cavity*, PAMM, **17** (2017) 669–670.

P7. H. Wu, F. Romanò, H. C. Kuhlmann, *Attractors for the motion of finite-size particles in a lid-driven cavity*, **25**. Fachtagung Experimentelle Strömungsmechanik, (2017), 62.

P8. H. Wu, F. Romanò, H. C. Kuhlmann, *Attractors for the motion of finite-size particles in a two-sided anti-parallel lid-driven cavity*, ICEFM (2018), 1–6.

P9. F. Romanò, H. Fujioka, M. Muradoglu, J. B. Grotberg, *CFD model of airway closure*, BMES (2018).

P10. M. Muradoglu, F. Romanò, H. Fujioka, J. B. Grotberg, *Effects of soluble surfactant on plug propagation and rupture in airways*, BMES (2018).

P11. H. Fujioka, F. Romanò, M. Metin, J. B. Grotberg, *Effect of gravity on the split of liquid plug at pulmonary bifurcation*, BMES (2018).

P12. F. Romanò, H. Fujioka, M. Metin, J. B. Grotberg, *Liquid plug formation in an airway closure model*, APS Bulletin (2018).

P13. M. Muradoglu, F. Romanò, H. Fujioka, J. B. Grotberg, *Effects of coughing on a surfactant-laden liquid plug in distal airways*, APS Bulletin (2018).

P14. P.-E. des Boscs, F. Romanò, H. C. Kuhlmann, *Forces and torques exerted by a Stokes corner flow on a moving sphere*, IFMC, (2019) 1–2.

P15. H. C. Kuhlmann, F. Romanò, *Finite-size coherent structures: a universal phenomenon?*, IFMC, (2019) 1–2.

P16. I. Barmak, F. Romanò, H. C. Kuhlmann, *Particle accumulation in high-Prandtl-number liquid bridges*, PAMM, **1** (2019) e201900058.

P17. F. Romanò, H. Fujioka, M. Muradoglu, J. B. Grotberg, *Effect of viscoelasticity and surfactant in airway closure model*, BMES (2019).

P18. V. Suresh, F. Romanò, P. A. Galie, J. B. Grotberg, *Peristaltic flow in the glymphatic system*, BMES (2019).

P19. H. Fujioka, F. Romanò, M. Muradoglu, J. B. Grotberg, *Effect of surfactant on the split of liquid plug at lung airway bifurcation*, BMES (2019).

P20. F. Romanò, H. Fujioka, M. Muradoglu, J. B. Grotberg, *Effect of viscoelasticity and surfactant on an airway closure model*, APS Bulletin (2019).

P21. M. Muradoglu, F. Romanò, H. Fujioka, J. B. Grotberg, *Effect of viscoelasticity and surfactant on the propagation and rupture of a liquid plug in an airway*, APS Bulletin (2019).

P22. M. Stojanovic, F. Romanò, H. C. Kuhlmann, *Modeling the heat transfer across the liquid-gas interface of a thermocapillary high-Prandtl-number liquid bridge*, IPHMT20 (2020).

P23. A. Dazin, P. Joseph, F. Romanò, Q. Gallas, J. Marty, G. Aigouy, M. Stoßel. and R. Niehuis, *The ACONIT project: an innovative design approach of active flow control for surge prevention in gas turbines*, IOP Conf. Ser.: Mater. Sci. Eng. **1024** (2021), 012068.

P24. M. Fan, G. Bois, A. Dazin, F. Romanò, *Effect of leakage on the performance of a centrifugal pump with a vaneless diffuser*, CMFF'22 (2022).

P25. J. B. Grotberg, F. Romanò, *Computational Pulmonary Edema*, APS Bulletin (2022).

P26. A. Baretter, P. Joseph, O. Roussette, F. Romanò, A. Dazin, *Experimental Analysis of an Axial Compressor Operating under Flow Distorsion*, Turbomachinery Technical Conference and Exposition GT2022 (2022).

P27. J. B. Grotberg, F. Romanò, J. C. Grotberg, *A Computational Model of Pulmonary Edema*, APS Bulletin (2023).

P28. B. Fazla, O. Erken, D. Izbassarov, F. Romanò, J. B. Grotberg, M. Muradoglu, *Airway Closure: Elastoviscoplastic and Kinematic Hardening Effects in a Mucus Model*, APS Bulletin (2023).

P29. R. K. Subramanian, Z. Yang, F. Romanò, O. Coutier-Delgosha, *Pressure measurement with shock wave, and liquid jet visualization of a cavitation bubble collapsing near the hard surface*, APS Bulletin (2023).

P30. M. A. Elhawary, F. Romanò, J.-C. Loiseau, and A. Dazin, *Deep neural networks for predicting and analyzing the performance of air-jets for active flow control in an axial compressor*, Proceedings of 15th European Conference on Turbomachinery Fluid dynamics Thermodynamics (2023).

Conferences

C1. F. Romanò, H. C. Kuhlmann, *SEM & DG-FEM applied to Fluid Dynamics*, 19th ERCOFTAC ADA-Pilot Center Meeting, Udine, Italy, May 2014.

C2. F. Romanò, H. C. Kuhlmann, *Interaction of a finite-size particle with the moving lid of a cavity*, GAMM 86th Annual Scientific Conference, Lecce, Italy, March 2015.

C3. F. Romanò, H.C. Kuhlmann, *Smoothed profile method for particle-laden flows*, 21st ERCOFTAC ADA-Pilot Center Meeting, Vienna, Austria, May 2015.

C4. F. Romanò, H. C. Kuhlmann, *Numerical investigation of the interaction of a finite-size particle with a tangentially moving boundary*, CMFF'15, Budapest, Hungary, September 2015.

C5. F. Romanò, H. C. Kuhlmann, *Modelling the motion of finite-size particles near a thermocapillary free-surface by a two-way-coupling approach*, ISPS-6/ITTW2015, Kyoto, Japan, September 2015.

C6. H. C. Kuhlmann, S. Masoudi, F. Romanò, *Multi-phase flow through converging nozzles*, 20th ERCOFTAC ADA-Pilot Center Meeting, Maribor, Slovenia, November 2015.

C7. F. Romanò, S. Albensoeder, H. C. Kuhlmann *Topology of three-dimensional steady cellular flow in a two-sided lid-driven cavity*, 68th Annual Meeting of the APS Division of Fluid Dynamics, Boston, USA, November 2015.

C8. H. C. Kuhlmann, F. Romanò, S. Albensoeder, *Flow topology and attractors for the motion of finite-size particles in a three-dimensional steady cavity flow*, 9th International Conference on Multiphase Flow, Firenze, Italy, May 2016.

C9. F. Romanò, H. C. Kuhlmann, *Modelling the motion of finite-size particles near a moving wall by a two-way coupling approach*, 9th International Conference on Multiphase Flow, Firenze, Italy, May 2016.

C10. F. Romanò, M. Ishimura, H. C. Kuhlmann, I. Ueno *On the role of the heat transfer in modelling axisymmetric particle accumulation in thermocapillary liquid bridges*, 8th Conference of the International Marangoni Association, Bad Honnef, Germany, June 2016.

C11. M. Ishimura, F. Romanò, H. C. Kuhlmann, I. Ueno *Experimental study on the finite-size particle behavior in a steady flow in a thermocapillary liquid bridge*, 8th Conference of the International Marangoni Association, Bad Honnef, Germany, June 2016.

C12. F. Romanò, H. C. Kuhlmann *Particle accumulation structures in steady closed flows driven by surface forces*, 11th European Conference of Fluid Dynamics, Seville, Spain, September 2016.

C13. F. Romanò, H. C. Kuhlmann *Topology of azimuthally travelling waves in thermocapillary liquid bridges*, 69th Annual Meeting of the APS Division of Fluid Dynamics, Portland, USA, November 2016.

C14. H.C. Kuhlmann, F. Romanò, H. Wu, S. Albensoeder, *Particle-motion attractors due to particle-boundary interaction in incompressible steady three-dimensional flows*, The 20th Australasian Fluid Mechanics Conference, Perth, Australia, December 2016.

C15. H. Wu, F. Romanò, H. C. Kuhlmann, *Attractors for the motion of finite-size particles in a two-sided lid-driven cavity*, GAMM 88th Annual Scientific Conference, Weimar, Germany, March 2017.

C16. F. Romanò, H.C. Kuhlmann, *Finite-size coherent structures in thermocapillary liquid bridges*, 25th ERCOFTAC ADA-Pilot Center Meeting, Vienna, Austria, April 2017.

C17. F. Romanò, H.C. Kuhlmann, *Instability of the flow in suspended thermocapillary thin films*, The 7th International Symposium "Bifurcations and Instabilities in Fluid Dynamics", The Woodlands, USA, July 2017.

C18. F. Romanò, H. C. Kuhlmann *Lagrangian finite-size coherent structures in thermocapillary liquid bridges*, ISPS-7/ELGRA-25, Juan les Pines, France, October 2017.

C19. H. Wu, F. Romanò, H. C. Kuhlmann *Attractors for the motion of finite-size particles in a lid-driven cavity*, Fachtagung "Experimentelle Strömungsmechanik", Karlsruhe, Germany, September 2017.

C20. F. Romanò, H. C. Kuhlmann *Finite-size Lagrangian coherent particle structures in thermocapillary liquid bridges*, 70th Annual Meeting of the APS Division of Fluid Dynamics, Denver, November 2017.

C21. H. Wu, F. Romanò, H.C. Kuhlmann, *Attractors for the motion of finite-size particles in two-sided lid driven cavities*, 26th ERCOFTAC ADA-Pilot Center Meeting, Graz, Austria, November 2017.

C22. H. Wu, F. Romanò, H. C. Kuhlmann *Attractors for the motion of finite-size particles in a two-sided anti-parallel lid-driven cavity*, ICEFM18, Munich, Germany, July 2018.

C23. F. Romanò, H. C. Kuhlmann *Heat transfer across the free surface of a thermocapillary liquid bridge*, CMFF'18, Budapest, Hungary, September 2018.

C24. F. Romanò, P.-E. des Boscs, H. C. Kuhlmann *Forces and torques on a spherical particle moving near the edge made by two rectangular walls in Stokes flow*, EFMC12, Vienna, Austria, September 2018.

C25. H. Wu, F. Romanò, H. C. Kuhlmann *Motion of finite-size particles in a lid-driven cubic cavity*, EFMC12, Vienna, Austria, September 2018.

C26. F. Romanò, H. Fujioka, M. Muradoglu, J. B. Grotberg, *CFD model of airway closure*, BMES, Atlanta, USA, October 2018.

C27. M. Muradoglu, F. Romanò, H. Fujioka, J. B. Grotberg, *Effects of soluble surfactant on plug propagation and rupture in airways*, BMES, Atlanta, USA, October 2018.

C28. H. Fujioka, F. Romanò, M. Metin, J. B. Grotberg, *Effect of gravity on the split of liquid plug at pulmonary bifurcation*, BMES, Atlanta, USA, October 2018.

C29. I. Barmak, F. Romanò, H. C. Kuhlmann *Particle accumulation in high-Prandtl-number liquid bridges*, 28th ERCOFTAC ADA Pilot Centre Meeting, Maribor, Slovenia, November 2018.

C30. F. Romanò, H. Fujioka, M. Metin, J. B. Grotberg, *Liquid plug formation in an airway closure model*, 71th Annual Meeting of the APS Division of Fluid Dynamics, Atlanta, November 2018.

C31. M. Metin, F. Romanò, H. Fujioka, J. B. Grotberg, *Effects of coughing on a surfactant-laden liquid plug in distal airways*, 71th Annual Meeting of the APS Division of Fluid Dynamics, Atlanta, November 2018.

C32. F. Romanò, H. Fujioka, M. Muradoglu, J. B. Grotberg, *Effect of viscoelasticity and surfactant in airway closure model*, BMES, Phyladelphia, USA, October 2019.

C33. V. Suresh, F. Romanò, P. A. Galie, J. B. Grotberg, *Peristaltic flow in the glymphatic system*, BMES, Phyladelphia, USA, October 2019.

C34. H. Fujioka, F. Romanò, M. Muradoglu, J. B. Grotberg, *Effect of surfactant on the split of liquid plug at lung airway bifurcation*, BMES, Phyladelphia, USA, October 2019.

C35. F. Romanò, H. Fujioka, M. Muradoglu, J. B. Grotberg, *Effect of viscoelasticity and surfactant on an airway closure model*, APS, Seattle, USA, November 2019.

C36. M. Muradoglu, F. Romanò, H. Fujioka, J. B. Grotberg, *Effect of viscoelasticity and surfactant on the propagation and rupture of a liquid plug in an airway*, APS, Seattle, USA, November 2019.

C37. M. Stojanovic, F. Romanò, H. C. Kuhlmann, *Stability of axisymmetric thermocapillary flow in high-Prandtl-number liquid bridges based on a Biot function approach for the liquid-gas heat transfer*, IMA10, Iași, Romania, June 2020.

C38. M. Stojanovic, F. Romanò, H. C. Kuhlmann, *Modeling the heat transfer across the liquid-gas interface of a thermocapillary high-Prandtl-number liquid bridge*, IPHMT20, Marseille, France, July 2020.

C39. A. Dazin, P. Joseph, F. Romanò, Q. Gallas, J. Marty, G. Aigouy, M. Stoßel. and R. Niehuis, *The ACONIT project: an innovative design approach of active flow control for surge prevention in gas turbines*, 10th EASN 2020, Virtual Conference, September 2020.

C40. C. Carré, T. Lacassagne, S. Hamidouche, F. Romanò, and A Bahrani, *Dynamique et rupture de bouchons liquides non-newtoniens en géométrie bifurquée*, Journée du GDR Micro et Nano Fluidique : Ondes, Fluides, Interfaces, Paris, France, September 2021.

C41. F. Romanò, O. Erken, M. Muradoglu, H. Fujioka, and J. B. Grotberg, *Surfactant, viscoelasticity, elastoviscoplasticity and two-layer lining in an airway closure model*, APS, Phoenix, USA, November 2021.

C42. M. Stojanovic, H. C. Kuhlmann, and F. Romanò, *Impact of dynamic surface deformations on the flow instability in high-Prandtl-number liquid bridges*, APS, Phoenix, USA, November 2021.

C43. M. A. Elhawary, F. Romanò, J.-C. Loiseau, A. Dazin, *Machine learning for optimal flow control in an axial compressor*, Challenges and Benchmarks for quantitative AI in Complex Fluids and Complex Flows, Rome, Italy, June 2022.

C44. A. Baretter, P. Joseph, O. Roussette, F. Romanò, A. Dazin, *Experimental Analysis of an Axial Compressor Operating under Flow Distorsion*, Turbomachinery Technical Conference and Exposition GT2022, June 2022, Rotterdam, Netherlands.

C45. M. Fan, G. Bois, A. Dazin, F. Romanò, *Effect of leakage on the performance of a centrifugal pump with a vaneless diffuser*, CMFF'22, Budapest, Hungary, September 2022.

C46. B. Fazla, O. Erken, F. Romanò, M. Muradoglu, *A viscoplastic mucus model with kinematic hardening for airway closure*, EFMC14, Athens, Greece, September 2022.

C47. J. B. Grotberg, F. Romanò, *Computational Pulmonary Edema*, APS, Indianapolis, USA, November 2022.

C48. M. Elhawary, F. Romanò, J.-C. Loiseau, and A. Dazin, *Deep neural networks for predicting and analyzing the performance of air-jets for active flow control in an axial compressor*, 15th European Conference on Turbomachinery Fluid dynamics Thermodynamics, Budapest, Hungary, April 2023.

C49. F. Romanò, *Instabilities, mixing and turbulence in single- and multi-phase systems*, Journées Scientifiques, Fluides et écoulements complexes : des solutions pour l'avenir, Nantes, France, June 2023.

C50. P. Koullapis, A. Syrakos, F. Stylianou, S. Kassinos, M. Muradoglu, Z. Yang, F. Romanò, J. B. Grotberg, *Assessment of 2-phase solvers for low capillary number flows in lung airways*, International Congress on Rheology, Athens, Greece, July 2023.

C51. F. Romanò, *A Microvascular Model of Alveolar Capillary and Interstitial Flow*, Journée Thématique M2VC Axe Biomécanique/Bio-ingénierie de la Fédération Lilloise de Mécanique, Lille, France, September 2023.

C52. J. B. Grotberg, F. Romanò, J. C. Grotberg, *A Computational Model of Pulmonary Edema*, APS, Washington, USA, November 2023.

C53. B. Fazla, O. Erken, D. Izbassarov, F. Romanò, J. B. Grotberg, M. Muradoglu, *Airway Closure: Elastoviscoplastic and Kinematic Hardening Effects in a Mucus Model*, APS, Washington, USA, November 2023.

C54. R. K. Subramanian, Z. Yang, F. Romanò, O. Coutier-Delgosha, *Pressure measurement with shock wave, and liquid jet visualization of a cavitation bubble collapsing near the hard surface*, APS, Washington, USA, November 2023.

Invited talks

S1. F. Romanò, *Particle accumulation structures in thermocapillary liquid bridges*, Tokyo University of Science, Tokyo, Japan, March 2016.

S2. F. Romanò, *A universal mechanism for rapid particle accumulation in fluids*, PPrime, Poitiers, France, November 2017.

S3. F. Romanò, *Lagrangian chaos: mixing and coherent structures*, Institute of Science and Technology, Vienna, Austria, January 2018.

S4. F. Romanò, *Liquid plug formation in an airway closure model*, Institute of Science and Technology, Vienna, Austria, September 2018.

S5. F. Romanò, *Airway closure in microscopic bronchioles* (talk held within the framework of the course BIOMEDE 476 001 WN 2019), University of Michigan, Ann Arbor, USA, April 2019.*

S6. F. Romanò, *Particle coherent structures in incompressible fluid flows*, Technische Universität München, Munich, Germany, June 2019.

S7. F. Romanò, *Peristaltic flow in the glymphatic system*, Technische Universität Wien, Vienna, Austria, June 2019.

S8. F. Romanò, *Peristaltic flow in the glymphatic system*, Institute of Science and Technology, Vienna, Austria, June 2019.

S9. F. Romanò, *Finite-Size Lagrangian coherent structures*, University of Lille, Lille, France, September 2019.*

S10. F. Romanò, *Effect of viscoelasticity and surfactant in an airway closure model*, University of Lille, Lille, France, May 2020.

S11. F. Romanò, *Flow Mixing and Particle Transport in Cavities*, **Keynote speaker**, 5th Jin Shan International Symposium on Fluids Machinery and Engineering, Zhenjiang, China, November 2020.

S12. F. Romanò, *Reconstructing the fluid flow by tracking of large particles*, **Invited symposium speaker**, 1st BICTAM-CISM Symposium on Dispersed Multiphase Flows, Beijing, China, March 2021.

S13. F. Romanò, *Airway closure: the effects of surfactant, viscoelasticity, elastoviscoplasticity and two-layer lining*, University of Udine, Udine, Italy, November 2021.

S14. F. Romanò, *Airway closure: the effect of surfactant, viscoelasticity, elastoviscoplasticity and two-layer lining*, **Keynote speaker**, Mathematics and Physics of Fluids 2021, IIT Gandhinagar, India, November 2021.

S15. F. Romanò, *The Fluid Mechanics of Lung Clogs in the Bronchioles*, Institute of Science and Technology, Vienna, Austria, November 2021.

S16. F. Romanò, *The Fluid Mechanics of Lung Clogs in the Bronchioles*, VirginiaTech, Roanoke, Virginia, USA, November 2021.

S17. F. Romanò, *The Fluid Mechanics of Airway Closure in the Bronchioles*, LMFL Fluid Mechanics Webinar, LMFL, Lille, France, February 2022. YouTube*

S18. F. Romanò, *Mixing and Accumulation of Particles in Cavities at Low and Moderate Reynolds Numbers*, LTEN, Polytech Nantes, Nantes, France, April 2022.

S19. F. Romanò, *Rotating instabilities in a centrifugal pump*, Lille Turbulence Program, LMFL, Lille, France, July 2022.*

S20. F. Romanò, *The Fluid Mechanics of Airway Closure in the Bronchioles*, DynFluid, Arts et Métiers, Paris, France, November 2022.

S21. F. Romanò, *The Fluid Mechanics of Airway Closure in the Bronchioles*, Department of Physics, University of Rome Tor Vergata, Rome, Italy, January 2023.

S22. F. Romanò, *Hydrodynamic Instability in Thermocapillary Liquid Bridges*, LEGI, Université Grenoble Alpes, Grenoble, France, January 2023.

S23. F. Romanò, *Hydrodynamic Instability in Thermocapillary Liquid Bridges*, ETSIAE-UPM and Numath's group, Spain, February 2023.

S24. F. Romanò, *Mixing and Accumulation of Particles in Cavities at Low and Moderate Reynolds Numbers*, VirginiaTech, Roanoke, Virginia, USA, May 2023.

S25. F. Romanò, *The Fluid Mechanics of Airway Closure in the Bronchioles*, Department of Biomedical Engineering, Atlanta, GeorgiaTech, Georgia, USA, May 2023.

S26. F. Romanò, *Interstitial Flow: Two Elucidating Examples of First-Principle Modeling applied to Microscale Bioflows*, **Invited speaker**, Nano S&T-2023, Osaka, Japan, May 2023.

S27. F. Romanò, *Machine Learning for Optimal Flow Control in an Axial Compressor*, **Keynote speaker**, Artificial Intelligence meets Fluid Dynamics, India, July 2023. YouTube

S28. F. Romanò, *Pulmonary Edema: A Microvascular Septal Tract Model*, Institute of Fluid Mechanics and Heat Transfer, TUWien, Vienna, Austria, July 2023.

S29. F. Romanò, *Instabilities in a Centrifugal Pump*, **Plenary speaker**, 17th Asian International Conference on Fluid Machinery (AICFM17), Zhenjiang, China, October 2023.

S30. F. Romanò, *The Fluid Mechanics of Airway Closure in the Bronchioles*, FAST, Université Paris-Saclay, Paris, France, October 2023.

S31. F. Romanò, *Self-organizing particles in a chaotic thermocapillary liquid bridge*, TU Dresden, Dresden, Germany, March 2024.

* = invited talks internal to the same affiliation